Numerical Modeling of Drift Resonance and Drift-bounce Resonance between Ultra-low Frequency Waves and Energetic Particles in the Inner Magnetosphere

by

Chengrui Wang

A thesis submitted in partial fulfillment of the requirements for the degree of

Doctor of Philosophy

Department of Physics
University of Alberta

Abstract

The main topic of this thesis is the investigation of drift resonance and drift-bounce resonance between energetic particles and Pc3-5 Alfvénic ultra-low frequency (ULF) waves in the Earth's inner magnetosphere. We have developed numerical models to simulate how the dynamics of O^+, H^+ ions and electrons are affected by Alfvén waves in a dipole magnetic field. These models are used to interpret observations on differential particle flux variations that are caused by interactions with ULF waves in the magnetosphere. Observational data from different satellite projects, such as Cluster and Van Allen Probes, and from the CARISMA ground magnetometer observatory array are introduced to investigate the characteristics of ULF waves and the corresponding energetic particle flux variations.

We present observational studies on two fast-damped ULF wave events observed by Cluster after an interplanetary shock. Comparisons between multi-satellite observations suggest that Landau damping is more effective in the plasmasphere boundary layer than in the plasmasphere due to the relatively higher proportion of Landau resonant ions that exist in the plasmasphere boundary layer. Also, the energy exchange between waves and particles through Landau damping is considered to be more efficient when heavier ions such as O^+ are present. Based on the analysis of these events, further studies with computation models are recommended for wave-particle interactions.

The test-particle simulations presented in this thesis reproduced several features of the pitch angle and energy spectrum of ion differential fluxes observed by the Van Allen Probes-A spacecraft on October 6, 2012. The observed and simulated fluxes are well correlated with giant pulsations of frequency $f \sim 10$ mHz and contain

modulations in a narrow range of energy, with stronger enhancements occurring for non-equatorially mirroring particles. For ions at 35° pitch angle, a maximum in the differential flux oscillations occurs at an energy of $\sim$ 150 keV, which is consistent with predictions made with drift resonance theory. The lack of enhanced differential fluxes of particles near the 90° pitch angle can be explained by the dependence of the resonance energy on the pitch angle.

The electron flux modulations in ULF waves observed by RBSP-A on October 31, 2012 [*Claudepierre et al.*, 2013] have been reproduced with our simulation results. The simulated fluxes have larger amplitudes and slower attenuation rates than observed fluxes due to the finite energy resolution of the MagEIS instrument on the spacecraft. When they are binned in energy as in the MagEIS instrument, they appear remarkably similar to the observed fluxes. Test particle simulations of $N = 0$ drift resonance and $N = -2$ drift-bounce resonance with O^+ ions reveal complex dynamics in which different wave-particle resonances can potentially interact. These simulations illustrate the expected behavior of ring current energetic ion populations in a region where poloidal mode ULF waves are ubiquitous.

Another MHD Alfvén wave model with a more realistic ionosphere boundary condition has been used to study the drift-bounce resonance of H^+ ions with second harmonic ULF field line resonance. We used the forward Liouville method and the Monte Carlo method to reconstruct the distribution function of H^+ ions when they interacted with ULF waves. It has been demonstrated that second-harmonic poloidal mode waves are efficient in energizing ions to tens of keV over timescales of tens of minutes. The test-particle simulations of bounce-resonance reproduce particle signatures which agree with theoretical predictions.

Preface

Chapter 3 of this thesis has been submitted as Wang, C., R. Rankin, and Q.-G. Zong, "Fast damping of ultralow frequency waves excited by interplanetary shocks in the magnetosphere", Journal of Geophysical Research: Space Physics. Vol.120 (4), 2438-2451, doi:10.1002/2014JA020761, 2015. I was responsible for the physical formulations, computational analysis, data analysis, as well as the manuscript composition. R. Rankin was supervisory author and was involved with concept formation and manuscript composition.

Chapter 6 of this thesis has been submitted as C. Wang, R. Rankin, Y. Wang, Q.-G. Zong, X. Zhou, K. Takahashi, R. Marchand, and A. F. Degeling, "Poloidal mode wave-particle interactions inferred from Van Allen Probes and CARISMA ground-based observations", Journal of Geophysical Research: Space Physics. I was responsible for the physical formulations, computational analysis, data analysis, as well as the manuscript composition. R. Rankin was supervisory author and was involved with concept formation and manuscript composition.

Chapter 7 have been submitted as C. Wang, R. Rankin, Y. Wang, Q.-G. Zong, X. Zhou, K. Takahashi, R. Marchand, A. F. Degeling, and D. Sydorenko "Ultra-low frequency wave-particle interactions in Earth's outer radiation belt" in the American Geophysical Union Monograph on "Dayside Magnetospheric Interactions". I was responsible for the physical formulations, computational analysis, data analysis, as well as the manuscript composition. R. Rankin was supervisory author and was involved with concept formation and manuscript composition.

Chapter 8 of this thesis has been published as C. Wang, R. Rankin, and D. Sydorenko, "Simulation of bounce resonance ULF wave-particle interactions", URSI

Asia-Pacific Radio Science Conference (URSI AP-RASC), IEEE, doi:10.1109/URSIAP-RASC.2016.7601363, 2016. I was responsible for the physical formulations, computational analysis as well as the manuscript composition. R. Rankin was supervisory author and was involved with concept formation and manuscript composition.

To
My parents

Acknowledgements

I would like to express my sincere gratitude to my supervisor Dr. Robert Rankin for his continuous support of my Ph.D. study. His patience and insightful guidance helped me in all the time of research and writing of this thesis. I would also like to thank the rest of my supervisory committee, Dr. Richard Marchand and Dr. Ian Mann, for their helpful comments and encouragement. Without their precious helps, it would not be possible to conduct this thesis. I am grateful to Dr. Dmytro Sydorenko and Dr. Alexander Degeling for all the invaluable discussions with them, and for their kindly helps on developing my models. Thanks to my parents for their selfless love. Their encouragements always help me throughout the difficult times in my life.

Contents

List of Tables

List of Figures

List of Symbols

$\mathbf{E}$	Electric field vector
$\mathbf{E}_1$	Electric field perturbation vector
$\mathbf{B}$	Magnetic field vector
$\mathbf{B}_0$	Unperturbed background magnetic field vector
$\mathbf{B}_1$	Magnetic field perturbation vector
$\mathbf{j}$	Current vector
t	Time
ρ	Mass density
ρ_c	The net charge density
μ_0	Permeability of free space
ϵ_0	Permittivity of free space
σ	Plasma conductivity
σ_P	Pedersen conductivity
Σ_P	Height-integrated Pedersen conductivity
σ_H	Hall conductivity
Σ_H	Height-integrated Pedersen conductivity
γ_s	The adiabatic index
$\mathbf{k}$	Wavenumber vector
v_A	Alfvén speed
v_{A0}	Alfvén speed at the equator
c_s	Plasma sound speed
r	Radius in spherical coordinate system
θ	Co-latitude in spherical coordinate system
ϕ	Azimuthal angle in spherical coordinate system
L	The L-shell, or McIlwain L-parameter
x_1, x_2, x_3	Components of dipolar coordinate system
h_1, h_2, h_3	The scale factors of dipolar coordinate system
E_1, E_2, E_3	Components of electric field vector in dipolar coordinate system
B_1, B_2, B_3	Components of magnetic field vector in dipolar coordinate system
B_{11}	Compressional component of wave magnetic field
j_1, j_2, j_3	Components of current vector in dipolar coordinate system
$S_{N,M}$	Eigenfunction of field line resonance, N, M here are the orders of field line resonance
$\widehat{S_N}$	Normalized eigenfunction of field line resonance

s	$s = \cos\theta$, θ is the co-latitude
s_{max}	Maximum value of s at one footprint of the field line
$\Re$	Real part operator on a complex value
R_D	External driver amplitude in unit of nT
ω_0	External driver frequency
ω_N	Eigenfrequency of field line resonance with order N
$\Delta\omega$	Difference between driver frequency and eigenfrequency $\omega_N - \omega_0$
W	Kinetic energy of particle
$W_\perp$	Perpendicular kinetic energy of particle
$W_\parallel$	Parallel kinetic energy of particle
m	Mass of particle. m also refers to azimuthal wavenumber. The usage of m will provide with specification.
$\mathbf{p}$	Particle momentum vector
$p_\parallel$	Parallel component of a particle's momentum
O^+	Oxygen ion
H^+	Hydrogen ion, also known as proton
e	Electron, or charge of electron
$v_\parallel$	Parallel velocity of particle
$v_\perp$	Perpendicular velocity of particle
μ	First adiabatic invariant of particle
α	Pitch angle of particle
α_{eq}	Equatorial pitch angle of particle
K	Second adiabatic invariant of particle.
Φ	Third adiabatic invariant of particle
Ω_g	Gyrofrequency of particle
T_{gyro}	Period of particle's gyro-motion
ω_b	Bounce frequency of particle
τ_b	Bounce period of particle
ω_d	Drift frequency of particle
τ_d	Drift period of particle
ω	Angular frequency of wave
T	Wave period
γ	Imaginary part of wave frequency, also known as damping rate. γ also refers to Lorentz factor in context related to relativistic effect. The usage of γ will provide with specification.
N	Order of drift-bounce resonance
f	The distribution function, also known as the phase space density. f also refers to wave frequency $f = \omega/2\pi$. The usage of f will provide with specification.
J	Differential flux
J_0	10-minutes running boxcar averaged differential flux used by *Claudepierre et al.* [2013]
R_e	Radius of the Earth, $R_e = 6,371$ km
c	Speed of light in vacuum, $c = 2.998 \times 10^8$m/s
ELF	Extremely-low frequency

ULF	Ultra-low frequency
VLF	Very-low frequency
Pc	Continuous pulsations, a type of ULF wave
Pi	Irregular pulsations, a type of ULF wave
Pgs	Giant pulsations, a type of ULF wave
FLR	Field line resonance
PSD	Phase space density
RBSP	Radiation Belt Storm Probes, also known as the Van Allen Probes
MagEIS	Magnetic Electron Ion Spectrometer, an instrument on RBSP
CARISMA	Canadian Array for Realtime Investigations of Magnetic Activity project
LHS	Left-hand side (of equation)
RHS	Right-hand side (of equation)

Chapter 1

Introduction

In this chapter, we introduce fundamental space physics phenomena that are relevant to this thesis. As solar wind is an important driver of ultra-low-frequency (ULF) waves in the magnetosphere, we first give an overview of the sun and solar wind. We then review different areas of the magnetosphere to provide insight into the plasma environment for ULF waves and high-energy particles in the radiation belts. The ionosphere is the boundary of field line resonance reflection, and its conductivity plays an important role in the wave energy damping process. We will also briefly review geomagnetic storms and substorms that are related to the generation of different plasma waves, including ULF waves. The motivation for this thesis will be summarized in Section 1.5.

1.1 The Sun as the Source of Solar Wind

The sun is the closest star to the Earth. It is not only the source of virtually all energy in the solar system but also the source of most of the space plasma throughout the solar system. Solar activity creates variations in the Earth's plasma environment. Some properties of the sun are shown in Table 1.1, while the sun's overall structure is shown in Figure 1.1. Regions of the sun are listed below [*Kivelson and Russell*, 1995]:

The sun's energy is generated in the core region by thermonuclear reactions. Thermonuclear reactions occur because the core of the sun has an extremely high

Table 1.1: Bulk parameters of the Sun. Modified from *Kivelson and Russell* [1995].

Age	4.5×10^9 yr
Mass	1.99×10^{30} kg
Radius	$696,000$ km
Mean density	1.4×10^3 kg $\cdot$ m^{-3}
Mean distance from the Earth (1AU)	150×10^6 km (215 solar radii)
Surface gravity	274 m $\cdot$ s^{-2}
Escape velocity	617.6 km/s
Radiation emitted (luminosity)	3.86×10^{26} W
Carrington rotation period	27 d
Mass loss rate	$\sim 10^9$ kg/s
Effective black-body temperature	$5,785$ K
Visual magnitude	-26.74
Spectral type	G2V (yellow dwarf, main sequence star)
Composition	90%H, 10%He, 0.1% other elements

temperature (more than $10,000,000$ K) and its dense gas has been compressed by tremendously large gravitational forces.

The radiative zone extends from a depth of $515,000$ km to $200,000$ km from the bottom of the solar atmosphere. Energy generated from the core propagates outwards and gets transported via diffusion of γ-ray photons. The photons are scattered, absorbed and remitted in the radiative zone and gradually transported to the outer zones of the sun. As the mean free path of photons in this region is very small, it takes millions of years for a photon to move to the next layer, which is called the convection zone.

The convection zone is the outer-most layer of the solar interior. This zone is located in the uppermost 30% of the solar interior. Energy is mainly transported by convection in this region.

The solar atmosphere is the only region that is visible from the outside. Solar energy is radiated into space from the solar atmosphere. From the interior to the exterior, the solar atmosphere is composed of several layers: the photosphere, the chromosphere, the transition region, and the corona. An example of the sun's atmosphere is also shown in Figure 1.1.

The thickness of the photosphere is about 500 km. Visible light originates in the

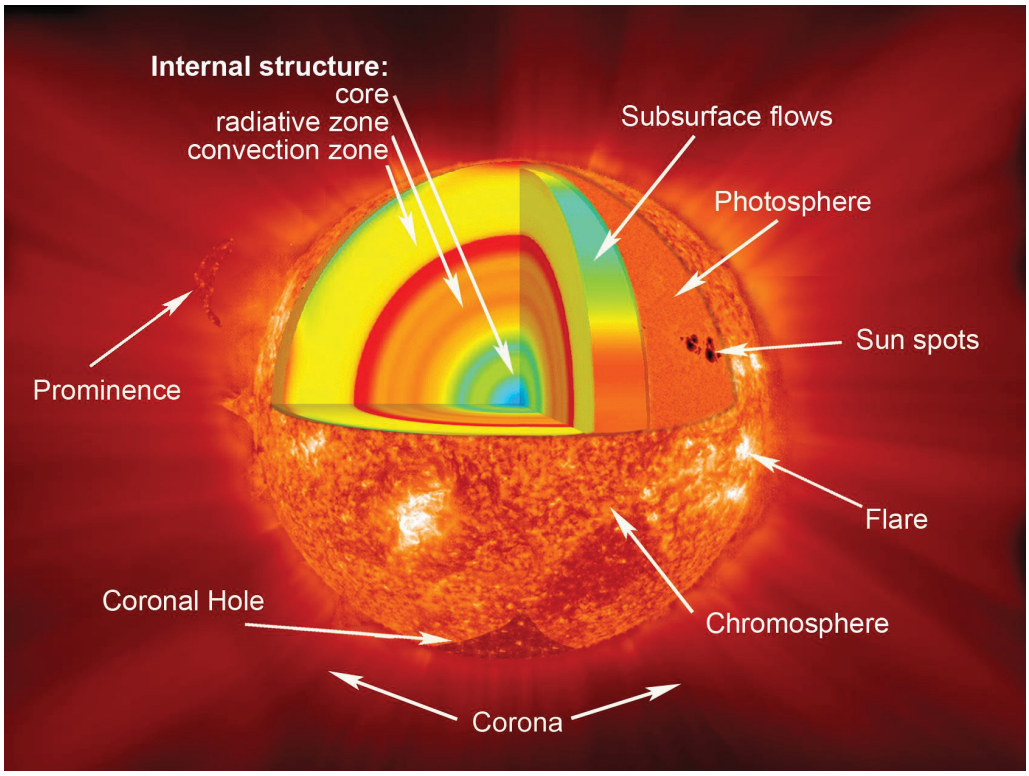

Figure 1.1: The interior of the Sun, and the structure of the Sun's atmosphere. Taken from: solarsystem.nasa.gov/planets/sun/indepth.

photosphere and accounts for the majority of the total solar luminosity. Radiation from the photosphere is primarily in the form of thermal black-body emissions with an effective temperature of about 5800 K. Relatively low temperatures and high magnetic field regions on the photosphere are called sunspots. The total number of sunspots observed on the sun's surface varies from year to year, but appears to be on an 11-year cycle. The total number of sunspots is also an indication of the sun's activity.

The thickness of the chromosphere is about $2000 - 3000$ km. The temperature increases from about 4300 K at the bottom to about 10^4 K at the top of the chromosphere. The transition layer connects the top of chromosphere to the bottom of corona.

The solar corona is the uppermost region of the solar atmosphere. It extends to several solar radii. The corona is a plasma with a temperature of around 10^6 K. The activity of the solar corona plasma is strongly connected to near-Earth space weather

since it extends out into interplanetary space and becomes the source of the solar wind.

As the solar wind plasma has high conductivity, the sun's magnetic field is frozen into the plasma throughout the solar system. The magnetic field in the solar wind is called the interplanetary magnetic field (IMF). *Parker* [1958] proposed that the IMF has a spiral form because the solar rotation distorts the magnetic field.

Typical observations of the solar wind at 1 AU record speeds of about $300 - 1400$ km/s, a density $1 - 10$ cm^{-3}, and a magnetic field of several nT. However, solar wind activity varies dynamically in density, temperature and speed over time and over solar latitude and longitude. Strong solar wind activities are associated with solar flares and coronal mass ejections (CMEs). A solar flare is a sudden flash of increased solar brightness. Solar flares release energetic particles and stored magnetic energy from the corona into space via magnetic reconnection. A CME is caused by a sudden and violent release of plasma and the magnetic field from unstable coronal structures.

As a result of solar activity, the IMF and particles in the solar wind affect the Earth's own magnetic field and near-earth plasma, and generate different magnetospheric processes. The structure and the important areas of the magnetosphere are described in the Section 1.2.

1.2 The Magnetosphere

The Earth's magnetic field protects its surface from being directly bombarded by high-energy particles in the solar wind. When solar wind encounters the Earth's magnetic field, it forms a magnetospheric cavity called the magnetosphere. The direction of the solar wind acts to compress the magnetosphere on the dayside and stretched it to the nightside. Figure 1.2 shows a schematic of the magnetosphere and its important structures.

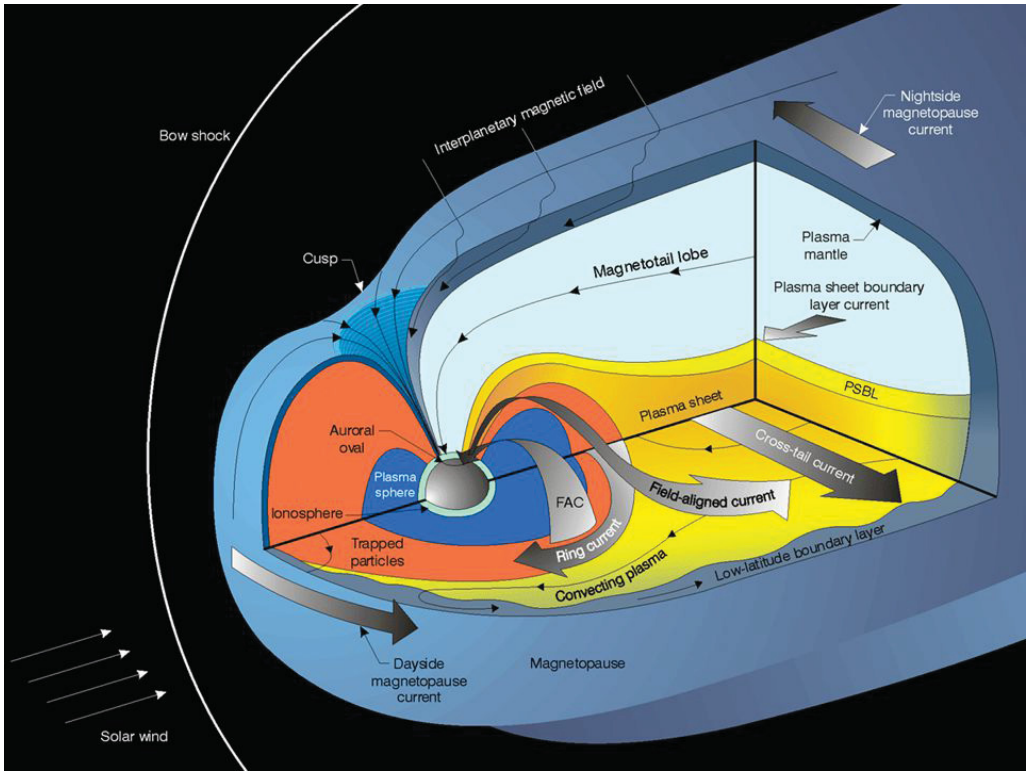

Figure 1.2: Schematic diagram of the magnetosphere. Taken from: mms.space.swri.edu/science-4.html.

1.2.1 The Bow Shock and the Magnetosheath

In Figure 1.2, the bow shock is the boundary where the supersonic solar wind abruptly slows to subsonic values at the upstream of the magnetosphere. The region between the outer boundary of the magnetosphere and the magnetopause is called the magnetosheath. In the magnetosheath region, the solar wind's kinetic energy is converted into thermal energy.

1.2.2 The Magnetopause

The day-side boundary between the solar wind plasma and magnetospheric plasma is defined as the magnetopause. A dynamic equilibrium between the dynamic ram pressure of the solar wind and the magnetic pressure of the Earth's magnetic field is established at the magnetopause. On the dayside, the equatorial standoff distance of the magnetopause is about $10R_e$ (Earth's radius) [*Roelof and Sibeck*, 1993] although

it varies depending on the activities of the sun and the solar wind.

At the day-side magnetopause, magnetic reconnection is known to be an important process for coupling solar wind mass and momentum into the Earth's magnetosphere across the entire magnetopause [e.g. *Sonnerup et al.*, 1981]. When the IMF encounters the magnetopause with different field line directions, the topology of field lines is rearranged and magnetic energy is converted to kinetic energy of plasma. Solar wind particles are able to enter the magnetosphere as the magnetic field lines break and reconnect.

The Kelvin-Helmholtz (K-H) instability also plays an important role in the dynamic of the magnetopause. The K-H instability arises where there is a velocity difference across the interface between two fluids [e.g. *Pu and Kivelson*, 1983; *Hasegawa et al.*, 2004]. The K-H instability under mainly northward IMF in magnetic reconnection is also an important source of ULF waves in the magnetosphere. Although the K-H instability excited surface waves at the magnetopause decay away from the boundary, the wave energy can penetrate deep into the magnetosphere in the form of fast mode Alfvén waves. These waves may couple to toroidal oscillations in the Pc3-Pc5 range and also excite field line resonances [e.g. *Walker et al.*, 1992]. The details of fast mode wave coupling to field line resonances will be discussed in Chapter 2.

1.2.3 Polar Cusp

The polar cusp region is defined as a region of open field lines extending poleward from the open/closed boundary (which is tied to the dayside merging region on the magnetopause) to where particles are no longer able to directly enter [*Fritz and Zong*, 2005]. The cusp region can be considered as part of the magnetospheric boundary layer system. It provides a direct entry for the plasma from the magnetosheath into the magnetosphere [e.g. *Reiff et al.*, 1977; *Marklund et al.*, 1990; *Yamauchi et al.*, 1996].

1.2.4 The Magnetotail

The magnetic field extension on the night side of the magnetosphere is called the magnetotail. Observations show that the magnetotail extension is on the order of $1,000$ R_e from the Earth [*Villante*, 1975]. The magnetotail contains the northern and southern tail lobes. Extended magnetic field lines in the north lobe point towards the Earth while those in the southern tail lobe point away from the Earth. The two lobes are separated by the plasma sheet, a layer with a weaker magnetic field and denser plasma. The plasma sheet is centered on the equator and is typically $2-6$ R_e thick. In the center of the magnetotail, a cross-tail current system flows across the plasma sheet from dawn to dusk.

1.2.5 The Plasmasphere

The plasmasphere consists of cold ($\sim$ 1 eV), dense ($10-10^4$ cm^{-3}) plasma in the inner magnetosphere between $2-7$ R_e. The dominant($\sim$ 80%) plasmaspheric ion species is H^+, while He^+ , O^+ , O^{2+} , N^+ and N^{2+} ions make up the remainder of the ions [*Kivelson and Russell*, 1995]. The main source of plasmasphere particles is an outflow of ionospheric plasma along mid- and low-latitude magnetic field lines.

The boundary of the plasmasphere, called the plasmapause, is commonly observed as a sharp boundary with an order of magnitude, steep drop in plasma density (for example, change of a factor of 5 in $L < 0.5$). Recently observations on plasmasphere [e.g. *Moldwin et al.*, 2002; *Carpenter et al.*, 2002; *Wang et al.*, 2011] show that the sharpness of the density profile and the extension of the plasmasphere boundary vary strongly according to the level of magnetospheric activity and geomagnetic local time.

An example of the plasmasphere is shown in Figure 1.3. The plasmasphere generally appears as the torus of plasma that surrounds the Earth, while there are also some irregular structures, such as the plume region [*Sandel et al.*, 2003], in the plasmasphere. A combination of corotational and solar wind driven convection electric fields control the behavior of particles in the plasmasphere and therefore

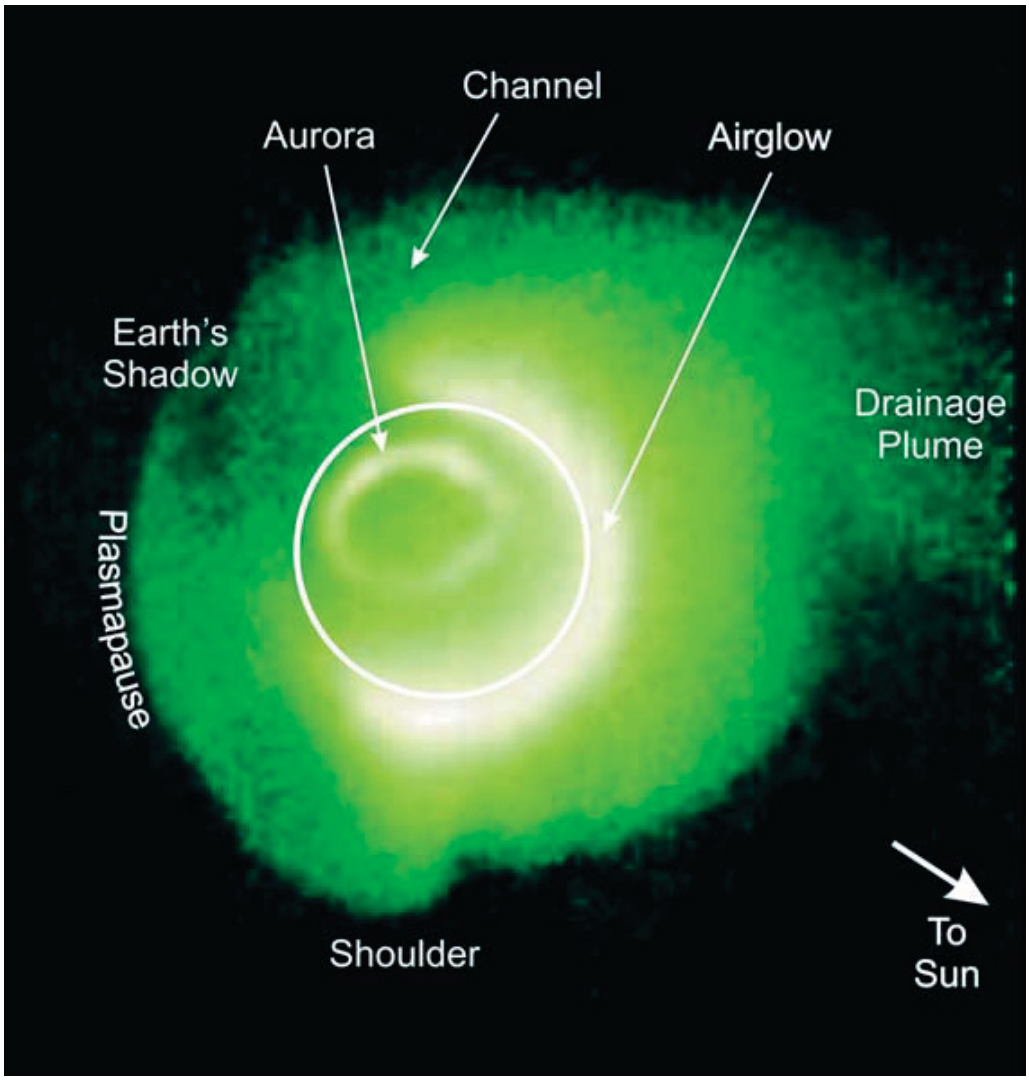

Figure 1.3: An example of the plasmasphere. The image is from the Extreme Ultravoilet Imager data at 07:34UT on 24th May, 2000, during a magnetic storm. Taken from *Sandel et al.* [2003].

control the forming of the plume. During geomagnetic storms, the convection electric field increases, eroding the outer region of the plasmasphere into a drainage plume that extends sunward toward the dayside magnetopause [*Grebowsky*, 1971; *Chappell et al.*, 1970, 1971].

1.2.6 The Radiation Belts

The radiation belts, or Van Allen belts, is a zone of energetic charged particles first discovered by James Van Allen [*Van Allen et al.*, 1959]. The radiation belts and

the plasmasphere occupy almost the same region in the magnetosphere. However, the radiation belts are composed of magnetically trapped very high-energy ions and electrons. Traditionally, the radiation belts are considered to be two separate shells surrounding the Earth: The inner radiation belt (in $L < 2$) and the outer radiation belt (in $L > 3$).

The inner radiation belt contains primarily energetic protons (exceeding 50 MeV) confined by an intense magnetic field to the inner regions of the magnetosphere. The main source of these energetic particles is the decay of neutrons freed when cosmic rays collide with nucleus in the upper atmosphere [*Hess et al.*, 1961; *Kivelson and Russell*, 1995]. Other sources of ions in the inner radiation belt include the sun or charged energetic cosmic particles [e.g. *Mewaldt*, 1994]. The outer radiation belt contains mainly very high energy ($0.1 - 10$ MeV) electrons trapped by the Earth's magnetosphere. Also, various ions, mostly in the form of energetic protons and a small amount of alpha particles and oxygen ions, are found in the radiation belts. Maximum intensity of electrons flux is usually around $L = 4 - 5$ and the intensity decreases rapidly as the energy increase. The outer radiation belt constantly changes with geomagnetic conditions while the inner radiation belt is quite stable.

Between the two radiation belts, a slot region at $L \sim 2.5$ is observed with low energy particles during geomagnetic quiet periods. The slot region is believed to be the result of pitch angle scattering. The pitch angle scattering effect theory [*Thorne et al.*, 1979] suggests that wave-particle interactions between the electrons and chorus/hiss (waves in the plasmasphere with 1 Hz$-$1 kHz) modify the pitch angle of the electrons which are then captured by the ionosphere. During severe magnetic storms, the slot region can fill up [e.g. *Blake et al.*, 1992a].

In recent years, new observations from Van Allen Probes have shown that a previously undetected third belt can sometimes appear and persist for approximately four weeks [*Shprits et al.*, 2013]. This new radiation belt contains ultrarelativistic electrons (> 2 MeV). The slot between the new radiation belt and the old ones is the result of electron losses in the interplanetary medium and electromagnetic ion cyclotron waves scattering to the Earth's atmosphere.

The interaction between energetic particles in the radiation belt and the magnetospheric ULF waves is one of the main topics of this thesis. The description of the single particle motions will be discussed in detail in Chapter 5.

1.3 The Ionosphere

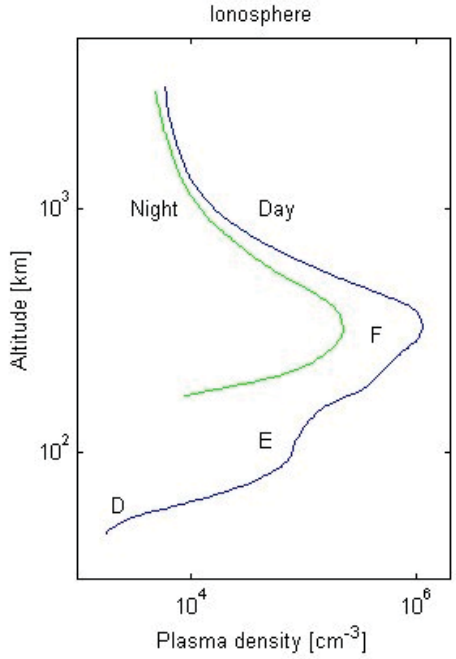

Figure 1.4: Schematic diagram of the density profile of the Ionosphere. The green and the blue curves correspond to the Ionospheric density profile during daytime and nighttime respectively (Taken from: magbase.rssi.ru/REFMAN/SPPHTEXT/ionosphere.html).

The ionosphere is the partially portion of the upper atmosphere of the Earth, at altitude of about $60 - 1000$ km. The atmospheric ionization in the ionosphere is because of solar extreme ultraviolet (EUV) radiation, x-ray photons, and energetic particles from the magnetosphere. From bottom to top, the ionosphere is divided into layers called the D layer, E layer, and F layer [e.g. *Baumjohann and Treumann*, 1996]. The D layer (60 km $- 90$ km) is very weakly ionized with an electron density of ~ 500 cm^{-3} because of high collision frequencies at this altitude. It is dominated by the dynamics of the neutral atmosphere and is known to absorb shortwave radio frequencies during the daytime. The ions in the E layer (90 km $- 130$ km) is mostly

ionized O_2^+ and NO^+ caused by UV radiation. As with the D layer, the degree of ionization in the E layer depends on the intensity of the radiation, the altitude and the time of day. During daytime, the electron density in the E-region is on the order of 10^5 cm^{-3}. The F layer (above 130 km) is the uppermost layer of the ionosphere. The ion component of the F layer is mainly O^+, and the plasma density in this layer is about 10^6 cm^{-3}. At night the F layer is the only layer of significant ionization present, while the ionization in the E and D layers is extremely low. During the day, the F layer splits into two layers, F_1 layer and F_2 layer. The F_1 layer is an additional, weaker ionization layer that occurs only in the daytime. The F_2 layer persists by day and night and is the main region responsible for the refraction and reflection of radio waves.

The ionosphere plays an important role in the electrodynamics of the space environment. For example, the most visible manifestation of space weather is the intense auroral activity, which occurs in the polar ionosphere during magnetic storms and substorms, resulting in ionospheric conductivity enhancement along the auroral oval. The aurora activity will be discussed in the next section. The ionosphere is also one of the energy sinks of the ULF waves in the magnetosphere. The ULF wave energy variation caused by the ionosphere will be discussed in Chapter 2 and 3.

1.4 Geomagnetic Storms and Substorms

1.4.1 Geomagnetic Indices

Different indices are used to measure geomagnetic activities. The most frequently used indices include the Dst (or SYM-H) index, Kp index, and A indices.

The disturbance storm-time (Dst, or Kyoto Dst) index is a measurement of the ring current's strength. The ring current forms because trapped positive ions and negative electrons are drifting in opposite directions, and that motion will create a westward electric current around the Earth. As an assessment of the severity of magnetic storms and substorms, the Dst index is monitored by the average of four ground-based magnetometers at middle or equatorial latitudes because strong ring

currents decrease the intensity of geomagnetic field on the Earth's surface. The Dst index is in units of nT. A negative Dst value means that the Earth's magnetic field is weakened and a positive value means that the field is strengthened. A more recent global storm index is the SYM-H index [*Wanliss and Showalter*, 2006]. It is calculated using a similar method but not identical to that used to calculate the Dst index. The SYM-H index has one-minute time resolution, while the Dst index has a one-hour time resolution.

The K-index is an alternative measurement of the magnitude of geomagnetic storms. It quantifies disturbances in the horizontal component of geomagnetic field in a 3-hour time interval with an integer in the range of $0-9$. Typically, a geomagnetic storm is related to a K-index of 5 or more. Different observatories have their own observed K-indicies. The official planetary Kp-index is derived by calculating the weighted average of K-indices from a network of geomagnetic observatories.

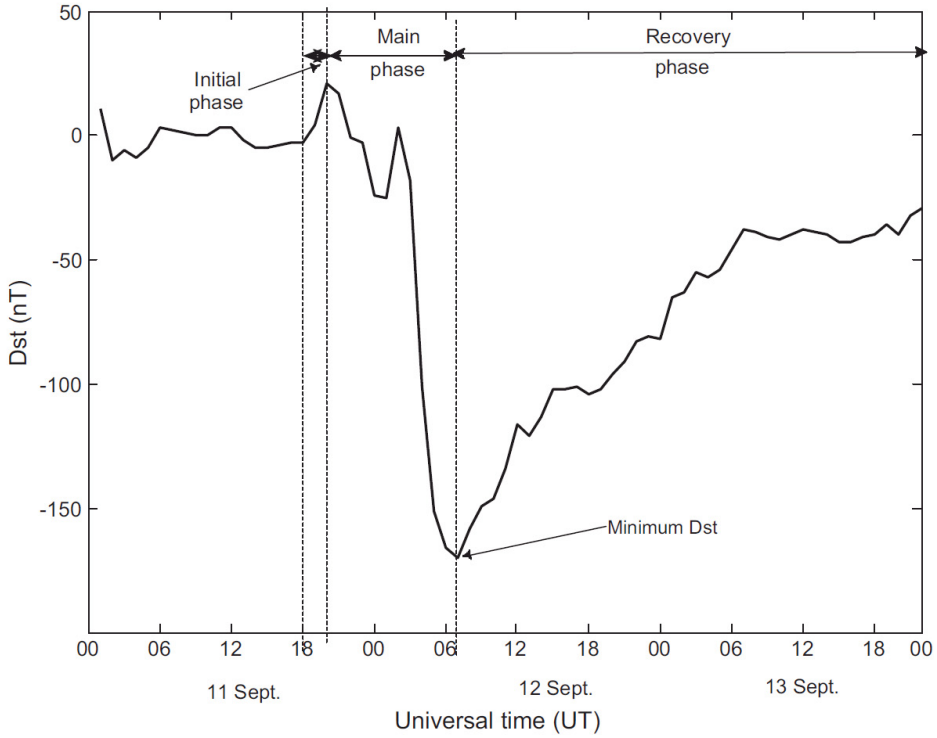

Figure 1.5: Development of the Dst index during a geomagnetic storm September 11-13, 1986. The initial phase, main phase, and recovery phase are indicated (Taken from *Okpala and Ogbonna* [2017]).

A-indices [*Davis and Sugiura*, 1966], include AU(Amplitude Upper), AE(Auroral Electrojet) and AL(Amplitude Lower) indices, describe the enhanced ionospheric currents flowing below and within the auroral oval. Horizontal magnetic component recordings from a set of globe-encircling stations are plotted to the same time and amplitude scales relative to their quiet-time levels and then superposed. The upper and lower envelopes of this superposition define the AU and the AL indices, respectively. The difference between the two envelopes determines the AE index.

1.4.2 Geomagnetic Storm

A geomagnetic storm is a strong disturbance of the Earth's magnetosphere caused by the interactions between the interplanetary magnetic field and the Earth's magnetic field [*Kivelson and Russell*, 1995]. When a large coronal mass ejection (CME) or co-rotating interaction region (CIR) is ejected from the sun, it can couple to the Earth's magnetosphere, increasing the solar wind pressure, which initially compresses the magnetosphere and then transfers increases energy into the magnetosphere. The size of a geomagnetic storm is classified by the minimum of the Dst index: moderate (-100 nT $<$ minimum of Dst $<$ -50 nT), intense (-250 nT $<$ minimum Dst $<$ -100 nT) or super-storm (minimum of Dst $<$ -250 nT).

Figure 1.5 shows an example of magnetic storm that occurred September 11-13, 1986 [*Okpala and Ogbonna*, 2017]. The evolution of a typical storm usually has three phases: initial, main and recovery phases. The initial phase usually begins with a sudden storm commencement (SSC) which is a sharp compression of the Earth's magnetic field that lasts from several minutes to an hour and is caused by increased solar wind dynamic pressure. The main phase comes after the initial phase. The magnetospheric ring current intensity increases largely, which causes a rapid decrease in the Dst over several hours. During the recovery phase, the Dst gradually returns to normal as ring current ions are lost. The recovery phase usually takes about $1-5$ days.

Geomagnetic storms produce major changes in the current systems, particle distribution and wave fields in Earth's magnetosphere. Enhancements in the relativistic

electron flux at energies of a few MeV are frequently observed in the outer radiation belt. Recent analysis suggests 50% of magnetic storms were found to be associated with relativistic electron flux enhancements at geostationary orbit [*O'Brien et al.*, 2001]. Since relativistic electrons are sufficiently energetic to penetrate spacecraft and cause internal charging, flux enhancement events pose an important risk to satellites. Several theories have been proposed. These theories include inward radial diffusion driven by fluctuations in the large-scale magnetospheric electric and magnetic fields [*Schulz and Lanzerotti*, 2012], drift resonance with ULF waves [*Rostoker et al.*, 1998; *Liu et al.*, 1999; *Hudson et al.*, 2000; *Elkington et al.*, 1999; *Zong et al.*, 2009], and Doppler-shifted cyclotron resonance with whistler mode waves [*Horne and Thorne*, 1998; *Summers et al.*, 1998; *Summers and Ma*, 2000].

1.4.3 Substorms

Compared to intense geomagnetic storms, magnetospheric substorms (also known as auroral substorms) occur more frequently, result in less geomagnetic variations ($Dst < -50$ nT) and last for shorter periods (usually one to a few hours). Substorms and storms are highly related: substorms can be more intense and occur more frequently during a geomagnetic storm. A substorm event is observed as a sudden brightening and increased movement of auroral arcs, and is characterized by an AE index. The morphology of aurora during a substorm was first described by *Akasofu* [1964].

Magnetic reconnection plays an important role in energy transfer from the magnetotail to the polar region during substorms [e.g. *Xiao et al.*, 2006]. In the magnetotail region, around $100 - 200$ R_e downtail, the two opposite open field lines on the two sides of the plasma sheet will reconnect. Then the reconnected field line will relax and shorten in the Earthward direction due to magnetic tension. Plasma frozen in the field line is transported toward the Earth along with the field line. During substorms, this reconnection process is stronger. There is an explosive release of stored magnetotail energy in the form of energetic particles and dissipated in the near-Earth nightside auroral region. This process excites the widespread and intense auroras.

The auroras are caused by the collision between the precipitating energetic par-

ticles and the neutral atmospheric constituents in the polar ionosphere. The color of the aurora depends on the type of atmospheric component, and on the energy of the participating particles. There are two basic types of auroras: discrete aurora and diffuse aurora. The discrete aurora is formed by field-aligned accelerated energetic particles [e.g. *Lyons and Evans*, 1984]. The diffuse aurora is formed by the lower energy electrons which are participating due to pitch angle scattering [e.g. *Lui et al.*, 1973].

Particle precipitation causes significant ionization in the auroral region, where the ionospheric conductivity is much higher than that in the polar cap. As a result, the high-latitude current flow is concentrated inside the auroral oval, in what are called auroral electrojets. The auroral electrojets are the most prominent currents at auroral latitudes. The total current in auroral electrojets is on the same order of magnitude as that in the ring current. However, the aurora contributes much higher geomagnetic magnetic disturbance on the ground since the height of this current system is about 100 km. Typically, the disturbance geomagnetic fields have magnitudes of $10-1000$ nT, and may reach 1760 nT during large magnetic storms [e.g. *Tsurutani et al.*, 2003].

1.5 Motivation

The principal objective of this dissertation is to provide a numerical method to better understand the dynamics of charged energetic particles such as H^+, O^+, and e^- in the Earth's radiation belts when an ULF wave is excited by the solar wind or by the plasma instability in the inner magnetosphere. We presented an analytic MHD Alfvén wave model about the field line resonance in the inner magnetosphere and firstly use Liouville methods to study the wave-particle interaction between Alfvén waves and energetic charged particles.

The behavior of charged particles in the Earth's magnetosphere is of interest to space weather research because of its potential impact on human space exploration. For example, relativistic and ultra-relativistic electrons, or "killer" electrons, can penetrate the shielding of satellites, and result in internal discharge which damages

and sometimes destroys satellites' vital onboard electronic components [*Robinson and Coakley*, 1992]. The dynamics of the oxygen ions in the magnetosphere are also important in space physics researches. Although the magnetosphere protects the Earth from atmospheric loss caused by solar wind, outflowing ionospheric O^+ ions from the ionosphere are a long-term but important loss mechanism of the oxygen in the Earth's atmosphere. Oxygen ions from the ionospheric outflow reach the lobe/plasma sheet region and then convect into the inner magnetosphere, where they accelerate and form a storm time ring current.

Different theories have been proposed to interpret the acceleration of charged particles in the inner magnetosphere. For example, local acceleration of electrons through electron cyclotron resonances with VLF waves has been widely considered one of the primary electron acceleration mechanisms in the magnetosphere during the storm time. However, the efficiency of VLF wave-particle interaction to accelerate electrons to relativistic energies [*Horne et al.*, 2005] is not enough to explain some quick acceleration events [e.g. *Blake et al.*, 1992b; *Chen et al.*, 2007]. The Pc3-5 ULF waves excited by solar wind dynamic pressure variations [*Claudepierre et al.*, 2008; *Zong et al.*, 2009; *Zhang et al.*, 2010] have much larger amplitudes than VLF waves. The Pc3-5 ULF waves are considered to be a more effective and important way to accelerate electrons [*Zong et al.*, 2009] and H^+, O^+ ions [*Zong et al.*, 2012b] and significantly enhance their radial diffusion [e.g. *Elkington et al.*, 2003; *Loto'aniu et al.*, 2006] through drift- or drift-bounce resonance. The role of ULF waves in magnetospheric energy transportation provides motivation for our development of numerical models that describe global properties of ULF waves controlled by solar wind variability, and how they affect energetic particle populations in the magnetosphere.

It has been common to use drift-bounce resonance theory developed by *Southwood and Kivelson* [1981, 1982] to qualitatively interpret satellite observations of differential flux modulation by ULF waves. This theory assumes the wave amplitude's infinitesimal growth, which is unlikely to be realized in practice. *Zhou et al.* [2016] extended this theory to account for the finite lifetime of ULF waves. Generalizing the theory to accommodate wave growth and damping stages makes the comparison between the theory and observations more accurate. However, both theories

exclude changes in L resonant ions experience during their interaction with waves. Test particle simulations in this thesis provide the full description of trajectories of ions and electrons as they interact with ULF waves. By backward tracing the test particles from the location of the satellite, we can, with high precision, reproduce the observation of differential flux at different energies and different pitch angles.

Although different ULF wave models [e.g. *Rankin et al.*, 2000; *Lui and Cheng*, 2001; *Degeling et al.*, 2010; *Lysak et al.*, 2013] exist, we developed a new analytic MHD model to describe the Alfvén waves in the inner magnetosphere. This model introduced a monochronic driver which can excite a wave from an unperturbed dipole model of the magnetic field. The compressional component of magnetic field proves that the first adiabatic invariant is conserved when we simulate the full trajectories of the test particles. In previous studies, the forward Liouville method [*Degeling et al.*, 2013; *Fei et al.*, 2006] was used to simulate the global distribution of the energetic particles' phase space density (PSD). When studying the time evolution of PSD at a point in the spatial scale of satellite size with the forward Liouville method, it is necessary to compensate for the statistical error caused by the size of the sampling volume. This can be done using a large number of test particles. In this thesis, we firstly used the backward Liouville methods to study the variations of PSD in ULF waves. This method does not include any statistical errors from the sampling volume size, so the time evolution of PSD at the sampling points can be precisely reproduced.

In this thesis, I have studied the interaction between charged particles and the Pc3-5 Alfvén waves in the Earth's magnetosphere. I developed computational models to retrieve the temporal evolution and spatial distribution of differential particle fluxes under the effect of the ULF waves. The simulations are in good agreement with the observational data from different satellites and ground magnetometer arrays. In Chapter 2, I provide an overview of the theoretical background of ULF waves, test particle motions, and drift/drift-bounce resonance. Chapter 3 presents observational studies about different ULF wave damping mechanisms. The mechanisms have been evaluated for two interplanetary shock-related ULF wave events observed by Cluster on November 7, 2004, and August 30, 2001. It was further confirmed that Landau damping is more efficient when heavy ions such as O^+ are present, which explains

why ULF waves excited by interplanetary shocks and solar wind pressure impulses can have higher decay rates in the plasmasphere boundary layer than in the plasmasphere. Our ULF wave models have been described in detail in Chapter 4. The simulations of drift-bounce resonance are combination of this wave model and the test particle models discussed in Chapter 5. The details about the Liouville methods used to reproduce the differential flux, along with the implementation of our computational code are also described in Chapter 5. In Chapter 6, the computational models are used to study drift resonance between H^+ ions and poloidal fundamental mode giant pulsations. The ULF wave and test-particle simulations presented in this chapter reproduce several important features of the pitch angle and energy spectrum of ion differential fluxes observed by the Van Allen Probes-A spacecraft on October 6, 2012. The simulations of the ULF wave events reproduce the observed behavior for poloidal mode wave parameters that are in general agreement with the data analysis presented by *Takahashi et al.* [2016]. The maximum of oscillation of differential fluxes for ions at a 35° pitch angle appears at an energy level of $\sim$ 150keV, which is consistent with the drift-resonance energy. The oscillation of differential fluxes near the 90° pitch angle is weaker than that at 35° because of the dependence of the resonance energy on the pitch angle. Chapter 7 looks at the drift resonance between electrons and ULF waves with the guiding center test particle model. Our simulations reproduced the phase differences and the amplitudes of the differential flux oscillation observed by different energy channels of the MagEIS instrument on Van Allen Probes-A. We have simulated high-energy resolution flux oscillations to show that the flux oscillations attenuate rapidly during the damping stage of the observed ULF waves is caused by the increasing phase difference between different energy particles within energy bins of the MagEIS instruments. We have also provided simulations of O^+ ions undergoing $N = 0$ drift resonance and $N = -2$ drift-bounce resonance provide insight into the dynamics of heavy ions that interact with ULF waves in this chapter. Chapter 8 introduces an MHD Alfvén wave model with a more realistic ionospheric boundary condition. The forward Liouville method is used to reconstruct the distribution function of ions when they are interacting with second harmonic ULF waves. It has been demonstrated that the second-harmonic poloidal mode waves are efficient at energizing ions to tens of keV over timescales of tens of minutes. The

test-particle simulations of bounce-resonance reproduce particle signatures that are commonly observed by satellites. The energy dispersion agrees with the theoretical predictions.

Chapter 2

ULF Waves and Particle Motion in the Earth's Magnetosphere

In this chapter, we will briefly review theories about ULF waves and wave-particle interactions in the magnetosphere to prepare the computational models provided in Chapter 4 and Chapter 5. The magnetohydrodynamic theory, is introduced as an important theory of ULF waves in Section 2.2. We describe the adiabatic motion of ions and electrons in the magnetosphere in Section 2.3. Theories on drift- and drift-bounce resonance are introduced in Section 2.4. Section 2.4 also introduces Landau damping and flux modulation, which are part of the main topics of Chapter 3, Chapter 6, Chapter 6, and Chapter 7.

2.1 Introduction

The terminology ultra-low-frequency (ULF) waves refers to waves in the frequency range of about 1 mHz to 1 Hz. The first recorded ULF wave event was geomagnetic pulsations observed at the Kew Observatory [*Stewart*, 1861]. Although there have been many observations of geomagnetic pulsations, the physical mechanism of ULF waves was not well explained until the theory of Alfvén waves in magnetized plasma [*Alfvén*, 1942] was developed. *Dungey* [1954] provided the theory of generalized Alfvén waves, also known as the magnetohydrodynamic (MHD) wave, to explain these geomagnetic pulsations.

The sources of ULF waves in the magnetosphere include external solar wind disturbances and internal plasma instabilities. External sources include solar wind dynamic pressure pulses [*Kepko and Spence*, 2003; *Hudson et al.*, 2004; *Takahashi and Ukhorskiy*, 2007; *Claudepierre et al.*, 2009, 2010; *Claudepierre et al.*, 2013], Kelvin-Helmholtz (K-H) instabilities on the magnetopause [*Hudson et al.*, 2004; *Claudepierre et al.*, 2008], and ion cyclotron resonance with back-streaming solar wind ions [*Odera*, 1986]. The K-H instability can excite ULF waves in the magnetosphere through the coupling that occurs between fast mode waves and toroidal field line resonances (FLRs) [*Fairfield et al.*, 2000; *Hasegawa et al.*, 2004; *Rae et al.*, 2005; *Claudepierre et al.*, 2008]. Interplanetary shocks and solar wind dynamic pressure pulses also excite ULF waves through substorm injections [*James et al.*, 2013]. A special type of standing Alfvén waves, the Giant Pulsations (Pgs), are considered to be generated by plasma instabilities inside the magnetosphere.

Wave-particle interactions involving Alfvén waves [*Dungey*, 1955] can dramatically alter the behavior of electrons [*Zong et al.*, 2007, 2009] and ions [*Yang et al.*, 2010, 2011a; *Zong et al.*, 2011; *Ren et al.*, 2016] in the inner magnetosphere. *Brown et al.* [1968] provided the first observation about modulations of energetic particle fluxes by ULF waves with periods of several minutes. Numerous observations have been reported also demonstrating that the modulation of energetic particle fluxes by ULF waves is common [e.g. *Baker et al.*, 1980; *Kremser et al.*, 1981; *Takahashi et al.*, 1985; *Takahashi et al.*, 1990; *Claudepierre et al.*, 2013; *Foster et al.*, 2015]. The theory developed by *Southwood and Kivelson* [1981, 1982] is used to interpret the modulations of ion and electron flux produced by ULF waves. This theory has recently been improved by *Zhou et al.* [2016], who accounted for the finite growth and decay of ULF waves.

2.2 Magnetohydrodynamic Description of ULF Waves

A typical classification scheme for the ULF waves uses the period and waveform of the pulsation [*Jacobs et al.*, 1964], as shown in Table 2.1. ULF waves can be excited by external solar wind disturbances and internal plasma instabilities.

Table 2.1: Typical classification scheme for ULF waves

	Name	T/s	f
Continuous pulsations	Pc1	$0.2-5$	$0.2-5$ Hz
	Pc2	$5-10$	$0.1-0.2$ Hz
	Pc3	$10-45$	$22-100$ mHz
	Pc4	$45-150$	$7-22$ mHz
	Pc5	$150-600$	$2-7$ mHz
Irregular pulsations	Pi1	$1-40$	$0.025-1$ Hz
	Pi2	$40-150$	$6-25$ mHz

As suggested by *Dungey* [1954], magnetohydrodynamic(MHD) theory combines electromagnetic theory and the theory of fluid dynamics. In general, ULF waves can be described by MHD theory because their temporal scale is longer than the particles' gyroperiod and their spatial scale is larger than the particles' gyroradius. The description of ULF waves is based on Maxwell's equations (Equation (2.1)- Equation (2.4)) and hydrodynamic fluid equations (Equation (2.8) - Equation (2.10)).

2.2.1 Fundamental Equations of MHD Theory

Maxwell's equations in SI units can be written as below,

$$\nabla \times \mathbf{E} = -\frac{\partial \mathbf{B}}{\partial t} \qquad (Faraday's\ law) \tag{2.1}$$

$$\nabla \times \mathbf{B} = \mu_0(\mathbf{j} + \epsilon_0 \frac{\partial \mathbf{E}}{\partial t}) \qquad (Ampere's\ law) \tag{2.2}$$

$$\nabla \cdot \mathbf{E} = \frac{\rho_c}{\epsilon_0} \qquad (Gauss's\ law) \tag{2.3}$$

$$\nabla \cdot \mathbf{B} = 0 \tag{2.4}$$

where $\mathbf{j}$ is the current, ρ_c is the net charge density, and ϵ_0 and μ_0 are the permeability and permittivity of free space, respectively. In space plasma physics, the plasma is neutrally charged. Thus the equation of Gauss's law can be simplified as

$$\nabla \cdot \mathbf{E} = 0 \tag{2.5}$$

The generalized Ohm's law is also included in the electromagnetic component of the MHD theory as

$$\mathbf{j} = \sigma(\mathbf{E} + \mathbf{v} \times \mathbf{B}) \tag{2.6}$$

where σ is the plasma conductivity and $\mathbf{v}$ is the velocity of the plasma fluid element. In the magnetosphere, the conductivity is so large that the assumption $\sigma = \infty$ is applied. Therefore Ohm's law (2.6) becomes

$$\mathbf{E} + \mathbf{v} \times \mathbf{B} = 0. \tag{2.7}$$

This equation shows that there are no electric fields in the frame moving with the plasma [e.g. *Baumjohann and Treumann*, 1996]. The fields are "frozen in" to the plasma element when the plasma is an ideal conductor.

Another important part of the MHD theory is the hydrodynamic fluid equations. The hydrodynamic component of the MHD theory incorporates the following equations.

$$\frac{\partial \rho}{\partial t} + \nabla \cdot (\rho \mathbf{v}) = 0 \qquad (Continuity\ equation) \tag{2.8}$$

$$\rho(\frac{\partial \mathbf{v}}{\partial t} + \mathbf{v} \cdot \nabla \mathbf{v}) = \mathbf{j} \times \mathbf{B} - \nabla p \qquad (Equation\ of\ motion) \tag{2.9}$$

$$\frac{p}{\rho^{\gamma_s}} = constant \qquad (Equation\ of\ state) \tag{2.10}$$

where $\mathbf{v}$ is the fluid velocity, ρ is the mass density, p is the plasma pressure, and $\gamma_s = C_p/C_v$ is the adiabatic index, which is defined as the ratio of the two specific heats at constant pressure and constant volume, respectively.

2.2.2 Shear Alfvén Waves and Compressional Wave Modes

Based on the MHD equations, two important kinds of hydromagnetic waves can be derived under the assumption of uniform, infinite, and fully-ionized cold plasma with a uniform background magnetic field ($\mathbf{B}_0 = B_0\widehat{\mathbf{z}}$). MHD equations can be linearized by dividing the following terms into a stationary homogeneous background part and

small perturbation part [*Allan and Poulter*, 1992].

$$\rho = \rho_0 + \rho_1 \tag{2.11}$$

$$\mathbf{B} = \mathbf{B}_0 + \mathbf{B}_1 \tag{2.12}$$

$$\mathbf{E} = \mathbf{E}_1 \tag{2.13}$$

$$\mathbf{j} = \mathbf{j}_1 \tag{2.14}$$

$$\mathbf{v} = \mathbf{v}_1 \tag{2.15}$$

where the subscript 0 indicates the background part and 1 indicates the perturbation part, $\mathbf{E}_0 = 0, \mathbf{v}_0 = 0$, and $\mathbf{j}_0 = 0$ is assumed. The linearized Maxwell equations (Equation (2.1), Equation (2.2)) and the equation of motion (Equation (2.9)) can be written as

$$\nabla \times \mathbf{E}_1 = -\frac{\partial \mathbf{B}_1}{\partial t} \tag{2.16}$$

$$\nabla \times \mathbf{B}_1 = \mu_0 \mathbf{j}_1 + \frac{1}{c}\frac{\partial \mathbf{E}_1}{\partial t} \tag{2.17}$$

$$\rho_0 \frac{\partial \mathbf{v}_1}{\partial t} = \mathbf{j}_1 \times \mathbf{B}_0 - \nabla p \tag{2.18}$$

where plasma pressure $p = 0$ in cold plasma, and the displacement current term $\frac{1}{c}\frac{\partial \mathbf{E}_1}{\partial t}$ in the RHS of Equation (2.17) is neglected because MHD motions in the magnetosphere are slow compared to the velocity of light. Combining Equation (2.16) - Equation (2.18) with the frozen-in condition Equation (2.7),

$$\frac{\partial^2 \mathbf{E}_1}{\partial t^2} + v_A^2 \nabla \times (\nabla \times \mathbf{E}_1) = 0 \tag{2.19}$$

where $v_A = B_0/\sqrt{\mu_0 \rho_0}$ is the so-called Alfvén speed.

According to Equation (2.7), the parallel component of $\mathbf{E}_1$ is zero because $\mathbf{E}_{1\parallel} = -(\mathbf{v}_1 \times \mathbf{B}_0)_\parallel = 0$. The other two components of the electric field in a Cartesian coordinate can be described by Equation (2.19)

$$(v_A^{-2}\frac{\partial^2}{\partial t^2} - \frac{\partial^2}{\partial y^2} - \frac{\partial^2}{\partial z^2})E_{1x} = -\frac{\partial^2 E_{1y}}{\partial x \partial y} \tag{2.20}$$

$$(v_A^{-2}\frac{\partial^2}{\partial t^2} - \frac{\partial^2}{\partial x^2} - \frac{\partial^2}{\partial z^2})E_{1y} = -\frac{\partial^2 E_{1x}}{\partial x \partial y} \tag{2.21}$$

Assuming that all perturbation quantities are uniform in the x direction, $\partial/\partial x \equiv 0$, and in the plane-wave form, $\propto \exp[i(k_y y + k_z z - \omega t)]$, the two dispersion relations

can be solved from Equation (2.20) and Equation (2.21).

$$\omega^2/k_z^2 = v_A^2 \tag{2.22}$$

$$\omega^2/k^2 = v_A^2 \tag{2.23}$$

where $k = \sqrt{k_y^2 + k_z^2}$.

Equation (2.22) is the dispersion relation of the well-known shear Alfvén wave. Its phase velocity is $\omega/k_z = v_A$ and group velocity is $\mathbf{v}_g = \pm v_A \widehat{\mathbf{z}}$. The energy flow of a shear Alfvén wave is always parallel or anti-parallel to the background magnetic field $\mathbf{B}_0$. The perturbation of magnetic field $\mathbf{B}_1$ is perpendicular to background $\mathbf{B}_0$, which makes the field lines oscillate like a stretched string.

Equation (2.23) is the dispersion relation of the fast magnetoacoustic mode. Its phase velocity is also $\omega/k = v_A$ but its group velocity is $\mathbf{v}_g = \pm v_A \widehat{\mathbf{k}}$, parallel to the wave vector $\mathbf{k}$. The wave magnetic field is not necessarily perpendicular to the background and is therefore compressional. Figure 2.1 shows the directions of all perturbation quantities in the shear Alfvén mode and fast mode.

When the plasma is not completely cold, the plasma pressure p is not zero in the equation of motion (Equation (2.18)). The magnetic compressional fast mode wave couples with the fluid compressional sound wave. For the shear Alfvén wave, which is non-compressional, the dispersion relation (Equation (2.22)) is unaffected. Solving the dispersion relation of the fast magnetoacoustic mode (Equation (2.23)) leads to two solutions [*Allan and Poulter*, 1992]

$$\frac{\omega^2}{k^2} = \frac{1}{2}(c_s^2 + v_A^2)\left[1 \pm \left(1 - \frac{4c_s^2 v_A^2 \cos^2\theta}{(c_s^2 + v_A^2)^2}\right)^{1/2}\right] \tag{2.24}$$

where θ is the angle between wave vector $\mathbf{k}$ and background magnetic field $\mathbf{B}_0$ to make $k_y = k\sin\theta$ and $k_z = k\cos\theta$, c_s is the sound speed; $c_s = \sqrt{\gamma_s p_0/\rho_0}$. In the case of the parallel propagation wave, $\theta = 0$, the two solutions of Equation (2.24) become

$$\omega^2/k^2 = v_A^2, \tag{2.25}$$

$$\omega^2/k^2 = c_s^2 \tag{2.26}$$

which correspond to a transverse fast mode with a phase velocity of v_A and a compressional sound wave with a phase velocity of c_s, respectively.

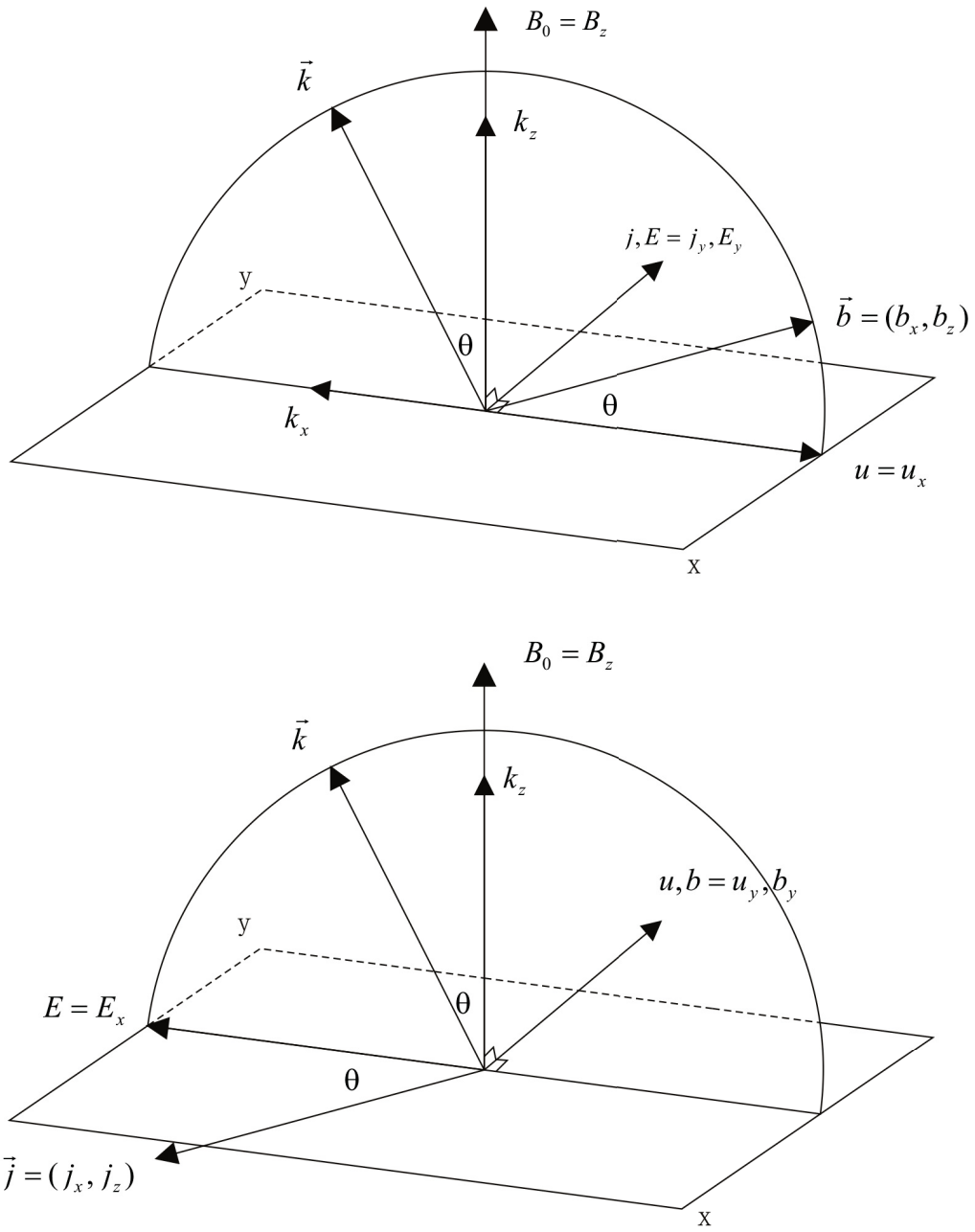

Figure 2.1: Polarizations of the fast mode and the Alfvén mode, taken from *Allan and Poulter* [1992]. Upper panel: the fast mode. Lower panel: the Alfvén mode.

In the case of oblique propagation wave ($\cos^2\theta \simeq 0$) and c_s is significantly smaller than v_A, Equation (2.24) can be approximately written as

$$\omega^2/k^2 \simeq (c_s^2 + v_A^2) \tag{2.27}$$

$$\omega^2/k_z^2 \simeq \frac{c_s^2 v_A^2}{c_s^2 + v_A^2} \tag{2.28}$$

The two modes described by Equation (2.27) and Equation (2.28) are known as the fast and slow magnetosonic modes respectively. The propagation behavior of the fast magnetosonic mode is similar to the slow magnetosonic mode as a compressional wave but has a higher phase velocity. The energy flow direction of slow magnetosonic mode is parallel to the direction of $\mathbf{B}_0$. Figure 2.2 shows the schematic diagram of wave phase velocities of the three magnetohydrodynamic waves on different directions of wave vectors for the two case $v_A > c_s$ and $v_A < c_s$. When the wave vector is perpendicular to $\mathbf{B}_0$, the phase velocity of the Alfvén wave and that of the slow magnetosonic mode is zero, which means these two modes do not propagate across magnetic field lines. The phase velocity of the fast magnetosonic wave is a combination of Alfvén speed and sound speed; $c_{ms} = \sqrt{c_s^2 + v_A^2}$ because the magnetic pressure and fluid pressure perturbations are in phase for the fast magnetosonic mode. In the case of the parallel propagation mode, the phase velocity of the fast magnetosonic mode is equal to or larger than the Alfvén speed and sound speed while that of the slow magnetosonic mode is equal to or smaller than both the Alfvén speed and sound speed.

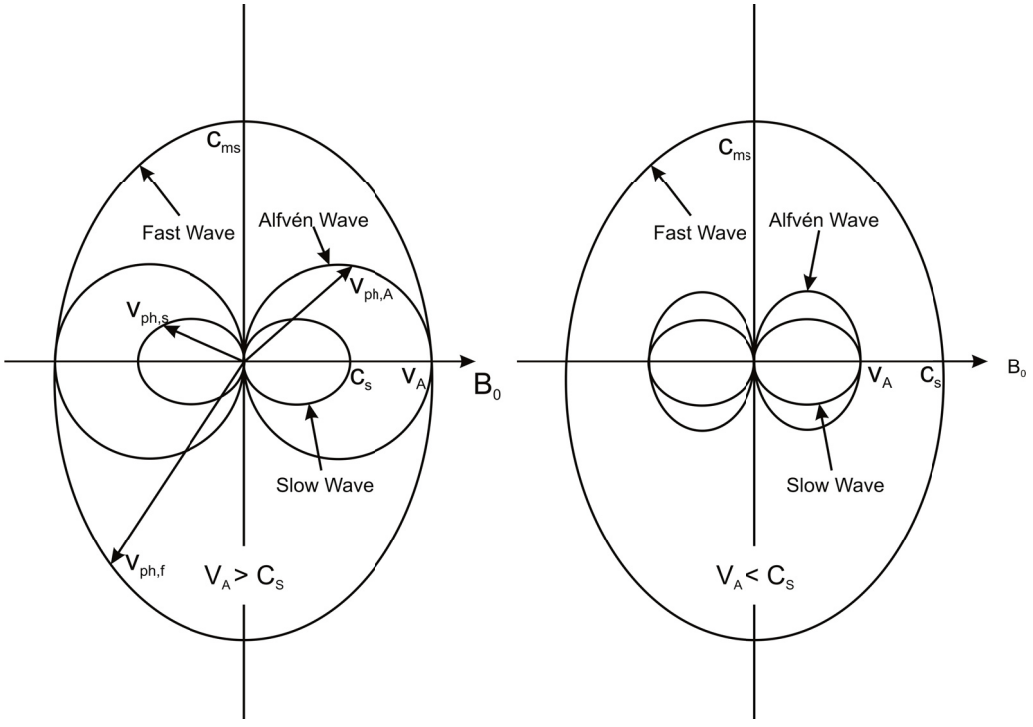

Figure 2.2: Schematic diagram showing the dependence of MHD wave phase velocities on the angle between $\mathbf{k}$ and $\mathbf{B}_0$. Taken from *Baumjohann and Treumann* [1996].

2.2.3 Coupling between MHD waves and Field Line Resonance

Field line resonances (FLR) are long duration standing waves along field lines in the magnetosphere. FLRs are caused by the inward energy transportation of fast mode waves in the magnetosphere. When the natural frequency of the field line matches that of the fast mode source, the fast and Alfvén modes will couple together, cause the field line oscillation with an enhanced amplitude, and thus establish the FLRs. Below we are going to discuss the mechanism of mode coupling between the fast and Alfvén modes by following the method derivations from *Allan and Poulter* [1992].

Assuming that the background magnetic field B_0 and plasma density ρ are not uniform in the direction perpendicular to the magnetic field, for example, x, the wave electric field E_x and E_y and the Alfvén speed can be written as

$$v_A = v_A(x) \tag{2.29}$$

$$E_x = E_x(x)\exp[i(k_y y + k_z z - \omega t) \tag{2.30}$$

$$E_y = E_y(x)\exp[i(k_y y + k_z z - \omega t). \tag{2.31}$$

Thus Equation (2.20) and Equation (2.21) become

$$\left[\omega^2/v_A^2(x) - k_y^2 - k_z^2\right] E_x = ik_y dE_y/dx \tag{2.32}$$

$$\left[\omega^2/v_A^2(x) - k_z^2\right] E_y = ik_y dE_x/dx - d^2E_y/dx^2. \tag{2.33}$$

The two equations of E_x and E_y decoupled when $k_y \equiv 0$

$$\left[\omega^2/v_A^2(x) - k_z^2\right] E_x = 0 \tag{2.34}$$

$$\left[\omega^2/v_A^2(x) - k_z^2\right] E_y = -d^2E_y/dx^2. \tag{2.35}$$

The dispersion relation of Equation (2.34) is $\omega^2/k_z^2 = v_A^2$. It corresponds to the shear Alfvén mode which is similar to Equation (2.22). Equation (2.35) is related to the fast mode wave dispersion relation (Equation (2.23)). The extra second-order ordinary differential term $-d^2E_y/dx^2$ on its RHS is the result of a spatial variation in the x direction.

If parameter $K^2(x) = \omega^2/v_A^2(x) > k_z^2$, the coefficient of E_y on the LHS of Equation (2.35) is positive. In this case, the solution of Equation (2.35) is oscillatory in space. One the other hand, $K^2(x) < k_z^2$, gives a wave solution which is evanescent in space. Assuming that $K^2(x)$ is monotonically increasing with x, there is a turning point x_r where $K^2(x) = 0$. A wave of frequency ω and wave number k_z has oscillatory spatial structure outside turning point ($x > x_r$) and growth or decay inside it ($x < x_r$). Here x_r is the reflection point for an inward propagation fast mode wave.

If $k_y \neq 0$, combining Equation (2.32) and Equation (2.33) to give

$$d^2E_y/dx^2 - CdE_y/dx + [K^2(x) - k_y^2 - k_z^2]E_y = 0 \tag{2.36}$$

where

$$C = \frac{k_y^2 dK^2(x)/dx}{(K^2(x) - k_z^2)(K^2(x) - k_y^2 - k_z^2)} \tag{2.37}$$

The coefficient C has two singular points x_r and x_c. One is $K^2(x_r) - k_z^2 = 0$, the reflection point. The other is $K^2(x_c) - k_y^2 - k_z^2 = 0$. x_c always lies inside of x_r if $\partial/\partial y \neq 0$ and $K(x)$ monotonically increases with x.

Figure 2.3 show a diagram of the coupling between the field line resonance and the incident fast mode waves in a box model magnetosphere [*Rankin et al.*, 1993]. As stated in the discussion above, fast mode waves have an oscillatory structure at $x > x_r$ and an evanescent structure at $x < x_r$. A physical explanation for the singular point x_c is that resonance happens between the incoming fast mode wave and local Alfvén mode wave. The phase speed of fast mode wave ω/k, where $k^2 = k_y^2 + k_z^2$, matches the local Alfvén speed $v_A(x_c)$ at x_c. The energy of the inward propagation fast mode wave is transferred into the standing Alfvén wave which propagates along the field lines.

2.2.4 Ionospheric Influence on ULF Waves: Pedersen and Hall Conductivities

The plasma in the ionosphere is not collisionless and thus it has non-zero plasma resistivity $\eta = m_e\nu_c/n_e e^2$ where $\nu_c > 0$ is the collision frequency. A collision term is

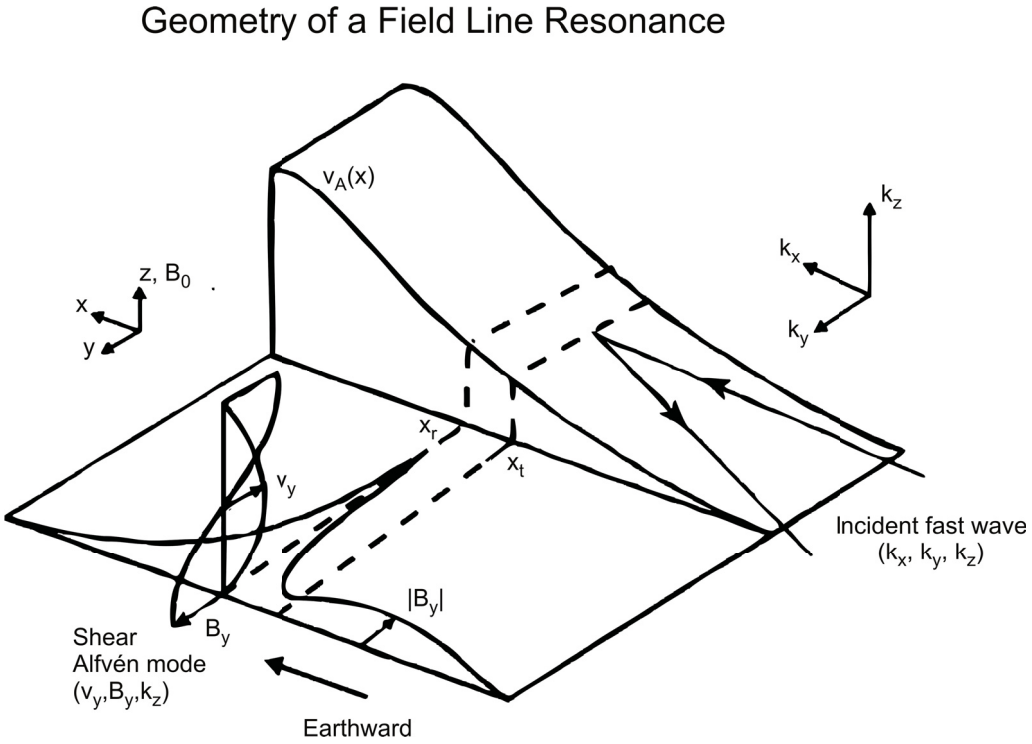

Figure 2.3: Diagram of the coupling between the field line resonance and the incident fast mode waves in a box model magnetosphere. Taken from *Rankin et al.* [1993].

introduced into the equation of motion,

$$m\frac{d\mathbf{v}}{dt} = q(\mathbf{E} + \mathbf{v} \times \mathbf{B}) - m\nu_c(\mathbf{u} - \mathbf{v}) \tag{2.38}$$

where $\mathbf{v}$ is electron velocity and $\mathbf{u}$ is the velocity of collision partners. Assuming that the collision partners are at rest ($\mathbf{u} = 0$) and the plasma is in steady state ($d/dt = 0$), the equation of motion can be written as

$$\mathbf{E} + \mathbf{v} \times \mathbf{B} = -\frac{m_e\nu_e}{e}\mathbf{v}. \tag{2.39}$$

Another form of Ohm's law can be obtained by using Equation (2.39) and the definition of current $\mathbf{j} = -en_e\mathbf{v}$

$$\mathbf{j} = \sigma_0\mathbf{E} - \frac{\sigma_0}{n_e e}\mathbf{j} \times \mathbf{B} \tag{2.40}$$

Write current vector $\mathbf{j}$ as a function of electric field components as

$$\mathbf{j} = \sigma_0 E_\parallel + \sigma_P E_\perp - \sigma_H(\mathbf{E}_\perp \times \mathbf{B})/B \tag{2.41}$$

where σ_0 is the plasma conductivity,

$$\sigma_P = \frac{\nu_c^2}{\nu_c^2 + \Omega_e^2}\sigma_0 \tag{2.42}$$

$$\sigma_H = -\frac{\Omega_e \nu_c}{\nu_c^2 + \Omega_e^2}\sigma_0 \tag{2.43}$$

are the Pedersen and Hall conductivity. Charged particles in the Hall current move in the direction transverse to the electric and magnetic fields and do not gain or lose energy. The Pedersen current driven by the perpendicular electric field is one of the most important wave energy sinks in the ionosphere.

2.2.5 Ionospheric Influence on ULF waves: Ionospheric Joule Heating

Ionospheric damping of Alfvén waves is one of their main sinks of energy. The damping takes place through Joule heating produced by the interaction of the waves with ionospheric particles. For a transverse wave, Joule dissipation through Pedersen currents can be calculated based on a boundary condition at the ionosphere: $b = \mu_0 \Sigma_P E$, where Σ_P is the height-integrated Pedersen conductivity. This boundary condition can also be written in another form [*Southwood and Hughes*, 1983]:

$$\frac{Eb}{\mu_0} = \Sigma_P \left|E\right|^2 . \tag{2.44}$$

In this equation, Joule heating is balanced by the net Poynting flux into the ionosphere.

2.3 Adiabatic Motion of Trapped Magnetospheric Charged Particle

The geomagnetic field can be approximately considered as a dipole field inside the inner magnetosphere. Charged energetic particles are trapped by the geomagnetic field and bounce back and forth between the northern and southern hemispheres. Figure 2.4 shows the three types of periodic motion of particles: gyro-motion, bounce

motion, and drift motion. Each type of particle motion is associated with one adiabatic invariant. An adiabatic invariant is a property of a physical system that stays constant compared with some typical periodicities of the particle motion. The magnetic moment, μ, is associated with the gyration motion around the magnetic field. The longitudinal invariant, K, is associated with the bounce motion along the magnetic field. The third invariant, Φ, is associated with the azimuthal drift due to the gradient and curvature of the magnetic field.

2.3.1 Gyro-motion around Field Line

The equation of motion for a particle of charge q under the action of the external electric field $\mathbf{E}$ and magnetic field $\mathbf{B}$ can be described as

$$m\frac{d\mathbf{v}}{dt} = q(\mathbf{E} + \mathbf{v} \times \mathbf{B}) \tag{2.45}$$

where m is the particle's mass and $\mathbf{v}$ is the particle's velocity. When $\mathbf{E} = 0$, this equation reduces to

$$m\frac{d\mathbf{v}}{dt} = q\mathbf{v} \times \mathbf{B}. \tag{2.46}$$

The solution of Equation (2.46) gives the periodic circular motion around the dipole background magnetic field. The frequency of this circular motion, so called gyrofrequency, is defined as

$$\Omega_g = \frac{qB}{m} \tag{2.47}$$

where opposite signs of charge q indicate different directions of gyro-motion. When the background magnetic field direction is along $+z$ in a right-handed cylindrical coordinate system, the gyro-motion of ions is in $-\phi$ direction while the gyro-motion of electrons is in the $+\phi$ direction. The radius of the gyro-motion, the gyroradius, is defined as

$$R_g = \frac{mv_\perp}{|q|\,B} \tag{2.48}$$

where $v_\perp$ is the velocity component perpendicular to the background magnetic field B. As long as the magnetic fields are slowly changing and can be considered as constant in one gyroperiod of a particle, the particle's first adiabatic invariant, μ is a

constant. The definition of μ is

$$\mu = \frac{W_\perp}{B} = \frac{mv_\perp^2}{2B} \tag{2.49}$$

where $v_\perp$ is the perpendicular component of particle velocity, $W_\perp$ is the perpendicular energy.

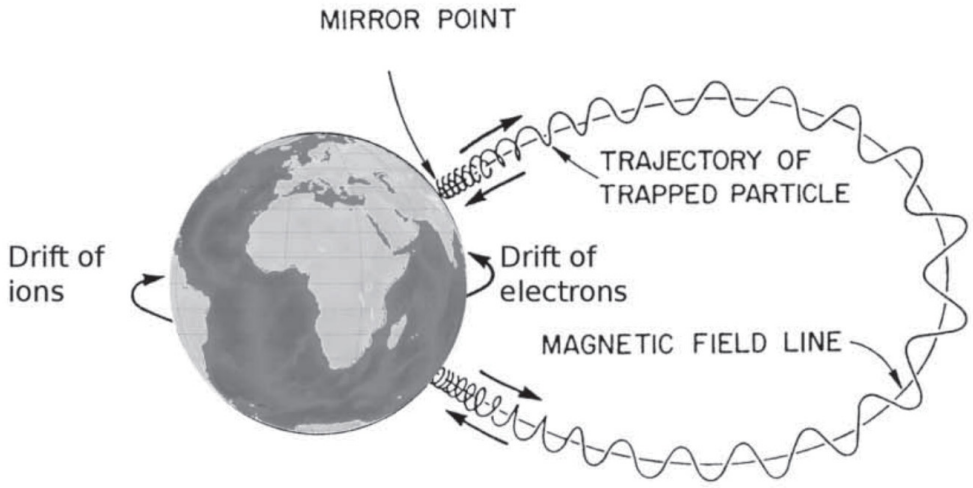

Figure 2.4: Schematic diagram of particle motions in the inner magnetosphere. Modified from:www-ssg.sr.unh.edu/tof/Smart/Students/lees/periods.html

2.3.2 Bounce Motion along Field Line

A particle also moves along the magnetic field line if its parallel velocity $v_\parallel$ is not zero. As a dioplar magnetic field has a minimum field strength at the equator and a stronger field strength at the polar region where the field lines converge, a particle will stop moving further along the field line at the mirror point and reverse its direction of motion due to the mirror force, which is defined as $F_m = -\mu\nabla_\parallel B$. The mirror point is a point along the field line where the parallel energy is zero. The particle's pitch angle α, which is defined as $\sin\alpha = v_\perp/v$, reaches $\alpha = \pi/2$ at the mirror point. When there is no perturbation of the ambient magnetic field, the particle's and first adiabatic invariant are conserved.

The period of bounce motion, τ_b, can be calculated by integrating $ds/v_\parallel$ over one

full bounce path along the field line

$$\tau_b = 4 \int_0^{\lambda_m} v_{\parallel}^{-1} ds \tag{2.50}$$

where λ_m is the magnetic latitude of the particle's mirror point. An approximation of this integration in a dipole field is [*Baumjohann and Treumann*, 1996]

$$\tau_b = \frac{LR_E}{\sqrt{W/m}}(3.7 - 1.6 \sin \alpha_{eq}) \tag{2.51}$$

where L is the L-shell, and α_{eq} is the equatorial pitch angle.

The second adiabatic invariant, K, is defined by the total length of the field line between the two mirror points of the particle l, and the average parallel momentum along the field line $< p_{\parallel} >= m < v_{\parallel} >$ [*Schulz*, 1971],

$$K = 2ml < v_{\parallel} >= \oint m v_{\parallel} ds. \tag{2.52}$$

K is an invariant related to the periodic bouncing motion of a particle trapped between two mirror points on a magnetic field-line.

2.3.3 Azimuthal Drift Motion

The radial gradient and latitudinal curvature of the Earth's dipole field leads particles to azimuthally drift around the Earth while the particles are gyrating and bouncing. Table 2.2 [*Baumjohann and Treumann*, 1996] summarizes the different kinds of electric drifts and the magnetic drifts of charged particles. When a particle drift around the Earth without an external electric field, the curvature drift and the gradient drift contribute to the particle's drift velocity:

$$v_d = (v_{\parallel}^2 + v_{\perp}^2/2) \frac{B \times \nabla B}{\Omega_g B^2} \tag{2.53}$$

where Ω_g is the gyrofrequency described in Equation (2.47). The averaged angular drift velocity can be obtained by numerical integration in one full bounce period, but a more widely-used approximation for the average period is given below *Baumjohann and Treumann* [1996]:

$$< \tau_d > \sim \frac{\pi q B_E R_E^2}{3LW}(0.35 + 0.15 \sin \alpha_{eq}) \tag{2.54}$$

Table 2.2: Drift velocities of different guiding center drifts

	Drift velocity
ExB drift	$\mathbf{v}_E = \frac{\mathbf{E}\times\mathbf{B}}{B^2}$
Polarization drift	$\mathbf{v}_P = \frac{1}{\Omega B}\frac{d\mathbf{E}_\perp}{dt}$
Gradient drift	$\mathbf{v}_\nabla = \frac{mv_\perp^2}{2qB^3}(\mathbf{B}\times\nabla B)$
Curvature drift	$\mathbf{v}_R = \frac{mv_\parallel^2}{qR_c^2B^2}(\mathbf{R}_c\times\mathbf{B})$

where α_{eq} is the equatorial pitch angle. The ions and electrons drift in opposite directions: westward for ions and eastward for electrons.

The third adiabatic invariant Φ, which is associated with drift motion, is the conserved magnetic flux encircled by the periodic orbit of a particle trapped in an axisymmetric mirror magnetic field configuration when it performs closed drift shell orbits around the magnetic field axis. This drift invariant can be written as

$$\Phi = \oint v_d r d\psi. \tag{2.55}$$

The drift motion of the particle is highly related to the activity of the Earth's inner magnetosphere. Because positive ions and negative electrons drift in opposite directions, the motion will create a westward electric current, the ring current, around the Earth. Also, if the Earth's magnetic field is compressed by slowly increasing or decreasing solar wind, dynamic pressure, charged particles move radially inward or outward to conserve the magnetic flux enclosed by their drift orbit.

2.4 Interactions Between ULF Wave and Charged Particles

According to Equations (2.51) and (2.54) in Section 2.3, charged particles' bounce motion periods are on order of several seconds to several hundred seconds and their drift motion periods are on order of several hundred seconds to several thousand seconds. Particles can respond to the magnetospheric waves in ULF range while

executing drift and bounce motion in the magnetosphere. Energy can be transferred between charged particles and standing poloidal ULF waves (azimuthally propagating waves) in the magnetosphere [e.g. *Southwood et al.*, 1969; *Kivelson and Southwood*, 1986]. Radiation belt electrons can be energized by ULF waves [*Elkington et al.*, 1999; *Ozeke and Mann*, 2008]. On the other hand, ULF waves can also be internally generated or damped via interaction with energetic particles. In this section, we will discuss the mechanism of drift-bounce resonance and its effect on ULF wave energy variation.

2.4.1 Drift Resonance and Drift-bounce Resonance

Drift and drift-bounce resonances are important interaction mechanisms between energetic particles and FLRs in the magnetosphere. The resonance occur between the drift-bounce motion of the particles and an azimuthally propagating ULF wave. Energy can be transferred between energetic particles and waves in the process.

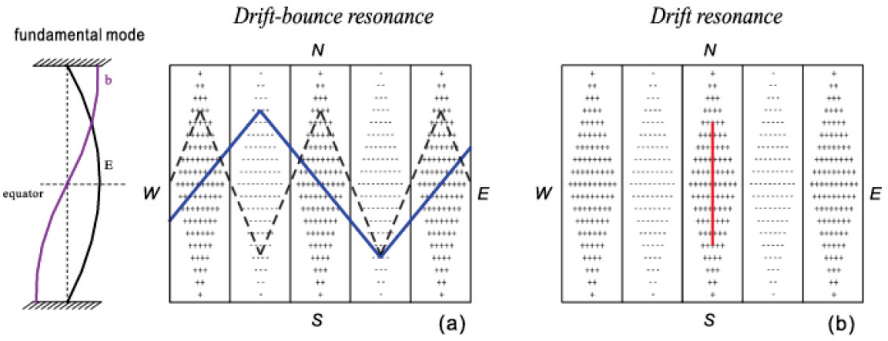

Figure 2.5: Schematic diagram showing the resonant trajectories of protons in the frame of azimuthally propagating fundamental mode poloidal Alfvén waves. Modified from *Yang et al.* [2011a]. The electric field intensity corresponds to the density of the signs. The positive and negative signs represent eastward and westward directed electric fields, respectively. (a) trajectory of resonant particles interacting with fundamental mode waves via the $N = 2$ resonance.(b) trajectory of resonant particles interacting with fundamental mode waves via $N = 0$ resonance.

Drift-bounce resonance will occur if the following condition is satisfied [*Southwood et al.*, 1969]

$$\omega - m\omega_d = N\omega_b \tag{2.56}$$

where ω_b is the particles' bounce frequency and ω_d is the drift frequency, m is the azimuthal wave number and $N = 0, \pm1, \pm2, ...$ is a parameter corresponding to different resonance conditions. The LHS of this equation is the Doppler-shifted angular frequency of a drifting particle in the wave frame. Figure 2.5 shows a diagram of $N = 0$ and $N = 2$ drift/drift-bounce resonance in the cases of a fundamental mode FLR. Electric field intensity is indicated as the density of signs. Negative (westward) and positive (eastward) signs represent the azimuthal direction of the wave electric field. Electrons, for example, will be accelerated in the region marked as minus signs and gain energy. Ions will be decelerated and lose energy in this region. When $N = 0$, the particles are relatively static and do not drift in the wave frame, but will only bounce along the field line. Particles with all pitch angles within the loss cone can drift resonate with the wave. We call it drift resonance, and call resonances when $N \neq 0$ drift-bounce resonance. Note that drift resonance only happens when the particle drift direction is the same as wave propagation direction. Electrons drift resonate with eastward-propagation waves and ions drift resonate with westward-propagation waves. In Equation (2.56), we define $m > 0$ for an eastward-propagation wave.

Another representative case is $N = \pm2$ in a fundamental mode standing wave. A N drift-bounce resonating particle travels exactly N wave periods in one of its bounce period in the wave frame. Depending on its initial position in the wave frame, particles gain or lose net energy in a bounce period because of the difference of electric field along the field line. Particles whose pitch angle is 90° will not gain or lose net energy when they drift within the wave frame because the wave amplitude is periodic at the equator. Generally speaking, the resonance of $N = 0, \pm2, \pm4...$ will only happen in odd harmonics while the resonance of $N = \pm1, \pm3, \pm5, ...$ will only happen in even harmonics. Both eastward and westward propagating waves can resonate with electrons and ions when $N \neq 0$. Figure 2.6 shows the $N = 0$ drift resonance energy and the $N = \pm2$ drift-bounce resonance energy of O^+ ions as functions of m. Note that drift-bounce resonance energy with negative $N = -2$ is higher than positive $N = 2$. We define $N > 0$ resonance condition as a particle travels exactly $|N|$ wave periods eastward in the wave frame. Higher energy ions drifting westward in the wave frame will meet the $N < 0$ drift-bounce resonance condition.

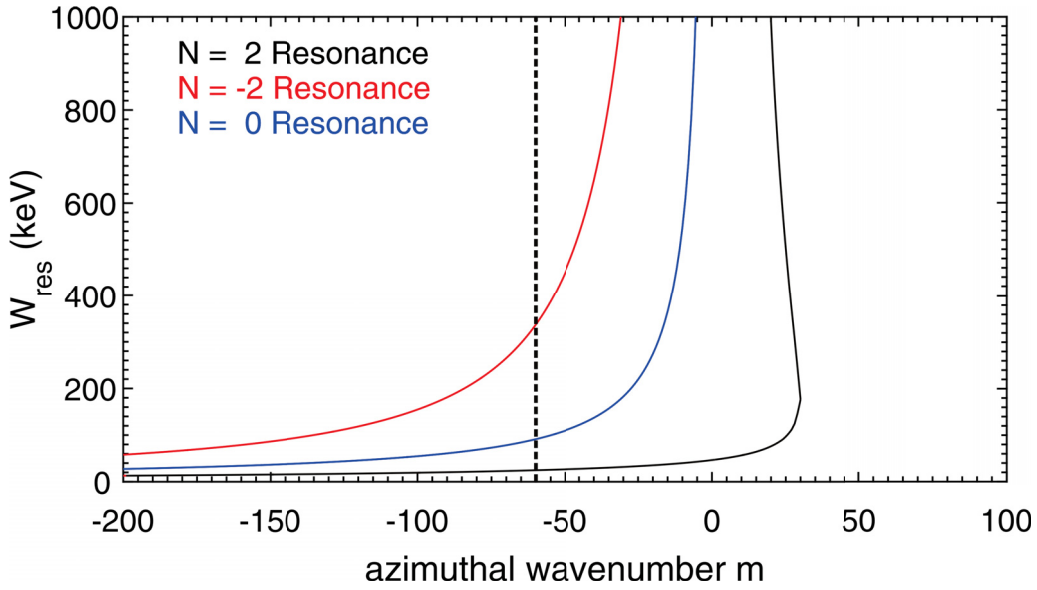

Figure 2.6: Resonance energy of O^+ ions as functions of azimuthal wavenumber m for different resonant coefficient N. The other parameters related to resonance conditions are $L = 5.7$, wave period $T = 100$ s, equatorial pitch angle $\alpha_{eq} = 30°$. In this plot, waves with $m > 0$ are propagating eastward. The resonant coefficient $N > 0$ corresponds to the drift-bounce resonance when particles are moving eastward in the wave frame. The dash line indicates the resonance energies in the case of $m = -60$.

2.4.2 Landau Damping and Flux Modulation

Consider the distribution function of particles f as a function of the particles' kinetic energy W, L-shell and magnetic moment: $f = f(W, L, \mu)$. If the first adiabatic invariant μ is a constant in the temporal scale of an ULF wave, then [*Southwood et al.*, 1969]

$$\frac{df}{dW} = \frac{\partial f}{\partial W} + \frac{dL}{dW}\frac{\partial f}{\partial L}. \tag{2.57}$$

The distribution function is stable when $df/dW < 0$. The Maxwell distribution without L-shell dependence is an example of stable distribution: More particles have lower energies while less particles have higher energies. In case of the drift/drift-resonance, ULF waves accelerate more particles in energies lower than the resonance energy and decelerate less particles higher than the resonance energy. The overall energy transfer is from ULF wave to the particles. In this thesis, we call this wave damping process Landau damping.

When $df/dW > 0$, the wave amplitude will gain energy from the unstable plasma.

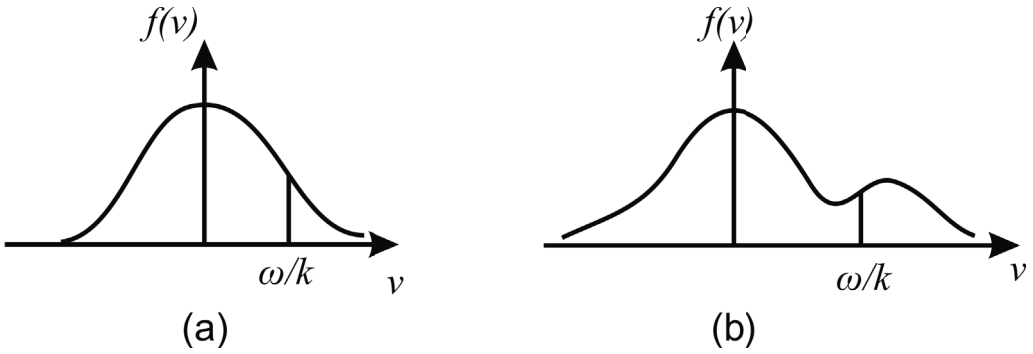

Figure 2.7: Schematic diagram of the Landau damping. (a) Stable distribution function $f(v)$ before interacting with ULF waves. (b) Unstable distribution function $f(v)$ after interacting with ULF waves. Taken from *Baumjohann and Treumann* [1996].

Particle's kinetic energy will be transferred to the wave and let its amplitude grow. This mechanism is considered to be a source of giant pulsations (Pgs) in the magnetosphere [*Green*, 1979, 1985].

The flux modulation of electrons and ions in the ULF wave field is widely observed by satelllites [e.g. *Zong et al.*, 2009; *Claudepierre et al.*, 2013]. The mechanism of observed flux modulations can be described by a more general form of the distribution function f [*Kivelson and Southwood*, 1985]

$$\delta f = -\frac{\mu b_{\parallel}}{B}\frac{\partial f}{\partial \mu} - \delta W \frac{\partial f}{\partial W} - \delta L \frac{\partial f}{\partial L} \tag{2.58}$$

where δL, δW, and $\delta \mu$ are the change of the L-shell, kinetic energy and magnetic moment caused by the ULF waves respectively. If we assume $\delta \mu = 0$ [*Southwood*, 1973],

$$\delta f = -\delta W \frac{\partial f}{\partial W} - \delta L \frac{\partial f}{\partial L} \tag{2.59}$$

The $\mathbf{E}\times\mathbf{B}$ drift of particles in the poloidal mode Alfvén wave is in radial direction. Inward particle displacement δL corresponds to increasing δW under assumption of conserved first adiabatic moment μ. The distribution function f will increase or decrease as the particles are displaced inward or outward. Although non-resonant particles experience radial displacement within poloidal mode ULF wave, only drift or drift-bounce resonant particles experience net inward/outward displacement in a bounce period. The net effect of electric field is dependent on the relative location of a particle in the wave reference frame. When a satellite moves relative to the

wave reference frame, it observes flux modulation because the inward and outward propagating fluxes driven by ULF waves are different. In Chapter 5, Chapter 6 and Chapter 7, we will discuss the flux modulation of ions and electrons in poloidal ULF waves. The L-dependence of the distribution function $\frac{\partial f}{\partial L}$ will be discussed in Chapter 6.

Chapter 3

Fast Damping of ULF Waves Excited by Interplanetary Shocks in the Magnetosphere

The work in Section 3.1 - Section 3.4 have been published on *Journal of Geophysical Research: Space Physics* [*Wang et al.*, 2015]. Although the damping of ULF waves caused by the wave-particle interaction is out of the scope of our simulation models in Chapter 4, we compared the energization effects of fast damped ULF wave on O^+ and H^+ ions in plasma environments with different thermal energy in Section 3.5. In this chapter, we studied the energy exchanging process between ions and ULF waves caused by interplanetary shocks. The observational evidences encourage us doing further studies on this process with computational models.

The analysis of Cluster spacecraft data shows that intense ultra-low frequency (ULF) waves in the inner magnetosphere can be excited by the impact of interplanetary shocks and solar wind dynamic pressure variations. The observations reveal that such waves can be damped away rapidly in a few tens of minutes [*Zong et al.*, 2009; *Zhang et al.*, 2010]. Here, we examine mechanisms of ULF wave damping for two interplanetary shocks observed by Cluster on November 7, 2004, and August 30, 2001. The mechanisms considered are ionospheric Joule heating, Landau damping, and waveguide energy propagation. It is shown that Landau damping provides the dominant ULF wave damping for the shock events of interest. It is further demonstrated that damping is caused by drift-bounce resonance with ions in the energy

range of a few keV. Landau damping is shown to be more effective in the plasmasphere boundary layer due to the relatively higher proportion of Landau resonant ions that exist in that region.

3.1 Introduction

Wave-particle interactions involving ULF standing waves [*Dungey*, 1955] can dramatically alter the behavior of electrons [*Zong et al.*, 2007, 2009] and ions [*Yang et al.*, 2010, 2011a; *Zong et al.*, 2011] in the inner magnetosphere. These waves can be excited by external solar wind disturbances and/or internal plasma instabilities. External sources include solar wind dynamic pressure pulses [*Kepko and Spence*, 2003; *Hudson et al.*, 2004; *Takahashi and Ukhorskiy*, 2007; *Claudepierre et al.*, 2009, 2010; *Claudepierre et al.*, 2013], Kelvin-Helmholtz (K-H) instabilities on the magnetopause [*Hudson et al.*, 2004; *Claudepierre et al.*, 2008], and ion cyclotron resonance with backstreaming solar wind ions [*Odera*, 1986]. The K-H instability can excite ULF waves in the magnetosphere through coupling that takes place between long wavelength surface mode waves and earthward field line resonances (FLRs) [*Fairfield et al.*, 2000; *Hasegawa et al.*, 2004; *Rae et al.*, 2005; *Claudepierre et al.*, 2008]. Interplanetary shocks and solar wind dynamic pressure pulses also excite ULF waves, although the precise mechanism that converts shock energy to waves of high azimuthal wavenumber (high-m) is not yet fully understood. A possible mechanism related to substorm injections has been discussed by *James et al.* [2013]. In this chapter we put aside the issue of how these waves are generated and focus on the wave-particle interactions they cause.

ULF waves excited by shocks and dynamic pressure variations can be very intense, and are sometimes damped away quickly over tens of minutes [*Zong et al.*, 2009; *Zhang et al.*, 2010]. In this chapter, it is shown that the observed fast damping is caused by drift-bounce resonance between ULF waves and ions having energies of a few keV. Such a mechanism has been described theoretically by *Southwood and Kivelson* [1981, 1982], and is possible because of the comparable periods of drift and bounce motion of energetic particles and ULF oscillations. As reported by *Yang et al.*

[2010, 2011a,b] and *Zong et al.* [2011], the associated damping takes place over time intervals where wave electric fields accelerate charged particles, a process that can also enhance radial diffusion (e.g., *Loto'aniu et al.* [2006]). Although energetic particle drift-bounce resonance may occur with different ULF modes, e.g. toroidal ULF waves [*Elkington et al.*, 1999] and compressional poloidal mode ULF waves [*Elkington et al.*, 2002, 2003, 2004; *Tan et al.*, 2011], the interaction with poloidal ULF waves [*Zong et al.*, 2009; *Zong et al.*, 2011, 2012a] is considered to be more efficient [*Zong et al.*, 2009; *Yang et al.*, 2011a,b; *Zong et al.*, 2012a], even leading to the formation of a new radiation belt [*Li et al.*, 1993; *Wygant et al.*, 1994; *Zong et al.*, 2011] in certain situations. It has been reported by *Zong et al.* [2007, 2009] and *Tan et al.* [2004, 2011], that acceleration of electrons by drift-bounce resonance can also take place.

In the auroral zone, *Wright et al.* [2003] studied FAST satellite data and showed that electron acceleration can dissipate an amount of energy similar to Joule heating. Dispersive scale Alfvén wave damping has been investigated by *Lysak and Lotko* [1996], who showed through analysis of the kinetic wave dispersion relation that Landau damping by electrons can be efficient at spatial scales where electron inertia and finite ion gyroradius become important. In a different context, *Evans et al.* [2009] evaluated the importance of Landau damping for surface Alfvén waves in the solar wind. Important as these studies are, they have not quantified Landau damping in regions of the magnetosphere where standing Alfvén waves and FLRs are common. One such attempt was made by *Rankin et al.* [2007], who showed through numerical simulations that electron particle trapping can be efficient in suppressing Landau damping in short perpendicular scale standing ULF waves. Another approach was considered by *Hollweg* [1971], who calculated the nonlinear Landau damping rate of Alfvén waves based on theoretical considerations of *Stix* [1962]. A general approach to estimate the damping rate of standing ULF waves has been given by *Southwood* [1976], who examined the drift-bounce mechanism that is the subject of the study presented here.

Besides Landau damping, other ways of energy loss from ULF waves include Joule heating in the ionosphere and the propagation of wave energy through the magnetospheric waveguide. Joule heating of ionospheric particles through Alfvén

waves has been widely studied and is usually considered the most effective energy sink. For example, *Newton et al.* [1978] numerically computed the damping rate for ULF waves for different height-integrated Pedersen conductivity, whereas *Greenwald and Walker* [1980] studied in detail the amount of energy loss in a particular ULF event. More sophisticated models [*Sydorenko and Rankin*, 2012] describing the propagation of ULF waves in the ionosphere have also been developed. Two-dimensional MHD computer models by *Sciffer et al.* [2005] and *Waters and Sciffer* [2008] include solutions for near vertical magnetic fields at high latitudes and for oblique magnetic fields applicable at lower latitudes. Observationally, *Rae et al.* [2007] found that more than 30% of the energy in FLRs was deposited via Joule heating during a substorm cycle. The same authors estimated that Joule heating can be an effective means of transporting energy from the solar wind into the high latitude ionosphere. Another mechanism of energy loss from ULF waves was considered by *Wright* [1994], who studied transport of waves through the magnetospheric waveguide. A related study by *Claudepierre et al.* [2008] studied transport of low-m ULF waves generated by the Kelvin-Helmholtz instability in a numerical simulation.

In this chapter, we study the temporal variation of shock-excited ULF waves under different damping mechanisms. Comparing the effects of Landau damping, Joule heating, and waveguide propagation, we find that the evolution of wave energy cannot be fully accounted for by Joule heating or waveguide propagation. We further show that in certain situations the Landau damping rate of Alfvén waves is higher than from Joule heating, i.e., as a result of fundamental mode ($N = \pm 2$) drift-bounce resonance with energetic ions. Our results suggest that Landau damping can induce fast damping of ULF waves when the drift-bounce resonance mechanism is effective, i.e., when particles in sufficient numbers satisfy the resonance condition. To our knowledge, we present the first reported explanation for the strong damping of ULF waves that can accompany interplanetary shocks.

The chapter is organized as follows: Section 3.2 describes two representative observations of fast damping of Alfvén waves in different regions of the magnetosphere. In Section 3.3, we compare wave propagation, Landau damping, and Joule heating. Finally, we suggest that the Landau damping mechanism is more effective for some

regions of the magnetosphere because such regions can support generation and/or propagation and damping of ULF waves excited by shocks without modifying the frequency of Alfvén waves. This feature is a characteristic of the observations we consider.

3.2 Observations

The magnetic and electric field data for ULF waves presented in this chapter are obtained from the Fluxgate Magnetometer (FGM) and Electric Field and Wave (EFW) experiment on the Cluster II satellite constellation [*Balogh et al.*, 2001]. The plasma density is calculated from the EFW experiment using the method from *Moullard et al.* [2002]. The four Cluster spacecraft are capable of observing three-dimensional, small-scale spatial structure in the space environment, including electromagnetic fields and particles. We present two shock-induced Alfvén wave events for detailed study.

3.2.1 Fast Damping of a Large-amplitude ULF Wave in the Plasmasphere Bounday Layer

First of all, we focus on the shock event on November 7, 2004. Figure 3.1 gives an overview of this event. An interplanetary shock hit the magnetosphere through a sudden increase in maximum solar wind dynamic pressure and plasma density at 18:27 UT. The locations of the Cluster spacecraft are shown in Figure 3.2(a) and Figure 3.2(b). During the event, Geotail was upstream in the solar wind at (19.28, 13.59, -2.66) R_e in GSE coordinates. The magnitude of the solar wind velocity x-component V_x increased from about 550 km/s to 700 km/s. The ion density increased from about 8 cm^{-3} to 15 cm^{-3}. The z-component of the interplanetary magnetic field B_z increased by about 15 nT. The dynamic pressure of the solar wind continually increased after the arrival of the shock and reached more than 70 nPa. An intense magnetic storm with minimum Dst of -373 nT followed the shock [*Tsurutani et al.*, 2008].

ULF waves accompanying shocks, especially Pc5-ULF waves, are usually excited

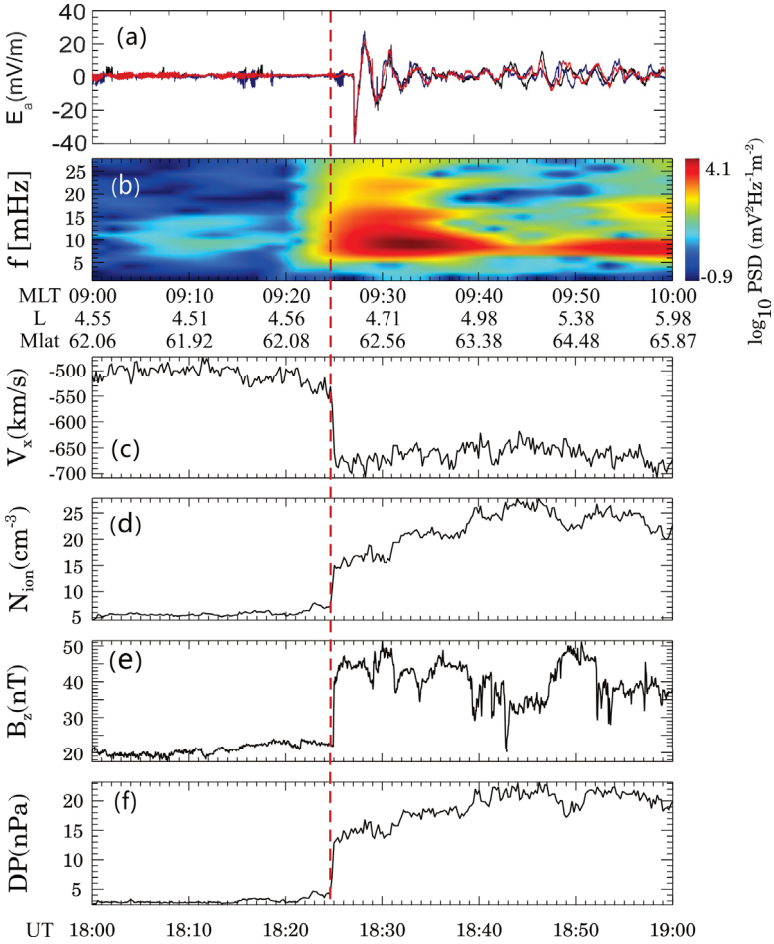

Figure 3.1: The overview of a shock event and the following ULF waves observed on November 7, 2004 from 18:00UT to19:00UT. From top to bottom panels show: (a) azimuthal component of electric field observed by Cluster spacecraft, black, red and blue lines are the observations of C1, C2 and C4 respectively; (b) The electric field dynamic power spectrum from C1 observed; (c) x component of solar wind velocity; (d)solar wind ion density; (e) z component of interplanetary magnetic field; (f) dynamic pressure of solar wind. (c)-(f) are observations from Geotail satellite. Geotail observed a shock event and Cluster observed the energy enhancement of ULF waves around the same time. Red dashed line indicates the arrival of interplanetary shock.

in the dayside of the magnetosphere [*Hudson et al.*, 2004; *Brito et al.*, 2012] but propagate to the nightside at the fast mode speed [*Wygant et al.*, 2002]. On November 7, 2004, the Cluster satellites observed ULF waves generated after a shock while the Cluster fleet was traveling in the morning side of the plasmasphere boundary layer (around 09:00MLT, $L = 4.5$). Figure 3.1 shows the observation of the azimuthal component of the electric field (E_a) in a local mean field-aligned coordinate system [*Takahashi et al.*, 1990] and the corresponding x-component of solar wind velocity (V_x) during the period from 18:00-19:00 UT . The observed quasi-sinusoidal electric field with a period of about 3 minutes had a peak amplitude of 10 mV/m and was attenuated over time. Figure 3.3 shows a comparison between satellite and ground observations in this event. Along adjacent flux tubes, both the ground and satellite observed amplitude attenuate over a similar time range. The power spectral density (PSD) of E_a is shown in Figure 3.1(b), and was obtained using dynamic spectral analysis [*Takahashi and Ukhorskiy*, 2007]. The central frequency of ULF waves is observed to be about 6.7 mHz. The PSD is also strong at a frequency around 17 mHz, which may be due to a higher harmonic resonance of 6.7 mHz. In this particular event, the azimuthal wave number for the poloidal mode was estimated to be around 50, with the wave propagating eastward [*Zong et al.*, 2009]. In the process of wave generation and damping, particles have been accelerated by ULF waves in this event as described by *Zong et al.* [2009]. It will be demonstrated that the interaction between particles and waves, especially resonant processes, can be a main factor in explaining the damping of the observed Alfvén waves in this event.

3.2.2 Fast Damping of Moderate Amplitude ULF Waves in the Plasmasphere and Plasmasphere Bounday Layer

Figure 3.4(a) shows shock-excited electric field variations measured by Cluster on August 30, 2001. During the event, the spacecraft were in the outer radiation belt with $L \sim 4.5$ (C1, C2 and C4) at about 12:00 MLT. The locations of spacecraft are shown in Figure 3.2(c) and Figure 3.2(d). C3 crossed into the plasmasphere boundary layer while the other three spacecrafts were in the plasmasphere proper. The Geotail spacecraft were located at $(15.19, -12.15, -1.13)$ R_e in GSE coordinates when they

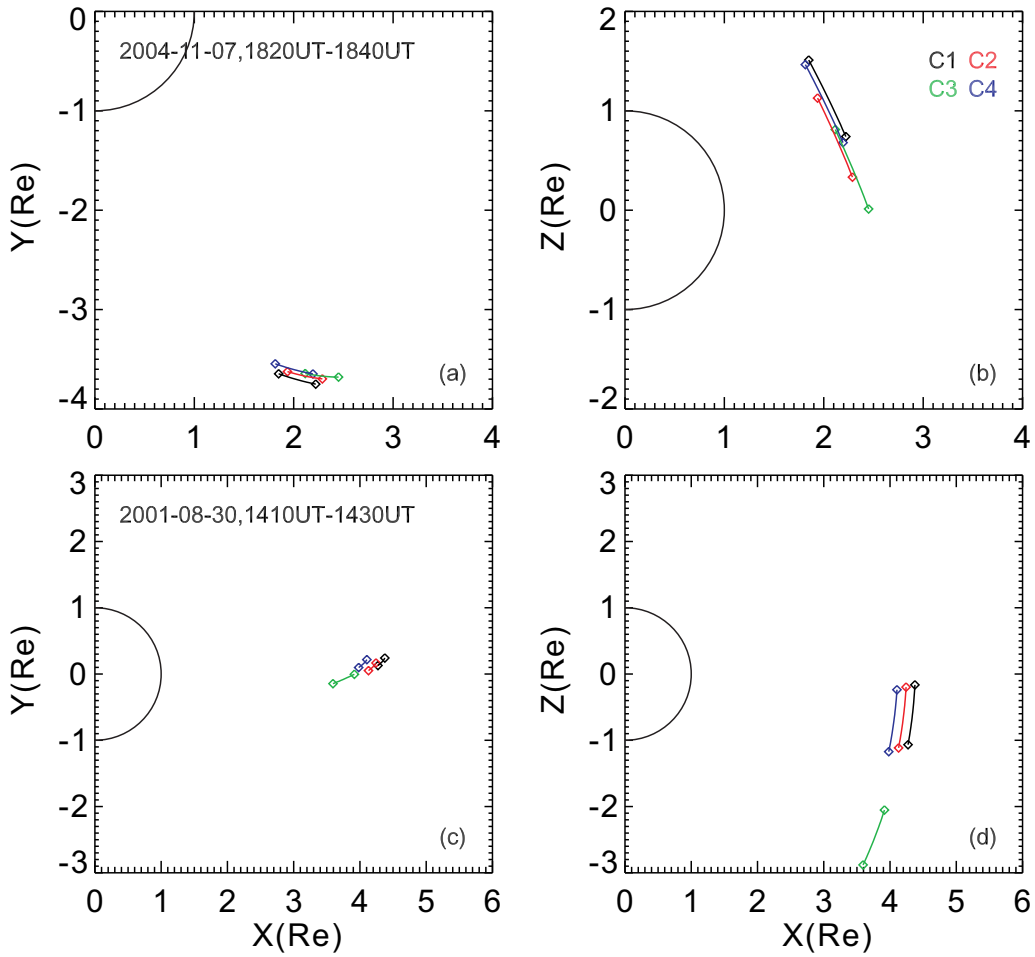

Figure 3.2: (a)Orbits of Cluster spacecraft in X-Y plane on November 7, 2004 from 18:20UT to 18:40UT. (b)Orbits of spacecraft in X-Z plane in the same time range as (a). (c)Orbits of Cluster spacecraft in X-Y plane on 30 August, 2001 from 14:10UT to 14:30UT. (b)Orbits of spacecraft in X-Z plane in the same time range as (c). Orbits of C1, C2, C3 and C4 are shown in black, red, green and blue lines. All orbits are shown in GSE coordinate.

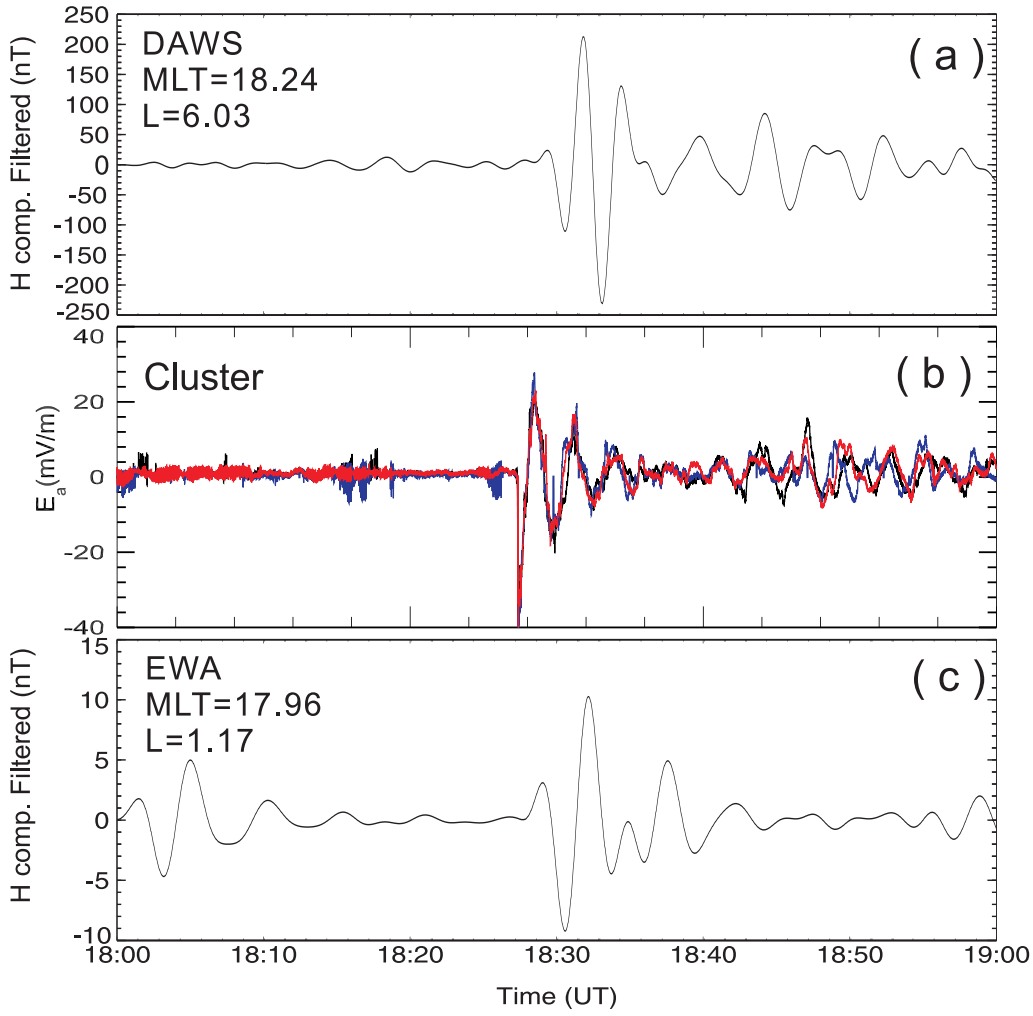

Figure 3.3: (a) and (c) Band filtered north-south component of geomagnetic field fluctuation. The elliptic band-pass filter is used and filter band is between 3 mHz and 8 mHz. Data to make panel (a) are from Dawson City (DAWS) station of CARISMA magnetometer network. Data to make panel (c) are from Ewa Beach (EWA) of station 210 Magnetic Meridian magnetometer network. (b) Azimuthal component of electric field observed by Cluster spacecraft in similar format as Figure 1(a). The three panels are arranged along the geomagnetic latitude of the footprint of satellite or the station.

observed the shock: the plasma density increased to 1.5 cm^{-3}, the amplitude of solar wind velocity increased from 450 km/s to 550 km/s, and the dynamic pressure increased from about 0.2 nPa to about 1.0 nPa. This event was induced by a weaker interplanetary shock than the one in 2004. The oscillations of the electric field azimuthal component were about 1.5 mV/m in this case and were attenuated over a few minutes. The central frequency with the largest power density was in the ULF range (about 7.8 mHz). In this event, the azimuthal wave number for the poloidal mode is estimated as 10 ± 3 [*Eriksson et al.*, 2006], with the wave propagating eastward.

The observed magnetospheric plasma density variation is shown in Figure 3.5(a). The density of ions in the plasmasphere bounday layer was about 8 cm^{-3} at C3 while being over 100 cm^{-3} in the location of C1, C2 and C4, which were in the plasmasphere. Such large differences in densities between the plasmasphere boundary layer and plasmasphere can induce distinct waves in the plasmasphere. Figure 3.5 shows wavelet analysis results for different satellites, where the electric field components have been converted into the mean field-aligned (MFA) coordinate system. E_a corresponds to the poloidal mode of ULF waves, assuming a dipolar geomagnetic field. Spacecraft C2 and C3 observed a power density increase for waves in the $5-10$ mHz range. The power of the waves observed by C3 is larger than that observed by C2, while their rate of decay (damping) is much faster than at C2. At 14:12 UT, C3 observed an electric field with power density fluctuations exceeding 100 $(mV/m)^2$ with a period of about 128 s, decreasing to about 10 $(mV/m)^2$ at around 14:20 UT. As for spacecraft C2, the power density of the electric field fluctuations decreased to 10 $(mV/m)^2$ after 14:30UT. This difference may be reflected by the spatial separation of the two spacecraft, which sampled a different local density and energy of particles. Previous studies have pointed out that the density gradient in the plasmasphere boundary layer should have an effect on VLF waves [*Wang et al.*, 2011] and this appears to be true also for ULF waves. The expected change in amplitude of ULF waves across the plasmapause was also discussed by *Allan and Knox* [1979] and *Menk et al.* [2004].

According to *Fraser et al.* [2005], the plasma mass density distribution near the plasmasphere boundary layer can affect the characteristics of ULF waves. But how it affects ULF wave damping has not yet been fully analysed. The Alfvén velocity

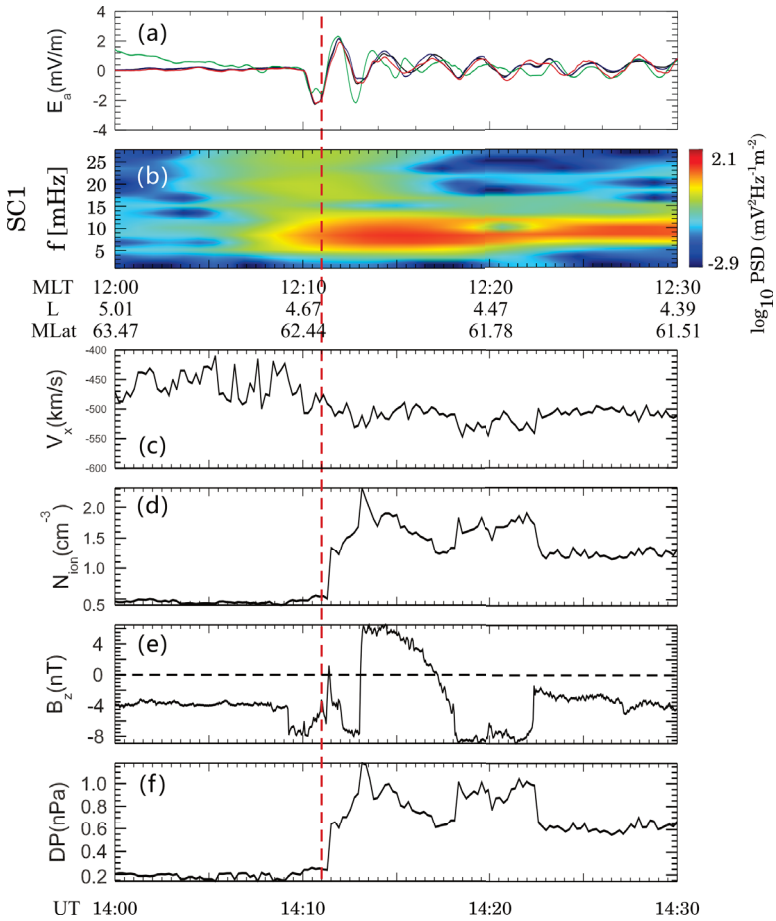

Figure 3.4: The overview of a shock event and the following ULF waves observed on August 30, 2001 from 14:00UT to 14:30UT. Panels are shown in a similar format like in Figure 3.1. Black, red, green and blue lines are the observations of C1, C2, C3 and C4 respectively in (a). Shock arrived at about 14:10UT and Cluster observed small amplitude ULF waves.

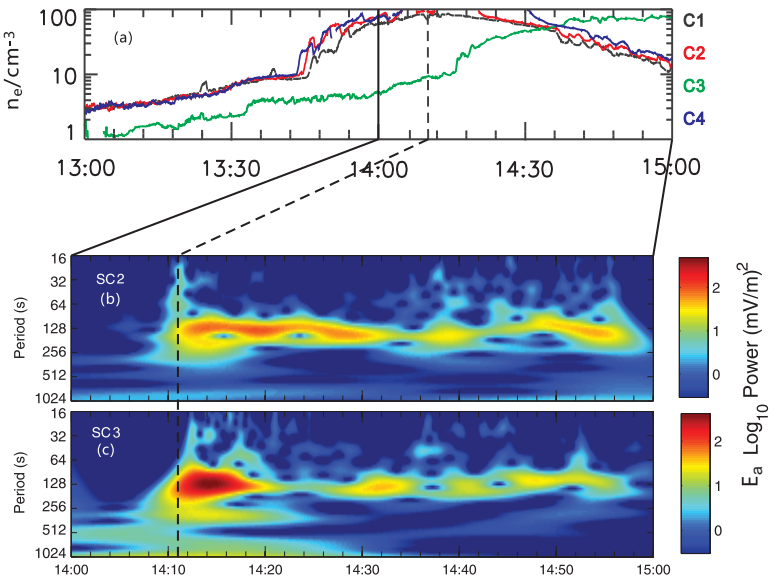

Figure 3.5: Observations of ULF waves inside the plasmasphere and in the plasmasphere boundary layer for the event on August 30, 2001. Panel (a) is the plasma density calculated from spacecraft potential measured by EFW instrument on Cluster. C1, C2, C3 and C4 are shown in black, red, green and blue lines. C3 was in the plasmasphere boundary layer and the other three spacecraft were in the plasmasphere. By comparing the wavelet spectrum analysis results from C2 and C3 shown in panels (b) and (c), we see that wave energy is damped faster in C3.

$V_A = B(s)/\sqrt{\mu_0 \rho(s)}$ (where μ_0 is the vacuum permeability and B is the magnetic field) depends on the plasma mass density $\rho(s)$ along field lines, and consequently the frequency and propagation characteristics of ULF waves are affected as the waves propagate through the plasmasphere boundary layer. It is also known that oxygen ions contribute significantly to mass loading along the field line during disturbed periods, which is another consideration at later times as the ring current develops ([e.g. *Jordanova et al.*, 1996]).

3.3 Interpretation and Discussion: Possible Mechanisms for Fast Damping of ULF waves

3.3.1 Joule Heating

Ionospheric damping of Alfvén waves is one of their main sinks of energy. The damping takes place through Joule heating produced by the interaction of the waves with ionospheric particles. For a transverse wave, Joule dissipation through Pedersen currents can be calculated based on a boundary condition at the ionosphere: $b = \mu_0 \Sigma_P E$, where Σ_P is the height integrated Pedersen conductivity. This boundary condition can also be written in another form *Southwood and Hughes* [1983]:

$$\frac{Eb}{\mu_0} = \Sigma_P \left| E \right|^2 . \tag{3.1}$$

In this equation, Joule heating is balanced by net Poynting flux into the ionosphere. In the events of interest, damping rates are calculated according to the simple model of *Newton et al.* [1978]. Although more sophisticated and more recent numerical models of ULF wave propagation in the ionosphere have been developed, we use Newton's calculations because it provides simple analytical expressions for damping that are valid for high-m waves and near vertical geomagnetic field; assumptions which hold for the events we are studying. As we shall see later, the damping rates for Joule heating turn out to be much smaller than Landau damping, and so it is reasonable to expect our conclusions will not change on using more complex models of damping. *Newton et al.* [1978] calculated the damping rate of Alfvén waves due to Joule heating and found that when the height-integrated Pedersen conductivity is large ($\Sigma_P > 1$ S)

in the dayside ionosphere, low harmonic poloidal Alfvén wave damping occurs at the rate: $\gamma/\omega = 2.2 \times 10^{-2}\Sigma_P^{-1}L^{3/2}$.

Using this last result, the damping rate of ULF waves in both shock events studied can be estimated based on a height-integrated conductivity calculated from the IRI2012 model (http://wdc.kugi.kyoto-u.ac.jp/ionocond/sigcal/index.html). The estimated damping rate at C1 is $\gamma/\omega \simeq 0.028$. The effect of ULF wave damping produced by Joule heating is shown in Figure 3.6. The wave amplitude reduces to 30% of the initial amplitude over the time indicated, and the calculated damping rate is similar in both C1 and C3 in the 2001 event. Although Joule heating is an effective damping mechanism, the two observations reported here reveal that the observed damping is much faster than can be provided by Joule heating alone.

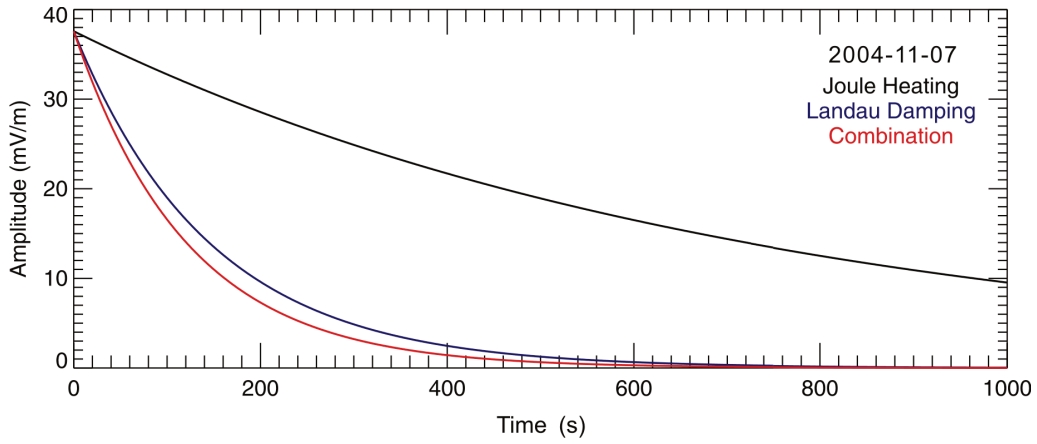

Figure 3.6: The variations of ULF waves amplitude caused by different damping mechanism. Black, blue and red lines are the calculated damping rates at C3, based on Joule heating, Landau damping and the combined effect.

3.3.2 ULF Wave Damping Through Drift-bounce Resonance

As discussed earlier in the chapter, Landau damping of large-amplitude standing Alfvén waves in geomagnetic fields can occur through wave-particle interactions. It represents an additional damping on waves over Joule heating. The most important interaction between charged particles and ULF waves, especially poloidal ULF waves, is drift-bounce resonance. The resonance condition is [*Southwood and Kivelson*, 1981]

$$\omega - m\omega_d = N\omega_b, \tag{3.2}$$

where ω , ω_d and ω_b are wave frequency, particle drift frequency, and bounce frequency, respectively, m is the azimuthal wave number, and N is an integer which depends on the harmonic mode of the standing wave. In each full bounce in latitude the particle moves westward exactly N wavelengths in the frame of wave. In the two events studied, electric fields of shear Alfvén waves are observed near equator or at mid latitude region. We choose a fundamental mode with $N = 2$ as representative of the events. According to *Southwood and Kivelson* [1982]; *Chen and Hasegawa* [1988], the electric field seen by an ion in drift bounce resonance (in this case with an $N = 2$ high-m ULF wave) will cause damping or growth of the wave as it maintains the same direction as the ion bounces between hemispheres. The resonance energy for different ions can be calculated from Equation (3.2) because ω_d and ω_b are dependent on the particle energy E [*Baumjohann and Treumann*, 1996], and take the following form in a dipole magnetic field:

$$\omega_b = \frac{(W/m)^{1/2}}{LR_E}(0.59 - 0.25\sin\alpha_{eq})^{-1}, \tag{3.3}$$

$$\omega_d = \frac{LW}{qB_E R_E^2}(2.1 + 0.9\sin\alpha_{eq}), \tag{3.4}$$

where α_{eq} is the pitch angle of a particle at the equatorial region. By substituting Equation (3.3) and Equation (3.4) into Equation (3.2), the resonance condition can be obtained once the azimuthal mode number m is specified. The azimuthal wave number can be calculated from multi-spacecraft data using the technique of *Takahashi et al.* [1985]:

$$m = \frac{\Delta\theta}{\Delta\phi}, \tag{3.5}$$

where $\Delta\theta$ and $\Delta\phi$ are, respectively, the cross phase difference in the time series, and the azimuthal separation of satellites. In the 2004 event, the m-value is estimated to be 50 for the poloidal mode [*Zong et al.*, 2009; *Zong et al.*, 2012a]. Combining the m-value of poloidal ULF waves with the spatial separation of the spacecraft, the resonance energy expected for oxygen ions in interaction with a wave of 7.8 mHz is between 8.13 keV and 16.75 keV in the pitch angle range of $45° - 75°$. For H ions the resonance energy is between 0.623 keV and 1.03 keV.

The bounce frequencies of energetic electrons with energy of tens of keV in the inner magnetosphere are much higher than either the energetic electron drift frequency

or the Pc5 wave frequency [*Zong et al.*, 2009]. Thus, the drift-bounce resonance of energetic electrons can only be excited with $N = 0$. The condition for resonance changes into:

$$\omega = m\omega_d. \tag{3.6}$$

For electrons interacting with poloidal mode waves, the resonant energy requirement is lowered because of their typically large m-value ($m \sim 50$). The resonance energy of electrons corresponds to $E_{res} = 110.1$ keV. From the considerations and estimates presented above, hydrogen ions resonate at the lowest energy, followed by oxygen, and then electrons. The approximate damping rate can be calculated following *Southwood* [1976]:

$$\frac{\gamma}{\omega} = \frac{\rho_{res} v_{res}^2}{\rho \omega^2 L^2}, \tag{3.7}$$

where γ is the damping rate, ω is the frequency of the wave, ρ and v are particle density and velocity, and the suffix "res" refers to the particle in resonance. This ULF wave damping rate requires assumptions of finite plasma β and an axisymmetric field with mirror symmetry. Around $L \sim 4$ the magnetic field can be considered a dipole field and so the model assumptions are valid for the observations of interest in this study. Although the damping rate derived by *Southwood* [1976] is approximate, it provides by far the largest damping rate and can explain the observed difference in damping between waves excited in the plasmasphere and plasmasphere boundary layer.

Figure 3.7 illustrates the differential particle flux data obtained from the CIS and RAPID instruments on Cluster. The top panel of the figure shows ion energy flux overlaid with electric field oscillations for the 2004 shock event. The bottom panel shows the flux in several energy channels as a function of time. There is a resonance peak between 6.94 keV and 9.23 keV that brackets the resonant energy expected for O^+, i.e., between 8.13 keV and 16.75 keV in the pitch angle range of $45 - 75$ degrees. The corresponding resonant energy for H^+ is between 0.623 keV and 1.013 keV. The ion flux data, especially the contribution from O^+, provides evidence of a link between the observed strong damping of waves and drift-bounce resonant wave-particle interactions. In the event pertaining to this figure, the relative density ρ_{res}/ρ is about 0.0143. Where ρ_{res} can be computed using data from the CIS and RAPID instruments on Cluster. The calculated damping rate corresponds to

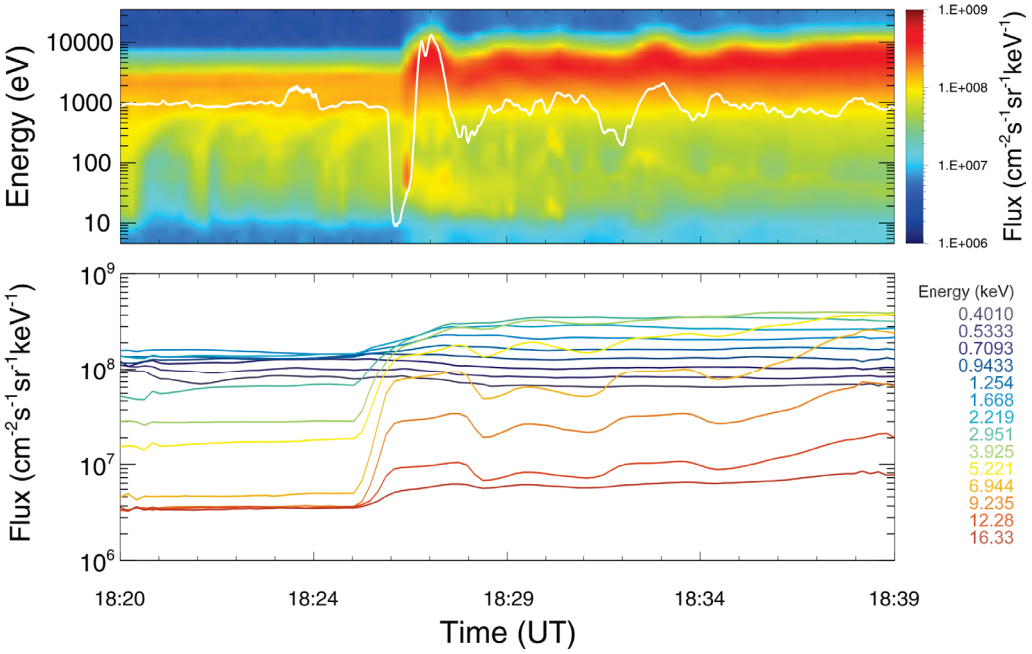

Figure 3.7: The resonance between ULF waves and ions in the 2004 event. The top panel shows ion spectrum overlaid with electric field oscillations for the 2004 shock event. The bottom panel shows the flux in several energy channels as a function of time.

$\gamma/\omega \simeq 0.117$, which is much larger than the damping rate induced by Joule heating. The effects of Landau damping and Joule heating are compared in Figure 3.6. It can be seen that the amplitude of ULF waves is damped to below 3.2% of the original amplitude in 600 seconds if there is only Landau damping. The combined effect of both mechanisms can damp the ULF wave to 1.4% of the initial amplitude in the same time span. The conclusion is that fast attenuation of the observed wave amplitude is mainly caused by Landau damping.

The results calculated from Cluster in the case of the 2004 event with the combined effect of Landau damping and Joule heating are shown in Figure 3.8. We choose the maximum amplitude of the electric field as the initial wave amplitude, and assume that damping proceeds from the time the maximum field is attained. The results are based on Equation (3.7) and the observed frequency of ULF waves. Comparing with the observation, the calculated damping rate gives a good fit to the observation. This demonstrates that the main part of the energy loss of Alfvén waves is due to bounce-resonant Landau damping in this event.

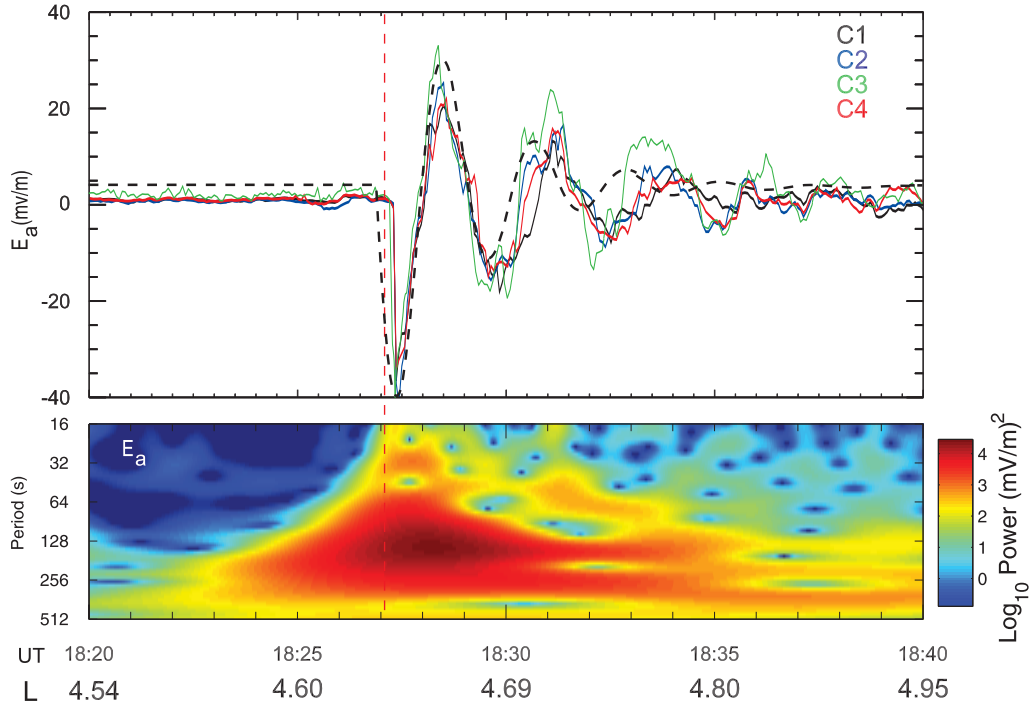

Figure 3.8: Above panel: the azimuthal component of electric field observed by Cluster in the 2004 event. Black, blue and red lines are the observation C1, C2 and C4. The black dasdh line multiplies the maximum amplitude by the damping rate calculated from Equation (3.2). Below panel: wavelet analysis spectrum of C3 observed electric field azimuthal component.

In the 2001 event, variations of electron number density imply that C3 was in the plasmasphere boundary layer region and C2 was in the plasmasphere. This allows us to consider damping rates of ULF waves in different regions of the magnetosphere. The estimated and observed damping rates are shown in Figure 3.9 and Figure 3.10. In this event, the resonant energy expected for O^+ is about 4.34 keV. This is consistent with a resonant response in ion flux oscillations in the energy channels between 1.16 keV and 4.94 keV. In Figure 3.9, the dashed lines and the solid lines show the damping rate with and without Joule heating, respectively. It can be seen that in the 2001 event, Landau damping is also the main damping mechanism in both the plasmasphere and plasmasphere boundary layer. As the damping rate caused by Joule heating depends on the ionospheric conductivity at the end of field lines, there is no significant difference in Joule heating rates between C2 and C3. According to the observations shown in Figure 3.6, however, the ULF oscillations of C3 damped faster than at the other satellites. Although C3 observed a larger amplitude maximum, it damped much faster within 600 s, by which time the amplitude of C3 was below 0.1 mV/m while that of C2 was still around 1.4 mV/m. A more detailed comparison between the observations and estimation of damping is shown in Figure 3.10. The $4 - 9$ mHz band-filtered ULF waves and the calculated damping curve are very close to each other in both the C2 and C3 observations. The different damping rate between C2 and C3 is likely caused by the different plasma densities at the position of C2 and C3 in the magnetosphere. The implication is that due to a dependence of the damping rate on density, wave energy is transferred into particle energy at a lower rate at C2. This can be inferred from Equation (3.7), which shows that the proportion of particles in resonance is the main factor in determining the damping rate. This proportion was smaller in the plasmasphere because the overall particle density was higher in the plasmasphere. Regardless, Landau damping is the main factor in explaining the different damping rate in the plasmasphere and plasmasphere boundary layer.

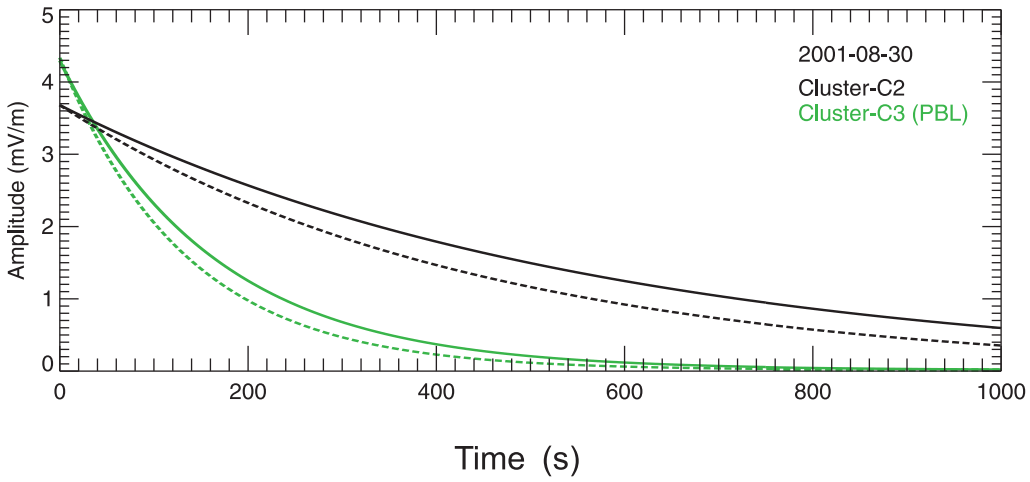

Figure 3.9: The variations of ULF waves amplitude inside and outside of plasmasphere. Black, green lines are the calculated damping rates at C1 and C3 for the 2001 event. They show that the Landau damping rate of ULF waves is largely affected by satellite position in the magnetosphere. The dashed lines indicate the damping rate in considering both of Joule heating and Landau damping.

3.3.3 Energy Propagation in the Magnetospheric Waveguide

In this section we consider the possibility that shear Alfvén waves observed by Cluster are field line resonances (FLRs) excited through mode-conversion of compressional waves that propagate in the magnetotail waveguide. The compressional waves will lose amplitude as they propagate, and this will manifest as an apparent damping of shear waves observed by the satellites. As FLRs can be reasonably approximated as 1D eigenmodes of standing wave electric and magnetic fields, this is consistent with the approach used to estimate Landau and ionospheric damping. We will estimate and compare damping as a result of wave propagation with Joule heating and Landau damping. The estimates provided are based on a point-like source of waves, which should correspond to the strongest level of damping.

Figure 3.11 is a schematic diagram of the magnetospheric waveguide viewed in the ecliptic plane according to *Wright* [1994]. A point-like source of fast mode waves in the waveguide will propagate energy isotropically throughout the magnetosphere. The wave energy arriving earliest in time at the observation point (satellite) will have travelled along a path of minimum distance between the source and observation point; it will therefore have the largest amplitude, having spread out the least. Wave

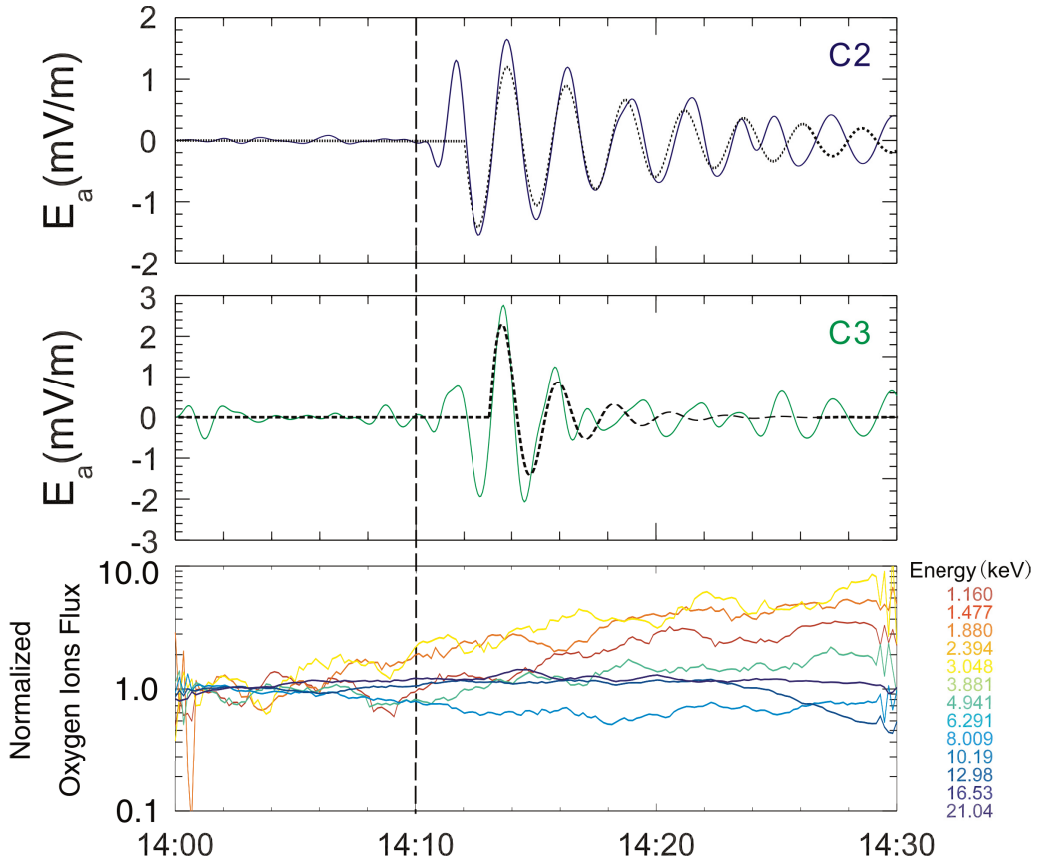

Figure 3.10: Above panel: the azimuthal component of electric field observed by Cluster C2 in the 2001 event. Blue line is the observation of C2. Middle panel: the same format as C3 while the green line is the observation of C3. Below: The flux of oxygen ions in different energy channels as a function of time. The flux in each energy channel has been divided with the average flux before the Shock arrival(the average flux between 14:00UT-14:08UT) in order to show the variation of each channel.

energy arriving at the observation point after reflection from the boundaries of the waveguide will arrive at the satellite with correspondingly smaller amplitude. Even if energy dissipation is neglected, the observed wave amplitude would appear attenuated because the amplitude as a function of time at the observation point represents arrival of waves along paths corresponding to fast mode waves that are increasingly spread out. *Wright* [1994] calculates this effect and gives an expression for the damping of wave amplitude,

$$b_z \propto b_{z0}/R^{1/2}, \tag{3.8}$$

where R is the propagation distance from the wave source to the satellite accounting for wave reflection, and b_{z0} is the amplitude of the fast mode wave at the source point. Here we assume that the medium is uniform. For different wave packets with different initial wave normal direction $\mathbf{k}$, their arrival times are discrete at a specified observation point. A wave leaving the center of the source region and bouncing off the boundaries j times will traverse a distance in x of jx_m. Only when j is a integer will the wave packet arrive at the observation point. According to Equation (3.8) from *Wright* [1994],

$$t = \sqrt{y_0^2 + j^2 x_m^2}/V_A, \tag{3.9}$$

where y_0 is the distance between the source and observation point along the waveguide, V_A is the local Alfvén speed and x_m is the width of waveguide. This feature is not consistent with our observation. In Figure 3.11, we consider damping of a single frequency source. Here the estimate of damping neglects mode conversion caused by reflection from the inner magnetosphere turning point. As a result of this process, wave energy can be absorbed depending on the angle of incidence of the fast mode wave as it approaches the turning point [*Kivelson and Southwood*, 1986]. According to *Zhu and Kivelson* [1989] and *Inhester* [1987], the turning point of the wave will be:

$$x_t - x_\omega = -\frac{\omega^2 \lambda^2}{[dV_A^2(x)/dx]_{x=x_\omega}}, \tag{3.10}$$

where x_t is the turning point and x_ω is the position of resonance on the field line. The gradient of Alfvén velocity will be largest near the plasmapause. As an estimation, we calculate the variation of V_A from satellite data and choose the average $\Delta V_A/\Delta x$ as the velocity gradient. The turning point should be in the place of $x_t \sim x_\omega + 1.108$ Re,

implying that wave energy absorption should be considerable in such a situation. The conclusion is that there should be two effects that cause the wave to be damped in the waveguide: the wave energy absorption effect and wave energy decreasing effect over greater propagation distance as waves are reflected at waveguide boundaries before reaching the spacecraft. The situation is in general more complicated because of the geometry of the waveguide and the fact that the source of waves is unlikely to be point-like. Nevertheless, based on our simple estimates the conclusion is that propagation effects leading to loss of energy cannot explain the energy loss from waves that is observed.

3.4 Conclusion

In this study, we have examined ULF wave damping mechanisms that include ionospheric Joule heating, Landau damping, and waveguide energy propagation. The mechanisms have been evaluated for two interplanetary shock-related ULF wave events observed by Cluster on November 7, 2004, and August 30, 2001. In the two events studied, we discuss mechanisms for damping of ULF waves. Specifically, using expressions in the published literature, we show that amongst Landau damping, Joule heating and wave propagation, Landau damping can best explain the rates observed. The experimental facts stemming from the interplanetary shock and the resulting fast-damped ULF waves that are observed can be summarized as follows:

1. In the event on November 7, 2004, the four Cluster spacecraft observed intense ULF waves with a period of about $100 - 200$ s near the plasmasphere boundary layer after arrival of the interplanetary shock. The resulting Alfvén waves with strong poloidal components can accelerate particles effectively [*Zong et al.*, 2009] and were damped very fast within several hundred seconds. In the event on August 30, 2001, C1, C2 and C4 observed relatively weak shock-induced ULF waves in the plasmasphere. C3 observed the same event in the plasmasphere boundary layer. By comparing the power of observed waves, it is found that Alfvén waves are damped faster in the plasmasphere boundary layer than within the plasmasphere in this event. The redistribution effect of plasma near the plasmapause is omitted in this study.

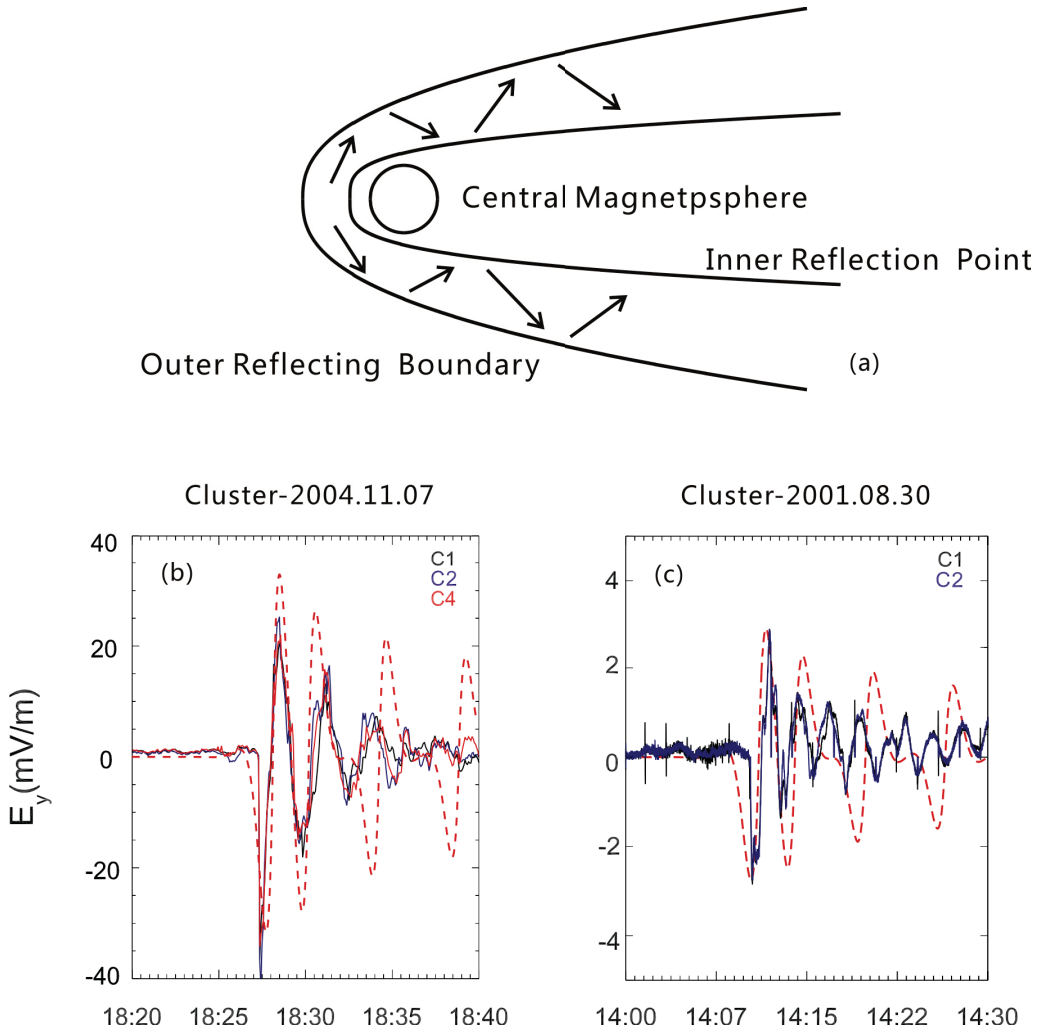

Figure 3.11: (a) Illustration showing the progress of the compressional waves propagation in the waveguide of magnetosphere (modified from *Wright* [1994]). (b) Comparison between the calculated waveguide-caused damping and the observation from Cluster for the event in 2004. (c) Similar comparison between calculation and observation from Cluster for the event in 2001.

2. Joule heating is found to be significant in the two events studied but cannot account for the fast damping of ULF waves that is observed. The damping rate due to Joule heating maintained in general the same rate in the plasmasphere and plasmasphere boundary layer.

3. Drift-bounce resonant (Landau damping) interactions between Alfvén waves and different kinds of particles provide an effective ULF wave energy exchange process. For the events considered, ULF wave damping rates for O^+ in the range of a few to several keV are large enough to explain damping rates of waves observed by Cluster. The energy of O^+ ions satisfying the drift-bounce resonance condition coincides with a resonance peak in ion flux modulations in the November 7, 2004 and August 30, 2001 events observed by Cluster. In the event on August 30, 2001, Landau damping is also higher in the plasmasphere boundary layer than in the plasmasphere. The observed higher damping rates in the plasmasphere boundary layer can be explained by the relatively higher proportion of Landau resonant ions present in that region. It can be concluded that fast Landau damping of shock-induced ULF waves occurs preferentially in the plasmasphere boundary layer region.

3.5 Simulations of Drift-bounce Resonance between Ions and Fast Damping ULF waves

The ULF wave model described in Chapter 4 and the full-Lorentz test particle model described in Chapter 5 are used in this section to discuss the energy changes of different ions in these two event. The damping mechanism of ULF wave is not in the scope of our wave model. However, our models will compare the responses of different ions in ULF waves with damping rate set as a simulation parameter. The simulation results about the ULF event on November 7, 2004 suggest that the energization of O^+ ions is more effective than H^+ ions during the drift resonance process with the same damping ULF wave. In this section, we have also compared the simulation results corresponding to Cluster C2 and Cluster C3 observations in the ULF wave event on August 30, 2001. For ULF waves with a larger damping rate, O^+ ions are energized within a larger energy range. The larger energy exchanging rate between ULF waves

and energetic particles is in agreement with the observation provided in this chapter.

Figure 3.12 shows the simulation results corresponding to the event on November 7 2004. The wave is excited with a large amplitude external driver, reaches amplitude of $\sim$ 50 mV/m and then damped out in two wave period. The middle panel and the bottom panel of Figure 3.12 show the energy changes of O^+ ions and H^+ ions respectively. The expected resonant energies of O^+ and H^+ obtained from the drift-bounce resonance condition are in good agreement with simulation results. The maximum energy change of O^+ ions at the resonance energy bin $\sim$ 10 keV is about 50 keV , which is much larger than that of H^+ ions at their resonance energy. The simulations suggest that more energy from the ULF waves are deposited to O^+ ions in this event.

Figure 3.13 shows the simulation results corresponding to the event on August 30, 2001. We simulated two different waves with different damping rates: In the top two panels, the wave profile corresponds to the C2 observation in the plasmasphere with smaller damping rate. The wave damped out in about 5 wave periods. In the bottom two panels, the wave profile corresponds to the C3 observation in the plasmasphere boundary layer with larger damping rates. The wave damped out in about 2 wave periods. The maximum energy changes in both cases are about 5 keV. In the case of lower damping rate, the energy changes is smaller than 1 keV in energy bins larger than 6 keV after 600 s. In the case of lower damping rate, the range of energy change $>$ 1 keV energy bins extends to $\sim$ 9 keV. The difference in wave-affected energy range suggests that the energy exchanging happens between more test particles in a faster damped ULF wave. A relatively higher proportion of resonating ions present plasmasphere boundary region is consistent with the observational results.

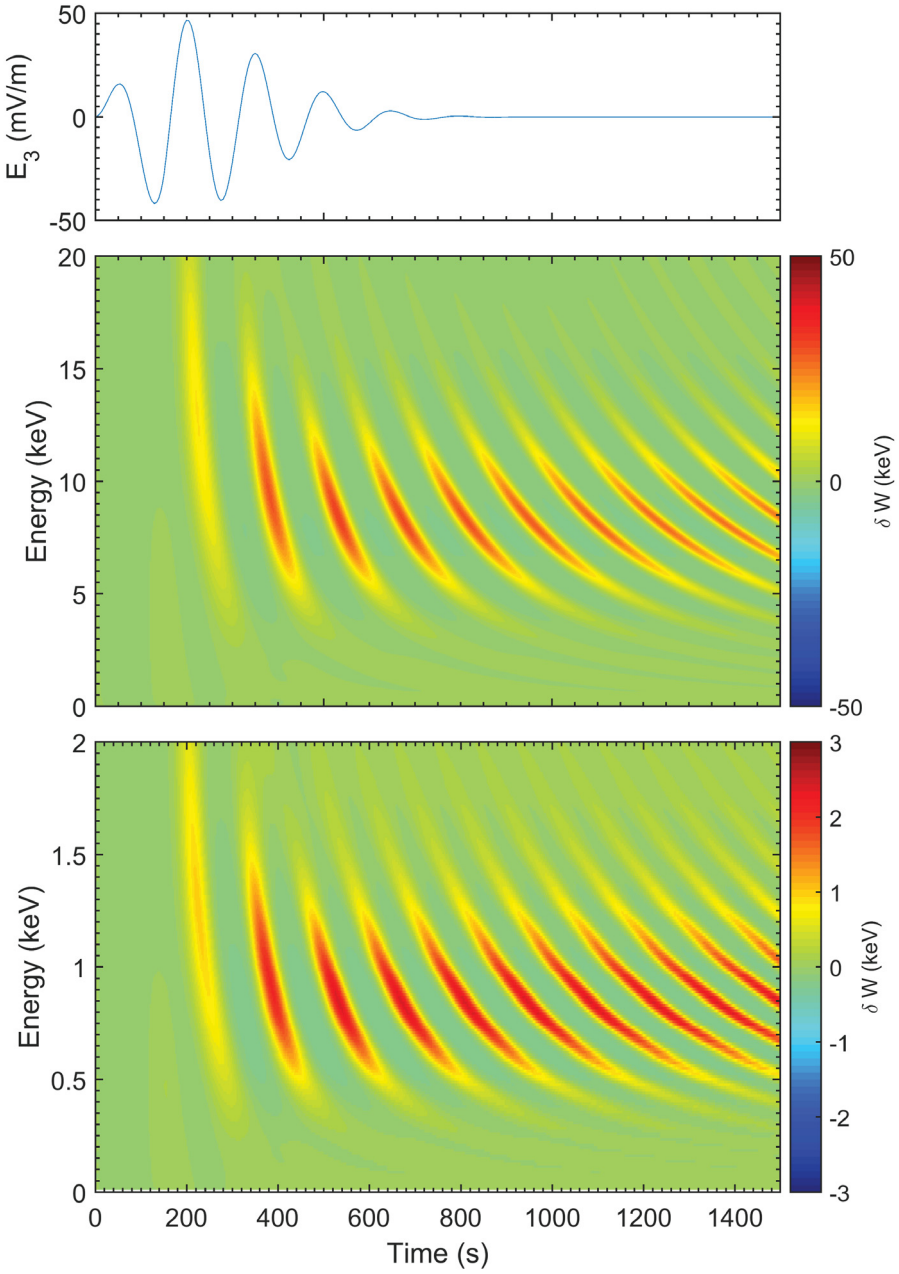

Figure 3.12: The top panel shows the simulated wave amplitude profile corresponds to the event on November 7, 2004. The middle panel shows the energy changes of O^+ ions as a function of measured energy bins and time. The bottom shows the energy changes of H^+ ions as a function of measured energy bins and time.

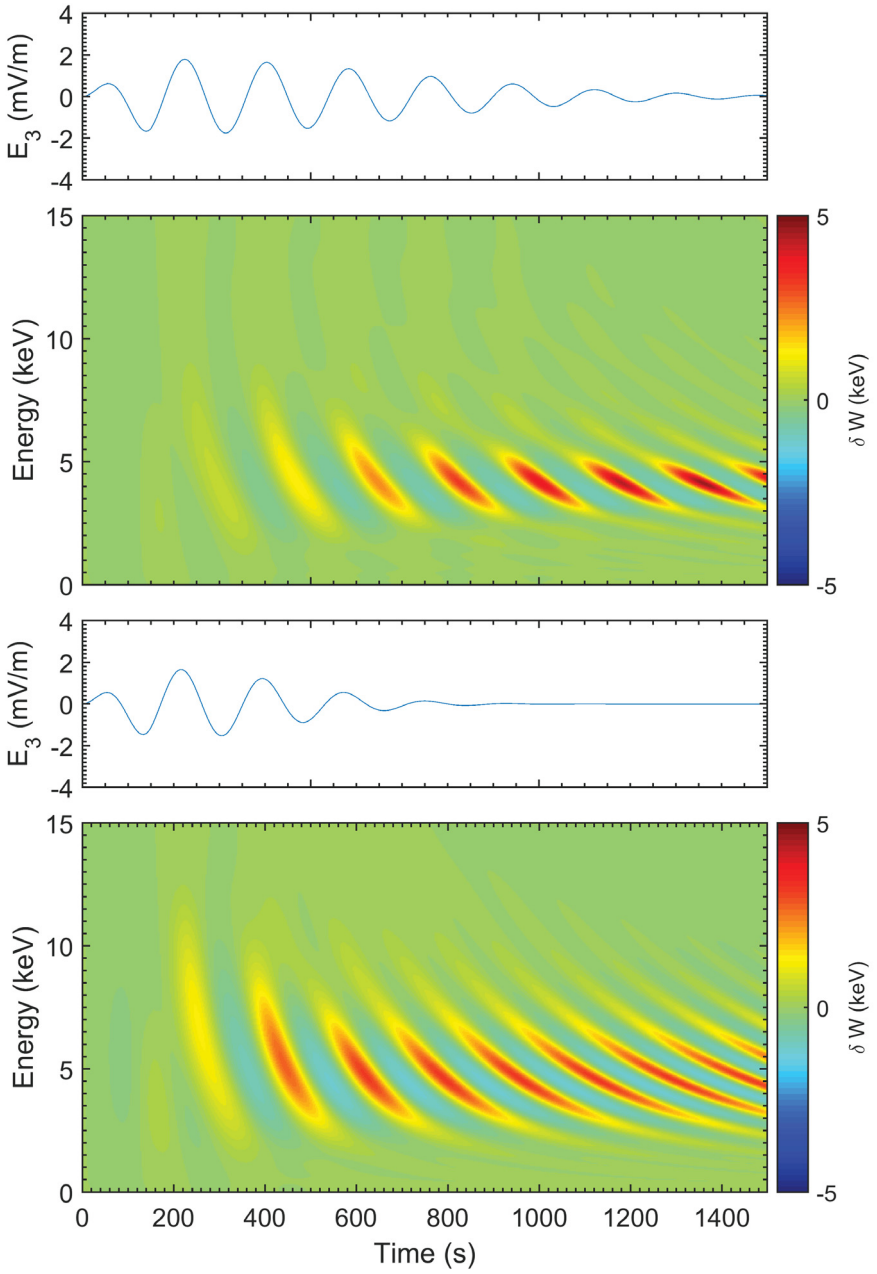

Figure 3.13: The top two panels show the simulated wave amplitude profile and the energy changes of O^+ ions corresponding to the C2 observations of a wave damped out in 5 wave periods in the event on August 30, 2001. The bottom two panels are in similar format as the top two, but correspond to the C3 observations of a wave that damped out in 2 wave periods in the same event.

Chapter 4

MHD Alfvén Wave Model with Monochromatic Driver

In this chapter, we developed an analytic MHD wave model with self-consistent electric and magnetic fields to describe Alfvén waves in the magnetosphere. The solutions of field line resonance eigenfunction describe the distribution of fields along the field line. Based on the free wave solutions, we include a monochromatic driver with harmonic dependence $\exp[i(\omega t - m\phi)]$ to excite poloidal/toroidal mode ULF waves with a radial/azimuthal magnetic field and azimuthal/radial electric field.

In Section 4.1, we provide derivations and the related assumptions about this model. We estimate the contribution of phase mixing terms in our model, and give an example of phase mixing of poloidal mode at the equator in Section 4.2.1. In Section 4.2.2, we show examples of fundamental mode wave, and discuss how the eigenmode is affected by the L-shell and by the plasma density.

4.1 Mathematical Description of ULF Wave Model

As described in Chapter 2, the linear shear Alfvén wave equation was derived using a combination of the Maxwell's equations and the momentum equation by assuming that the wave was in ideal cold plasma with infinite conductivity. In this section, we will start deriving our Alfvén wave model in the dipole magnetosphere.

4.1.1 ULF Waves in the Dipole Magnetosphere

The geomagnetic field inside the inner magnetosphere is approximately dipolar. It is useful to work in dipolar coordinate system even though the vector operations are somewhat more complicated than in a Cartesian or spherical polar representation. The dipolar coordinate system (x_1, x_2, x_3) is defined in terms of the spherical polar coordinates (r, θ, ϕ),

$$x_1 = \frac{\cos\theta}{r^2}, x_2 = \frac{r}{\sin^2\theta}, x_3 = \phi. \tag{4.1}$$

where x_1 parameterizes the displacement parallel to the field: $x_1 = 0$ at the equator, $x_1 \to -\infty$ as $\theta \to \pi$ and $x_1 \to +\infty$ as $\theta \to 0$. The value of x_2 is constant along a dipolar field line and corresponds to L-shells. The x_3 direction is identical to the azimuthal direction in the spherical coordinate. The associated scale factors of the dipolar coordinate are:

$$h_1 = \frac{r^3}{\sqrt{1+3\cos^2\theta}}, \tag{4.2}$$

$$h_2 = \frac{r^2}{\sin\theta\sqrt{1+3\cos^2\theta}}, \tag{4.3}$$

$$h_3 = r\sin\theta \tag{4.4}$$

Radoski and McClay [1967] derived the linearized wave equation (Equation (2.19)) in a dipolar coordinate with the assumption that the perturbations are in the form of $\exp i(m\phi - \omega t)$ where m is the azimuthal wave number. The equations are written as

$$h_3^{-2}\left[\frac{\partial}{\partial x_1}(h_1^{-2}\frac{\partial h_2 E_2}{\partial x_1}) + \frac{\partial}{\partial x_3}(\frac{\partial h_2 E_2}{\partial x_3} - \frac{\partial h_3 E_3}{\partial x_2})\right] + k^2 h_2 E_2 = 0 \tag{4.5}$$

$$h_2^{-2}\left[\frac{\partial}{\partial x_1}(h_3^{-2}\frac{\partial h_3 E_3}{\partial x_1}) + \frac{\partial}{\partial x_2}(\frac{\partial h_2 E_2}{\partial x_3} - \frac{\partial h_3 E_3}{\partial x_2})\right] + k^2 h_3 E_3 = 0 \tag{4.6}$$

where E_2 and E_3 are the r-component and ϕ-component of the electric field $\mathbf{E}$ respectively. E_2, which correspond to the guided toroidal mode, is in the radial direction while E_3, which corresponds to the guided poloidal mode, is in the azimuthal direction [*Dungey*, 1954].

The toroidal mode and poloidal modes are coupled in Equation (4.5) and Equation (4.6). When the wave is axisymmetric (say, $m = 0$), Equation (4.5) and Equation

(4.6) are decoupled and give

$$h_3^{-2}\frac{\partial}{\partial x_1}(h_1^{-2}\frac{\partial h_2 E_2}{\partial x_1}) + k^2 h_2 E_2 = 0, \tag{4.7}$$

$$h_2^{-2}\left[\frac{\partial}{\partial x_1}(h_3^{-2}\frac{\partial h_3 E_3}{\partial x_1}) - \frac{\partial^2 h_3 E_3}{\partial x_2^2}\right] + k^2 h_3 E_3 = 0. \tag{4.8}$$

The poloidal mode and toroidal mode are oscillating independently in this condition. A diagram of the fundamental toroidal and poloidal modes' field line resonance is shown in Figure 4.1. Equation (4.7) describes the guided toroidal mode and Equation (4.8) describes the guided poloidal mode. The poloidal mode is also called the axisymmetric poloidal mode because it represents the axisymmetric compressional oscillation of the dipole magnetic field.

On the other hand, Equation (4.5) and Equation (4.6) are also decoupled in the case of highly azimuthal asymmetry perturbation ($m \to \infty$) [*Radoski and McClay*, 1967]. These two equations give

$$h_2^{-2}\frac{\partial}{\partial x_1}\left[h_3^{-2}\frac{\partial h_3 E_3}{\partial x_1}\right] + k^2 E_3 h_3 = 0 \tag{4.9}$$

when the electric field is dominantly poloidal, $E_3 \gg E_2$.

4.1.2 Interactions between Toroidal and Poloidal Modes via the Ionospheric Effect

As explained in Section 4.1.1, toroidal and poloidal modes are decoupled in axisymmertic dipole magnetic field as described in Equation (4.7) and Equation (4.8). *Allan and Knox* [1979] considered the boundary effect of ionosphere and indicated that the axisymmetric toroidal and poloidal modes interact via the ionospheric Hall effect.

Because the "frozen in" condition (Equation (2.7)) is no longer available in the ionosphere, the current can be written in the following form in the dipole coordinate

$$j_2 = \sigma_P E_2 + \sigma_H E_3 \tag{4.10}$$

$$j_3 = \sigma_P E_3 - \sigma_H E_2 \tag{4.11}$$

by assuming that the displacement currents can be neglected. Combining Equation (4.10) and Equation (4.11) with Equation (2.17) and integrating them along the field

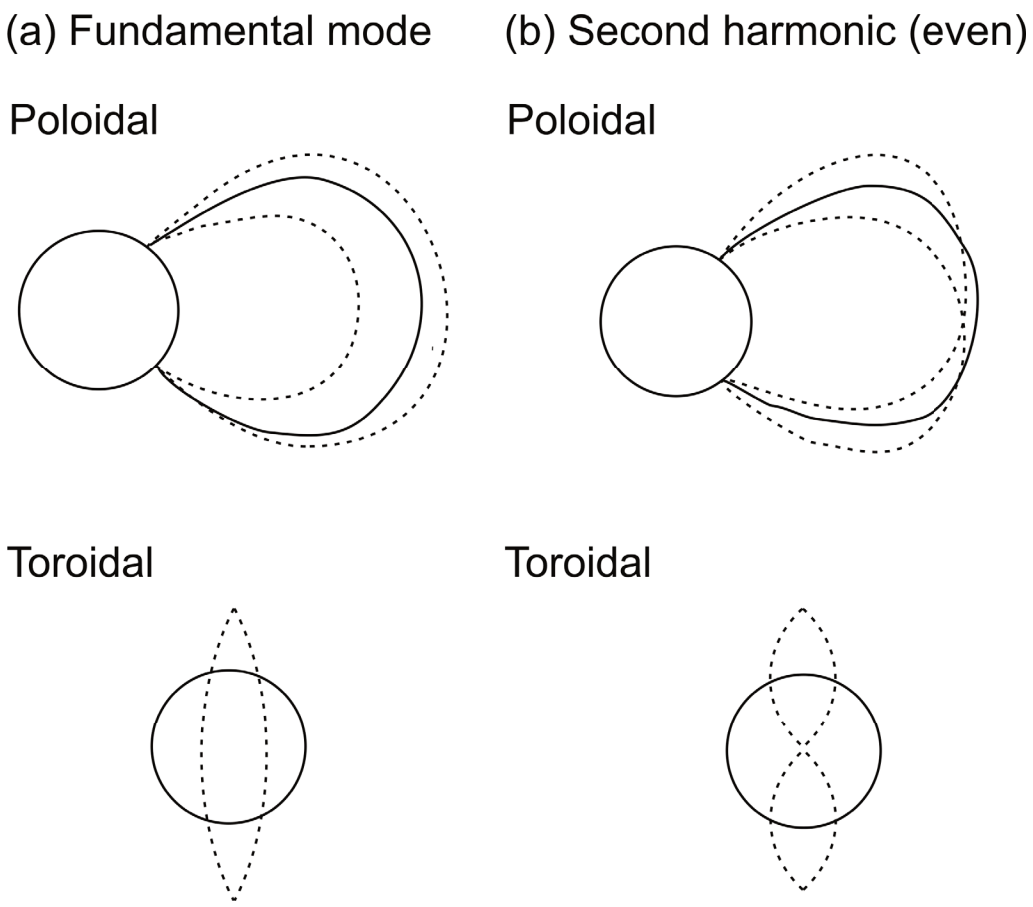

Figure 4.1: Schematic diagram of (a) fundamental (odd mode) and (b) second harmonic (even mode) standing oscillations of geomagnetic field lines. Decoupled toroidal and poloidal modes are shown, with dashed lines depicting the displaced field lines. Taken from [*Menk and Waters*, 2013].

line through the ionosphere, we get equations of the electric field at the top and the bottom of the ionosphere

$$\Sigma_P E_2^0 + \Sigma_H E_3^0 = \pm\frac{1}{\mu_0} B_{13}^0 \tag{4.12}$$

$$\Sigma_P E_3^0 - \Sigma_H E_2^0 = \mp\frac{1}{\mu_0}(B_{13}^0 - B_{12}^1) \tag{4.13}$$

where superscripts 0 and 1 refer to the top and the bottom of the ionosphere, Σ_H and Σ_P are height-integrated Hall and Pedersen conductivity, the RHS of Equation (4.12) takes a positive sign and the RHS of Equation (4.13) takes a negative sign at the southern ionosphere. By substituting Equation (2.16) into Equation (4.12) and Equation (4.13), we can get coupled equations of the electric fields E_2 and E_3

$$\Sigma_P E_2^0 + \Sigma_H E_3^0 = \pm\frac{i}{\mu_0\omega}\left[\frac{1}{h_1 h_2}\frac{\partial}{\partial x_1}(h_2 E_2)\right]^0 \tag{4.14}$$

$$\Sigma_P E_3^0 - \Sigma_H E_2^0 = \pm\frac{1}{\mu_0}\left\{\frac{i}{\omega}\left[\frac{1}{h_2 h_3}\frac{\partial}{\partial x_1}(h_3 E_3)\right]^0 + b_2^1\right\} \tag{4.15}$$

Equation (4.14) and Equation (4.15) show that an initial toroidal mode electric field E_2 generates an poloidal mode electric field E_3, in the ionosphere through the Hall conductance Σ_H. Thus an isolated toroidal mode is only possible if $\Sigma_H = 0$.

4.1.3 Free Wave Equations for Toroidal Mode Alfvén Wave

Although Section 4.1.1 gives examples of decoupled toroidal mode and poloidal mode in specified m values, we will provide a ULF model with decoupled toroidal mode and poloidal mode without assumptions on m value. In this model, the interaction between toroidal mode and poloidal mode discussed in Section 4.1.2 is not under consideration by assuming $\Sigma_H = 0$.

The toroidal mode corresponds to the perpendicular disturbance of the magnetic field in the x_3 direction. The electric field disturbance is in the x_2 direction. Combining the corresponding components of the Faraday equation (Equation (2.1)) and the frozen-in condition (Equation 2.7), we have

$$\frac{\partial h_3 B_3}{\partial t} = \frac{h_3}{h_1 h_2}\frac{\partial}{\partial x_1}(h_2 v_3 B_{10}) \tag{4.16}$$

where $B_{\{1,2,3\}}$, $E_{\{1,2,3\}}$, $v_{\{1,2,3\}}$, are the three components of the magnetic field, electric field and plasma velocity in the dipolar coordinate, respectively. $h_{\{1,2,3\}}$ are the associated scale factors, B_{10} is the background geomagnetic field. The toroidal component of the momentum equation (Equation (2.9)) is

$$\rho_0 \frac{\partial v_3}{\partial t} = \frac{B_{10}}{\mu_0 h_1 h_3} \frac{\partial}{\partial x_1}(h_3 B_3) \tag{4.17}$$

where ρ_0 is the plasma mass density. From Equation (4.16) and Equation (4.17),

$$h_2^2 \frac{\partial^2}{\partial t^2}(h_3 B_3) = \frac{\partial}{\partial x_1}\left[\frac{v_A^2}{h_3^2}\frac{\partial}{\partial x_1}(h_3 B_3)\right]. \tag{4.18}$$

where $v_A = B_{10}/\sqrt{\mu_0 \rho_0}$ is the Alfvén speed.

The eigenfunction of Equation (4.18) can be written as

$$h_3 B_3 = b_N e^{-i\omega t} S_N(x_1), x_1 \in [x_-, x_+] \tag{4.19}$$

where $S_N(x_1)$ is the N-th order eigenfunction of field line resonance, and ω_N is the N-th order eigenfrequency, x_- and x_+ are the corresponding x_1 coordinates of the northern and southern ionosphere. In general, the field line resonance can be expressed as:

$$h_3 B_3 = \sum_N b_N e^{-i\omega_N t} S_N(x_1) \tag{4.20}$$

The eigenfunctions are orthogonal in the absence of ionospheric damping. Set $\partial^2/\partial t^2 \to -\omega_N^2$, we have

$$\frac{d}{dx_1}\left[\frac{v_A^2}{h_3^2}\frac{dS_N}{dx_1}\right] + h_2^2 \omega_N^2 S_N = 0 \tag{4.21}$$

To find out the relationship between different eigenmodes, we perform an integration along the field lines:

$$\int_{x_-}^{x_+} dx_1 S_M [\frac{d}{dx_1}(\frac{v_A^2}{h_3^2}\frac{dS_N}{dx_1}) + h_2^2 \omega_N^2 S_N] = 0 \tag{4.22}$$

where $S_M = S_M(x_1)$ is another eigenmode. Integrating Equation (4.22) by parts, we have:

$$\omega_N^2 \int_{x_-}^{x_+} h_2^2 S_M S_N dx_1 + S_M \frac{v_A^2}{h_3^2}\frac{dS_N}{dx_1}\Big|_{x_-}^{x_+} - \int_{x_-}^{x_+} \frac{v_A^2}{h_3^2}\frac{dS_M}{dx_1}\frac{dS_N}{dx_1} dx_1 = 0 \tag{4.23}$$

Switching M to N gives the orthogonality condition after subtracting, i.e.,

$$(\omega_N^2 - \omega_M^2) \int_{x_-}^{x_+} h_2^2 S_M S_N dx_1 = Const \cdot \delta_{N,M} \tag{4.24}$$

A normalized solution of S_N is:

$$\int_{x_-}^{x_+} h_2^2 S_N^2 dx_1 = 1 \tag{4.25}$$

The eigenfunctions and corresponding eigenfrequencies are solutions of Equation (4.21) and Equation (4.25), which can be solved numerically. However, an analytic solution of S_N will be discussed in Section 4.1.4.

4.1.4 Analytical Solution of Field Line Resonance Eigenfunction

To solve the eigenfunction S_N in dipolar geometry, we start from normalizing the eigenfunction. Rewriting Equation (4.25) by substituting $\widetilde{S_N} = R_E L S_N$ and assuming a fundamental mode field line resonance:

$$2 \int_0^{s_{max}} h_2 \frac{dx_1}{ds} \frac{\widetilde{S_N}}{R_E^2 L^2} ds = 1 \tag{4.26}$$

where $s = \cos\theta$, θ is the co-latitude, and $s_{max} = \sqrt{1 - 1/L}$ is the maximum of $\cos\theta$ at one of the two footprint points of the field line.

In Equation (4.26), term dx_1/ds is:

$$\frac{dx_1}{ds} = \frac{d}{ds}\left(\frac{\cos\theta}{r^2}\right) = \frac{1}{L^2 R_E^2} \frac{1 + 3s^2}{(1 - s^2)^2} \tag{4.27}$$

Substitute Equation (4.27) and Equation (4.3) into Equation (4.26), we have:

$$2 \int_0^{s_{max}} ds \widetilde{S_N}^2 = 1 \tag{4.28}$$

It shows that $\widetilde{S_N}$ is the normalized eigenfunction.

The normalized eigenfunction can be analytically solved in Equation (4.21) by assuming a special density profile. Rewrite Equation (4.21) as

$$-h_2^2 \omega_N^2 \frac{\widetilde{S_N}}{R_E L} = \frac{ds}{dx_1} \frac{d}{ds} \left[\frac{v_A^2}{h_3^2} \frac{1}{R_E L} \frac{d\widetilde{S_N}}{ds} \frac{ds}{dx_1} \right] \tag{4.29}$$

Note that the Alfvén velocity is a function of the magnetic field and density; it varies as a function of s:

$$v_A = \frac{B}{\sqrt{\mu_0 \rho}} = \frac{B_{eq}}{\sqrt{\mu_0 \rho_{eq}}} \sqrt{\frac{\rho}{\rho_{eq}}} \frac{\sqrt{1+3s^2}}{(1-s^2)^3} = v_{A0} \sqrt{\frac{\rho}{\rho_{eq}}} \frac{\sqrt{1+3s^2}}{(1-s^2)^3} \tag{4.30}$$

where B_{eq} and ρ_{eq} are the magnetic field and number density at the equator respectively, v_{A0} is the normalized Alfvén velocity. Substitute Equation (4.30) into Equation (4.29), we have:

$$\widetilde{S_N} = -\frac{v_{A0}}{\omega_N^2 L^2 R_E^2} \frac{d}{ds} \left[\frac{1}{\rho(s)} \frac{1}{(1-s^2)^6} \frac{d\widetilde{S_N}}{ds} \right] \tag{4.31}$$

Equation (4.31) can be largely simplified when $\rho(s) = (1-s^2)^{-6}$:

$$\widetilde{S_N} = -\left(\frac{\omega_N L R_E}{v_{A0}} \right)^2 \frac{d^2 \widetilde{S_N}}{ds^2} \tag{4.32}$$

It shows that an analytical solution of the eigenfunction is simply

$$\widetilde{S_N} = A \cos(f_0 s + \phi_0) \tag{4.33}$$

where A and ϕ_0 are constants, and $f_0 = \omega_N L R_E / v_{A0}$. The corresponding eigenfrequencies ω_N for different order of standing wave modes can be estimated by fitting to the boundary condition at the end of the field line ($s = s_{max}$) and at the equator ($s = 0$) for different oscillation modes. For example, the boundary condition for fundamental mode is $\widetilde{S_N}(s = s_{max}) = 0$ and $\widetilde{S_N}(s = 0) = 1$.

4.1.5 Toroidal Mode Alfvén Wave Model with an External Driver

Self-consistent electric and magnetic fields of standing mode ULF waves can be calculated using the approach described in *Rankin et al.* [1999, 2005]. On the other hand, a monochromatic driver with harmonic dependencies will be added to the wave equations in Section 4.1.3 to excite poloidal and toroidal mode ULF waves in the dipole magnetosphere. The amplitude of the driver can be made time-dependent, but only when the constant leads to linear growth of the wave amplitude with time. As geomagnetic field lines evolve independently in ideal MHD, the eigenfunction of wave is explicitly a function of L. This enables growth, damping, and phase mixing to be

accounted for in the model under the assumption of infinite ionospheric conductivity. The absence of finite height-integrated Pedersen conductivity, and hence ionospheric damping, means the wave amplitude is a free parameter. The mode structure along field lines will change under finite conductivity, but as the differences are expected to be minor for conductivities on the order of a few to several mho, effects of finite conductivity are neglected to simplify the analysis.

The above analysis in Section 4.1.3 and Section 4.1.4 deal with free Alfvén waves, the eignenmodes are linearly independent. To excite the field line oscillation, a driver is added to the system to find the solution of field line resonance. The momentum Equation (4.17) is rewritten as

$$\rho\frac{\partial v_3}{\partial t} = \frac{B_{10}}{\mu_0 h_1 h_3}\frac{\partial}{\partial x_1}(h_3 B_3) + D \tag{4.34}$$

where $D = \rho\omega_0 v_D \sin\omega_0 t$, ω_0 is the frequency of the driver, and v_D is the plasma velocity of the driver. This equation can be written as

$$\frac{\partial}{\partial t}(h_2 B_{10} v_3) = \frac{v_A^2}{h_3^2}\frac{\partial}{\partial x_1}(h_3 B_3) + h_2 B_{10}\omega_0 v_D \Re(ie^{-i\omega_0 t}) \tag{4.35}$$

where $\Re(ie^{-i\omega_0 t})$ is the real part of $ie^{-i\omega_0 t}$. Substitute Equation (4.35) into the toroidal Faraday Equation (4.16), we have a modified field line resonance equation with an external driver

$$\begin{aligned}\frac{\partial^2}{\partial t^2}(h_3 B_3) = &\frac{1}{h_2^2}\frac{\partial}{\partial x_1}\left[\frac{v_A^2}{h_3^2}\frac{\partial}{\partial x_1}(h_3 B_3)\right] \\ &+ \frac{1}{h_2^2}\frac{\partial}{\partial x_1}\left[h_2 B_{10}\omega_0 v_D \Re(ie^{-i\omega_0 t})\right].\end{aligned} \tag{4.36}$$

According to Equation (4.21), $h_3 B_3 = \Re(b_N e^{-i\omega_N t})S_N$. For a monochromatic driver with the frequency ω_0, we rewrite Equation (4.21) as

$$h_3 B_3 = b_{N0}\Re(e^{-i\Delta\omega t})\Re(e^{-i\omega_0 t})S_N = b_N \Re(e^{-i\omega_0 t})S_N \tag{4.37}$$

where $\omega_N = \omega_0 + \Delta\omega$, $b_N = b_{N0}\Re(e^{-i\Delta\omega t})$, and b_{N0} is a constant. Assuming that $\Delta\omega^2 \ll \omega_0^2$,

$$-\omega_0^2 b_N S_N - 2i\omega_0\frac{\partial b_N}{\partial t}S_N = \frac{b_N}{h_2^2}\frac{\partial}{\partial x_1}\left(\frac{v_A^2}{h_3^2}\frac{\partial S_N}{\partial x_1}\right) + i\frac{\omega_0}{h_2^2}\frac{\partial}{\partial x_1}(h_2 B_{10} v_D) \tag{4.38}$$

Equation (4.22) for eigenfunction $S_N(x_1)$ can be substituted into the first term in the RHS of Equation (4.38), then

$$-\omega_0^2 b_N S_N - 2i\omega_0 \frac{\partial b_N}{\partial t} S_N = -\omega_N^2 S_N + i\frac{\omega_0}{h_2^2}\frac{\partial}{\partial x_1}\left(h_2 B_{10} v_D\right) \tag{4.39}$$

Multiplying by $h_2^2 S_N$ and integrating, we have:

$$-\omega_0^2 b_N + \omega_N^2 b_N - 2i\omega_0 \frac{\partial b_N}{\partial t} = i\omega_0 \int_{x_-}^{x_+} dx_1 S_N \frac{\partial}{\partial x_1}\left(h_2 B_{10} v_D\right) \tag{4.40}$$

Integrate by parts assuming $v_D(x_-) = v_D(x_+) = 0$,

$$\frac{\partial b_N}{\partial t} = i\frac{\omega_0^2 - \omega_N^2}{2\omega_0} b_N - \frac{\omega_0}{2\omega_0}\int_{x_-}^{x_+} dx_1 S_N \frac{\partial}{\partial x_1}\left(h_2 B_{10} v_D\right) \tag{4.41}$$

$$\frac{\partial b_N}{\partial t} \sim -i\Delta\omega b_N + \frac{\omega_0}{2} R_D \tag{4.42}$$

where $R_D = \frac{1}{2\omega_0}\int_{x_-}^{x_+} dx_1 h_2 B_{10} v_D \frac{\partial S_N}{\partial x_1}$ is the amplitude of the driver in the unit of nT which is considered as a parameter of our model. By solving equation b_N in Equation (4.42) and taking $b_N(t=0) = 0$, we have

$$-i\Delta\omega b_N + \frac{\omega_0}{2} R_D = \frac{\omega_0}{2} R_D e^{-i\Delta\omega t} \tag{4.43}$$

$$b_N(t) = -\frac{\omega_0 R_D}{2i\Delta\omega}(e^{-i\Delta\omega t} - 1) \tag{4.44}$$

Then $h_3 B_3 = \Re(b_N e^{-i\omega_0 t}) S_N$ can be easily evaluated as

$$h_3 B_3 = \frac{\omega_0 R_D S_N(x_1)}{\Delta\omega} cos(\omega t - m\phi) \sin\left(\frac{\Delta\omega t}{2}\right) \tag{4.45}$$

where the term $m\phi$ corresponds to the wave propagation in the azimuthal direction, and $\omega = (\omega_N + \omega_0)/2$. Note that for $\Delta\omega t/2 \ll 1$, $h_3 B_3 \propto \omega_0 t$. This means that the wave grow linearly when the driver frequency is close to the eigenfrequency. In a constant amplitude wave a desired width (in L) can be obtained by setting $\Delta\omega t/2$ to some corresponding value.

Equation (4.45) gives the azimuthal magnetic field of the driven Alfvén wave. Substituting this solution into Equation (4.16), we can have the radial electric field

E_2:

$$\begin{aligned} h_2E_2 = & -h_2B_{10}v_3 \\ = & -\frac{v_A^2}{h_3^2}\frac{R_D}{\Delta\omega}\frac{\partial S_N}{\partial x_1}\left[\frac{\cos(m\phi-\omega_N t+\Delta\omega t/2)}{2\omega_0-\Delta\omega}-\frac{\cos(m\phi-\omega_N t-\Delta\omega t/2)}{2\omega_0+\Delta\omega}\right] \end{aligned} \tag{4.46}$$

Having considered that $\Delta\omega^2 \ll \omega_0^2$, we have:

$$\begin{aligned} h_2E_2 = & -h_2B_{10}v_3 \\ = & -\frac{v_A^2}{h_3^2}\frac{\omega_0 R_D}{\Delta\omega}\frac{\partial S_N}{\partial x_1}\sin(\omega t-m\phi)\sin\left(\frac{\Delta\omega}{2}t\right) \end{aligned} \tag{4.47}$$

Equation (4.47) is the electric field of the toroidal model Alfvén wave. For the magnetic field of wave disturbance, only terms related to E_2 in Faraday's law need to be kept, so we have:

$$\frac{\partial B_{11}}{\partial t} = -(\nabla\times\mathbf{E_1})_1 = \frac{1}{h_2h_3}\frac{\partial}{\partial x_3}(h_2E_2) \tag{4.48}$$

Combining Equation (4.48) with Equation (4.47), we have:

$$\frac{\partial B_{11}}{\partial t} = \frac{m}{h_2h_3}\frac{v_A^2}{h_3^2}\frac{R_D}{\Delta\omega}\frac{\partial S_N}{\partial x_1}\cos(\omega t-m\phi)\sin(\Delta\omega t/2) \tag{4.49}$$

After integrating Equation (4.49) with time, we have:

$$B_{11} = \frac{m}{\omega_0h_2h_3}\frac{v_A^2}{h_3^2}\frac{R_D}{\Delta\omega}\frac{\partial S_N}{\partial x_1}\sin(\omega t-m\phi)\sin(\Delta\omega t/2) \tag{4.50}$$

Substitute Equation (4.50) into Equation (4.47), we have

$$B_{11} = \frac{m}{h_3\omega_0}E_2 \tag{4.51}$$

Therefore, there will be a corresponding compressional wave magnetic component $B_{11} \propto m$, which cannot be ignored when the analytic solution are used in the test particle simulation.

For the azimuthal magnetic field B_3, we have:

$$\frac{\partial B_3}{\partial t} = -(\nabla\times\mathbf{E_1})_3 = \frac{1}{h_1h_2}\frac{\partial}{\partial x_1}(h_2E_2) \tag{4.52}$$

Substituting E_2 in Equation (4.47) into Equation (4.52), we have:

$$\frac{\partial B_3}{\partial t} = -\frac{1}{h_3}\frac{R_D\omega_N^2 S_N}{\Delta\omega}\sin(\omega t - m\phi)\sin(\Delta\omega t/2) \tag{4.53}$$

Integrating this equation with time, we have:

$$B_3 = \frac{1}{h_3}\frac{R_D\omega_0 S_N}{\Delta\omega}\cos(\omega t - m\phi)\sin(\Delta\omega t/2) \tag{4.54}$$

The combination of the electric field component E_2 and magnetic field components B_{11} and B_3 describes the wave field of a toroidal Alfvén wave.

4.1.6 Poloidal Mode Alfvén Wave Model with an External Driver

The perpendicular magnetic and electric field of the toroidal mode are orthogonal to that of the poloidal mode. We just need to modify the above equations by reversing the dipolar coordinate subscripts $h_2 \to h_3$ and $h_3 \to h_2$. Equation (4.16) have become:

$$\frac{\partial}{\partial t}\left(h_3 B_{10} v_2\right) = \frac{v_A^2}{h_2^2}\frac{\partial}{\partial x_1}\left(h_2 B_2\right) \tag{4.55}$$

Rewrite Equation (4.18) with the poloidal components,

$$\frac{\partial^2}{\partial t^2}\left(h_2 B_2\right) = \frac{1}{h_3^2}\frac{\partial}{\partial x_1}\left[\frac{v_A^2}{h_2^2}\frac{\partial}{\partial x_1}(h_2 B_2)\right] \tag{4.56}$$

The radial magnetic field and corresponding azimuthal electric field are:

$$h_2 B_2 = \frac{\omega_0 R_D S_N(x_1)}{\Delta\omega} cos(\omega t - m\phi)\sin\left(\frac{\Delta\omega t}{2}\right), \tag{4.57}$$

$$h_3 E_3 = h_3 B_{10} v_2 = \frac{v_A^2}{h_2^2}\frac{R_D}{\Delta\omega}\frac{\partial S_N}{\partial x_1}\sin(\omega t - m\phi)\sin(\Delta\omega t/2). \tag{4.58}$$

Also, the parallel magnetic field B_{11}can be obtained from the poloidal electric field E_3:

$$\begin{aligned}
\frac{\partial B_{11}}{\partial t} &= -\left(\nabla \times \mathbf{E_1}\right)_1 \\
&= -\frac{1}{h_2 h_3}\frac{\partial}{\partial x_2}(h_3 E_3) \\
&= -\frac{1}{h_2 h_3}\frac{\partial}{\partial x_2}\left(\frac{v_A^2}{h_2^2}\frac{R_D}{\Delta\omega}\frac{\partial S_N}{\partial x_1}\right)\sin(\omega t - m\phi)\sin(\Delta\omega t/2).
\end{aligned} \tag{4.59}$$

By using $x_2 = r^{-1}$, $h_2 = r^2$ at the equator, B_{11} can be simplified as

$$B_{11} \sim \frac{1}{\omega_0 h_2 h_3} \frac{\partial}{\partial x_2} \left(\frac{v_A^2}{h_2^2} \frac{R_D}{\Delta\omega} \frac{\partial S_N}{\partial x_1} \right) \sin(\omega t - m\phi) \sin(\Delta\omega t/2). \tag{4.60}$$

4.2 Discussion

4.2.1 Phase Mixing

The concept of phase mixing in plasma physics was introduced in coronal heating where magnetic gradients are large [*Heyvaerts and Priest*, 1983]. Phase mixing is a mechanism of Alfvén wave dissipation caused by the inhomogeneity of a background magnetic field or plasma density perpendicular to the background magnetic field direction. According to the MHD Alfvén wave theory, shear Alfvén waves propagate parallel to the magnetic field line. Shear Alfvén waves on different magnetic field lines oscillate independently with the phase speed of local Alfvén speed. When there is inhomogeneity of Alfvén speed in a direction perpendicular to the local magnetic field, the phase difference of wave perturbation on different field lines increases with time. As a result, friction between field lines with large gradient of phase dissipate wave energy to the plasma.

The theory of Alfvén wave phase mixing explains the localization of ULF waves in the magnetosphere [*Mann et al.*, 1995]. On the closed magnetic field lines in the magnetosphere, the phase mixing effect is limited by the energy dissipation caused by ionospheric Joule heating or kinetic effects such as Landau damping. In our model, we assume the ionosphere as a boundary of infinite conductivity, and the kinetic effect of the plasma is not introduced as a sink of wave energy. The minimum perpendicular scale of waves is a free parameter in our model. Here we will discuss how the phase mixing effect is limited in our model.

In Section 4.1.5 and Section 4.1.6, the electric field of toroidal mode E_2 and poloidal mode E_3 both include terms related to phase mixing. For example, the sine cardinal function term $\sin(\Delta\omega t/2)/\Delta\omega$ in Equation (4.58) suggests that the wave amplitude increases with time if the driver frequency ω_0 is close to local eigenfrequency $\omega_N(L)$. This term also defines the width of the localized ULF wave since

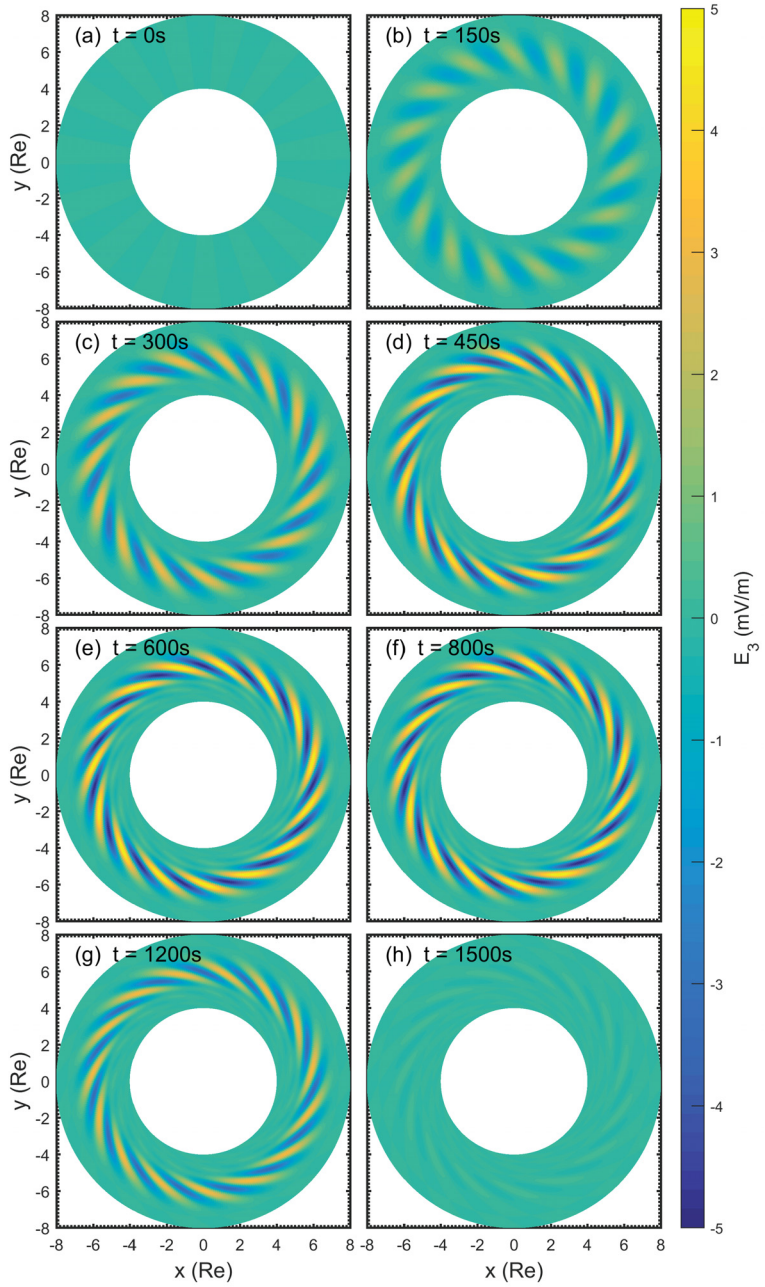

Figure 4.2: Snapshots of the poloidal mode electric field on the equator at different times. Panels (a)-(d) are snapshots at times (a) $t = 0$ s, (b) $t = 150$ s, (c) $t = 300$ s and, (d) $t = 450$ s. The wave amplitude and phase mixing increase in these four panels. Panels (e) and (f) are snapshots at times (e) $t = 600$ s and (f) $t = 800$ s. The wave amplitude and phase mixing stop growing and keep constant in these two panels. Panels (g) and (h) are snapshots at times (g) $t = 1200$ s and (h) $t = 1500$ s. The wave amplitude starts decaying after $t = 1200$ s.

$\sin(\Delta\omega t/2)/\Delta\omega = 0$ when $\Delta\omega t = \pi$. The wave becomes localized in the radius direction with increasing time. Another term, $\sin(\omega t - m\phi)$, where $\omega = (\omega_0 + \omega_N)/2$, suggests that the gradient of E_3 in the radius direction will increase with time. Figure 4.2 shows the equatorial electric field of a fundamental poloidal mode ULF wave simulated with our model. In this simulation, the eigenfrequency is set as $\omega_N = \omega_0$ at $L = 6.0$, the wave frequency is $f = 100$ mHz, the maximum wave amplitude is about 5 mV/m, and the azimuthal wave number is $m = 15$ and propagating westward. Panel (a)-(d) shows the effect of the two terms related to $\Delta\omega$: the wave field on different L-shells becomes more distorted while the wave amplitude increases with time. To avoid strong phase mixing, and to include the effect of ionospheric dissipation, we let the wave damp out with a rate of γ after a "damping time" $t_{damping}$. Also, the phase mixing can be limited without damping out the wave by specifying the terms related to phase mixing. The term $\sin(\omega t - m\phi)$ is set as $\sin(\omega_0(t - t_{limit}) - m\phi + \phi_0)$ after a "phase-limitation time" t_{limit}. Here $\phi_0 = \phi_0(L)$ is the wave phase at time $t = t_{limit}$ on different L-shells. The wave amplitude will also stop growing if we set the wave growing term $\sin(\Delta\omega t/2)/\Delta\omega = \sin(\Delta\omega t_{limit}/2)/\Delta\omega$ as a constant after the phase-limitation time t_{limit}. In this example, we set $t_{limit} = 500$ s and $t_{damping} = 1000$ s and $\gamma = 3.0\omega_0$. Panels (e) and(f) of Figure 4.2 show the snapshots of the equatorial field at $t = 600$ s and $t = 800$ s when the wave stops growing up, but does not start damping. These two panels show that the distortion across the L-shells stops growing up, and the wave propagates in azimuthal direction with the same speed for different L-shells. Panels (g) and (h) of Figure 4.2 show the snapshots of the equatorial field at $t = 1200$ s and $t = 1500$ s after the wave damped out. The amplitude of the wave decreases exponentially after $t = 1000$ s.

4.2.2 Eigenmodes of Fundamental Mode Field Line Resonance

The eigenfunction in Equation (4.33) provides the distribution of the electric field and magnetic field along the field lines for different standing wave modes. The electric field component of the toroidal mode wave in Equation (4.47) and that of the poloidal mode wave in Equation (4.58) both include the same term, $\partial S_N/\partial x_1$, which provides

similar wave amplitude profiles along the field line for the toroidal mode and the poloidal mode. The studies in this thesis are concentrated on the poloidal mode wave, so in this section we show the fundamental mode of the poloidal Alfvén wave as an example of Alfvén wave eigenmodes.

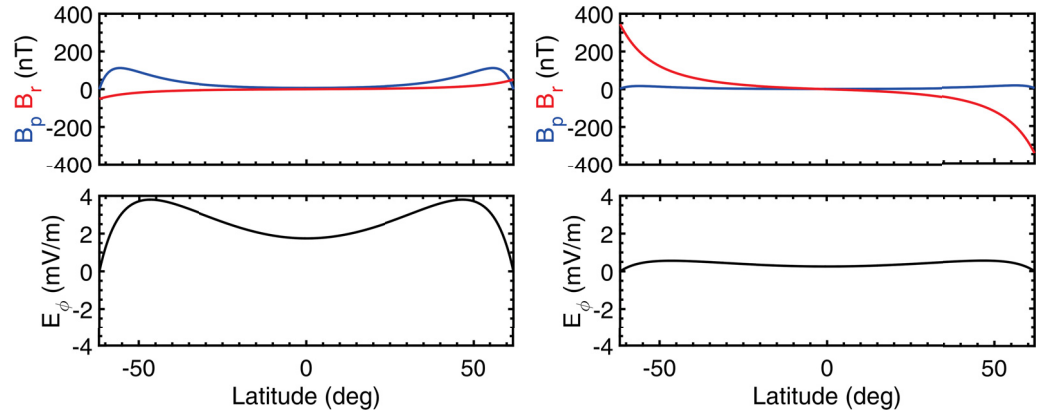

Figure 4.3: Eigenmode for a 20.94 mHz poloidal mode excited at $L = 4.5$. The compressional magnetic field (top left panel) and azimuthal electric field (bottom left panel) are in phase. The radial magnetic field (top right panel) and azimuthal electric field (bottom right panel) are in anti-phase. The background density is specified to have an r^{-6} dependence along geomagnetic field lines.

Figure 4.3 shows an example of a poloidal Alfvén produced by our ULF wave model. A fundamental mode poloidal wave was excited at $L = 4.5$. The left and right columns of this figure show the in-phase and 90-degree out-of-phase wave electric and magnetic field components along the $L = 4.5$ field line, respectively. The amplitude of the azimuthal electric field is about 2 mV/m at the equator and about 4 mV/m off the equator. The distribution of the compressional component of the wave magnetic field along the field line is similar than that of the azimuthal electric components. The maximum amplitude of the compressional magnetic field is less than 10 nT within a latitude range of $-20°$ and $+20°$ around the equator.

The profile of the poloidal mode along field line depends on the mass loading, the L-shell of the field line and possible distortion from a dipole field. The results presented here are valid at relatively low L-shells in the inner magnetosphere where a dipole field model is justified. Here we compare the wave profile for different L-shells and different background plasma densities. Figure 4.4 shows the profile of the maximum poloidal electric field E_3 at two different L-shells and with two different

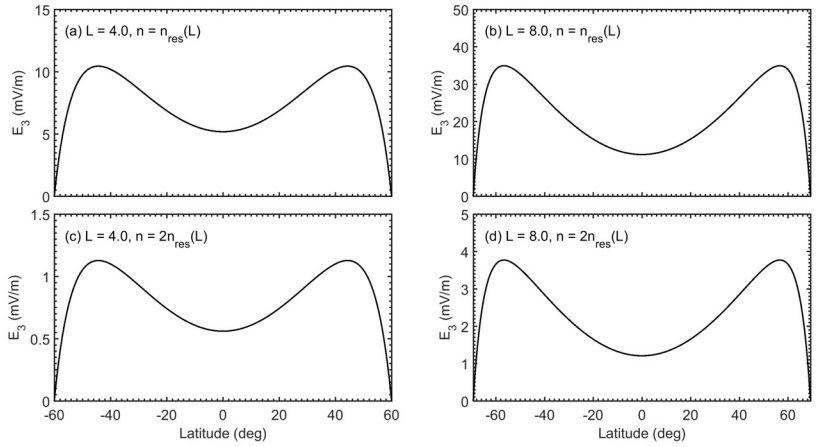

Figure 4.4: The electric field of the poloidal fundamental mode Alfvén wave's along the field line in different L-shells and background plasma number density. Panel (a) shows the wave profile at $L = 4$. The equatorial density $\rho_{eq} = \rho_{res}(L)$ corresponds to the local eigenfrequency at $L = 4$. Panel (b) shows the wave profile at $L = 8$, and the equatorial density $\rho_{eq} = \rho_{res}(L)$ corresponds to the local eigenfrequency at $L = 8$. Panel (c) and Panel (d) show the wave profile at $L = 4$ and $L = 8$ respectively, but their equatorial densities are set to double of $\rho_{res}(L)$ in Panel (a) and (b) respectively.

equatorial mass densities. The other wave parameters, such as the wave driver's frequency amplitude and the m value in these four cases, are identical to the wave parameter in Figure 4.2. As the local Alfvén speed depends on the background density of the plasma, the equatorial density $\rho_{res}(L)$ corresponding to the local eigenfrequency are calculated on the two L-shells $L = 4.0$ and $L = 8.0$ respectively. In each L-shell, the profile of the electric field is calculated with two different equatorial densities: $\rho = \rho_{res}(L)$ and $\rho = 2\rho_{res}(L)$. The maximum wave amplitude at $L = 8.0$ is much larger than that of $L = 4.0$. Comparing the wave profiles for the two different densities, the wave amplitude decreases greatly when the frequency of the driver is different from the local eigenfrequency, and the wave profile along the magnetic field line is generally the same in different L-shells.

Chapter 5

Methodologies and Implementation of Test Particle Simulations

In this chapter, we introduce the mathematical models, methodologies, and numerical codes we developed and implemented to investigate wave-particle interactions in the magnetosphere. The new results that are presented in this chapter illustrate how the improved theory can be used in combination with numerical techniques to better characterize resonant wave-particle interactions.

In Secton 5.1, we use the full Lorentz model and the guiding center model to describe the 3D dynamics of ions and electrons respectively. Large gyro-radius ions are described by the full Lorentz model, while the high gyro-frequency electrons are described by the guiding center model.

In Section 5.2, we introduce the forward Liouville method and backward Liouville method as two important test particle simulation methods used in this thesis. The fundamental assumptions and the mechanisms of these methods are discussed in this section. The implementation details of using these techniques, including how to initialize the velocities and the locations of the test particles, are discussed in Section 5.3.

In Section 5.4, we describe the implementation details of the numerical code. This section also includes the numerical methods used in test particle trajectory integration, the workflow of the code, and the parameters used to generate simulation jobs.

Examples of our simulation results are presented in Section 5.5. In Section 5.5.1, we show an example of successfully reproducing the drift resonance between H^+ ions and ULF waves on April 11, 2014 by comparing with results of *Zhou et al.* [2016]. Simulation results about $N = 0$ drift resonance with relativistic electrons are presented in Section 5.5.2.

5.1 Test Particle Models

5.1.1 Full Lorentz Force Simulation for Large Gyro-radius Ions

For charged particles in the magnetosphere, gravity force from the Earth is weak compared to the electromagnetic force and can be omitted. Motion for a charged particle can be fully described by the equation of Lorentz force

$$\frac{d\mathbf{p}}{dt} = q(\mathbf{E} + \mathbf{v} \times \mathbf{B}) \tag{5.1}$$

where $\mathbf{p}$ is the momentum of the particle, q is the charge of the particle, $\mathbf{E}$ is electric field, $\mathbf{v}$ is particle velocity, and $\mathbf{B}$ is the magnetic field. This equation is relativistically correct if particle momentum is

$$\mathbf{p} = \gamma m \mathbf{v} \tag{5.2}$$

where $\gamma = \sqrt{1/(1 - v^2/c^2)}$ is the Lorentz factor. For ions in the range of several hundred keV to a few MeV, the relativistic effect is weak, and we assume that $\gamma \sim 1$.

In our test particle model, Equation (5.1) is integrated with time in the Cartesian coordinate

$$\frac{dv_x}{dt} = \frac{q}{m}(E_x + v_y b_z - v_z b_y), \tag{5.3}$$

$$\frac{dv_y}{dt} = \frac{q}{m}(E_y + v_z b_x - v_x b_z), \tag{5.4}$$

$$\frac{dv_z}{dt} = \frac{q}{m}(E_z + v_x b_y - v_y b_x). \tag{5.5}$$

The 4th order Runge-Kutta method is implemented in the numerical integration. Because the magnetic field and electric field in our model are defined with the dipolar

coordinate, $B_{\{1,2,3\}}$ and $E_{\{1,2,3\}}$ are converted into Cartesian coordinate

$$\begin{bmatrix} F_x \\ F_y \\ F_z \end{bmatrix} = \begin{bmatrix} -\frac{2\cos\theta}{\delta}\frac{x}{r} - \frac{\sin\theta\cos\theta\cos\phi}{\delta} & -\frac{\sin\theta}{\delta}\frac{x}{r} + \frac{2\cos^2\theta\cos\phi}{\delta} & -\sin\phi \\ -\frac{2\cos\theta}{\delta}\frac{y}{r} - \frac{\sin\theta\cos\theta\sin\phi}{\delta} & -\frac{\sin\theta}{\delta}\frac{y}{r} + \frac{2\cos^2\theta\sin\phi}{\delta} & \cos\phi \\ -\frac{2\cos\theta}{\delta}\frac{z}{r} + \frac{\sin^2\theta}{\delta} & -\frac{\sin\theta}{\delta}\frac{z}{r} - \frac{2\cos\theta\sin\theta}{\delta} & 0 \end{bmatrix} \begin{bmatrix} F_1 \\ F_2 \\ F_3 \end{bmatrix} \tag{5.6}$$

where $F_{\{x,y,z\}}$ are components of a vector in the Cartesian coordinate and $F_{\{1,2,3\}}$ is the same vector, but described as being in a dipolar coordinate, and $\delta = \sqrt{(}1 + 3\cos^2\theta)$.

The full Lorentz force method will describe the full trajectory of any charged test particle without any theoretical approximation. However, a precise description of the trajectory the use of a time step of integration that is much smaller than the period of gyro motion

$$T_{gyro} = \frac{2\pi m}{q|B|}. \tag{5.7}$$

T_{gyro} is on the order of $0.01 - 1$ s for ions in the inner magnetosphere and on the order of $10^{-5} - 10^{-3}$ for electrons. The largely increasing requirements on computing resource make simulations on a large number of electrons unrealistic. To improve the effectiveness of electron simulation, we use a guiding center approach to study the motion of electrons in the magnetosphere.

5.1.2 Guiding Center Simulation for High Gyro-frequency Electrons

The guiding center approach treats test particle motion as two parts: fast gyro motion around a point called the guiding center, $\dot{\boldsymbol{\rho}}$, and the relatively slow motion of the guiding center, $\dot{\mathbf{R}}$. Figure 5.1 shows a schematic diagram of the gyro motion of a test particle and its guiding center. If the test particle motion $\langle\dot{\mathbf{r}}\rangle = \langle\dot{\mathbf{R}} + \dot{\boldsymbol{\rho}}\rangle$ is time-averaged over a gyration period, and if the overall contribution of the gyro motion relative to the guiding center over a gyro period is zero $\langle\rho\rangle = \langle\dot{\rho}\rangle = \langle\ddot{\rho}\rangle = 0$, the guiding center can be considered as the time-averaged location of a particle. In our ULF wave model, the characteristic distance over which the electric field and magnetic field change is much larger than the gyro radius of electrons. The characteristic time of ULF wave is also much longer than the gyro-period of electrons. The magnetic

and electric field effects on the electrons are considered as constants during a gyro period.

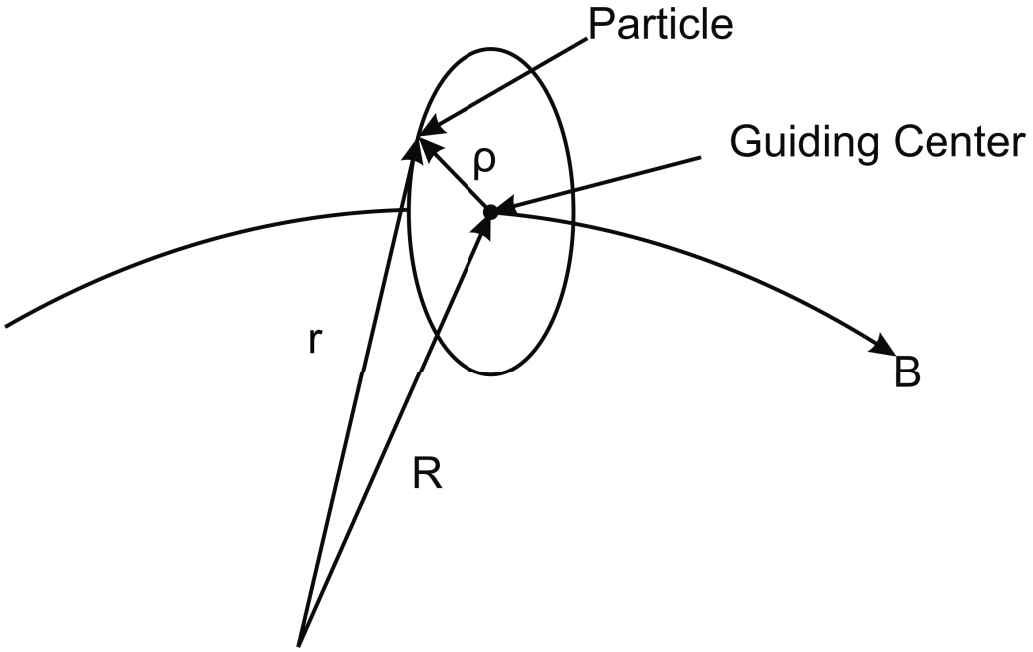

Figure 5.1: Schematic diagram of the gyro motion of a test particle and its guiding center. Taken from *Northrop* [1963].

The non-relativistic guiding center motion equations were derived by *Northrop* [1963]. The perpendicular drift motion of the guiding center is a combination of the $E \times B$ electric drift, the gradient drift, and the curvature drift [*Baumjohann and Treumann*, 1996], which are discussed in Section 2.3.3. Combining the drift velocities, we obtain an equation of motion for the guiding center

$$\frac{d\mathbf{R}}{dt} = \frac{\mathbf{E} \times \mathbf{B}}{B^2} + \frac{\mu}{qB^2}(\mathbf{B} \times \nabla B) + \frac{p_{\parallel}^2}{mqB^2}(\mathbf{B} \times \frac{d\mathbf{b}}{ds}) + \mathbf{v}_{\parallel} \tag{5.8}$$

where $\mu = W_{\perp}/B$ is the first adiabatic invariant assumed as a constant in our simulation, $p_{\parallel} = mv_{\parallel}$ is the parallel momentum, and $\mathbf{b} = \mathbf{B}/|B|$ is the direction of the magnetic field. The first three terms of Equation (5.8) correspond to the E × B drift, gradient drift, and curvature drift, respectively, and the last term $v_{\parallel}$ is the parallel velocity of the particle. Since the parallel electric field is zero in a shear Alfvén wave, the parallel motion of the guiding center is only affected by the magetic field along the field line. The equation of parallel motion of the guiding center is [*Northrop*,

1963]

$$m\frac{dv_\parallel}{dt} = -\mu\frac{dB}{ds} + \mathbf{v}_{\mathbf{E}\times\mathbf{B}} \cdot (p_\parallel \frac{d\mathbf{b}}{ds}) \tag{5.9}$$

where $\mathbf{v}_{\mathbf{E}\times\mathbf{B}} = \mathbf{E}\times\mathbf{B}/B^2$ is the $E \times B$ drift speed.

The previous equations of motion are non-relativistic. The relativistic form of these equations was derived by *Northrop* [1963]

$$\frac{dp_\parallel}{dt} = -\frac{\mu}{\gamma}\frac{dB}{ds} + \mathbf{v}_{\mathbf{E}\times\mathbf{B}} \cdot (p_\parallel \frac{d\mathbf{b}}{ds}) \tag{5.10}$$

$$\frac{d\mathbf{R}}{dt} = \frac{\mathbf{E}\times\mathbf{B}}{B^2} + \frac{\mu}{\gamma q B^2}(\mathbf{B}\times\nabla B) + \frac{p_\parallel^2}{\gamma m_0 q B^2}(\mathbf{B}\times\frac{d\mathbf{b}}{ds}) + \frac{\mathbf{p}_\parallel}{m_0\gamma} \tag{5.11}$$

where $\mathbf{p} = \gamma m_0 \mathbf{v}$ is relativistic momentum, m_0 is the rest mass of the electron.

Different from the full Lorentz approach in Section 5.1.1, the guiding center approach implicitly assumes the conservation of the first adiabatic invariant. To test the guiding center model, the L-shell variation of freely bouncing electrons in different energies has been simulated. It shows that particles are bouncing in the same L-shell without external ULF wave. Secondly, trajectories of H^+ ions have been simulated by using the full Lorentz model and guiding center model respectively within the same wave field. The results from these two models show identical trajectories and energy variations. The detailed parameters of the H^+ ions simulations will be provided in Section 5.5.1. The guiding center model has also been tested with backward integrating. An electron's trajectory was first simulated in the forward direction in time from $t = 0$ to $t = 10,000$ s; and then backward integration was used to trace the trajectory backward. The forward and backward integration trajectories are almost identical; the error is less than 0.1 %. These tests on the guiding center model have provided preliminary evidences about the correctness of the model. In Section 5.5.2, we will show more simulations with the guiding center model about drift resonance between the ULF wave and relativistic and non-relativistic electrons.

5.2 Phase Space Density Reproduction Methods: Liouville Methods

The differential flux measurements on different charged particles are an essential part of satellite particle observation. It is defined as the particle number flux incident on a unit surface at a given energy, pitch angle, and position. The interactions between the ULF wave perturbation and charged particles are observed by satellites as the fluctuation of differential fluxes [*Zong et al.*, 2007; *Claudepierre et al.*, 2013]. For non-relativistic particles, the relationship between the differential particle flux and the distribution function, or the phase space density (PSD), is expressed as [*Baumjohann and Treumann*, 1996]

$$J(W, \alpha, \mathbf{x}) = \frac{v^2}{m} f(v_\parallel, v_\perp, \alpha, \mathbf{x}) \tag{5.12}$$

where J is the differential particle flux, f is the phase space density, and α is the pitch angle. The forward and backward Liouville methods introduced in this section will provide ways to study the global variation of phase space density, and an accurate history of phase space density for comparison with satellite measurements.

5.2.1 Forward Liouville Method

The time evolution of the phase space distribution function in a Hamiltonian dynamical system follows the Liouville equation

$$\frac{df}{dt} = \frac{\partial f}{\partial t} + \sum_{i=1}^{n} \left(\frac{\partial f}{\partial q_i} \dot{p_i} + \frac{\partial f}{\partial p_i} \dot{q_i} \right) = 0 \tag{5.13}$$

where $f = f(p, q, t)$, and $q_i, i = 1, 2, ..., n$ is canonical coordinate, and $p_i, i = 1, 2, ..., n$ is canonical momentum. From Liouville's equation, it follows that the phase-space distribution function is constant along the trajectories of the system. Consider a piece of a plasma element moving in a Hamiltonian dynamical system: the trajectory is equivalent to the trajectory of single particle when the phase space volume of this element is small enough.

The forward Liouville method is applied to simulate collisionless plasmas. Test particles are "tagged" with a specified distribution function $f_0(t_0, \mathbf{v}_0, \mathbf{x}_0)$. The dis-

tribution function is determined by the particle's initial location in phase space at initial time. To study the wave-particle interactions in the magnetosphere, the initial location and initial time here are defined as the location at and time in which a particle is released without being affected by any magnetic or electric field other than the Earth's dipole magnetic field. By assuming a Maxwell distribution, Kappa distribution, or any other distribution functions, f_0 is obtained without statistical error. After the particles are released within the ULF wave, the distribution function in a sampling volume can be determined by the tagged particles in the volume. The statistical errors of this method come from the number of test particles in the sampling volume in configuration space. The discrete distribution function inside the sampling volume can be used to interpolate onto a regular velocity grid.

Satellite observations about particle differential flux can be reproduced using the forward Liouville method. Test particles collected by an appropriately chosen sampling volume represent the distribution function of particles measured by the particle instruments on the satellites. On the other hand, the time evolution of global particle distribution can be obtained if enough test particles are introduced in the system. The assumptions and the test particle initialization methods are discussed in Section 5.3.1.

5.2.2 Backward Liouville Method

If test particle models and wave field models have specific temporal and spatial dependence, and if test particle trajectories can be integrated exactly backward in time, the backward Liouville method can be applied to reproduce the particle distribution function at any specified point and at any time. In contrast to the forward Liouville method described in Section 5.2.1, this approach integrates particle trajectories at a given observation time t_1, observed position $\mathbf{r}_1$, and velocity $\mathbf{v}_1$ backward in time until it reaches an input region at time t_0, position $\mathbf{r}_0$, and velocity $\mathbf{v}_0$, where the undisturbed distribution function $f_0(t_0, \mathbf{r}_0, \mathbf{v}_0)$ is known. Following from Liouville's theorem, the distribution function at observed region 1 is obtained from input region 0 since $f_0(t_0, \mathbf{r}_0, \mathbf{v}_0) = f_1(t_1, \mathbf{r}_1, \mathbf{v}_1)$.

One of the main advantages of this approach over the forward Liouville method is that it does not rely on sampling over a volume element, and therefore is free from statistical sampling errors. By considering that the spatial size of a spacecraft is much smaller than the size of the magnetosphere system, the backward Liouville method is more suitable for studying the differential particle flux observed by the satellites without any error from the size of sampling volume. In Section 5.3.2, we will describe the process we used to initialize test particles and discuss the performance of this method by comparing it with the resolution of real instruments on the Van Allen Probes.

5.3 Initial conditions of Test Particles

5.3.1 Initializing the Global Forward Liouville Simulation with Monte-Carlo Method

Ideally, the sampling volumes in configuration space, velocity space, and time should uniformly include a large enough number of test particles in the forward Liouville simulations. However, the total number of test particles we can use is limited by the computing resource. In this section, we will describe how the locations and velocities of test particles are initialized in the forward Liouville simulations with Monte-Carlo methods.

The dipole-field ULF wave model has rotational symmetry on the order of m. Here, m is the azimuthal wave number. The azimuthal boundary condition is considered to be periodic. Test particles are uniformly distributed in an azimuthal wave period. The probability density function of the test particle's initial azimuthal angle is:

$$f(\phi) = \frac{m}{2\pi}, 0 < \phi < 2\pi/m \tag{5.14}$$

The initial azimuthal location of a test particle is

$$\phi = R_\phi / f(\phi) \tag{5.15}$$

where R_ϕ is a uniformly distributed random variable between 0 and 1.

In order to distribute test particles uniformly on an equatorial plane between the minimum radius r_{min} and maximum radius r_{max} in a unit of Re, the distribution function of the test particle's initial radius on the equatorial plane is:

$$f(r) = Ar^{\beta}, \beta = 1 \tag{5.16}$$

where A is a normalization coefficient. By calculating the cumulative distribution function of $f(x)$, we can solve A

$$A = \frac{\beta + 1}{r_{max}^{\beta+1} - r_{min}^{\beta+1}} \tag{5.17}$$

Generally, a negative gradient of the test particle's radius distribution will build up if $\beta < 1$ and a positive gradient will build up if $\beta > 1$. In the simulation studies in Chapter 8, we are using a uniform radial distribution $\beta = 1$. The initial r of the test particle is

$$r_{=}[r_{min}^{\beta+1} + (r_{max}^{\beta+1} - r_{min}^{\beta+1})R_r]^{\frac{1}{\beta+1}} \tag{5.18}$$

where R_r is a uniformly distributed random variable between 0 and 1.

The maximum latitude a test particle can reach depends on the particle's equatorial pitch angle. When the wave is not present, all particles bounce freely along field lines. To uniformly fill the field line with test particles, we use a different method to randomize the particles' initial latitude. First, using an isotropic Maxwell distribution, we randomize the initial equatorial pitch angle, initial energy, and initial gyro-phase of a test particle:

$$f(W) = f_0\sqrt{W}exp(-W/W_{th}) \tag{5.19}$$

$$f(\alpha) = \frac{1}{\pi - 2\alpha_m} \tag{5.20}$$

$$f(\phi_v) = \frac{1}{2\pi} \tag{5.21}$$

where ϕ_v is the direction of velocity perpendicular to the Earth's magnetic field. ϕ_v corresponds to the initial phase of the particle's gyro-motion. Note that W is uniformally distributed when $W_{th} \to \infty$. Particles are released at a random time t_{rand} from the equator with a randomized initial pitch angle and energy and bounce freely without an external wave. If the particle releasing time is long enough, the particles along the field line are uniformly distributed.

Two methods can be used to generate randomized particle energy for a Maxwell distribution: the accept-rejection method, and the inverse transform method. For the accept-rejection method, we first generate a uniform-random number W_R between W_{min} and W_{max}:

$$W_R = W_{min} + R_W(W_{max} + W_{min}). \tag{5.22}$$

Then, a second uniform-random number f_R between 0 and 1 is generated. Repeat generating W_R and f_R until

$$f_R \leq f(W_R)/c \tag{5.23}$$

where c is the maximum of f. Then the accepted random numbers W_R follow the distribution $f(W)$.

The inverse transform method uses a cumulative distribution function (CDF) of the Maxwell distribution function

$$\begin{aligned} F(x) = -f_0 W_{th} \left[\sqrt{x}\exp(-x/W_{th}) - \sqrt{W_{min}}\exp(-W_{min}/W_{th})\right] \\ + \frac{\pi}{2} f_0 W_{th}^{3/2} \left[\mathrm{erf}(x/W_{th} - \mathrm{erf}(W_{min}/W_{th}))\right] \end{aligned} \tag{5.24}$$

where the constant f_0 can be solved numerically by considering that CDF is 1 at maximum energy, $F(W_{max}) = 1$. To generate a random number W_{rand} for the Maxwell distribution, we first generate a uniform-random number R between 0 and 1, and then numerically solve Equation (5.24) with $R = F(W_{rand})$ to get W_{rand}.

5.3.2 Three-dimensional Grids in Velocity Space for Backward Liouville Simulations

As discussed in Section 5.2.2, the backward Liouville simulation does not require any randomization on the test particles on initialization because the final locations (known as sampling points) of the test particles are known precisely, and their initial locations are also known precisely after backward integration. At a sampling point, particles can be initialized from uniform grids in the three-dimensional velocity space. Although there are different choices in defining the form of grids in practice, we chose to use uniform velocity space grids of (W, α, v_ϕ) to initialize test particles because this is one of the best approaches to compare the simulation outputs with satellite

measurements. For example, the Level 3 pitch-angle resolved differential energy flux data of electrons and protons measured by a MagEIS instrument on the Van Allen Probes [*Blake et al.*, 2013], which will be used in Chapter 6 and Chapter 7, are measured using different pitch angle channels and different energy channels.

In most backward Liouville simulations in this thesis, we released the particles with the same gyro-motion direction v_ϕ because the azimuthal wavenumber m in these studies is in the range of 30 to 60, and the energy range of the particles is in tens of keV to several hundred keV. The spatial scale of the gyro-radius of protons/electrons and the temporal scale of the gyro-frequency are both much smaller than those of the ULF waves studied in these events. Therefore the gyro-motion of particles and their initial phase are not important and are considered as uniform in these studies.

5.4 Computational Code for the Models

5.4.1 Numerical Computing Methods

Equations of particle trajectories described by the Lorentz and the guiding center approaches are both ordinary differential equations (ODEs). In our test particle code, the fourth-order Runge-Kutta method is used to integrate Equation (5.3)- Equation (5.5) and Equation (5.10)- Equation (5.11). The numerical time-dependent solution of an ODE fourth-order Runge-Kutta method (RK4) is expressed as

$$y_{n+1} = y_n + \frac{h}{6}(k_1 + 2k_2 + 2k_3 + k_4), \tag{5.25}$$

$$t_{n+1} = t_n + h \tag{5.26}$$

where y_n, $n = 0, 1, 2, 3, ...$ is the numerical solution of ODE $\dot{y} = f(t, y), y(t_0) = y_0$ and h is the time step size. An explicit expression of k_1 to k_4 is

$$k_1 = f(t_n, y_n), \tag{5.27}$$

$$k_2 = f(t_n + \frac{h}{2}, y_n + h\frac{k_1}{2}), \tag{5.28}$$

$$k_3 = f(t_n + \frac{h}{2}, y_n + h\frac{k_2}{2}), \tag{5.29}$$

$$k_4 = f(t_n + h, y_n + hk_3). \tag{5.30}$$

The local truncation error of the RK4 method is on the order of $O(h^5)$, and the total accumulated error is on the order of $O(h^4)$. The main advantages of using RK4 in this study is that it is very stable, and we do not have to treat the first few steps taken by a single-step integration method as special cases.

5.4.2 Implementation of Code

The test particle code is written with the Fortran90 programming language based on Dr. Richard Marchand's original code. The code is designed to have two main objectives. The first purpose is to simulate the trajectory of a single particle in the wave field. The second one is to determine the particles' initial locations and velocities with backward Liouville method. Output data of the simulation results are written as plain text files, but their formats are different for different simulation purpose. For a single particle trajectory simulation, each output data line includes the position, velocity, and the magnetic/electric field effect on the particle at one simulation time step. For a backward Liouville simulation, each line of output data represents the information about a test particle. The information of each test particle includes its position and velocity before and after backward integrating to the input region, and its phase space density determined by the initial condition of in the input region. The backward tracing simulation data usually include a series of files at different observation times. By combining data from these time slices, we can reproduce the overall evolution of phase space density observed by a spacecraft. The list of input parameters is shown in Table 5.1.

This test particle code has high scalability and high computing resource utilization rate. Large-scale simulation tasks can be divided into smaller jobs and run independently on different computing systems, such as local server, cluster computing systems, or cloud computing systems. An external input-parameter-generating script is implemented to divide the simulation job into smaller tasks. Each job runs as an independent process, and the CPU resource is dynamically distributed by the system. Output data visualization codes are written with MATLAB.

Table 5.1: Main input parameters of test particle simlation code.

Parameter name	Description
Global parameters	
option	The purpose of simulation: Compute particle distribution function from particle backtracking, or forward integrate a single particle trajectory.
time	Total time range of test particle simulation.
step_size	Time integration step size.
Parameters of test particle	
xyzPosition0	Initial position of test particle for trajectory simulation, or the observation position for backward tracing simulation.
mass	Mass of test particle.
charge	Charge of test particle.
temp	Plasma thermal temperature.
density	Density of cold plasma, used to calculate Alfvén speed.
v0	Initial velocity of test particle, only available in single particle trajectory simulation.
Parameters of wave	
omega_driver	Angular frequency of the external driver.
amp_driver	Amplitude of the driver in unit of nT.
m_value	Azimuthal wavenumber of wave.
	Time when the wave start decaying.
decay_rate	Decaying rate of wave, wave amplitude will decay exportationally after decay_time.
Parameters of backward tracing simulation	
Emin, Emax	Minimum and maximum energies of test particles.
Egridnumber	Number of energy grids between Emin and Emax.
PAmin, PAmax	Minimum and maximum pitch angle of test particles.
PAgridnumber	Number of pitch angle grids between PAmin and PAmax.
Vphigridnumber	Number of gyro-phase grids between 0 and 2π.
Snapshot_interval	Time interval between two backward tracing snapshots.

5.5 Simulations on Drift resonance and Drift-bounce Resonance with H^+ and O^+ Ions

5.5.1 N=0 Drift-resonant between Fundamental Mode Wave and H^+ Ions

In Figure 5.2, the test particle simulations with backward Liouville method reproduced the interaction between H^+ ions and input ULF wave observed by Van Allen Probes on April 11, 2014 [*Zhou et al.*, 2016]. The top left panel of Figure 5.2 shows the time profile of such an ULF wave with an $m = 8$, frequency $f = 20.94$ mHz, and a poloidal mode wave excited at $L = 4.5$. The two bottom left panels show the changes in energy and distribution function of the H^+ ions interacting with the wave. The right column of Figure 5.2 shows values of L, total energy W, normalized magnetic moment μ/μ_0 (here μ_0 is the initial magnetic moment), azimuthal electric field E_3, the $\mathbf{E} \times \mathbf{B}$ drift velocity $v_{E\times B}$(black line in bottom panel), and the polarization drift velocity v_p(blue line in bottom panel) computed along the trajectory of a drift-resonant ion of energy 244 keV. The magnetic moment is normalized by its value at $t = 0$ to highlight possible regions of non-adiabatic behavior. In this case, the particle trajectory is not strongly perturbed (right column) by the wave, which has as a maximum electric field of 2 mV/m at the equator. The linear theory of drift resonance improved by *Zhou et al.* [2016] predicted the variations of differential flux in this case. The results come from our model are in good agreements with both drift resonance theory and the satellite observations.

The pitch angle dependence of drift resonance is illustrated in Figure 5.3, with panel (a) in the left column showing the time profile of the wave and panels (b) and (c) showing changes in particle energy for pitch angles of 90° and 35°, respectively. The differential flux oscillation caused by drift-resonance is more efficient at 35° pitch angle because ions experience a larger electric field off the equator (see Figure 4.3) and hence a larger net acceleration/deceleration along their bounce trajectory. The differential particle flux in the right column of Figure 5.3 is binned in energies similar to a MagEIS-like instrument on the Van Allen Probes. The modulations of the differential flux in Figure 5.3 have a maximum amplitude in the $\sim$ 240 keV energy channel,

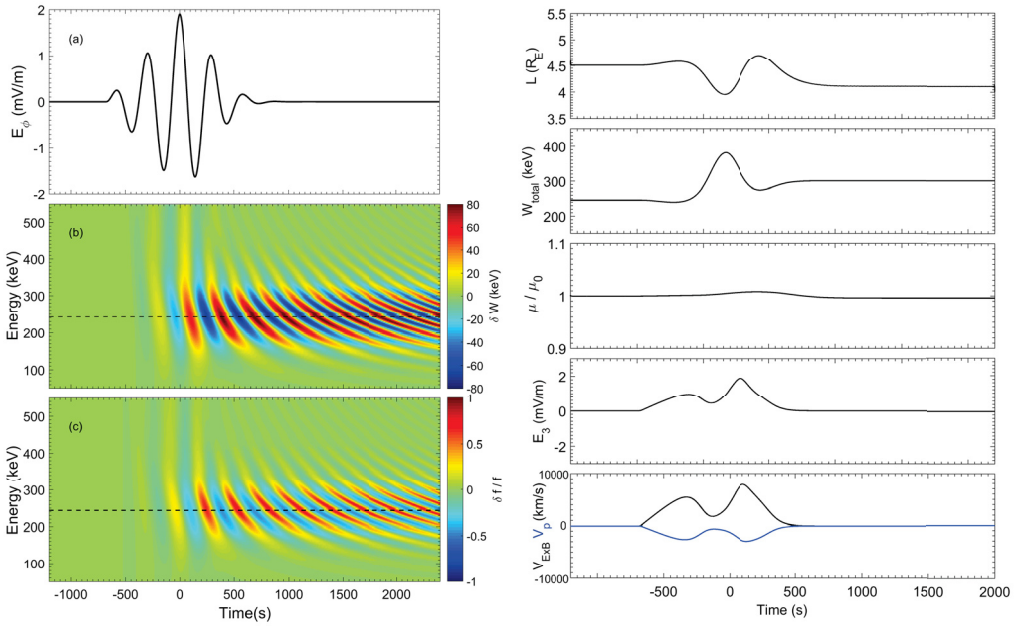

Figure 5.2: H^+ ions interacting with a $m = 8$ poloidal wave of frequency 20.94 mHz. The left panels show (a) the wave profile; (b) the change in particle energy; (c) the relative change in the distribution function. The right panels show values of L, total energy W, normalized magnetic moment μ/μ_0 (here μ_0 is the initial magnetic moment), azimuthal electric field E_3, and the $\mathbf{E} \times \mathbf{B}$ drift velocity $v_{E\times B}$(black line in bottom panel), and the polarization drift velocity v_p(blue line in bottom panel), of a drift-resonant ion of initial energy 244 keV placed initially at $L = 4.5$. This figure is published in *Zong et al.* [2017].

which is consistent with the drift-resonance condition of $N = 0$. The differential flux also exhibits a 180° phase change with energy across the resonance, as discussed in *Southwood and Kivelson* [1981].

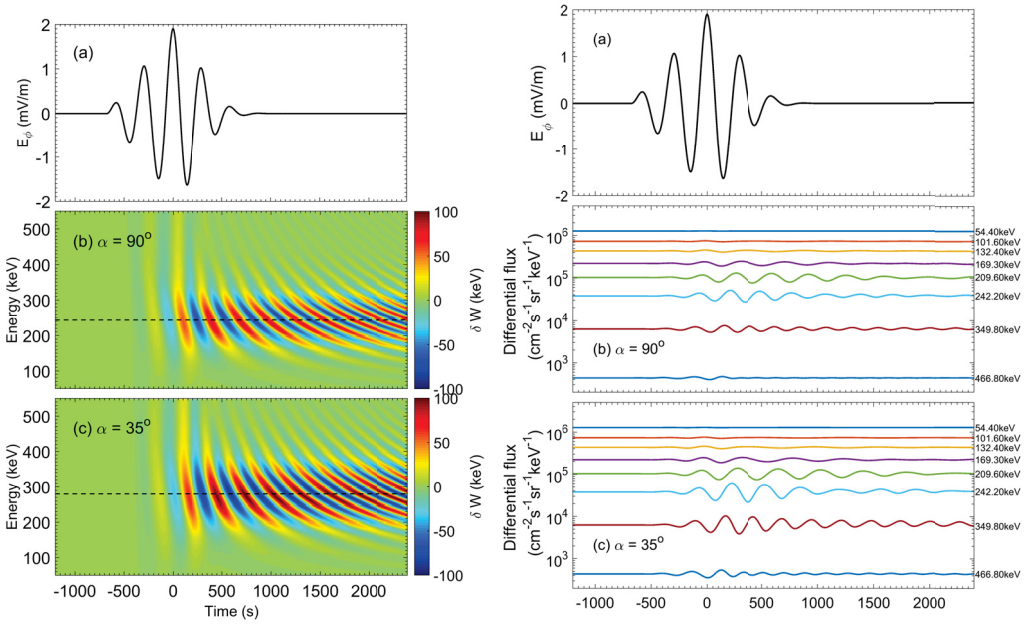

Figure 5.3: Test particle simulation of H^+ ions. Panel (a) in the left column shows the time profile of the wave. The energy changes of particles with pitch angles of 90° and 35° are shown in panels (b) and (c), respectively. Panels (b) and (c) in the right column show corresponding modulations in differential particle flux for the two values of pitch angle. This figure is published in *Zong et al.* [2017].

Figure 5.4 shows the trajectory of a 90° pitch angle H^+ ion of drift-resonant energy 244 keV. The trajectory is overlaid with snapshots of the electric field as a function of L at the equator. Parameters are the same as in Figure 5.2 and Figure 5.3 except that the wave reaches a maximum amplitude of 2 mV/m at the equator after 800 s and is held constant for a longer time scale of 3400 s before decaying over a time interval of 800 s. The left and right panels of Figure 5.4 show different parts of the orbit of the drift-resonant ion up to 4200 s and 5000 s, respectively. The left panel of Figure 5.4 clearly shows that resonant H^+ ions are trapped in an effective potential well in the wave frame and are continually accelerated and decelerated as they move periodically back and forth across L along their drift path. In the right panel of Figure 5.4, the H^+ ion then drifts azimuthally with constant energy and L

after the wave decays out.

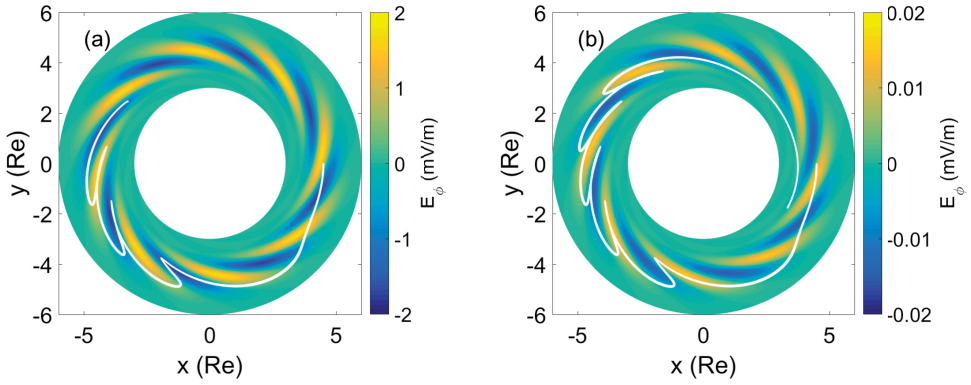

Figure 5.4: Test particle simulation of drift-resonant H^+ ions of energy 244 keV and 90° pitch angle interacting with a $m = 8$ poloidal mode ULF wave at $L = 4.5$. In the left panel the electric field grows linearly with time for 800 s and is then held constant for 3400 s. The right panel shows the remaining part of the trajectory up to $t = 5000$ s after the wave has decayed. Other parameters are defined in Figure 5.2. This figure is published in *Zong et al.* [2017].

Figure 5.5 shows the time dependence of L, W, μ/μ_0, E_3, $v_{E\times B}$, and v_p along the ion trajectory marked in Figure 5.4. For the wave parameters used in this example, the first adiabatic invariant normalized by its value at $t = 0$ is subject to small variations during successive aperiodic excursions between $L = 4 - 5$. The bottom panel of Figure 5.5 shows that the magnitude of the drift velocity is much larger than the polarization drift velocity, which implies the former is more important in causing radial motion. shows the trajectory of a 90° pitch angle H^+ ion of drift-resonant energy 244 keV.

In Chapter 6, the same models are applied to the study of waves with different amplitudes and azimuthal wave numbers. The effects of gradients in phase space density will also be investigated in order to better understand the complex behavior of resonant processes affecting ions and electrons in the Earth's inner magnetosphere.

5.5.2 Simulations of Relativistic Electrons Drift Resonance with ULF Waves

In this section, we simulate the drift resonance of relativistic electrons with a fundamental poloidal mode ULF wave which has a low azimuthal wavenumber $m = 3$.

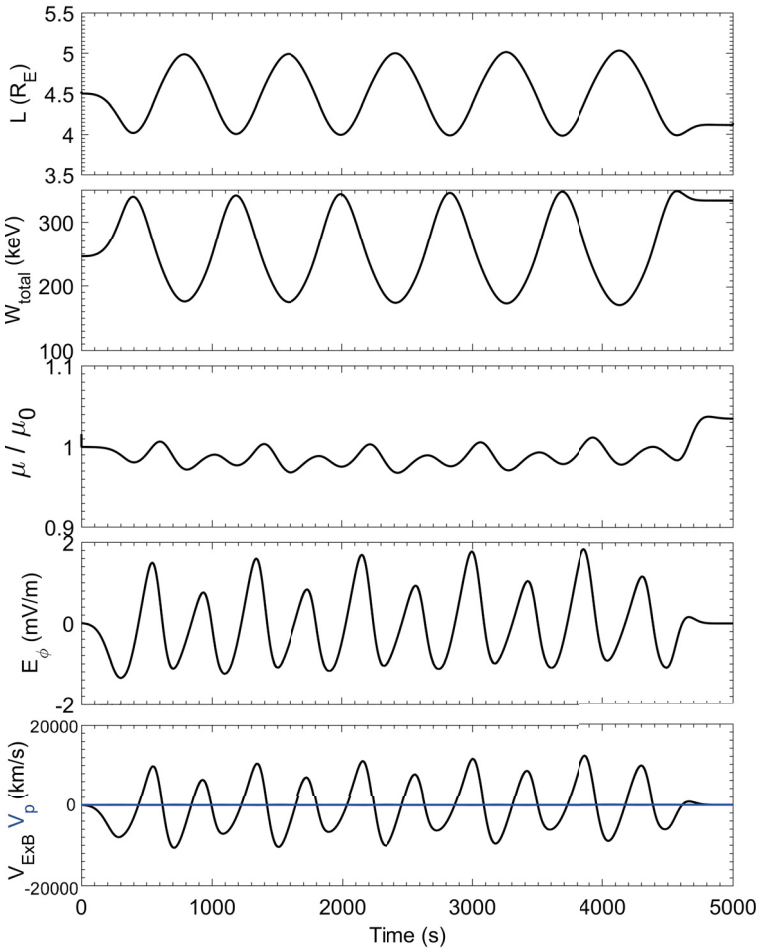

Figure 5.5: Equatorially mirroring H^+ ions of resonant energy 244 keV interacting with an initially growing and then decaying poloidal mode wave with azimuthal wavenumber $m = 8$ and frequency 20.94 mHz. The quantities in each panel are in the same format as the right panel of Figure 5.2, and are computed along the ion trajectory. Other parameters are the same as in Figure 5.4. This figure is published in *Zong et al.* [2017].

Although low-m ULF waves are mostly toroidal mode waves [*Radoski and McClay*, 1967], the drift resonance energy in this case provides a proper condition to compare the drift resonance with relativistic electrons and with non-relativistic H^+ ions, respectively. Using the backward Liouville method provided in Section 5.2.2, the responses of different energy electrons within a poloidal mode wave have been studied.

Figure 5.6 shows the energy changes δW of electrons and H^+ ions at 90° pitch angle affected by a fundamental poloidal mode ULF wave. The wave has a frequency of $f = 3.3$ mHz and an azimuthal wavenumber $m = 3$. Depending on the different drift directions of electrons, we use westward propagating wave in the case of H^+ ions and use eastward propagating wave in the case of relativistic electrons. As shown in the top panel of Figure 5.6, the wave reaches a maximum amplitude of ~ 2 mV/m at the equator at ~ 800 s, and is damped out after 1800 s. The strongest flux modulation of H^+ ions in the bottom of Figure 5.6 is about 500 keV, which is in good agreement with the non-relativistic resonant energy $W_{res} = 492.60$ keV calculated from the drift resonant condition $\omega = m\omega_d$. Relativistic effects in this energy range are not obvious for H^+ ions. However, electrons are relativistic in an energy range of several hundred keV. For 90° pitch angle electrons, the relativistic drift angular frequency ω_d is

$$\omega_d = \frac{3\mu}{\gamma e L^2 R_E^2} \tag{5.31}$$

where γ is the Lorentz factor. The theoretical drift resonant energy calculated from Equation (5.31) shows that $W_{res} = 689.67$ keV. The middle panel of Figure 5.6 shows that the residual flux variation for electrons near drift resonant energy is similar to that in the bottom panel of Figure 5.6. The wave propagation direction is reversed from that for the case of the ions, since the drift direction of the electrons is opposite to that of the ions. The relativistic resonant energy has obviously shifted to about 700 keV which is consistent with the theoretical expectation.

Figure 5.7 shows the L-shell, energy changes, azimuthal electric field, and $\mathbf{E} \times \mathbf{B}$ drift velocity of a single electron which drift resonates with an eastward propagating wave. The initial energy of the test particle $W_e = 700$ keV. The frequency, azimuthal wave number, and amplitude profile of the wave are identical to the simulations in Figure 5.6. Unlike the ions' simulation with the full Lorentz force approach, electron

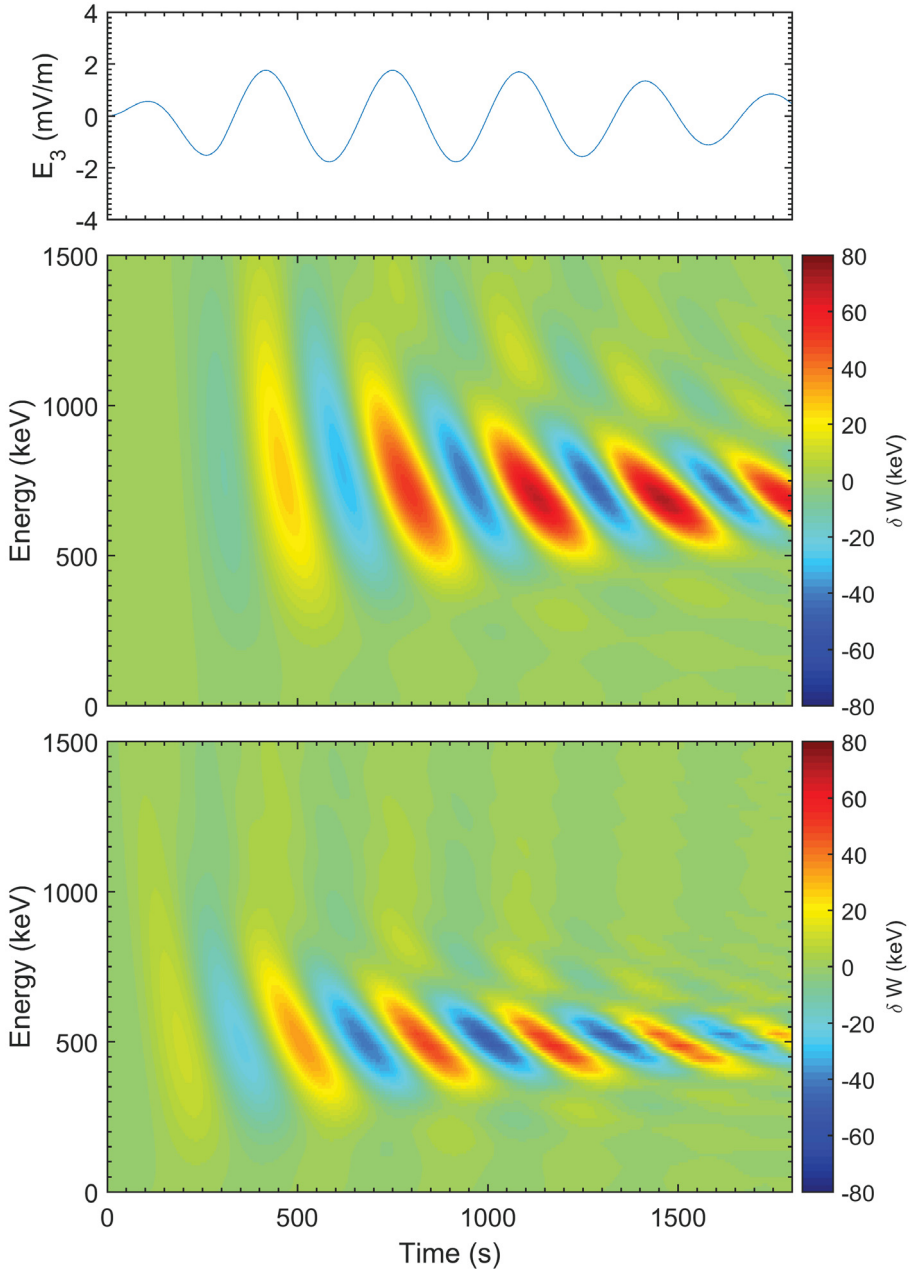

Figure 5.6: From top to bottom: The first panel shows wave amplitude profile of an $m = \pm 3$, poloidal wave with a frequency of 3.33 mHz. The second panel shows electrons energy changes as a function of measured energy within an eastward propagating wave with amplitude profile in the top panel. The third panel shows H^+ ions energy changes as a function of measured energy within a westward propagating wave with an amplitude profile in the top panel.

simulations with a guiding center assumed that the first adiabatic invariant μ is conserved. The guiding center model and the full Lorentz force model both imply that the radial motion of resonating particles is caused by the drift motion under the electric field of ULF waves.

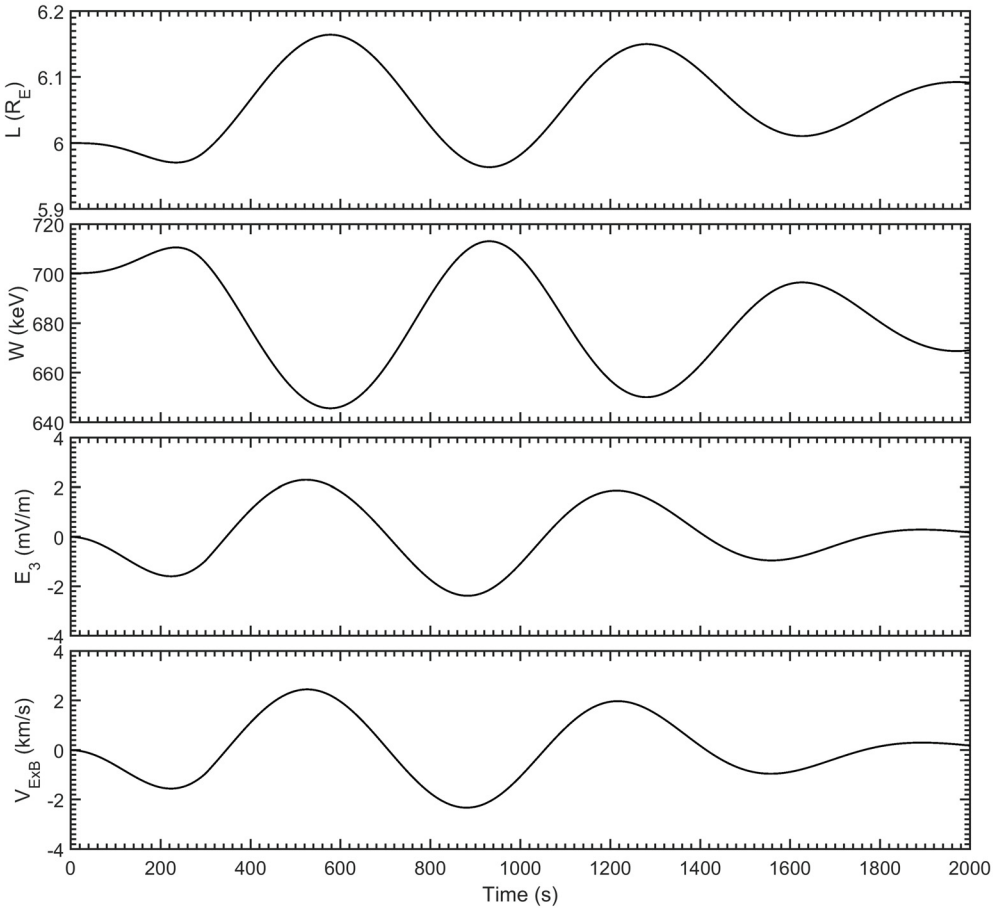

Figure 5.7: The panels from top to bottom show the L-shell, energy changes, azimuthal electric field, and $\mathbf{E} \times \mathbf{B}$ drift velocity for an electron with energy of 700 keV. The wave profile is identical to the top panel of Figure 5.6.

Figure 5.8 and Figure 5.9 are the Poincaré maps showing the equatorial motions of electrons which have the same first adiabatic invariant μ. The poloidal wave amplitude is a constant of $\sim$ 2 mV/m. The wave's frequency is 3.3 mHz, and its azimuthal wave number is 3. In Figure 5.9, particles are accelerated and decelerated in different locations of the wave frame. The trajectories of particles in Poincaré maps

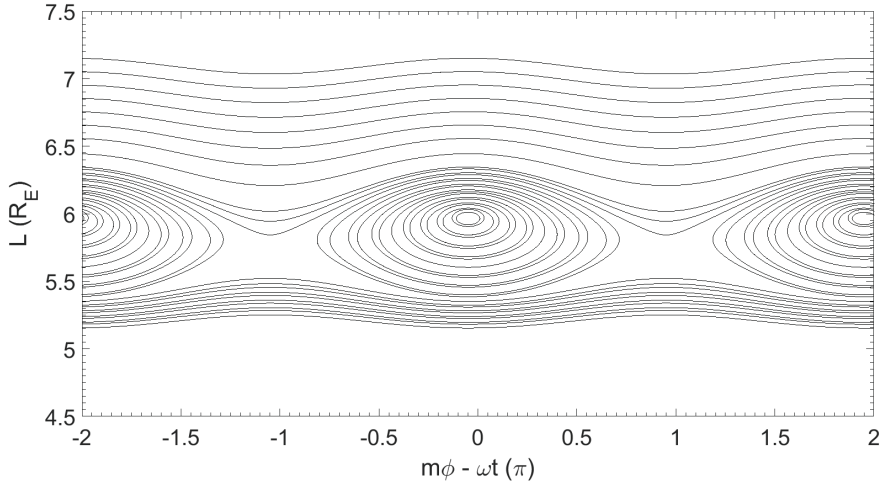

Figure 5.8: Poincaré map shows the trajectories of electrons' L-shell in the wave frame for 90° pitch angle electrons with identical first adiabatic invariant. The wave has frequency of $f = 3.3$ mHz, an azimuthal wave number $m = 3$ and is propagating eastward. The wave amplitude is ~ 2 mV/m and does not change with time.

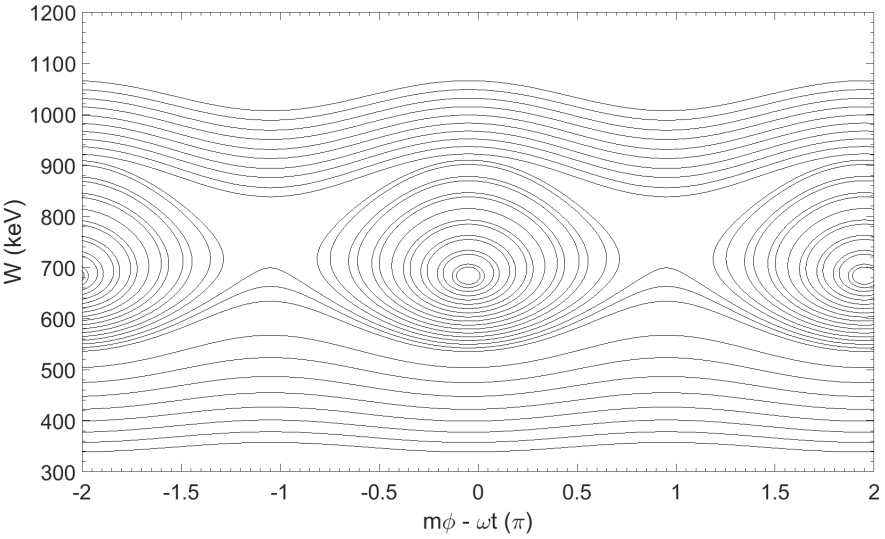

Figure 5.9: Poincaré map shows the trajectories of electrons' energy in the wave frame for 90° pitch angle electrons with identical first adiabatic invariant. The wave has a frequency of $f = 3.3$ mHz, an azimuthal wavenumber $m = 3$ and is propagating eastward. The wave amplitude is ~ 2 mV/m and does not change with time.

illustrate that particles resonating with the wave change their energy and move in the wave frame. Their trajectories in the wave frame form closed circles around the relativistic resonance energy of $W \sim 700$keV because their first adiabatic invariant is conserved while interacting with ULF waves. These closed circles in the Poincaré maps prove that our model has high precision in long-time integration.

Chapter 6

Test Particle Simulations of Poloidal Mode Wave Drift Resonating with H^+ Ions and Flux Oscillation Observed by Van Allen Probes and CARISMA

In this chapter, the ULF wave model in Chapter 4 and the full-Lorentz test particle model in Chapter 5 are used to provide studies on the flux modulation of H^+ ions during a giant pulsations event produced by kinetic instabilities. The work in this chapter have been submitted to *Journal of Geophysical Research: Space Physics*. Two referee reports have been received, both of which state the paper should "return to author for minor revisions".

Ultra-low-frequency (ULF) wave and test particle models are used to investigate the pitch angle and energy dependence of ion differential fluxes measured by the Van Allen Probes spacecraft on October 6, 2012. Analysis of the satellite data reveals modulations in differential flux resulting from drift resonance between H^+ ions and fundamental mode poloidal Alfvén waves detected near the magnetic equator at $L \sim 5.7$. Results obtained from simulations reproduce important features of the observations, including a substantial enhancement of the differential flux between $\sim 20^\circ - 40^\circ$ pitch angle for ion energies between $\sim 90 - 220$ keV, and an absence of flux modulations at 90°. The numerical results are in good agreement with observa-

tions and predictions of drift-bounce resonance theory and demonstrate that the flux modulation caused by ULF waves in the Earth's magnetosphere can be understood using relatively simple wave and test particle models.

6.1 Introduction

Ultra-low-frequency (ULF) waves strongly affect the dynamics of electrons and ions in the Earth's radiation belts. Resonant interactions between Pc5 waves and energetic ions can result in substantial changes in particle energy over timescales of tens of minutes or hours [*Elkington et al.*, 1999; *Hudson et al.*, 2000]. Higher frequency Pc1 electromagnetic ion cyclotron (EMIC) waves can pitch-angle scatter electrons on even shorter time periods and contribute to outer radiation belt particle loss [*Summers et al.*, 1998]. It is therefore crucial to quantify the physical conditions that lead to efficient energy exchange between ULF waves and inner magnetosphere hot plasma. Drift bounce resonance theory introduced by *Southwood and Kivelson* [1981, 1982] suggests that efficient energy transfer between ULF waves and charged particles occurs when particle drift rates and wave frequencies are comparable. In the Earth's magnetosphere, poloidal mode ULF waves fall into this category [e.g. *Elkington et al.*, 2003; *Ozeke and Mann*, 2008] and are the main topic of this chapter.

Zong et al. [2007, 2009] have reported observational evidence of drift-resonance between radiation belt electrons and standing ULF waves with wave periods of several minutes (Pc5-range). There are also numerous observations demonstrating that modulation of energetic particle fluxes by ULF waves is common [e.g. *Baker et al.*, 1980; *Kremser et al.*, 1981; *Takahashi et al.*, 1985; *Takahashi et al.*, 1990; *Claudepierre et al.*, 2013; *Foster et al.*, 2015]. Here, we investigate quasi-periodic modulations of ring current ion fluxes by a class of fundamental mode ULF waves known as Giant Pulsations (Pgs). These standing Alfvén waves are relatively rare but when they occur they have an easily identifiable signature in ground magnetometer data [*Motoba et al.*, 2015] that makes them ideal for analysis. As they support poloidal electric fields sufficient to accelerate ions to relatively high energy, they are also good candidates for studying resonant wave-particle interactions [e.g. *Chisham et al.*, 1992; *Chisham and*

Orr, 1997]. Ground observations of Pgs reveal they are quasi-monochromatic waves in the Pc4-5 band with periods of approximately $45 - 150$ seconds. The magnetic field vector of the wave in the magnetosphere is mainly meridional but rotates by $\sim 90^\circ$ through the ionosphere when sufficient Hall conductivity is present [*Hughes and Southwood*, 1976]. From ground observations, Pgs are inferred to have westward phase velocities and azimuthal wavenumbers m on the order of $16 - 35$ [*Rostoker et al.*, 1979; *Glassmeier*, 1980].

Statistical studies of giant pulsations show they are predominantly a morning side phenomena with both a seasonal and solar cycle dependence. Wave activity is stronger at equinox near the solar cycle minimum [*Green*, 1979; *Brekke et al.*, 1987]. The generation mechanism for giant pulsations is considered to be plasma instabilities, with different types proposed. *Glassmeier* [1980]; *Poulter et al.* [1983]; *Chisham et al.* [1990]; *Chisham and Orr* [1991] all conclude that Pgs are second-harmonic standing waves excited through bounce resonance. As bounce resonance is only possible for even harmonics, this mechanism is not viable for Pgs, which are fundamental mode standing waves. *Glassmeier et al.* [1999] present clear evidence that Pgs are odd mode ULF waves and argue that a modified bounce resonance mechanism is viable. The modified drift-bounce theory has been criticized by *Mann and Chisham* [2000]. *Green* [1979, 1985] correctly concludes that Pgs are odd mode standing waves excited by drift resonance rather than bounce resonance (with bounce harmonic $N = +1$ or -1). A kinetic instability known as the drift-wave instability [*Hasegawa*, 1971] suggests another process by which fundamental mode standing waves can be excited. In the modeling presented, the generation mechanism is not considered as waves are excited by a specified source.

Drift resonance between equatorially mirroring electrons and Pc5 waves has been investigated extensively by *Degeling et al.* [2007, 2010, 2014]. In their numerical calculations, a source placed in the vicinity of the noon magnetopause is used to excite low-m compressional waves that couple to field line resonances in the inner magnetosphere. This interaction can produce radial peaks in electron phase space density (PSD) [*Degeling et al.*, 2008], drift-echoes, phase mixing during and after waves have decayed [*Degeling and Rankin*, 2008], and both radial diffusion and local

acceleration [*Degeling et al.*, 2011]. Magnetopause excited compressional waves and associated field line resonances can also drive transport leading to magnetopause shadowing [*Degeling et al.*, 2013] and betatron acceleration [*Mann et al.*, 2013]. It is clear then that Pc4-5 wave-particle interaction processes manifest many observed characteristics of inner magnetosphere particle dynamics. As high-m waves launched from a magnetopause source cannot easily penetrate the outer radiation belt, particle acceleration resulting from such a source is not expected to increase electron and ion energies in this region significantly. One exception is waves induced by interplanetary shocks in the recovery phase of magnetic storms [*Zong et al.*, 2009].

The theory of drift bounce resonance developed by *Southwood and Kivelson* [1981, 1982] is useful in providing a qualitative interpretation of ion acceleration by ULF waves. Satellite differential flux can be analyzed by making use of the drift-bounce resonance condition $\omega - m\omega_d = N\omega_b$, which requires specification of the ion drift and bounce frequencies ω_d and ω_b, respectively, and the order N of the resonance. In the original formulation of the theory, the assumption of infinitesimal growth of the wave amplitude is made, which is unlikely to be realized in practice. This led *Zhou et al.* [2016] to extend the theory to account for the finite lifetime of ULF waves. The generalization of the theory to accommodate wave growth and damping stages enables better comparison between theory and observations. However, it excludes changes in L resonant ions experience during their interaction with waves. Therefore, in the studies presented here, test particle simulation is used to follow the full nonlinear trajectory of ions as they interact with ULF waves. The drift-bounce resonance condition is not imposed a priori, and so resonant wave-particle interactions take place without special constraints placed on the initial particle distribution.

Section 6.2 of the paper describes the methodology used to model ULF waves. Single particle test particle simulations that illustrate new features of ion dynamics not previously reported are discussed in Section 6.3. Section 6.4 summarizes ground and satellite observations of giant pulsations and ion flux modulations observed by the Van Allen Probes (RBSP) spacecraft on October 6, 2012. Section 6.5 presents results of test particle simulation that are used to investigate the energy and pitch angle (PA) dependence of these observations. Section 6.6 provides a summary and

conclusions.

6.2 Simplified Model of Uncoupled MHD Poloidal Mode ULF Waves

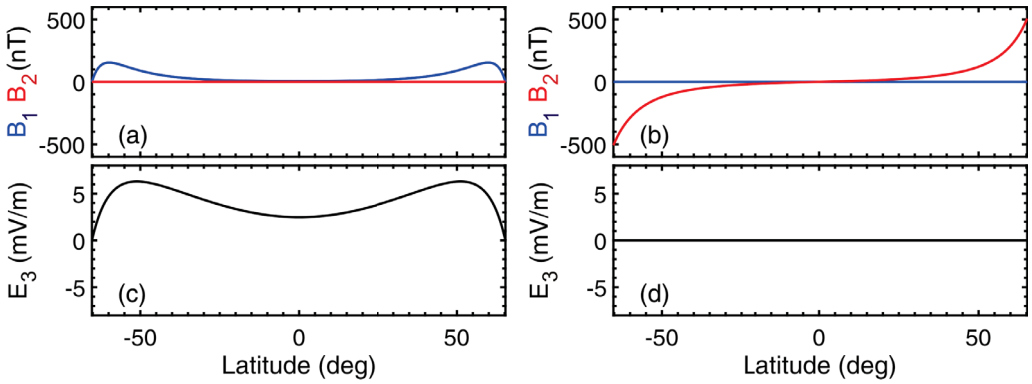

Figure 6.1: Electric and magnetic field perturbations at $L = 5.7$. The density varies as described in the text; the wave frequency is 10 mHz and the azimuthal wavenumber $|m| = 35$. The left column shows that the compressional magnetic field (B_{11} in the top panel) and azimuthal electric field (E_3 in the bottom panel) are in phase. The right column panels show the fields 1/4 wave period later.

To model observations of one hour duration giant pulsations observed by the RBSP-A spacecraft on October 6, 2012, we use a simplified model of driven ULF waves and a full Lorentz force test-particle code. We focus on the poloidal mode, but illustrate the procedure for obtaining the toroidal mode as well. The limiting assumption is that coupling between modes is neglected and that the toroidal (poloidal) mode has an azimuthal (radial) perturbation in the magnetic field and a radial (azimuthal) perturbation in electric field. The equations describing the toroidal mode are obtained from Ampere's law, the cold plasma form of the linearized fluid momentum equation, and Ohm's law expressed as $\mathbf{E} = -\mathbf{v} \times \mathbf{B}$,

$$\frac{\partial(h_3 B_3)}{\partial t} = \frac{h_3}{h_1 h_2}\frac{\partial}{\partial x_1}(h_2 \nu_3 B_{10}) \tag{6.1}$$

$$\rho_0 \frac{\partial \nu_3}{\partial t} = \frac{B_{10}}{4\pi h_1 h_3}\frac{\partial}{\partial x_1}(h_3 B_3) + D \tag{6.2}$$

In these equations, the coefficients $h_{1,2,3}$ are the usual metric factors for a dipole magnetic field, with subscripts 1 and 3 denoting directions along the background

magnetic field, and in the azimuthal direction, respectively. Subscript 2 denotes the direction perpendicular to field lines in a meridian plane and x_1 is the spatial coordinate along the background field. Note that $h_1 = h_2 h_3$, while D in the second equation is a constant frequency driving term with a time-dependent amplitude used to describe growing and then decaying ULF waves. In our model,$D = \rho\omega_0 v_D \sin\omega_0 t$, ω_0 is the frequency of the driver, and v_D is the plasma velocity of the driver. The background magnetic field is denoted by B_{10} while single-subscript variables such as B_1 indicate perturbed wave quantities, the wave compressional magnetic field in this case. Multiplying Equation (6.2) by $h_2 B_{10}$ and combining the result with Equation (6.1), provides the wave equation describing the toroidal mode magnetic field,

$$\frac{\partial^2}{\partial t^2}(h_3 B_3) = \frac{1}{h_2^2}\frac{\partial}{\partial x_1}\left[\frac{V_A^2}{h_3^2}\frac{\partial}{\partial x_1}(h_3 B_3)\right] \tag{6.3}$$

Assuming free oscillations ($D = 0$), Equation (6.3) can be solved for the eigenfunction $S_n(x_1)$ by substituting the expression

$$h_3 B_3(x_1, t) \propto S_n(x_1)\exp(-i\omega_n t) \tag{6.4}$$

into Equation (6.3). To obtain the corresponding equations for the poloidal mode one simply makes the replacement $h_2 \rightarrow h_3$ and $h_3 \rightarrow h_2$ in Equation (6.1) and Equation (6.4). The procedure for deriving equations that apply in the driven oscillator case with $D \propto \sin(\omega_0 t - m\phi)$ proceeds as described in *Rankin et al.* [1994, 1999].

Figure 6.1 shows electric and magnetic field profiles of a fundamental mode poloidal wave on an $L = 5.7$ dipole field line in the inner magnetosphere. Wave parameters are chosen to match the observations discussed in Section 6.3; the azimuthal wave number is set to $|m| = 35$ (westward propagation) and the wave frequency $f = 10$ mHz. The eigenfrequency on the dipolar geomagnetic field line at $L = 5.7$ is controlled by the variation of the background mass density $\rho = \rho_{eq}(r/L)^{-6}$ along the field line. Here, $r = LR_E\cos^2\lambda$ is the geocentric radius of the field line, λ is colatitude, and ρ_{eq} is the equatorial mass density. To obtain the results shown in Figure 6.1, the wave amplitude is increased to the value indicated by setting the driver D in the model constant for a fixed time interval, and $D = 0$ thereafter.

The bottom-left panel in Figure 6.1 shows the profile of the azimuthal electric field at its maximal value over a wave period. Local maxima occur at positions off the equator due to the curvilinear geometry and Alfvén speed variation along field lines. In the top-left panel the wave compressional magnetic field component B_1 is in phase with the electric field. As B_1 is proportional to dS_n/dx_1 this component is non-zero at the equator. For the given parameters, the amplitude of B_1 is less than 5 nT within $\pm 20^\circ$ latitude with respect to the equator. In passing, note that in the case of the toroidal mode in a dipole field, a non-zero compressional component also exists, except in the limit $m \to 0$. The right-panels in Figure 6.1 show wave fields one quarter-period later when the poloidal mode wave magnetic field component B_2 is at its maximum value and the azimuthal electric field E_3 is instantaneously zero.

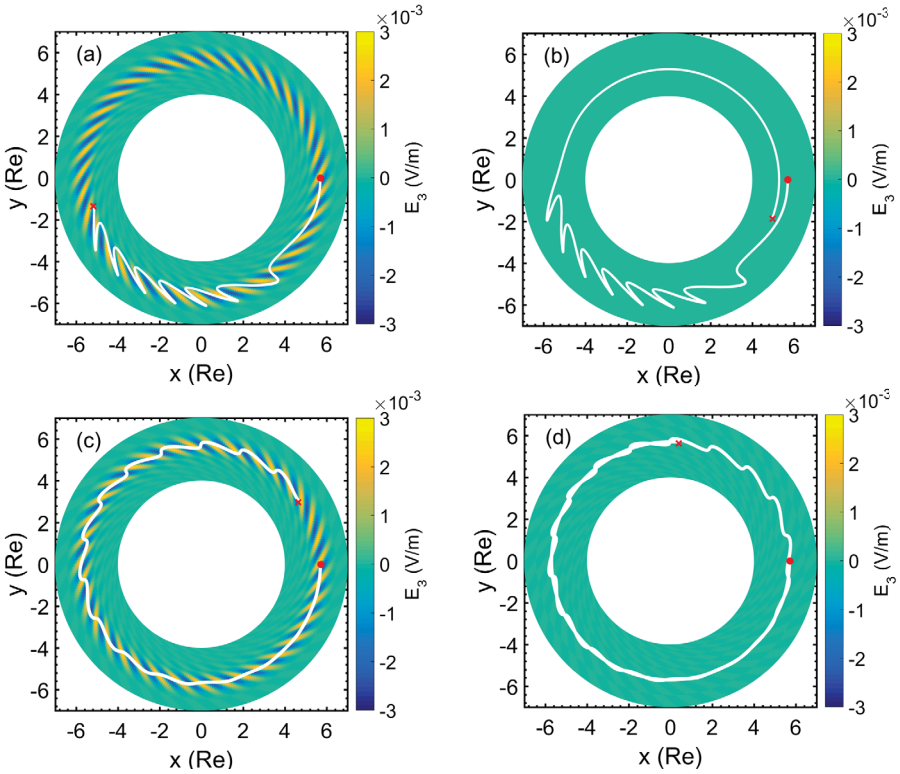

Figure 6.2: The left panels show the trajectories of (a) 130 keV and (c) 260 keV H^+ ions superimposed on snapshots of the poloidal mode electric field at the instant of time where the wave amplitude is just about to decay (at $t = 1500$s). The dot and cross on each panel denote the start and end-points of the trajectory. The right panels show subsequent trajectories during the decaying part to the wave (at $t = 2500$s). Note the different amplitude of the electric field in the left and right panels. Wave parameters are as in Figure 6.1.

6.3 Single Particle Dynamics in ULF Wave Fields

The interaction between poloidal mode waves and a specified background ion distribution function is discussed in detail in Section 6.5. Here, it is instructive to compare single particle trajectories of equatorially mirroring ions of different energy.

Figure 6.2 shows two trajectories of 90° PA H^+ ions of energy 130 keV (see panels (a) and (b)) and 260 keV (see panels (c) and (d)). The 130 keV ion has an energy satisfying the drift-resonance condition for an $L = 5.7$ field line, with $|m| = 35$ and $f = 10$ mHz. Ion trajectories are overlaid with snapshots of the wave azimuthal electric field in the equatorial plane at $t = 1500$ s (see panels (a) and (c)), and at $t = 2500$ s when the wave has decayed appreciably (see panels (b) and (d)). The wave amplitude grows linearly for 800 s and then remains constant for 700 s before decaying by $t = 2500$ s. From Figure 6.2 it is evident that orbits of ions satisfying the drift-resonance condition (see panels (a) and (b)) are more perturbed than for non-resonant ions (see panels (c) and (d)).

Figure 6.3a-b shows trajectory parameters for the resonant and non-resonant H^+ ions illustrated in Figure 6.2. The particle radial position L, change in energy, first adiabatic invariant $\mu = mv_\perp^2/2B_{10}$, azimuthal electric field E_3, and $\mathbf{E}\times\mathbf{B}$ drift velocity experienced by each particle along its trajectory is plotted. The top two panels in each column of Figure 6.3 show that ions move inward and outward across L-shells in response to periodic acceleration and deceleration by the wave. The changes in L, energy, and μ are largest for resonant ions (compare the left and right panel trajectories in Figure 6.3).

An important consideration not previously reported is that resonant ions become deeply trapped in an effective moving potential well after the wave amplitude has increased sufficiently (cf. Figure 6.2a-b and the top-left panel in Figure 6.3). When the wave has decayed appreciably, ions that were trapped in the wave potential move along an unperturbed final drift path that depends on their radial position at the point where the wave has dropped to sufficiently small amplitude. The middle panels of Figure 6.3 show that during the elapsed time of 2500 s, the maximum variation in the first adiabatic invariant is less than five percent for resonant ions and significantly

smaller for non-resonant ions of twice the energy.

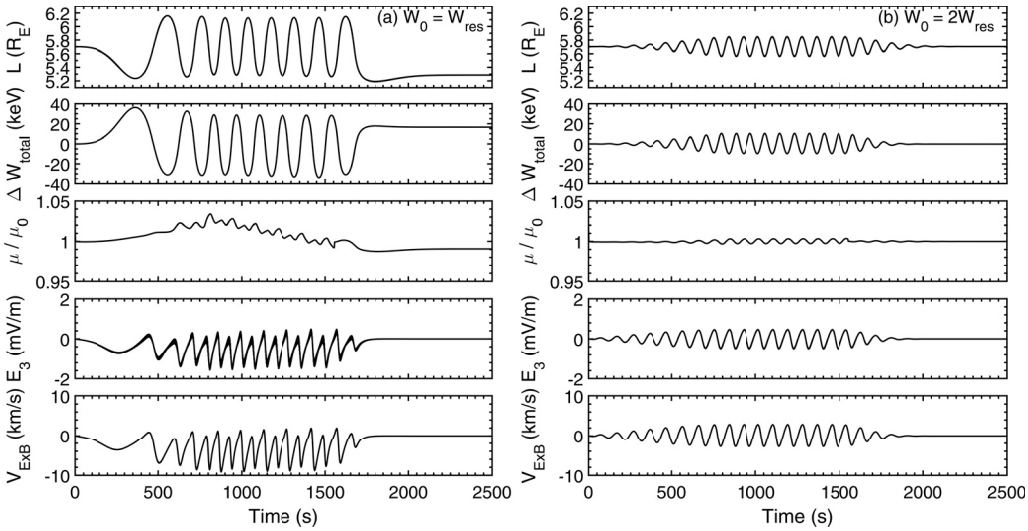

Figure 6.3: The panels on the left and right columns show the L-shell, change in energy, normalized magnetic moment, azimuthal electric field, and E×B drift velocity for H^+ ions with energy equal to (a) the drift resonance energy, 130 keV and (b) twice the drift-resonance energy, 260 keV. Wave parameters are defined in the caption of Figure 6.1.

6.4 Van Allen Probes and Ground-based Observation of Pgs Event

Giant pulsations were observed by the RBSP-A spacecraft on October 6, 2012 during a period of relatively low geomagnetic activity, $Dst = -14$ nT, $Kp = 2^+$. When the spacecraft was in the vicinity of the equatorial magnetosphere toroidal and poloidal mode electric field perturbations were detected, with the toroidal component lasting for about 20 minutes longer than the poloidal mode [*Takahashi et al.*, 2016]. Time series of the electric and magnetic fields are shown in Figure 6.4 in a mean field aligned coordinate system [*Takahashi et al.*, 1990]. In the second panel of Figure 6.4, the poloidal electric field $E\phi$ increases to $\sim$ 4 mV/m between 14:10-14:20 UT before slowly decaying. The amplitude drops below 1mV/m at around 14:40 UT. The toroidal electric field E_r in the top panel of the Figure 6.4 has a smaller amplitude than the poloidal component, on the order of 2 mV/m, but is present between $\sim$14:15-15:00 UT, i.e., until 20 minutes after the poloidal mode has decayed. The suggestion

of a slight delay in the growth of E_r and its persistence after E_ϕ has decayed is discussed briefly below. The RBSP-B spacecraft did not observe signatures of ULF wave activity as it was far to the east of RBSP-A. That the Pgs observed on October 6 are fundamental mode ULF waves is confirmed by the small values of the near-equatorial wave magnetic field components in the last three panels of Figure 6.4.

The ground track of RBSP-A traced using the Tsyganenko T89c magnetic field model is shown in Figure 6.5, along with locations of ground magnetometer sites in northern Canada. The MCMU (Fort McMurray) station is nearly conjugate to RBSP-A during the observation period, which explains why it measured the clearest wave signatures.

In Figure 6.6, wavelet analysis of the toroidal (H-component, top panel) and poloidal (D-component, bottom panel) mode ground magnetic field perturbations at MCMU show features similar to the in-situ data, i.e., both components have essentially the same frequency, $f \sim 10$ mHz, and the poloidal mode appears slightly before the toroidal component. The H-component spectra are slightly weaker after 14:40 UT in comparison to the D-component, but in contrast to the satellite data both components are present during the interval from 14:40-15:00 UT. Note that GILL (Gillam) station in Figure 6.5 is eastward of the MCMU station and at approximately the same latitude. The wavelet spectra at GILL (not shown) is similar to MCMU although the H-component is more variable. That being said, the H and D component ground magnetic field data show no clear evidence of strong wave decay after 14:40 UT. A possible explanation is that the decay of the poloidal electric field after 14:40 UT is a mixture of spatial and temporal effects affected by spacecraft motion across a structure localized to a narrow range of L. The D-component time series at MCMU and GILL shown in Figure 6.7 are also continuous after 14:40 UT, which further suggests decay of the poloidal mode observed by RBSP-A is not exclusively temporal decay. Spatial localization in L-shell and spacecraft motion may also explain why the RBSP-A ion flux oscillations are observed after the E_ϕ component drops below 1 mV/m. Another possible explanation is that the observed ions are energized at a different location and transported to the location of RBSP-A. The top-left panel of Figure 6.3 provides an illustration of how this might occur.

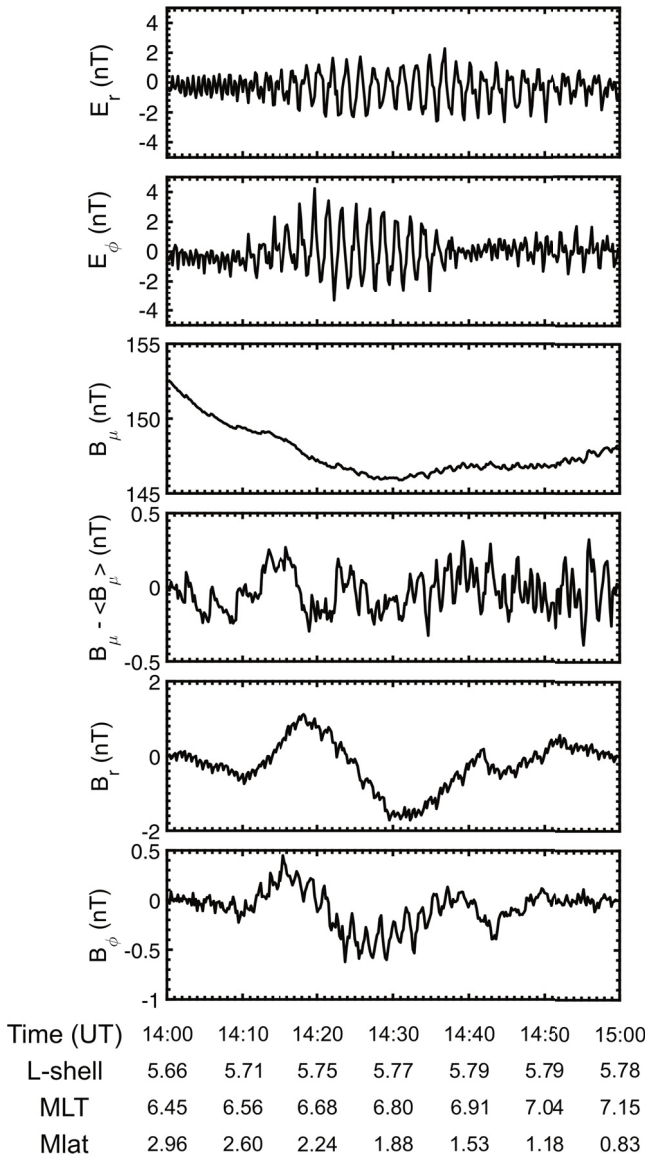

Figure 6.4: The top two panels show toroidal (E_r) and poloidal (E_ϕ) electric fields from the EFW instrument on RBSP-A. The third panel is the total parallel magnetic field (B_μ). A 5 min average of B_μ is subtracted to obtain the fourth panel. The bottom two panels show the magnetic field components for the poloidal (B_r) and toroidal (B_ϕ) modes. The magnetic fields are obtained from the FGM instrument on the spacecraft.

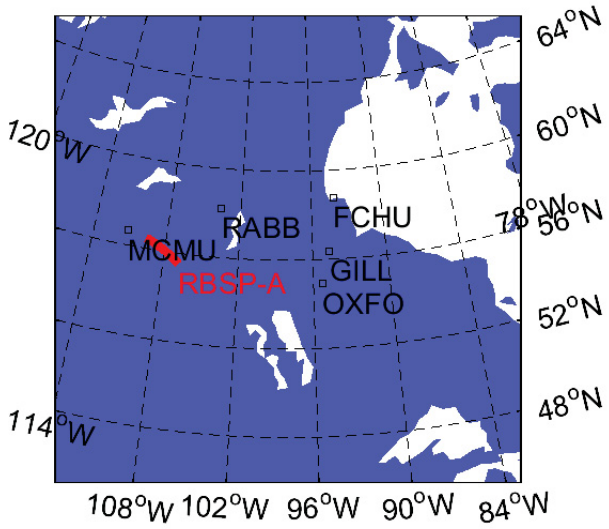

Figure 6.5: RBSP-A ground track from 14:00-15:00 UT on October 6, 2012. The locations of CARISMA ground magnetometer stations are also indicated. Geographic coordinates are used. The station nearest the magnetic foot-point is MCMU.

Differential fluxes of 35° PA ions measured by the MagEIS instrument on RBSP-A are shown in Figure 6.8. The $\sim$ 100 s period of the modulations matches the periodicity of Pgs observed in-situ and on the ground. The differential flux at 90° PA (not shown) contains no obvious evidence of modulations. A visual inspection of Figure 6.8 reveals that differential flux modulations at 35° PA have their maximum amplitude at an energy of about 150 keV, and cover the energy range of $\sim 88 - 191$ keV. There is also a phase change of 180° across this range of energy, which is consistent with a resonant wave-particle interaction process. It is easily confirmed that ions of energy 150 keV and 35° PA satisfy the condition $\omega - m\omega_d = N\omega_b$ for $|m| = 35$, $\omega = 2\pi \times 10$ mHz, $L = 5.7$, and $N = 0$. The flux oscillations clearly correspond to drift resonance.

The observed decay of the poloidal mode after 14:40 UT at the location of RBSP-A, together with the apparent persistence of the signal detected on the ground, is an interesting feature that deserves further analysis. However, as the numerical results presented in the paper are not significantly affected by the uncertainty in the duration of the signal, this aspect is considered to be outside the scope of this thesis. Section 6.5 describes the results of test particle simulations using the ULF wave models described

in Section 6.2. The model is constrained using information from the in-situ electric field and ground magnetic field observations in order to reproduce the differential flux oscillations observed by RBSP-A.

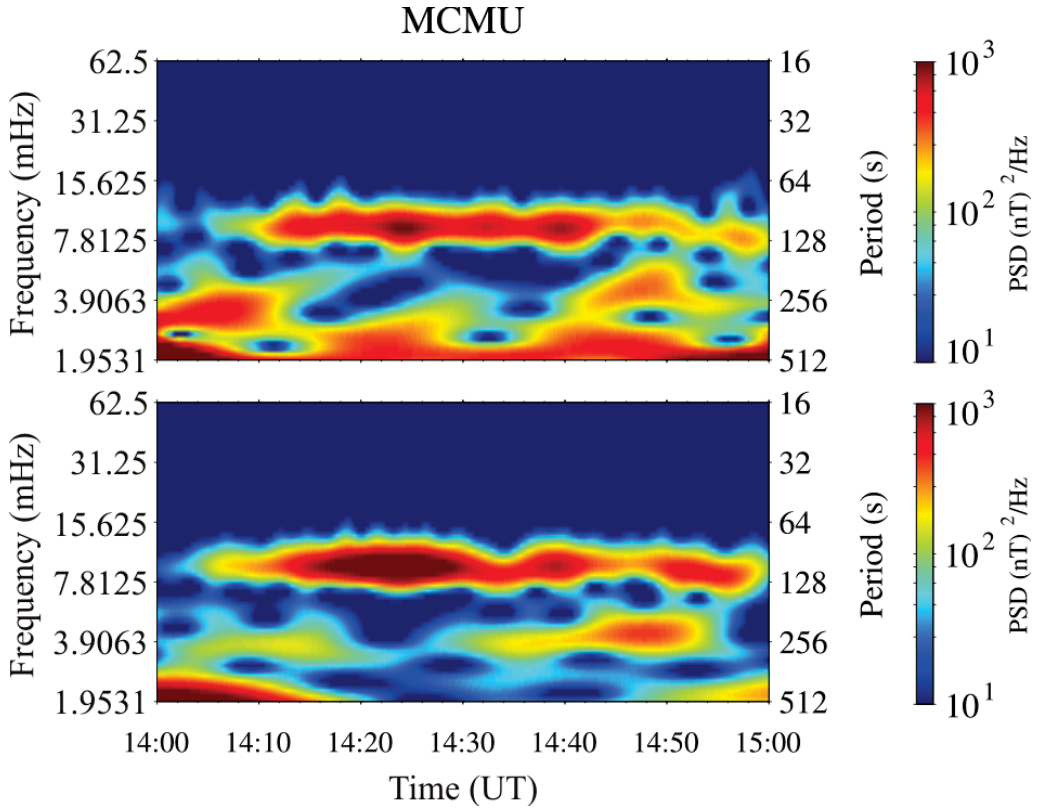

Figure 6.6: Wavelet analysis of the MCMU ground magnetometer data between 14:00-15:00 UT on October 6, 2012. The top and bottom panels show the toroidal (H-component) and poloidal (D-component) magnetic field perturbations, respectively.

6.5 Simulation of Van Allen Probes Differential Flux Modulations

In drift bounce resonance theory, an estimation of the first-order energy change of resonant particles is made under the assumption that the particle L-shell is constant and the energy change is small. Here, we compute ion differential fluxes by using a full Lorentz force test particle code to evolve the distribution function of H^+ ions in ULF wave fields that are solutions to the equations introduced in Section 6.2. The compressional wave field B_1 is included to ensure conservation of the first adiabatic

invariant μ. Note that guiding-center test particle calculations conserve μ regardless of whether the compressional wave field is included. Excluding this field component in a guiding center formalism may, however, lead to different results.

Backward-in-time test particle simulation is used for the event study of interest. A phase space grid is defined in energy and PA at a point in configuration space, and the test particle code is used to trace virtual particles backward to a time before waves are present. For each phase space cell defined at a selected sampling point, initial conditions in the past are chosen for each virtual particle such that it lies in the equatorial plane. Liouville's theorem is then used to map the distribution function defined by virtual particles forward in time to the observation point. The distribution function is assumed to be gyro-phase independent in order to avoid using a 3D phase space grid.

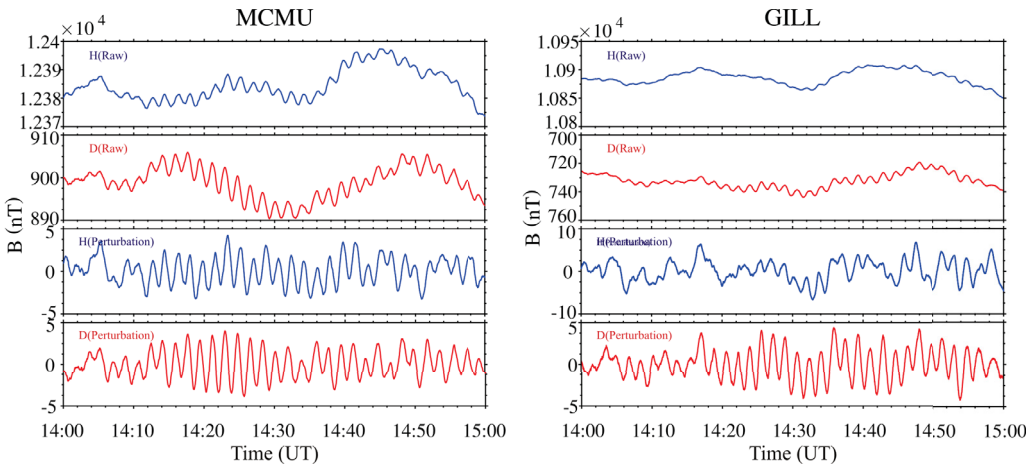

Figure 6.7: Time series of the MCMU and GILL ground magnetometer data between 14:00-15:00 UT on October 6, 2012. In each column, the top two panels show the raw data and the bottom two panels show the toroidal (H-component) and poloidal (D-component) magnetic field perturbations, respectively.

The wave amplitude variation with time in the October 6, 2012 event is controlled by the amplitude of the driver D in the wave model, cf. Equation (6.2). The amplitude variation is divided into three stages (i) linear growth with time for eight wave periods (ii) constant amplitude at around 4 mV/m for seven wave periods (iii) exponential decay to below 1 mV/m over four wave periods. The other wave parameters needed are the azimuthal wave number and wave frequency, for which we take $|m| = 35$

and $f = 10$ mHz. The observation point is selected to be on the equatorial plane at $L = 5.7$ where the largest electric field strength (across L) occurs.

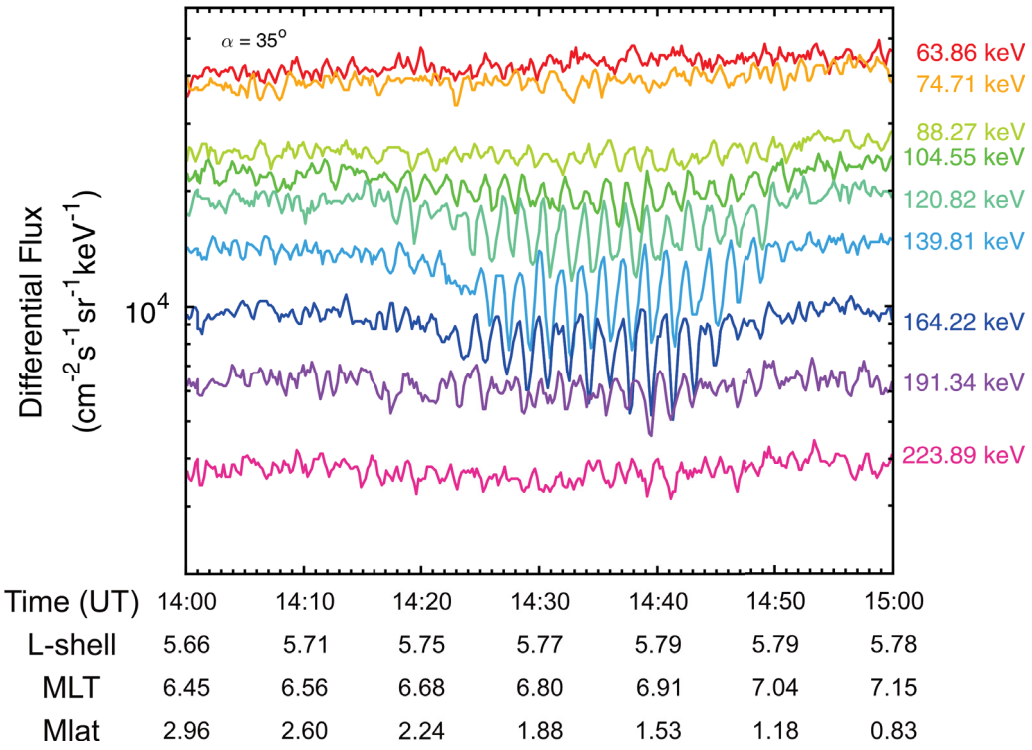

Figure 6.8: Differential ion flux observed by the Van Allen Probe A satellite from 14:00-15:00 UT on October 6, 2012.

Phase space density (PSD) gradients are included in the simulations but temperature anisotropy is omitted. An initial Maxwellian distribution function f_d is specified that has a specified dependency on L. The ambient temperature of the H^+ plasma is obtained from the RBSP-A measured differential flux $F = f_d W/2m_p$ and the expression $\ln f_d = W/T + \ln f_{d0}$ where W and m_p are the proton energy and mass, respectively, and $\ln f_{d0}$ is a constant. Figure 6.9 shows a time average of f_d between 14:30-14:50 UT for two pitch angles and energy bins covered by the MagEIS instrument on RBSP-A. The linear fit indicated by the solid lines in the figure gives $T_i \sim 34 - 41$ keV, with the latter value used in test particle simulations of the event for simplicity.

Figure 6.10 shows simulation results obtained from the test particle and ULF wave model described in Section 6.2. The azimuthal electric field in the upper panels of the figure reaches a maximum amplitude of ~ 4 mV/m in the equatorial plane.

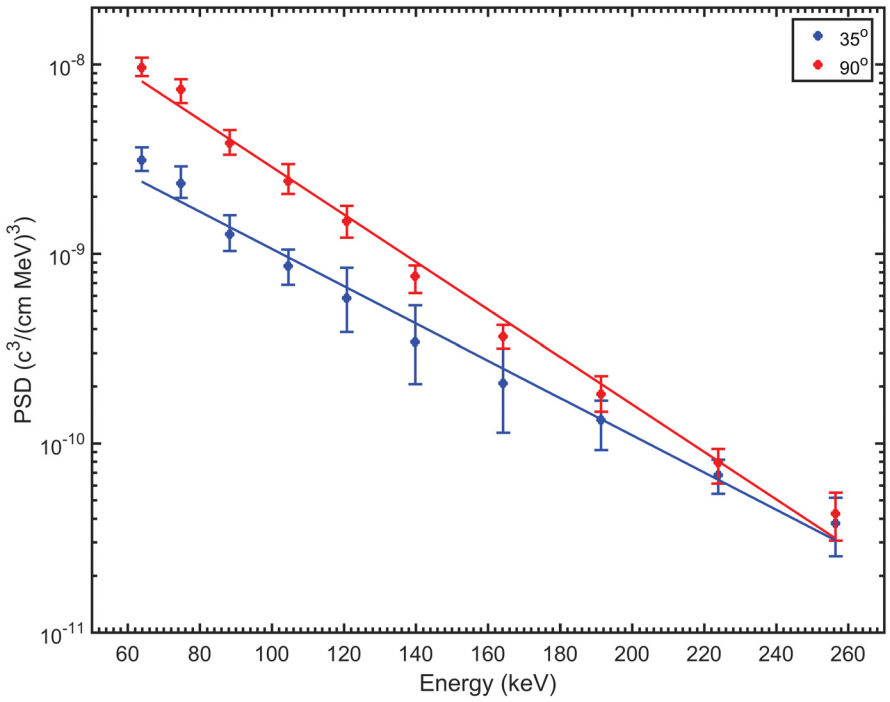

Figure 6.9: Time averaged phase space density from 14:30-14:50 UT for energy channels ranging from 63.86 keV to 256 keV. Red circles are measured MagEIS values in 35°. Blue squares show measured MagEIS values in 90°. The red and blue lines are obtained from linear regression of 35° and 90° results, respectively.

The results shown are for a wave with a spatial extent across L that was estimated from the H and D ground-component magnetic field data. Specifically, we use the fact that RABB indicated on Figure 6.5 is poleward of the MCMU station at which the ULF wave signal is most pronounced. As the ULF waves recorded at RABB are weak, while those at MCMU and GILL (further to the east and at approximately the same latitude) are strong and similar in magnitude, we use the latitudinal separation of RABB and MCMU as an estimate of the resonance width. Mapping the magnetic footprint of these stations to L-shells in the equatorial plane in a dipole field gives $\Delta L_{eq} \sim 0.5$, i.e., at approximately the location of RBSP-A. To limit the L-shell extent of waves in the simulations, phase mixing to a scale less than ΔL_{eq} is prevented. This also has the effect of limiting the energy range over which flux modulations are significant. In this manner, the simulation is tailored to predict the energy range of flux oscillations based on measured wave properties sampled by (in this case) ground stations closely spaced in latitude and extended in longitude.

Panels (b) and (c) in the left column of Figure 6.10 show the residual flux [*Claudepierre et al.*, 2013] of ions of given PA as a function of their observed energy and time. The flux is slightly larger at 35° PA than at 90° and is spread over a broader energy range. The dashed horizontal lines in the figure show drift-resonance energies computed from the expression $\omega = m\omega_d$. The initial PSD has no variation with L in this case. In the right column of Figure 6.10, panels (b) and (c) show line traces of differential particle flux for the same pitch angles. Values on the figure are averages across the energy range of each channel of the MagEIS instrument on RBSP-A. The amplitudes of the flux oscillations are largest at energies between 120.82-139 keV and 139.81-164.22 keV , and corresponding pitch angles of $\sim 90°$ and $\sim 35°$, respectively. These resonant energies are in agreement with measured values on RBSP-A and drift-resonance theory. The phase difference across the flux modulations is close to 180° and is consistent with observed values in Figure 6.8.

Comparing the amplitudes of flux oscillations at 35° and 90° pitch angle in the right column of Figure 6.10, it can be seen that ions are modulated more strongly at 35° than at 90°, although the relative differences are small. It is tempting to associate this behavior with there being a stronger electric field at higher latitude, cf. Figure

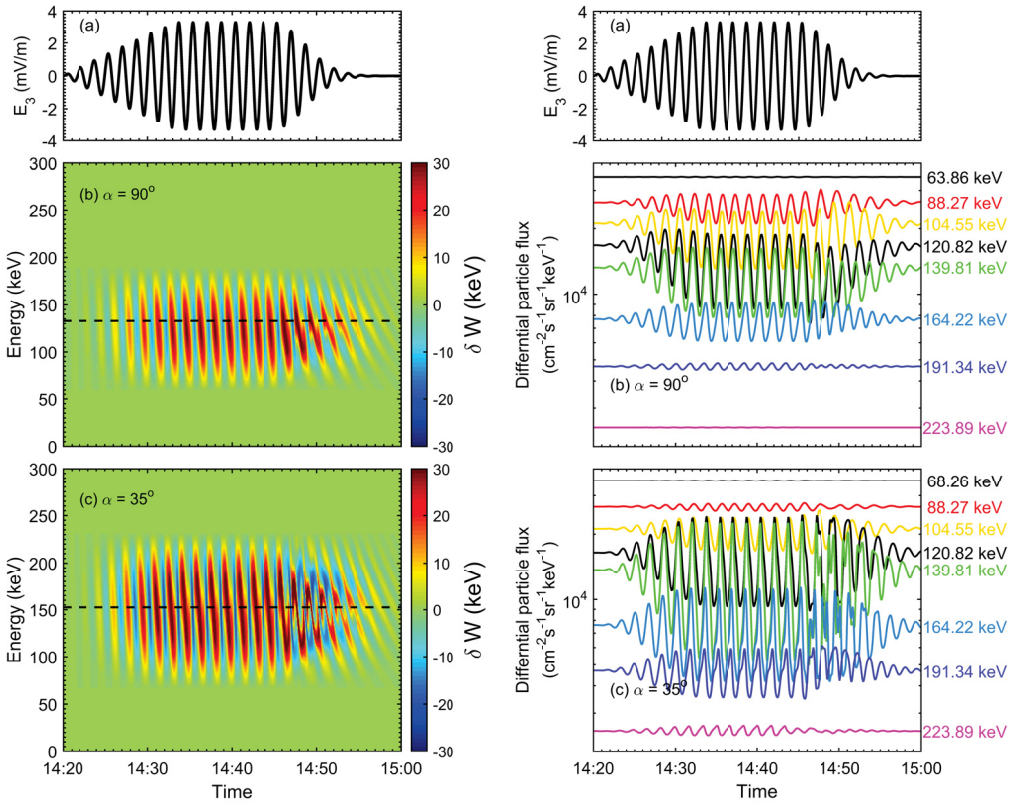

Figure 6.10: The panels labeled (a) show the wave amplitude profile used in simulations. In the left column, panels (b) and (c) show the residual flux experienced by H^+ ions as a function of their measured energy and time. The right column panels (b) and (c) show corresponding differential fluxes for energies binned in the same manner as the MagEIS detector on the Van Allen Probes spacecraft.

6.1c. According to *Southwood and Kivelson* [1981, 1982], the mean energy variation of a particle is proportional to its drift velocity and the electric field along its trajectory. However, for fundamental mode poloidal mode waves, the variation in the electric field magnitude with latitude is small, and the dominating effect is the pitch angle dependence of the resonance energy, as discussed below.

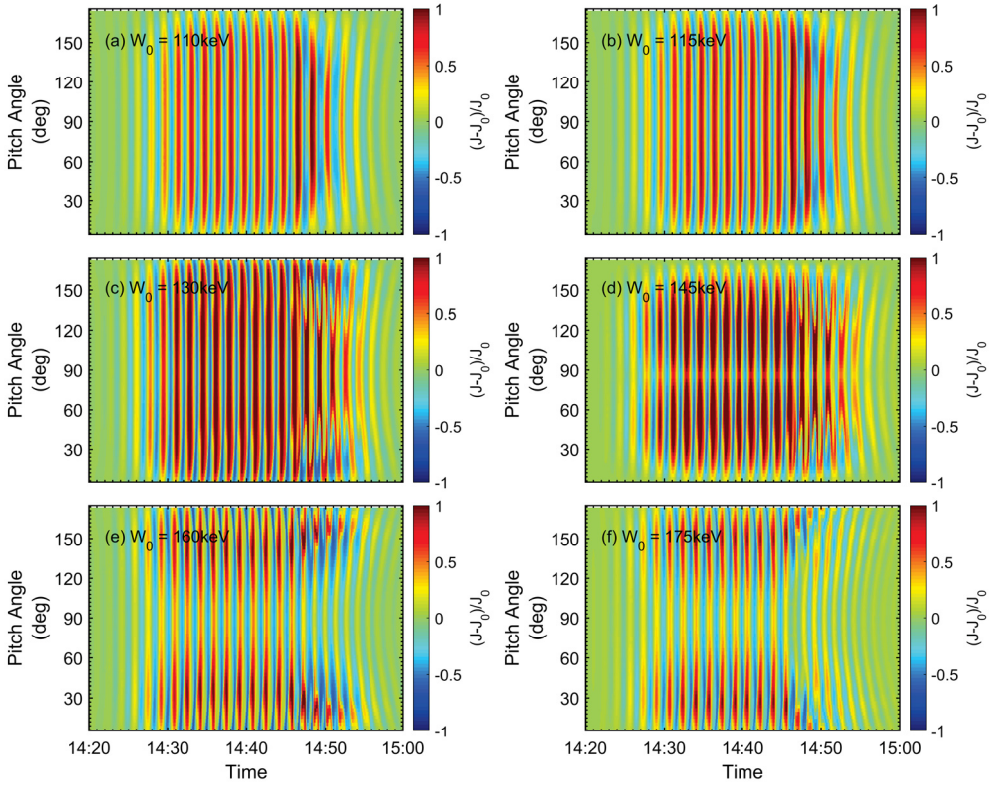

Figure 6.11: Residual particle flux as a function of pitch angle and time for ions of different energy (a) 110 keV, (b) 115 keV, (c) 130 keV, (d) 145 keV, (e) 160 keV, (f) 175 keV. The resonance energy is in the neighbourhood of 130 keV.

Figure 6.11 displays residual differential particle flux as a function of pitch angle and time for ions of various energies. In Figure 6.11, panels (d)-(f), the maximum in the flux occurs at a pitch angle and energy for which the drift resonance condition $\omega = m\omega_d$ is satisfied. In panels (a)-(c) of Figure 6.11, the flux gradually diminishes for energies below the resonance energy because the drift-resonance condition becomes increasingly more difficult to satisfy. The "boomerang" shape of the pitch angle

distributions after 14:45 UT in Figure 6.11 appears during the decaying phase of the wave. These ions stream freely and undergo energy dispersion at a rate that depends on their final velocity and pitch angle [*Hao et al.*, 2017].

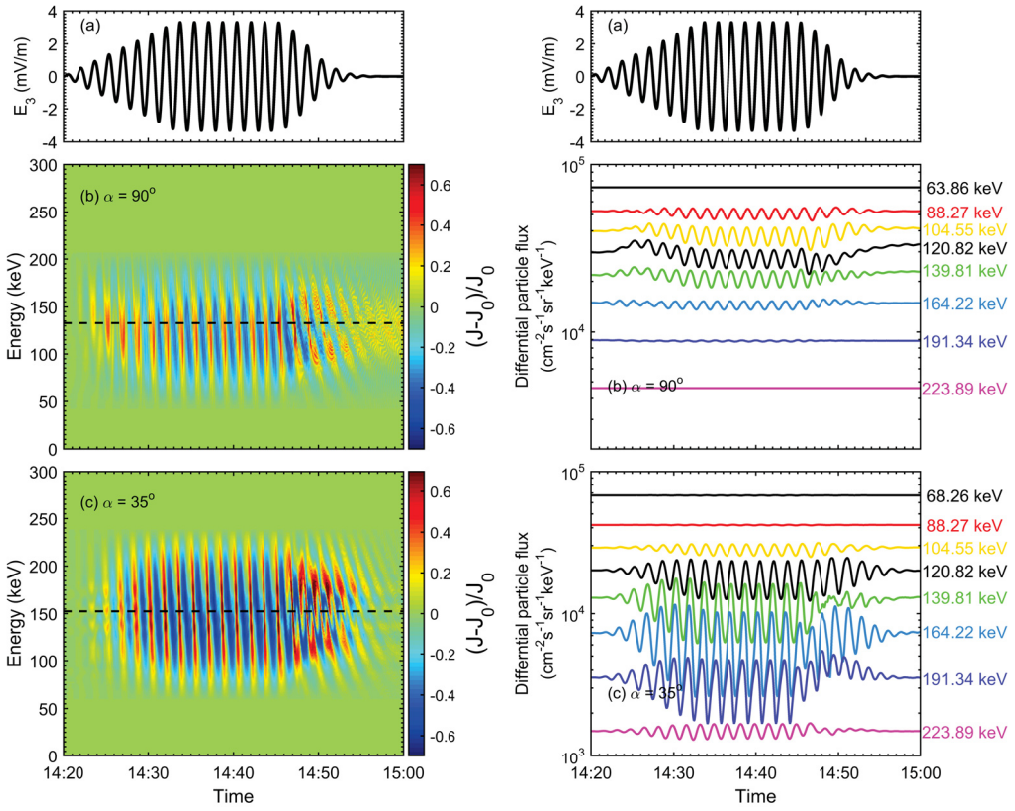

Figure 6.12: The residual particle fluxes and corresponding binned differential fluxes variation, with additional L-shell dependence of L-shell $f \propto L^{-3}$, as functions of their measured energy. The panels are arranged in a similar format as Figure 6.10.

An obvious question is why the observed differential flux modulation at 90° pitch angle has smaller amplitude than that at 35° pitch angle. A possible explanation is that PSD gradients are responsible. Figure 6.12 shows results of test particle simulations in the same format as Figure 6.10, except that the initial PSD has an imposed L-shell dependence of the form $f_d = f_0 L^{-s}$. It is immediately obvious that the residual flux at 90° pitch angle is much reduced in comparison to Figure 6.10, whereas the flux at 35° pitch angle is relatively unchanged. Figure 6.13 shows the pitch angle distribution for this case, which can be compared with Figure 11. PSD

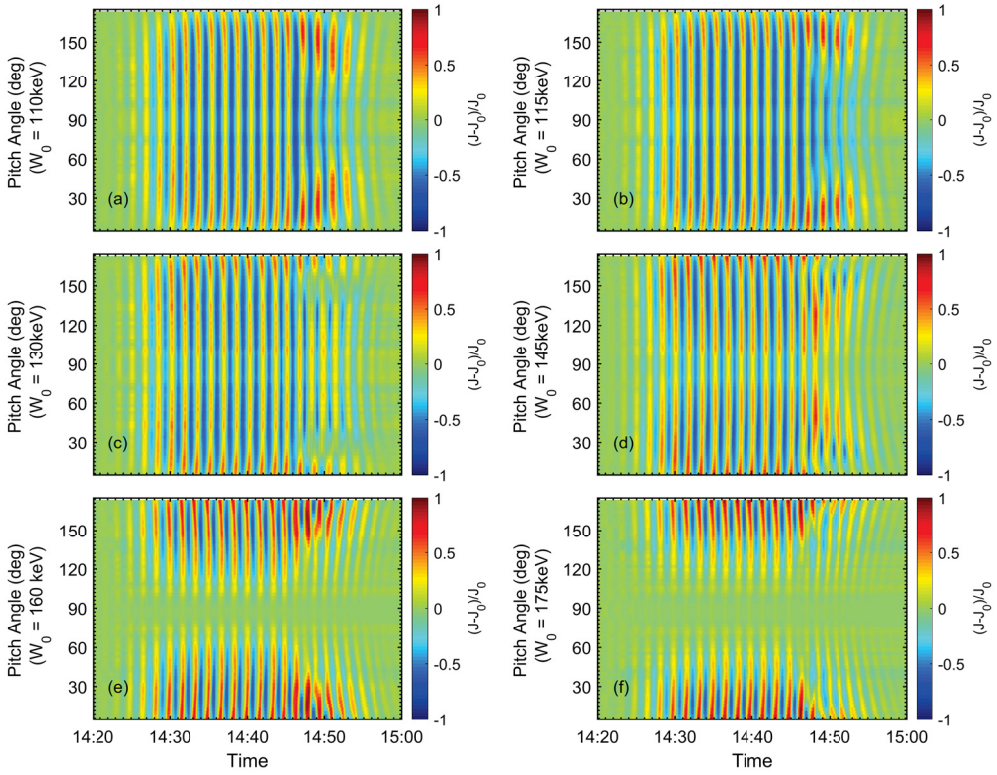

Figure 6.13: Residual particle flux as a function of pitch angle and time for ions of different energies. The panels are arranged in a similar format as Figure 6.11. In this figure, additional L-shell dependence of L-shell $f \propto L^{-3}$ is added.

as a function of L for energies matching the MagEIS instrument is shown in Figure 6.15. The left column panels have no explicit PSD gradient, $s = 0$, corresponding to results shown in Figures 6.10 and 6.11, whereas the right column panels are for $s = -3$, matching results shown in Figures 6.12 and 6.13. The effect of the L^{-3} spatial dependence is to change positive gradients visible in Figure 6.14a,c into negative gradients, Figure 6.14b,d. At 90° pitch angle, Figure 6.14b, the PSD has a nearly flat profile at the location of the wave at almost all energies, which explains why the flux is not significantly enhanced. The gradients at the wave location for ions of 35° pitch angle in Figure 6.14d are negative (cf. panels c and d of Figure 6.13) and consequently the flux in this range of pitch angles is not appreciably different.

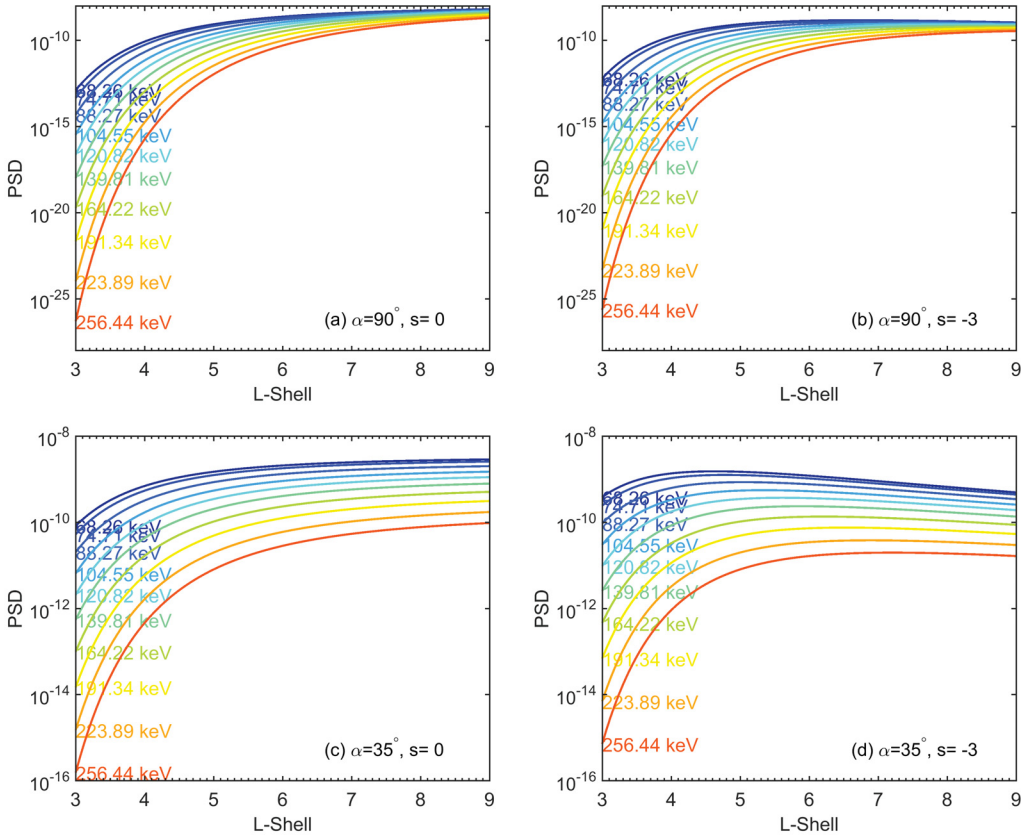

Figure 6.14: PSD distribution of first adiabatic μ conserved particles as functions of L-shell. Energies at the left axis indicate the energies at $L = 5.7$, centers of energy bins of MagEIS. (a) Pitch angle $\alpha = 90°$, without L-dependence. (b) Pitch angle $\alpha = 90°$, $PSD \propto L^{-3}$. (c) Pitch angle $\alpha = 35°$, without L-dependence. (d) Pitch angle $\alpha = 35°$, $PSD \propto L^{-3}$.

It is of interest to notice that the pitch angle distributions in Figure 6.11 and

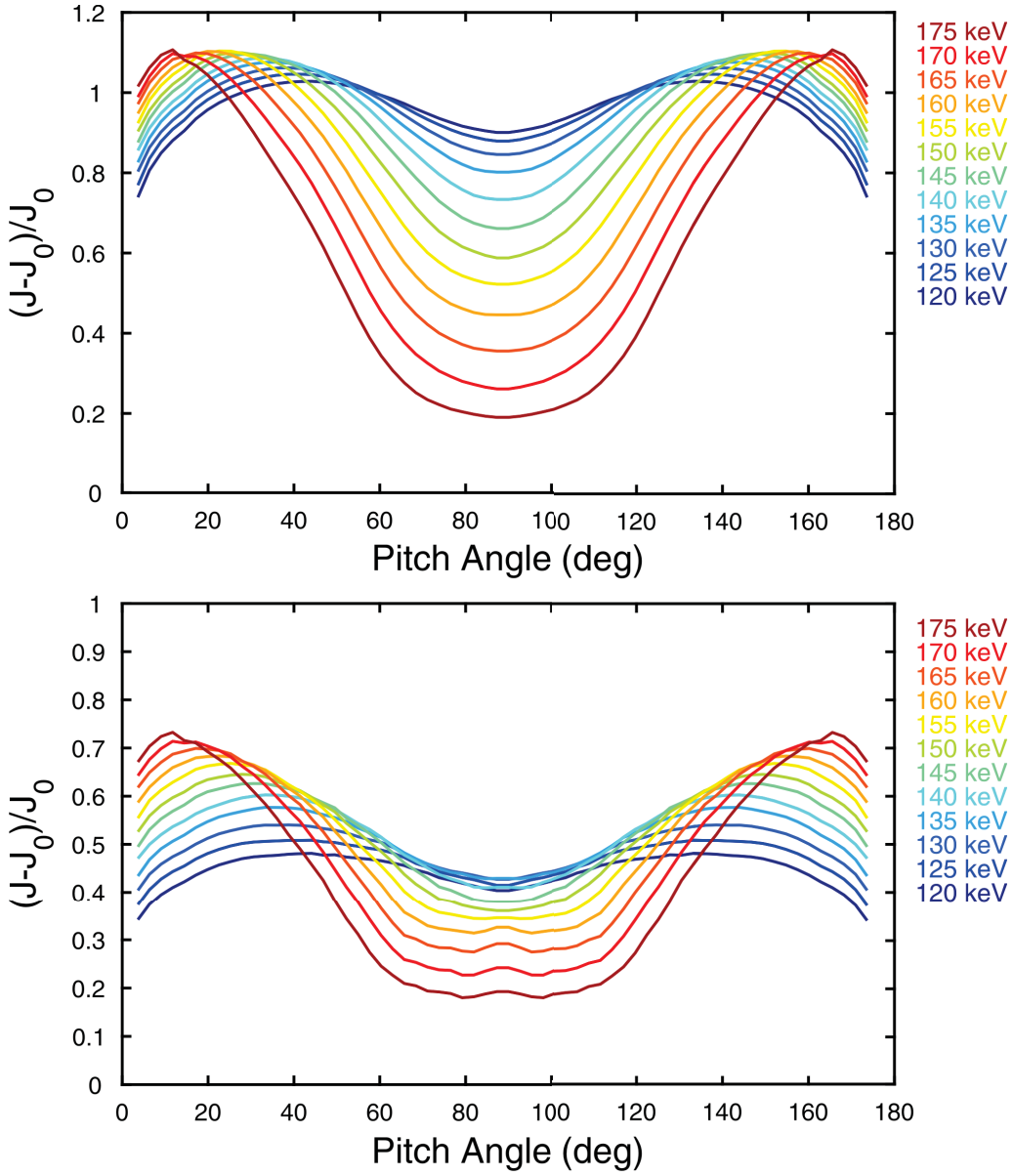

Figure 6.15: Residual flux at 14:40UT (cf. Figure 6.11) as a function of pitch angle and for different energies. The energy bin size is 10 keV. In the upper panel, PSD is independent of L-shell. In lower panel, PSD is proportional to L^{-3}.

Figure 6.13 have a butterfly appearance similar to distribution functions produced by VLF waves [*Lyons et al.*, 1972]. Ions with pitch angles in the vicinity of 90° move increasingly out of resonance at lower energies while at higher energies and increasingly field-aligned pitch angles the resonance condition is more easily satisfied. Figure 6.15 shows the residual flux of ions as a function of pitch angle at the virtual satellite position at 14:40 UT. The top panel corresponds to Figure 6.11 and the bottom panel to Figure 6.13. Each coloured line on the figures corresponds to the energy indicated in the legend, and illustrates that high energy particles are able to satisfy the resonance condition at small and large pitch angles, while lower energy particles move out of resonance. Interestingly, the largest energy change of particles occurs in a pitch angle range $\alpha_m \sim 20 - 40°$ and $180° - \alpha_m$, respectively. This PA dependence is consistent with the RBSP-A observations.

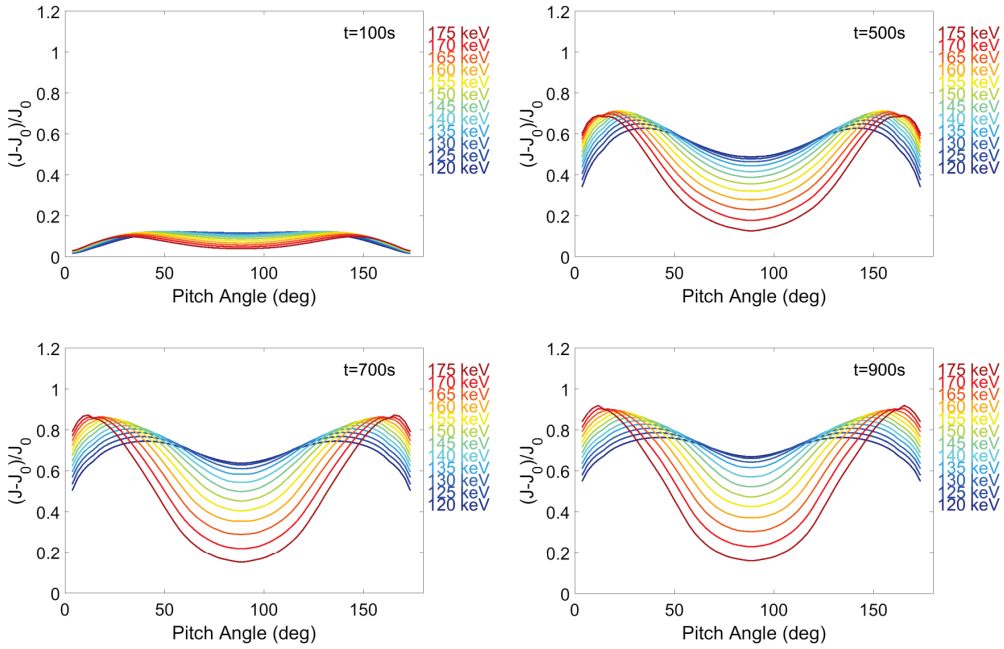

Figure 6.16: Residual flux as a function of pitch angle and for different energies at different time. Initial time $t = 0$ corresponds to 14:20UT. The energy bin size is 10 keV. In the upper panel, PSD is independent of L-shell in this figure. This figure is not in the paper submitted to *Journal of Geophysical Research: Space Physics*.

6.6 Conclusion

Test particle simulation is used to describe the dynamics of H^+ ions moving in electric and magnetic fields obtained from a simplified model of poloidal mode ULF waves. The simulations reveal phenomena not previously reported, such as the formation of a trapped population of drift-resonant ions over a range of L that depends on the strength and spatial extent of the electric field of the wave. Those particles satisfying the drift resonance condition $\omega = m\omega_d$ have trajectories that follow constant wave phase and move toward or away from Earth until they reach the low electric field region where their $\mathbf{E} \times \mathbf{B}$ drift decreases. They are then re-captured during the next period of the wave and periodically transported inward and outward by an amount that depends on the strength of the accelerating electric field. This corresponds to nonlinear particle trapping in a moving electric potential well.

The ULF wave and test-particle simulations presented in the paper reproduce several features of the pitch angle and energy spectrum of ion differential fluxes observed by the Van Allen Probes-A spacecraft on October 6, 2012. The observed and simulated flux is well correlated with giant pulsations of frequency $f \sim 10$ mHz and contains modulations in a narrow range of energy, with stronger enhancements occurring for non-equatorially mirroring particles. For ions of 35° pitch angle, a maximum in the differential flux occurs at an energy of $\sim$ 150 keV predicted by drift resonance theory. Simulations of the ULF wave event reproduce the observed behavior for poloidal mode wave parameters that are in general agreement with the data analysis presented by *Takahashi et al.* [2016]. The lack of enhanced differential fluxes of particles near 90° pitch angle can be explained by the dependence of the resonance energy on pitch angle.

In conclusion, the results presented in this chapter provide a verification of drift-bounce resonance theory, and demonstrate that satellite observations of particle acceleration in Earth's inner magnetosphere can be understood using relatively simple models.

Chapter 7

Test Particle Simulations of Drift and Drift-bounce resonances with Electrons and O^+ Ions in Earth's Outer Radiation Belt

As a complement to the studies on the drift resonances of H^+ ions in the previous chapters, the drift resonances of energetic electrons and the drift/drift-bounce resonance of O^+ in the earth's outer radiation belt have been studied in this chapter with our models in Chapter 4 and Chapter 5. Charged particle acceleration and radial transport by ultra-low-frequency (ULF) waves in Earth's magnetosphere are investigated quantitatively by solving equations of motion for test particle electrons and ions in electric and magnetic fields of the waves. Characteristics of poloidal mode drift resonance are contrasted and compared with modulations in differential electron flux observed by the Van Allen Probes spacecraft on 31 October 2012, 15:30-16:00 UT following an interplanetary shock. Simulated fluxes have larger amplitudes and slower attenuation rates than observed fluxes due to the finite energy resolution of the MagEIS instrument on the spacecraft. When they are binned in energy as in the MagEIS instrument, they appear remarkably similar to the observed fluxes. Simulations of O^+ ions undergoing $N = 0$ drift resonance and $N = -2$ drift-bounce resonance provide insight into the dynamics of heavy ions that interact with ULF waves. These simulations illustrate the expected behavior of ring current energetic ion populations in a region where poloidal mode ULF waves are ubiquitous.

The work in this chapter have been submitted as C. Wang, R. Rankin, Y. Wang, Q.-G. Zong, X. Zhou, K. Takahashi, R. Marchand, A. F. Degeling, and D. Sydorenko "Ultra-low frequency wave-particle interactions in Earths outer radiation belt" in the American Geophysical Union Monograph on "Dayside Magnetospheric Interactions".

7.1 Introduction

It is established that various types of plasma waves exert control of energetic electron [*Zong et al.*, 2007, 2009] and ion [*Yang et al.*, 2010, 2011a; *Zong et al.*, 2011; *Ren et al.*, 2016] dynamics in Earth's radiation belts. Ultra-low-frequency (ULF) standing waves with frequencies in the Pc4-5 band (2-22 mHz) [*Dungey*, 1955] cause rapid order of magnitude changes in energetic particle fluxes over timescales of tens of minutes to a few hours [*Elkington et al.*, 1999; *Hudson et al.*, 2000]. ULF waves classified as toroidal [*Elkington et al.*, 1999], compressional [*Elkington et al.*, 2002, 2003, 2004; *Tan et al.*, 2011], and poloidal mode Alfvén waves are involved to varying extent [*Zong et al.*, 2009; *Zong et al.*, 2011, 2012a] . Compressional and poloidal mode Alfvén waves have greater influence on charged particle dynamics than the toroidal mode as they carry azimuthal electric fields that accelerate particles directly along their drift-bounce path. Resonant energy transfer is possible for ions and electrons moving at or near the wave phase velocity, i.e., westward and eastward in the wave frame, respectively. Gyroresonant interactions between energetic electrons and ELF (extremely low frequency) and VLF (very low frequency) chorus and hiss elements, respectively, are known to cause local acceleration and transport, as well as particle loss to the atmosphere via pitch angle diffusion. However, the relatively small amplitudes of these waves makes the rate of transport small in comparison to ULF waves, which have much larger amplitudes.

ULF waves are understood to be drivers of radial diffusion but can also produce radial transport through non-diffusive processes such as prompt acceleration [*Li et al.*, 1993]. Radial transport occurs when electrons and ions are in drift-resonance or drift-bounce resonance with ULF waves, with the poloidal and compressional modes providing more efficient energy transfer than the toroidal mode [*Zong et al.*, 2009;

Yang et al., 2011a,b; *Zong et al.*, 2012a]. Low-m compressional waves excited by solar wind disturbances are effective in the outer magnetosphere, while high-m poloidal waves excited by plasma instabilities, e.g., drift resonance, operate mainly in the inner magnetosphere. The importance of drift resonance as a mechanism for forming new radiation belts has been reported by *Wygant et al.* [1994] and *Zong et al.* [2011].

Sources of ULF waves in Earth's magnetosphere include solar wind dynamic pressure pulses [*Kepko and Spence*, 2003; *Hudson et al.*, 2004; *Takahashi and Ukhorskiy*, 2007; *Claudepierre et al.*, 2009, 2010], interplanetary shocks [*Claudepierre et al.*, 2013], Kelvin-Helmholtz (K-H) instabilities on the magnetopause [*Hudson et al.*, 2004; *Claudepierre et al.*, 2008], and internal plasma instabilities [*Takahashi et al.*, 2016]. Recently, *Claudepierre et al.* [2013] reported clear signatures of fundamental mode poloidal ULF waves and energetic electrons observed by the RBSP on October 31, 2012, 15:30-16:00 UT, following an interplanetary shock. This event provides an excellent opportunity to test predictions of drift resonance theory using the methodology described in Chapter 4 and Chapter 5. The electron differential flux in the event is perturbed in the energy range of $57 - 80$ keV where the resonance condition $\omega - m\omega_d = N\omega_b$ of *Southwood and Kivelson* [1981, 1982] is satisfied, and is modulated at the wave period. Here, ω is the wave frequency, m the azimuthal wave number, $N = 0$ the order of the resonance, ω_d the drift angular speed, and ω_b the bounce angular frequency.

The drift-bounce resonance theory of *Southwood and Kivelson* [1981, 1982] accounts for waves that grow slowly without limit over an indefinite amount of time. To describe how differential flux modulations evolve during the growth and decay stages of ULF waves the theory was modified by *Zhou et al.* [2016]. However, the original and modified theory account only for first-order changes in the distribution function as they assume particles follow unperturbed trajectories and the energy change is small. Arbitrary variations in L and particle energy are accounted for in our studies by solving equations of motion for electrons and ions in ULF wave fields without apriori use of the resonant condition. Section 7.3 presents results using this approach that are in good agreement with observations. Although MeV electrons are not registered in the *Claudepierre et al.* [2013] event, the observation facilitates quantitative

analysis of wave-particle interactions that form one of the primary goals of the RBSP mission. *Southwood and Kivelson* [1981, 1982] evaluate the effect of sensor bandwidth and phase mixing on the detection of signatures of drift resonance in the magnetosphere. Here, simulations are used to quantify phase mixing within MagEIS energy channels by averaging particle fluxes in energy bins similar to the RBSP.

Test particle simulations of drift resonance between equatorially mirroring electrons and Pc5 waves have been reported by *Degeling et al.* [2007, 2010, 2014]. Their simulations describe low-m compressional waves excited by a source placed in the vicinity of the noon magnetopause. Coupling between compressional waves and toroidal mode field line resonances in the outer magnetosphere is included and leads to radial peaks in electron phase space density [*Degeling et al.*, 2008; *Degeling and Rankin*, 2008], and both radial diffusion and local acceleration [*Degeling et al.*, 2011].

In the studies presented in this chapter, we consider high-m poloidal modes that are more characteristic of the inner magnetosphere. Section 7.2 describes the test particle and ULF wave models used to study the dynamics of electrons and ions. Section 7.3 presents results of guiding-center test particle simulations of ULF wave electron dynamics and their comparison with RBSP observations during the 31 October, 2012 event. Full Lorentz force test particle simulations of O^+ undergoing $N = 0$ drift resonance and $N = -2$ drift-bounce resonance are presented in Section 7.4. Section 7.5 provides a discussion of our results and conclusions.

7.2 ULF Wave and Test Particle Models

To calculate distribution functions in fields of ULF waves, we use a test particle model with guiding-center and full Lorentz force options, and a simplified model for driven poloidal mode ULF waves [*Wang et al.*, 2018] excited by a monochromatic source of frequency ω_0. The electric and magnetic perturbations of poloidal mode are described by Equations (4.57)-(4.59) in Chapter 4. On the resonant L-shell where $\omega_N = \omega_0$, the poloidal magnetic field B_2 grows with time at a rate $\propto R_D\omega_0 t$, while at other values of L phase mixing narrows the radial scale to a width at time t defined by $\Delta\omega t/2 = \pi$. When plasma conductivity is included, narrowing terminates at a time

when wave Poynting flux directed onto the resonant field line is balanced by Joule heating in the ionosphere. However, as infinite ionospheric conductivity is assumed in the wave model used here, the minimum perpendicular scale after a specified elapsed time is set as an adjustable parameter. The variation of the field line eigenfrequency and frequency mismatch with L is illustrated in Figure 7.1 for a resonant field line at $L = 5.8$.

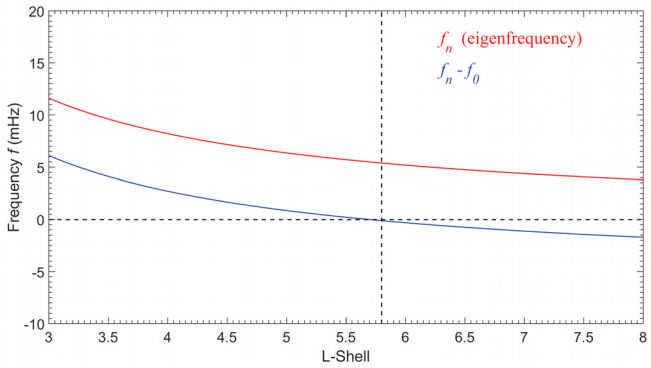

Figure 7.1: Field line eigenfrequency, f_N, and frequency mismatch parameter, $f_n - f_0$, as a function of L for a resonant field line at $L = 5.8$. Equatorial plasma number density at $L = 5.8$ is about $n_{eq} = 23.3\text{cm}^{-3}$.

Figure 7.2 shows the poloidal mode electric and magnetic field components for a resonant field line at $L = 5.8$. Wave parameters are chosen to match the observation described in Section 7.3. The wave period of 180s is obtained by setting the density equal to a constant in the equatorial plane and choosing a power law variation along field lines: $\rho(r) = \rho_{eq}(r_{eq}/r)^6$, where r is the geocentric radius and $r_{eq} = LR_e$. In the left column of Figure 7.2 the bottom panel shows the electric field as a function of latitude at its maximum value over a wave period. The top-left panel shows magnetic field components of the wave at the same moment of time, from which it is clear that B_2 and E_3 are 90° out of phase, while B_1 and E_3 are in phase. In the right column of Figure 7.2 wave fields are shown a quarter wave period later when B_1 and E_3 are instantaneously zero and B_2 is at maximum. It is important to note that the compressional magnetic field component is included, and that it is small near the equatorial plane and relatively large near the ionosphere. The amplitude of B_1 depends mainly on the strength of meridional gradients, as seen on inspection of Equation 4.59. The radial width in the equatorial plane in Figure 7.2 is a constant

set equal to $1.5R_e$.

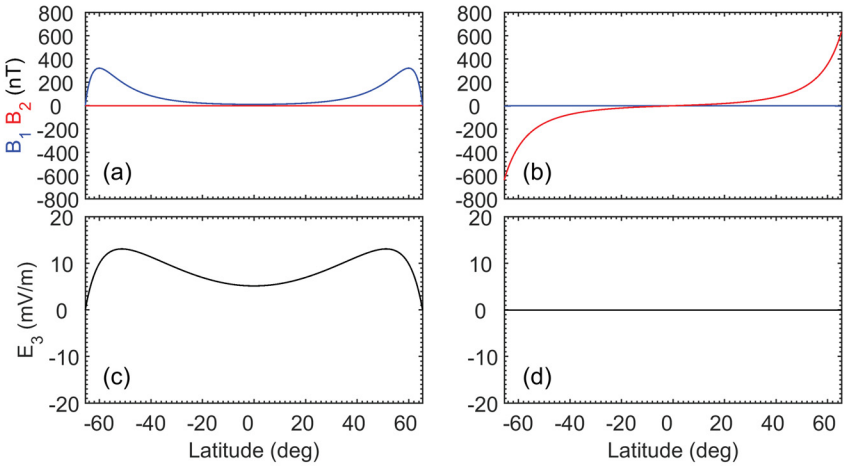

Figure 7.2: Electric and magnetic field perturbations at $L = 5.8$ for a wave frequency is 5.5 mHz. Equatorial plasma number density at $L = 5.8$ is about $n_{eq} = 23.3\text{cm}^{-3}$. The left column shows that the compressional magnetic field (B_1) and the azimuthal electric field (E_3) are in phase and that the wave magnetic field component B_2 and electric field E_3 are 90° out of phase. The right column panels show the fields 1/4 wave period later.

With ULF wave fields determined by Equations (4.57)-(4.59) we now turn to consideration of charged particle dynamics. The guiding-center approximation is used for the electron energy range considered, but for heavy ions, the possibility of non-adiabatic behavior requires that the full cyclotron orbit of particles be resolved. The Lorentz force equations of motion is used in the latter case, as described in Section 7.4. For the electron dynamics presented in Section 7.3, the guiding-center equations are used. The drift motion of the guiding center is a combination of the $\mathbf{E}\times\mathbf{B}$ drift, gradient drift, and curvature drift. The relativistic form of the equations [*Northrop*, 1963] is defined by,

$$\frac{dp_{\|}}{dt} = -\frac{\mu}{\gamma}\frac{dB}{ds} + \mathbf{v}_{\mathbf{E}\times\mathbf{B}}\cdot(p_{\|}\frac{d\mathbf{b}}{ds}) \tag{7.1}$$

$$\frac{d\mathbf{R}}{dt} = \mathbf{v}_{\mathbf{E}\times\mathbf{B}} + \frac{\mu}{\gamma qB^2}(\mathbf{B}\times\nabla B) + \frac{p_{\|}^2}{\gamma m_0 qB^2}(\mathbf{B}\times\frac{d\mathbf{b}}{ds}) + \frac{\mathbf{p}_{\|}}{m_0\gamma}. \tag{7.2}$$

The first three terms on the right hand side of Equation 7.2 are the $\mathbf{E}\times\mathbf{B}$ drift, gradient drift, and curvature drift, respectively, and the last term $\mathbf{p}_{\|}$ is the electron parallel velocity. The $\mathbf{E}\times\mathbf{B}$ drift speed $\mathbf{v}_{\mathbf{E}\times\mathbf{B}} = \mathbf{E}\times\mathbf{B}/B^2$, $\mathbf{p} = \gamma m_0\mathbf{v}$ is the

relativistic momentum, m_0 the electron rest mass, $\mu = W_\perp/B$ the first adiabatic invariant, $p_\parallel = mv_\parallel$ the parallel momentum, and $\mathbf{b} = \mathbf{B}/|B|$ the direction of the magnetic field. The parallel electric field of a shear Alfvén wave is zero under the ideal MHD approximation.

7.3 Simulation of Electron Drift Resonance Observed by the Van Allen Probes on October 31, 2012

Observations of electron drift resonance by *Zong et al.* [2009] and others demonstrate the importance of Pc5 waves in the dynamics of energetic electrons in the inner magnetosphere. Radial electron transport caused by these waves violates the third adiabatic invariant keeping the first and second invariants conserved [*Hudson et al.*, 2008]. This process is often quantified by a diffusion coefficient that depends on the amount of wave power in the Pc4-5 band. In storm sudden commencements, on the other hand, prompt-acceleration by shock-induced compressional waves proceeds coherently and non-diffusively [*Li et al.*, 1993]. Another possible acceleration mechanism involves substorm-injected eastward drifting electrons that excite poloidal ULF waves via drift resonance [*James et al.*, 2013]. In *Claudepierre et al.* [2013] this is suggested as an explanation of modulations in differential particle flux observed by the RBSP on October 31, 2012. Test particle simulations exploring this scenario are presented in Section 7.3. That being said, it is an open question as to whether local acceleration or radial transport dominates energization of outer zone electrons to relativistic energies. The precision will undoubtedly be improved as more observations are made of energy dependence of the amplitude and phase of electron differential flux modulations and their relation to phase space density gradients [*Takahashi et al.*, 2018].

Test particle simulations enable drift-bounce resonance theory to be validated and quantify observations of the type reported by *Zong et al.* [2009], *Claudepierre et al.* [2013], and *Mann et al.* [2013], which show evidence of electron acceleration during the passage of interplanetary shocks. The amplitudes of differential flux mod-

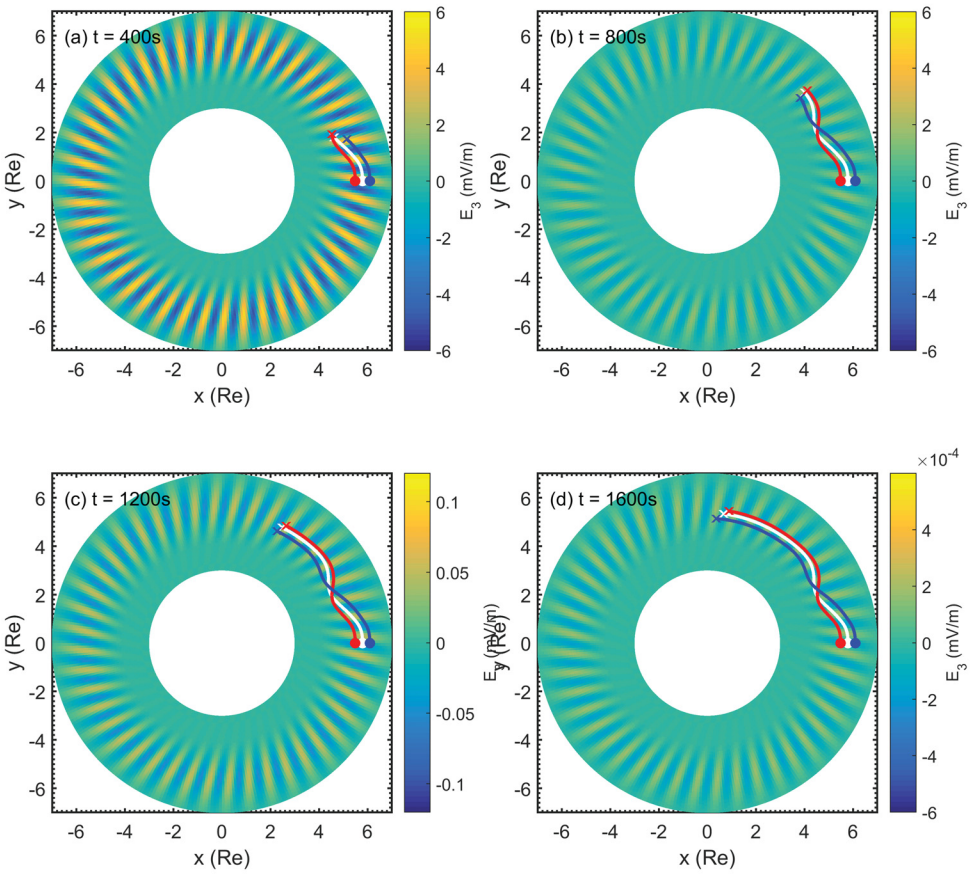

Figure 7.3: The four panels show the trajectories of a ~ 60 keV electron superimposed on snapshots of the poloidal mode electric field at (a) $t = 400$s, (b) $t = 800$s, (c) $t = 1200$s, and (d) $t = 1600$s. The electrons are released at $t = 0$ at $L = 5.5$, 5.8, and 6.1, corresponding to the red, white, and blue lines on each panel of the figure, respectively.

ulations in the October 31, 2012, event are largest between $50-100$ keV, and smaller at energies above and below this range. Electrons of energy 60 keV satisfy the drift-resonance condition at $L \sim 5.8$ for waves with a period of $180s$, azimuthal wavenumber $m = 44$, and $N = 0$. The m-value cannot be estimated directly as only RBSP-A observed signatures of drift resonance. The absence of waves at RBSP-B suggests the electron acceleration process in the event is highly localized over the approximately five-period time scale of the event.

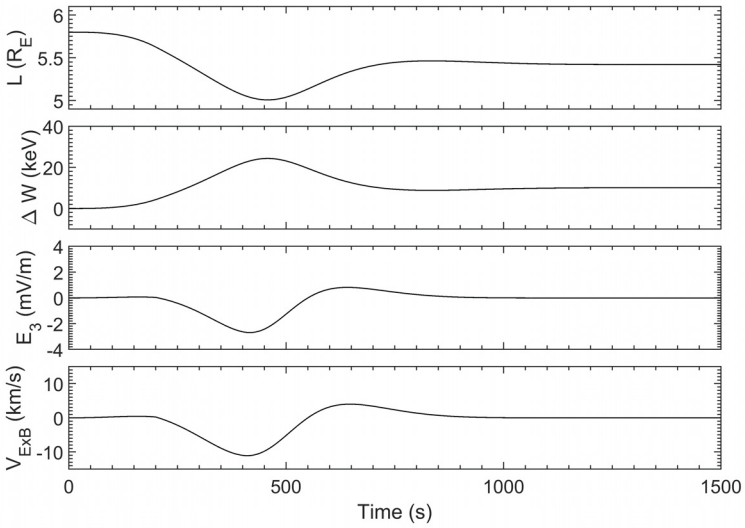

Figure 7.4: From top to bottom the panels show the L-shell, change in energy, azimuthal electric field, and $\mathbf{E} \times \mathbf{B}$ drift velocity for electrons of energy equal to the drift resonance energy of ~ 60 keV.

Figure 7.3 shows trajectories drift-resonant ~ 60 keV electrons superimposed on snapshots of $E_3(L,t)$ at $t = 400$s,800s,1200s, and 1800s, respectively. Three resonant energy trajectories are shown for electrons released at different values of L, with the red, white, and blue lines corresponding to initial particle positions at $L = 5.5$, 5.8, and 6.1, respectively. It is clear that electrons follow trajectories that depend on the phase of E_3 they experience. The L-shell, change in energy ΔW, electric field E_3, and the $\mathbf{E} \times \mathbf{B}$ drift velocity experienced by the resonant electron at $L = 5.8$ over a period of 2000s is shown in Figure 7.4. The growth and decay of the wave over this timescale in the test particle simulation leads to an azimuthally localized interaction region that is consistent with the event reported by *Claudepierre et al.* [2013].

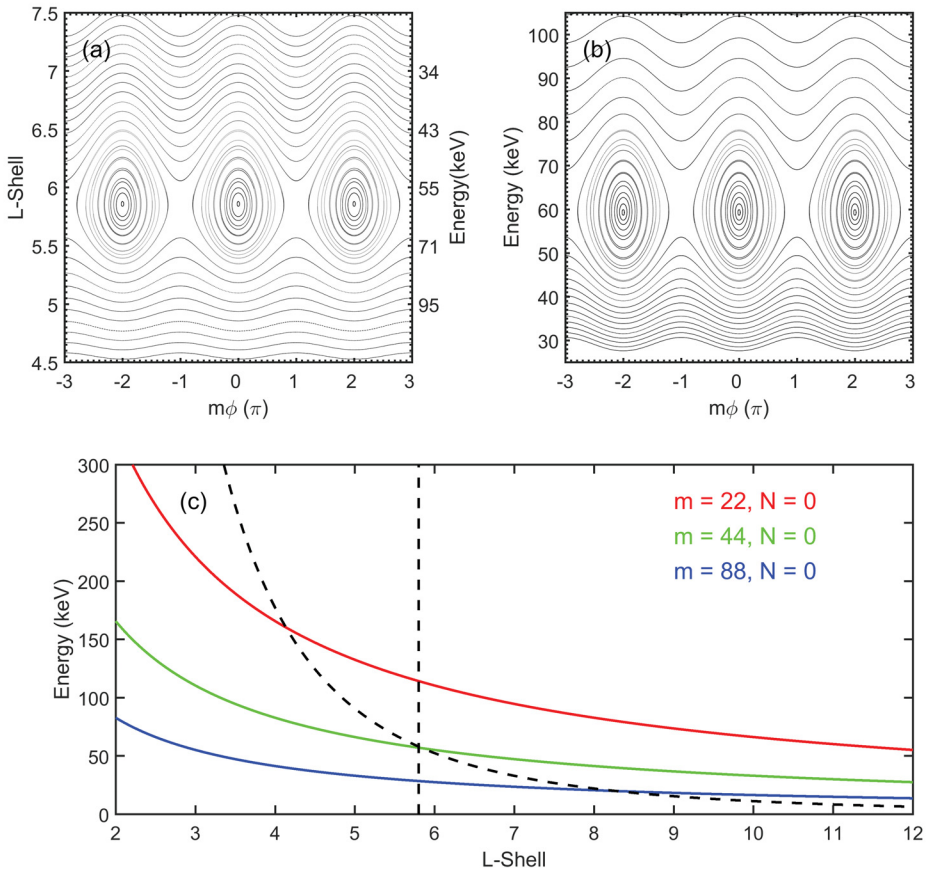

Figure 7.5: Panels (a) and (b) show Poincaré maps of test electrons that all have the same first and second adiabatic invariant. Panel (a) shows the change in energy in the wave frame for an azimuthal wavenumber $m = 44$. Panel (b) shows corresponding changes in L-shell. The first and second adiabatic invariants μ_{res} and K are assigned values defined by the strength of the dipole magnetic field at $L = 5.8$ and a 60 keV electron satisfying the drift resonance condition $\omega = m\omega_d$. Panel (c) shows the resonance energy as a function of L for different values of m, including $m = 44$. The vertical dashed line marks the L-shell for the RBSP-A observation, while the other dashed line corresponds to constant $\mu = \mu_{res}$.

Poincaré plots for electrons subjected to acceleration and deceleration by poloidal mode waves observed on October 31, 2012, are shown in Figure 7.5. Panels (a) and (b) were obtained by releasing test particle electrons at different values of L with initial particle energies defined by $W_\perp = \mu_{res} B(L)$. Here, μ_{res} takes a value defined by the strength of the dipole magnetic field at $L = 5.8$ and a 60 keV electron satisfying the drift resonance condition $\omega = m\omega_d$. Panel (c) in the figure shows the resonance energy as a function of L for different values of m, including $m = 44$. The vertical dashed line marks the L-shell for the RBSP-A observation on October 31, 2012, while the second dashed line corresponds to the first adiabatic invariant for resonant energy electrons, $\mu = \mu_{res}$. The Poincaré plot shows that electrons near resonance experience changes in L and energy that are comparable to the energy range of differential flux modulations on RBSP-A.

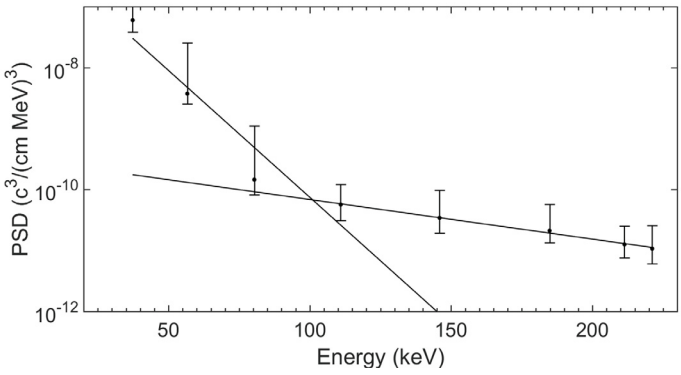

Figure 7.6: Time averaged phase space density from 15:35-16:00 UT for RBSP-A energy channels ranging from 37 keV to 221 keV. The two lines indicated are obtained from linear regression of the observations from 37 keV to 110 keV and from 110 keV to 221 keV, respectively.

The initial particle distribution function is assumed known in the test particle approach used here to investigate drift-resonance. For simplicity, an initial isotropic Maxwellian distribution function f_d is assumed. The ambient temperature T_e is obtained from measured RBSP-A differential fluxes $F = f_d W/2m_e$ and the expression $\ln f_d = -W/T + \ln f_{d0}$. Here, W and m_e are the electron energy and mass, respectively, and $\ln f_{d0}$ is a constant. Figure 7.6 shows a time average of f_d for RBSP-A between 15:30-16:00 UT utilizing 11 pitch angle channels and 8 energy bins covering 37.3 keV to 221.1 keV. The two solid lines on the figure show linear fits based on

the four lowest and highest energy bins, respectively. The energy bins in the range 57 keV to 80 keV yield $T_e \sim 10$ keV, which is the ambient temperature we use in our test particle simulations.

Given the initial distribution function, Liouville's theorem is used to calculate the evolution of f_d with time due to the action of ULF waves. This is done by defining a phase space grid in energy and pitch angle at the approximate location of RBSP-A during the October 31, 2012, event; $L = 5.8$, magnetic latitude 6.0°, assuming a dipole field. Phase space points representing virtual electrons are traced backward in time from this location by solving the relativistic guiding center equations numerically. The distribution function at time t can be reconstructed once the initial positions and velocities of virtual electrons have been obtained from backward-tracing. This is achieved by applying Liouville's theorem, which states that particles preserve f_d along their trajectory to the observation point at time t.

Simulated residual fluxes $(J - J_0)/J_0$ are shown in Figure 7.7 following the definition used by *Claudepierre et al.* [2013]. In their paper J_0 is a 10-minute running boxcar average of the observed flux, which is introduced to take into account interplanetary shock compression effects not accounted for in the studies presented here. In the simulations, the background differential flux defines values of J_0. The top panel in Figure 7.7 shows the simulated poloidal mode magnetic and electric fields for the October 31, 2012, event. The wave amplitude reaches a maximum after two wave periods and then decays over five wave periods similar to the observation. As the electric field data is not available in the event, it is estimated using the magnetic field component b_r measured by RBSP-A as ~ 4 mVm^{-1}. The middle panel of Figure 7.7 shows simulated residual fluxes as a function of time at various energies. Inspection of flux modulations on either side of the resonance energy $W_{res} = 60$ keV marked by a red line on the figure, indicates that modulation amplitudes decrease away from the resonance energy within the energy range of matching the observations. There is also a 180° phase shift across this range of energy as predicted by *Southwood and Kivelson* [1981]. The bottom panel of Figure 7.7 presents residual fluxes in 1 keV energy bins to make it more obvious that the phase difference increases with time as the wave decays. This behavior arises due to the dependence of the electron drift speed on L,

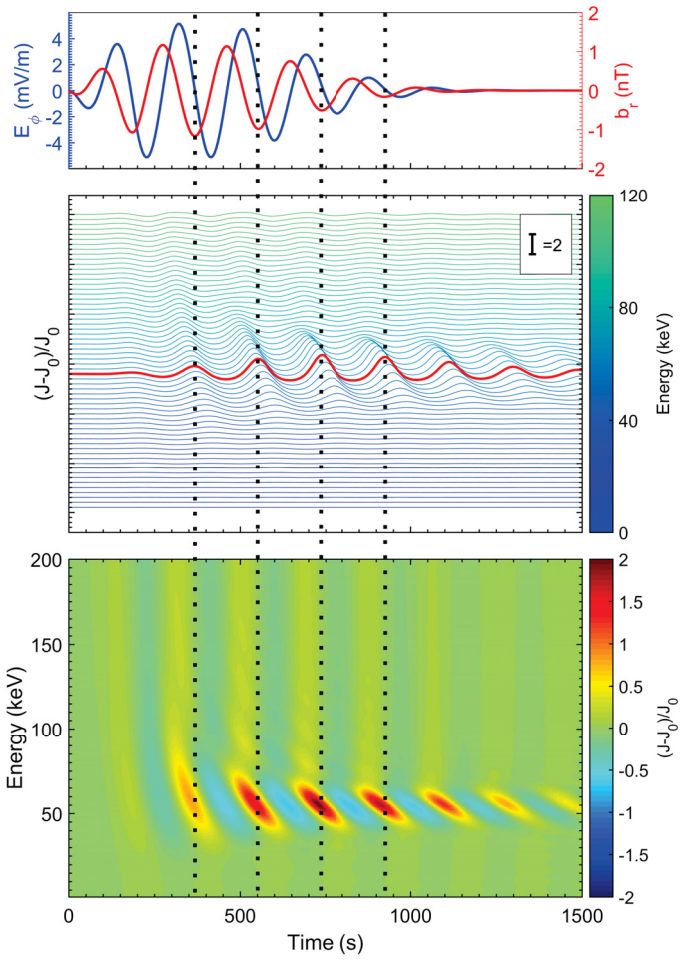

Figure 7.7: Simulation of the RBSP-A drift resonance event on 31 October, 2012. The wave period is 180 s and the azimuthal wavenumber $m = 44$. The observation point used for backward Liouville tracing is at $L = 5.7$ on the equatorial plane. The top and middle panels show the wave profile and the simulated residual flux of equatorial electrons at 1 keV resolution (the phase space grid size in the simulation), respectively. The bottom panel shows simulated electron residual flux as a function of energy and time.

and is known as phase mixing in phase space. Phase mixing makes it a challenge to observe signatures of drift resonance when the affected energy range is small.

The phase mixing effect discussed above is potentially problematic for satellite instrumentation with variable and relatively large energy bin sizes [*Schulz and Lanzerotti*, 2012; *Degeling and Rankin*, 2008]. It has the effect of diminishing the measured amplitude of flux oscillations artificially as waves decay. Figure 7.8 shows the same data as Figure 7.7 except that averaging of the simulated flux in the third panel of the figure is done identically to the MagEIS-A instrument. The second panel of Figure 7.8 shows simulated residual fluxes at the center of each energy channel of MagEIS-A without binning. Although the phase difference between the wave magnetic field and the 57 keV flux oscillation remains 180°, the averaged residual fluxes within MageEIS-like energy bins attenuate faster and have slightly smaller amplitudes. The bottom panel of the figure shows the observed residual flux adapted from Figure 2(a) of *Claudepierre et al.* [2013], from which it is clear that simulated and observed Mag-EIS residual fluxes are in close agreement.

The test particle simulation results discussed up until now are for electrons of 90° pitch angle. Figure 7.9 summarizes the simulated pitch angle dependence of electrons accelerated by electric fields in the *Claudepierre et al.* [2013] event. The top panel of the figure shows the wave profile, the middle panel shows the residual flux in an energy bin matching the $\sim$ 80 keV MagEIS energy channel, and the bottom panel shows the observed electron differential flux adapted from Figure 2(d) of *Claudepierre et al.* [2013]. The simulated and observed electron fluxes for 90° pitch angle are strongly modulated in comparison to smaller pitch angles and are in good agreement. Figure 7.10 shows the simulated residual flux as a function of pitch angle at different energies, illustrating that fluxes at all energies are strongest at 90° pitch angle, as expected for ULF drift-resonance.

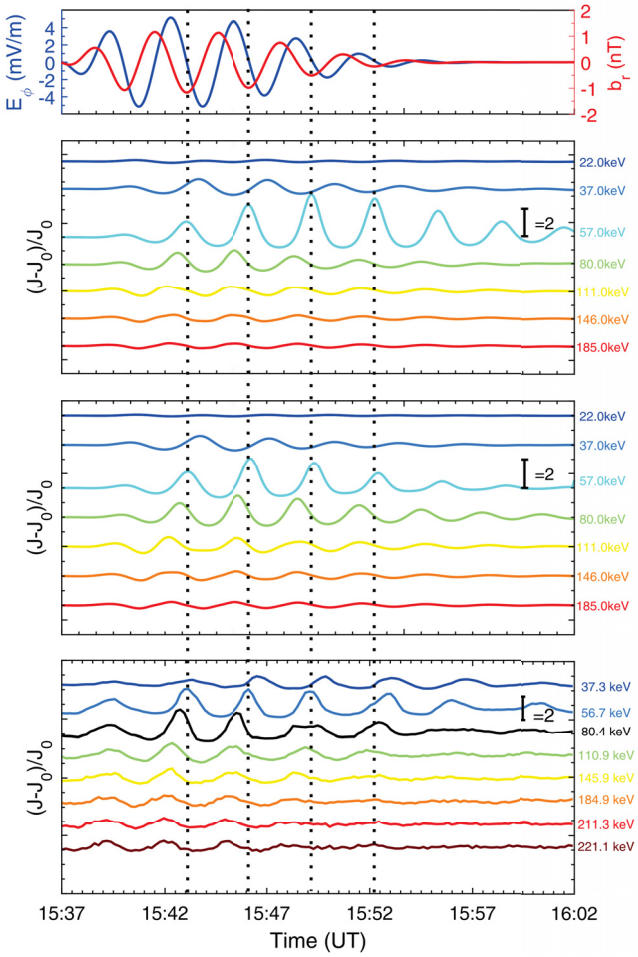

Figure 7.8: The first panel shows wave profile used in simulations. The second panel shows simulated residual fluxes at energies matching the center of energy channels of the MagEIS-A instrument. Note that these fluxes are binned at the resoloution of the phase energy grid in the simulation. The third panel shows simulated residual flux for energies that are binned in energy the way it is done on the MagEIS detector on RBSP-A. The fourth panel adapted from *Claudepierre et al.* [2013] shows observed residual fluxes from 37 keV to 221 keV on MagEIS-A.

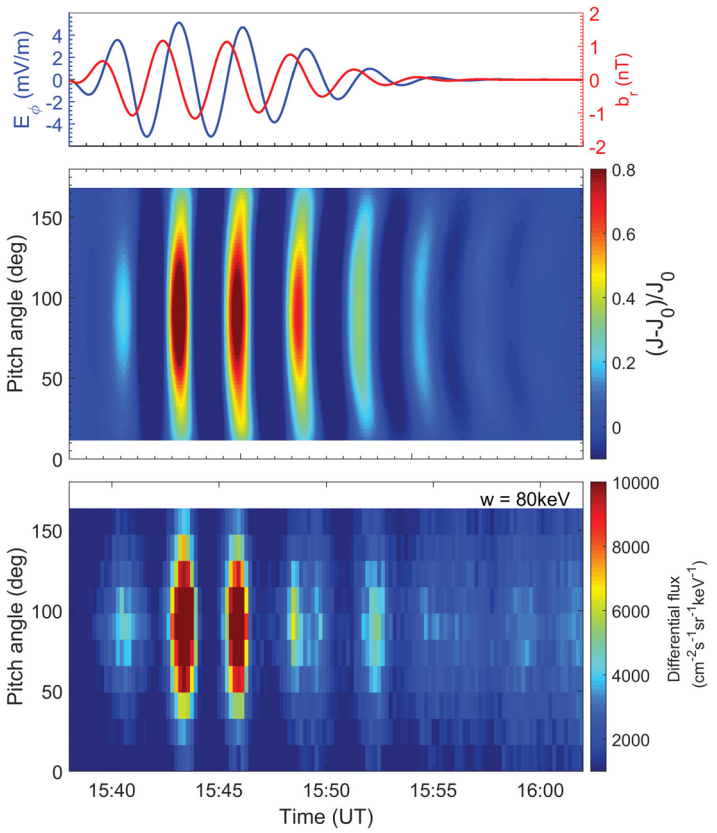

Figure 7.9: The top and middle panels show, respectively, the simulated wave profile and residual flux as a function of pitch angle and time for electrons matching the MagEIS instrument energy channel at 80 keV. The bottom panel, adapted from *Claudepierre et al.* [2013], shows the observed differential flux in the actual energy channel of MagEIS-A.

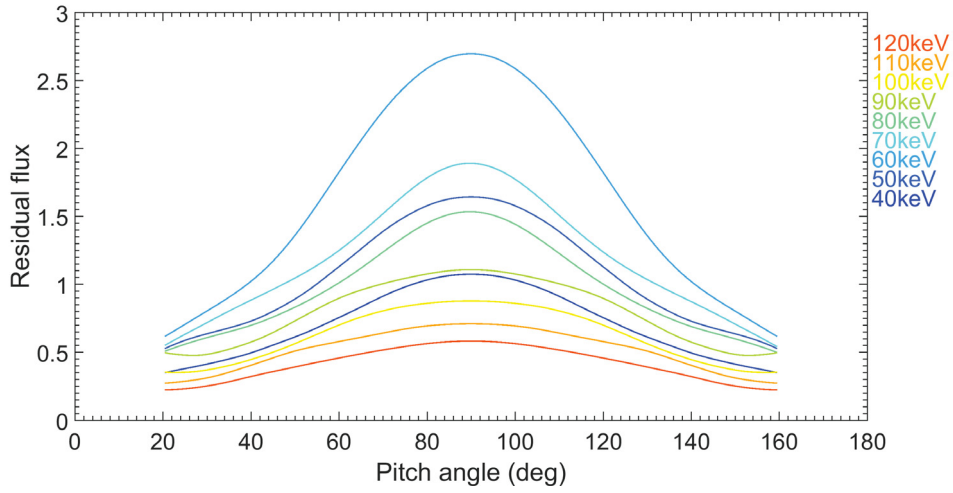

Figure 7.10: Residual flux at 15:46 UT as a function of pitch angle and for different energies. The energy bin size is 10 keV.

7.4 Drift-Bounce Resonance Involving Fundamental Mode Poloidal Waves and O^+ Ions

In Earth's magnetosphere, heavy ions are often present during and after geomagnetic storms and interplanetary shocks. In this section, we briefly discuss some aspects of the expected response of O^+ ions to poloidal mode ULF waves that accompany these space weather disturbances. For ions drifting westward N wavelengths in the wave frame in a single bounce period, the resonance condition $\omega - m\omega_d = N\omega_b$ can be satisfied for $N = 0$ and $N = -2$. Resonant ions experience net acceleration or deceleration over a bounce period depending on their initial position and velocity in the wave frame [*Southwood and Kivelson*, 1981, 1982].

In fundamental mode poloidal waves the energy of resonant ions is lower for $N = 0$ than for $N = -2$. Drift resonant ions remain at a fixed azimuthal position in the wave frame while bouncing between mirror points, and precipitate to the atmosphere within a single bounce period if they are initially in the loss cone. Outside the loss cone the resonance energy of ions is smaller the further they are from the loss cone. Figure 7.11 illustrates that the electric field E_3 increases gradually from the equator before dropping rapidly near the ionosphere. It is of interest to consider whether modulations in ion differential flux are strongest at 90° pitch angle where

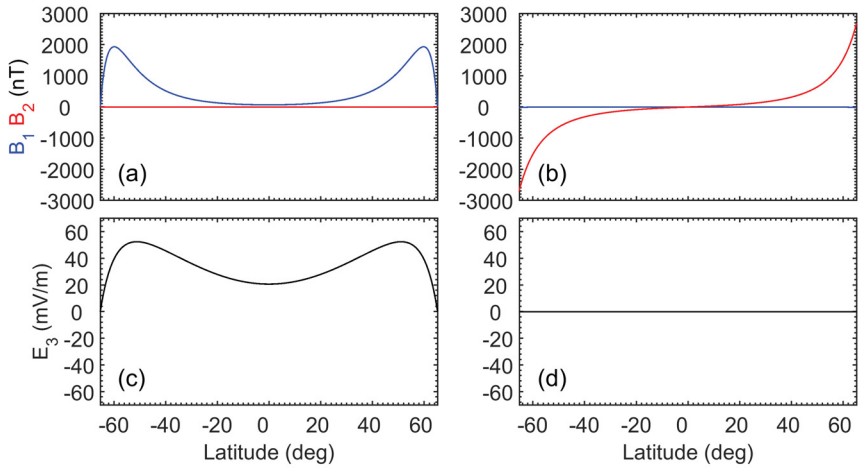

Figure 7.11: Electric and magnetic field perturbations at $L = 5.7$. The wave frequency corresponds to $f = 10$ mHz. The format of the figure is the same as Figure 7.2. Equatorial plasma number density at $L = 5.7$ is about $n_{eq} = 7.8\text{cm}^{-3}$.

resonant ions have the lowest possible energy, c.f. Section 7.3, or at a pitch angle where the mirror point is nearer to the electric field maximum off the equator. The pitch-angle dependence of O^+ ions is investigated below. Poincaré plots for O^+ subjected to acceleration and deceleration by poloidal mode waves are shown in Figure 7.12.

In Figure 7.13 the direction of wave propagation is assumed to be westward, with the azimuthal wavenumber, wave period, and resonant field line taking values $m = -60$, 100 s, and $L = 5.7$, respectively. The differential particle flux in the figure shows clear evidence of $N = 0$ and $N = -2$ resonances. The electric field amplitude in the top-left and top-right panels of the figure both increase with time, but at different rates. The maximum wave amplitude is 8.5 mVm^{-1} in the top-left panel and 3 mVm^{-1} in the top-right panel. The lower panels of the figure show corresponding changes in ion energy, δW, as a function of energy and time on the equator at $L = 5.7$. Dashed lines in Figure 7.13 indicate resonance energies predicted by drift-bounce resonance theory. In the bottom-right panel, the pattern of positive and negative δW falls within the linear regime [*Southwood and Kivelson*, 1981; *Zhou et al.*, 2016]. The vortex-like pattern of δW in the bottom-left panel is evidence of nonlinear dynamics in which resonant ions experience large changes in L during each bounce period.

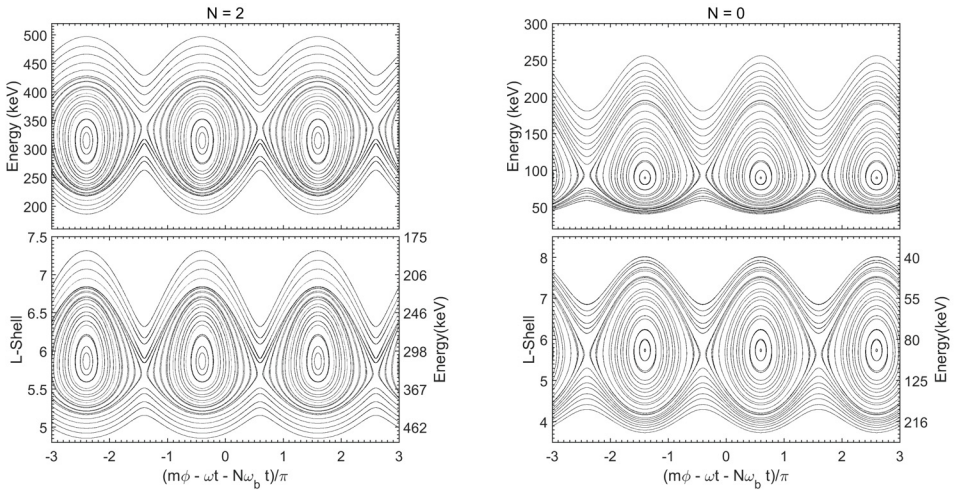

Figure 7.12: Poincaré plots of test particles for fixed first and second adiabatic invariants. Wave parameters are the same as Figure 7.11. The top-left and bottom-left panel shows variations in particle energy and L-shell for $N = -2$ drift-bounce resonance. The panels on the right show Poincaré plots for particles satisfying the $N = 0$ drift resonance condition in the same format as the left column panels.

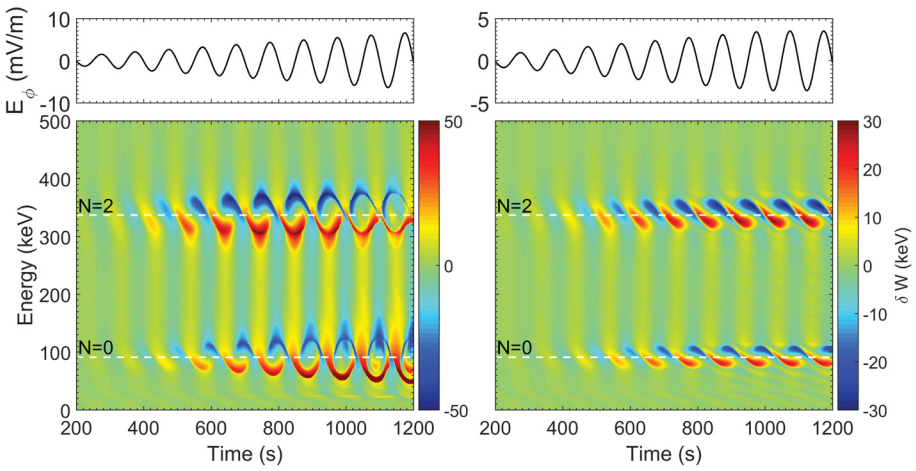

Figure 7.13: The top-left and top-right panels show the electric field profile as a function of time. The bottom panels show corresponding energy changes, δW, experienced by O^+ ions as a function of their energy and time on the equator at $L = 5.7$. The wave frequency and azimuthal wavenumber correspond to $f \sim 10$ mHz and $m = -60$, respectively.

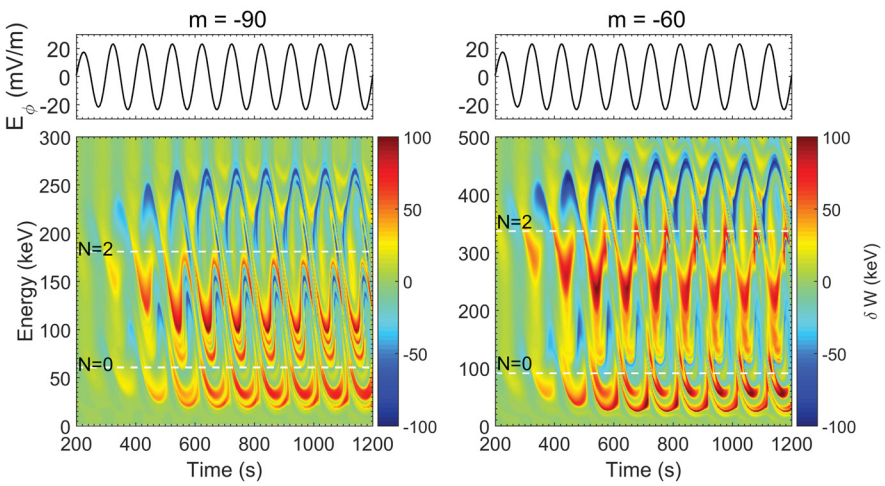

Figure 7.14: The panels are arranged in the same format as Figure 7.13 except $m = -90$ in the left column, $m = -60$ in the right column, and the maximum electric field amplitude is 23.8 mVm^{-1} at the equator.

The $N = 0$ and $N = -2$ resonance structures in Figure 7.13 are well separated in energy and therefore do not interact. To investigate conditions under which island overlap is possible, we increase the amplitude of the electric field to 23.8mVm^{-1} in the equatorial plane and compare results for azimuthal wavenumbers $m = -60$ and $m = -90$. Figure 7.14 shows results in the same format as Figure 7.13 except that in the left column $m = -90$ and in the right column $m = -60$. Resonant islands have a smaller separation for $m = -90$ to the extent that an intermediate island forms between the $N = 0$ and $N = -2$ islands.

Stroboscopic Poincaré plots in the laboratory frame are shown in Figure 7.15, with panels (a) and (b) showing changes in L and energy for the $m = -90$ case, and panels (d) and (e) showing those for the $m = -60$ case. The overlap of $N = 0$ and $N = -2$ resonant islands is more significant for $m = -90$. The bottom panels of Figure 7.14 show resonance energies as a function of L, with dashed lines indicating the first adiabatic invariant for ions in drift-resonance ($N = 0$) and drift-bounce resonance ($N = -2$) at $L = 5.7$. For $m = -90$ ions with $\mu = \mu_{res}$ lie on trajectories that can potentially migrate between a resonant island at $L = 5.7$ and an island at $L = 9.2$. The implications of resonant island overlap and radial transport are deferred to a future study.

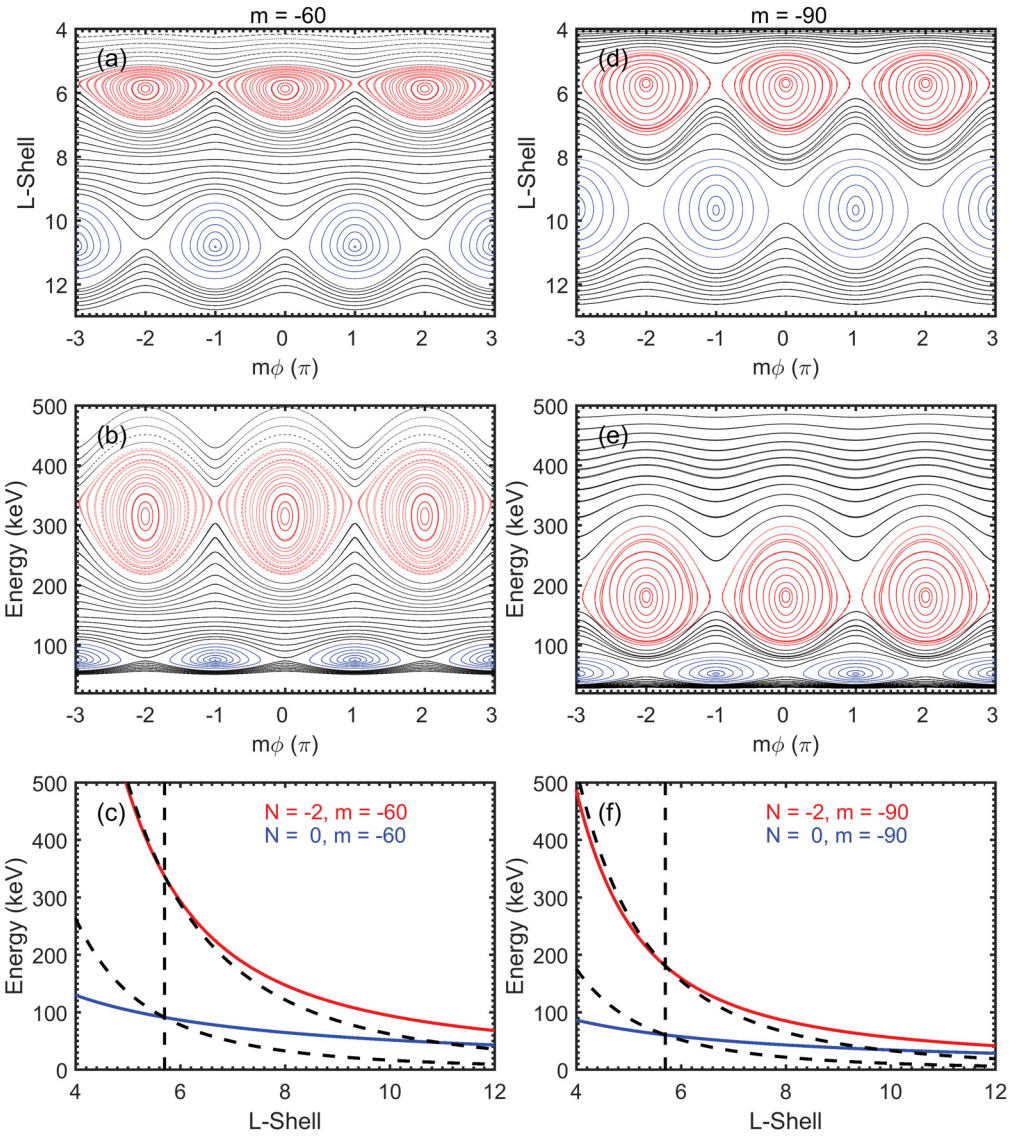

Figure 7.15: Stroboscopic Poincaré plots with particle positions and energies calculated at intervals of the drift-bounce period for $N = 0$ and $N = -2$. Panels (a) and (b) show changes in ion energy and L for $m = -60$, and panels (d) and (e) show corresponding values for $m = -90$. The bottom panels show $N = 0$ and $N = -2$ resonance energies as a function of L with dashed lines indicating the first adiabatic invariant for ions with an energy equal to the $N = 0$ and $N = -2$) resonance condition at $L = 5.7$. In panels (a), (b), (d) and (e), the red lines indicate the $N = -2$ resonance, and the blue lines indicate the $N = 0$ resonance.

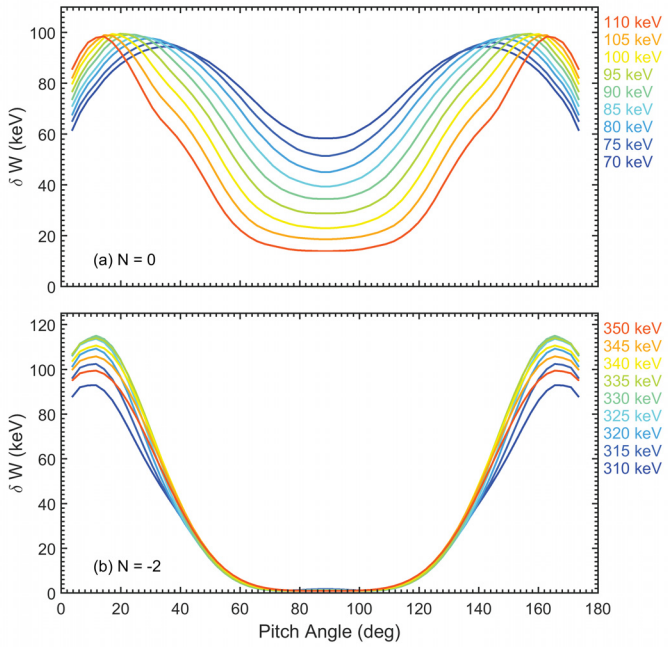

Figure 7.16: Maximum energy changes $|\delta W|$ over a wave period as a function of pitch angle for different energies. Each curve corresponds to an energy bin size of 10 keV. The top panel shows energy changes close to the $N = 0$ drift resonance energy and the bottom panel shows energy changes close to the $N = -2$ drift-bounce resonance energy.

Finally, Figure 7.16 shows the pitch angle dependence of changes in energy, ΔW, of ion that have various energies in the vicinity of the $N = 0$ and $N = -2$ resonances. Unlike electrons, the maximum energy gain for heavy ions occurs at pitch angles substantially different from 90°. An obvious question is whether the pitch-angle dependence of the energy changes in Figure 7.16 are related to the off-equator peak in the wave azimuthal electric field. This is not the case as ions with pitch angles that mirror more toward the ionosphere have a correspondingly larger resonance energy. This is more obvious in the $N = -2$ drift-bounce resonance case where the resonance energy is large in comparison to $N = 0$ drift resonance energy. Correspondingly, resonant ions in the $N = -2$ case are concentrated near the high and low latitude segments of geomagnetic field lines.

7.5 Conclusion

In this chapter, we have presented ULF wave and test particle simulation results on drift resonance and drift-bounce resonance involving energetic ions and electrons in Earth's magnetosphere. The simulation results presented in Section 7.3 reproduce the amplitude, phase difference with energy, and pitch angle dependence of modulations in electron differential flux observed by the MagEIS instrument on RBSP-A between 15:30-16:00 UT, October 31, 2012 [*Claudepierre et al.*, 2013]. They confirm that the wave and electron signatures observed by the spacecraft are due to localized drift resonance wave-particle interactions between fundamental poloidal mode Alfvén waves and electrons near 60 keV. The flux oscillations attenuate rapidly during the damping stage of the observed ULF waves because of the increasing phase difference between different energy particles within energy bins of the MagEIS instruments.

The effect of finite energy bin size on satellite instruments is estimated by comparing residual flux obtained from high energy resolution simulations with and without energy binning. Although the binned electron residual flux is in better agreement with observations, the more rapid attenuation rate due to energy binning may give a distorted picture of the actual process. The electron drift resonance results presented in our study provide a verification of electron drift resonance theory in the mag-

netosphere, and offer a path toward development of more realistic models that aid interpretation of wave-particle interactions observed by spacecraft such as NASA's Van Allen Probes and MMS missions, and the Japanese ERG mission.

Test particle simulations of $N = 0$ drift resonance and $N = -2$ drift-bounce resonance with O^+ ions reveal complex dynamics in which different wave-particle resonances can potentially interact. The pitch angle response of ions to ULF waves is also strikingly different from electron drift resonance. For electrons, differential particle fluxes peak at 90° pitch angle at all energies, and are relatively unaffected by the profile of the accelerating electric field that peaks at latitudes well off the equator. In the case of O^+, the ion differential flux is strongly peaked at pitch angles that place particle mirror points well of the equator. The drift-bounce resonance $N = -2$ differential flux also peaks at much higher latitudes than $N = 0$ drift resonance, which is explained by the pitch-angle dependence of the resonance energy. More observations and simulations are necessary to understand in more detail the features of differential flux modulations resulting from drift-bounce resonance, and the resulting radial transport caused by poloidal mode ULF waves in Earth's magnetosphere.

Chapter 8

Test Particle Simulations of Drift-bounce Resonance with Advanced ULF Wave Model and Forward Liouville method

The ULF wave model we used in previous chapters makes assumptions about infinite ionosphere conductivity and specifies the plasma density distribution in the radial direction. The infinite ionosphere conductivity decoupled the toroidal mode and the poloidal mode of Alfvén waves on the field lines. In this chapter, we use a global MHD ULF wave model developed by D. Sydorenko et al.. This model is more advanced because it includes self-consistent coupling between the compressional mode and both the toroidal and poloidal modes by introducing more realistic ionospheric boundary condition and plasma density distribution. Although different ionospheric boundary conditions are considered in previous MHD ULF wave models [e.g. *Degeling et al.*, 2011], the spatial domain of the model covers a range of altitudes stretching from the ground to the magnetosphere. Different global distributions of plasma density can also be specified in this model. The plasma density distribution can either be previous models such as the Global Core Plasma Model [*Gallagher et al.*, 2000], or from the real data.

Other realistic features of ULF waves in the magnetosphere have also been introduced in this model. For example, the ULF waves in the magnetosphere are usually

combination of multiple frequency components. In Section 8.2, we will show that this model provides a way to simultaneously excite FLRs with different harmonic orders. The cold plasma convection has also been included in this model. The convection electric field can be specified either from observations such as Super Dual Auroral Radar Network (SuperDARN) [*Chisham et al.*, 2007], or from global models such as the Volland Stern model [e.g. *Burke*, 2007].

The test particle model we use in this chapter to simulate trajectories of H^+ ions in this chapter is the full Lorentz model. In previous chapters, we used backward Liouville method to reproduce PSD variation at the sampling point. The method we use in this chapter to reproduce PSD variation is the forward Liouville method in Section 5.2, Chapter 5. This method simulates behavior of charged particles distributed throughout a larger simulation domain (e.g., the inner magnetosphere) rather than at a single point. Combining this method with the Monte Carlo method, this method allows us to study the variation of PSD in an arbitrary sampling volume in the simulation domain. We can also study particle transport throughout the system if enough test particles are collected in the sampling volumes.

In this chapter, we combine the advanced ULF wave model and the Forward Liouville method to provide some preliminary studies about the drift-bounce resonance between the second-harmonic poloidal mode waves and H^+ ions. It has been shown that second-harmonic waves can energize ions to tens of keV. The test-particle simulations also predict ion flux oscillations that have energy dispersion similar to satellite observations.

The work presented in this chapter had been done earlier than the other chapters. However, as we discussed in Section 8.5, we realized that the computing resources we have do not allow us to effectively study the wave-particle interactions in the other chapters. In this chapter, we only provide some preliminary simulations with this advanced model.

The work in this chapter is based on an invited oral presentation given at the URSI Asia-Pacific Radio Science Conference in Seoul, Korea in 2015. The IEEE published a short paper summarizing the results [*Rankin et al.*, 2016].

8.1 Introduction

The electric fields associated with magnetospheric poloidal ULF waves [*Dungey*, 1955] are known to accelerate electrons and ions in the inner magnetosphere. These waves, with frequencies ranging from about 1 mHz to 1 Hz, can be excited by external sources including solar wind dynamic pressure pulses [*Kepko and Spence*, 2003], Kelvin-Helmholtz (K-H) instabilities on the magnetopause [*Hudson et al.*, 2004; *Claudepierre et al.*, 2008], and internal plasma instabilities. The K-H instability can excite ULF waves in the magnetosphere through coupling that takes place between long-wavelength surface-mode waves and earthward ULF Alfvén waves [*Claudepierre et al.*, 2008]. Interplanetary shocks and solar wind dynamic pressure pulses also excite ULF waves, although the precise mechanism that converts shock energy to waves of a high azimuthal wave number is not yet fully understood.

Wave-particle interactions involving these ULF waves can dramatically accelerate electrons [*Zong et al.*, 2007, 2009] and modulate flux of ions [*Yang et al.*, 2010; *Zong et al.*, 2011] in the inner magnetosphere. The energization process following shocks consists of a prompt increase in particle energy that initially shows little or no energy dispersion. This is followed by a temporal response that exhibits a phase change of π with energy that is characteristic of drift-bounce resonance.

ULF waves excited by shocks and dynamic pressure variations can be very intense and are sometimes damped away quickly over tens of minutes [*Zong et al.*, 2009; *Zhang et al.*, 2010]. A recent study [*Wang et al.*, 2015] (cf. Chapter 3) suggests that the observed fast damping is caused by drift-bounce resonance between ULF waves and ions with energies of a few keV. Such a mechanism has been described theoretically [*Southwood and Kivelson*, 1981, 1982] and is possible because of the comparable periods of drift and bounce motion of energetic particles and ULF oscillations. The mechanism of drift/drift-bounce resonance is the main topic of this thesis. Among different kinds of ULF waves with different wave field components the resonance between ions and poloidal ULF waves [*Zong et al.*, 2012a] is considered to be more efficient [*Yang et al.*, 2011b], even leading to the formation of a new radiation belt [*Li et al.*, 1993; *Wygant et al.*, 1994] in certain situations. In the previous chapters,

the acceleration and transportation of ions caused by ULF waves were evaluated by combining observations and simulations. In this chapter, by using electric fields from the full-wave model developed by Sydorenko et al. [*Sydorenko and Rankin*, 2013], studying global ions dynamics offers a path to being able to model the response of the entire radiation belt to solar disturbances. To our knowledge, this study is the first to implement the forward Liouville tracing method on this ULF wave model to explain particle flux modulation caused by drift-bounce resonance.

This chapter examines the energization and modulation of radiation belt ions caused by poloidal mode ULF waves. Electric fields from a full-wave model presented in Section 8.2 are used to drive a full Lorentz force test particle model of drift-bounce resonance. In Section 8.3, the forward Liouville method is used to reconstruct the PSD response to 2nd-harmonic poloidal mode waves. A discussion of particle signatures of heating and energy dispersion, along with limitation of this model is presented in Section 8.4. The conclusion and future work are in Section 8.5.

8.2 Global ULF Wave Model with Advanced Plasma Conditions

To model FLRs in the magnetosphere, we utilize a newly developed 3D linear MHD simulation code. Although other approaches are possible [*Degeling et al.*, 2010; *Lysak et al.*, 2013], using a structured grid and spherical geometry simplifies the specification of inner boundary conditions, as well as enabling high scalability on parallel computers. Parallel electric fields are accounted for, together with a realistic ionosphere with height-resolved ionospheric Pedersen and Hall conductivities. The model can use non-dipole magnetic fields, but it is assumed in this study that the plasma is azimuthally symmetric, and that the geomagnetic field is a dipole. The spatial domain of the model covers a range of altitudes stretching from the ground to several tens of thousands of km. Electromagnetic wave propagation in the neutral atmosphere will be included to improve the accuracy of the calculation of the signal created by magnetospheric ULF perturbations on the ground. It will encompass the atmosphere, ionosphere, and inner magnetosphere (to $L \sim 10$). The plasma of the ionosphere and

magnetosphere consists of electrons and multiple ion species (H^+ , He^+ , N^+ , O^+ , N^{2+} , NO^+ , O^{2+}). The multi-species plasma is represented as fluids that are coupled through Maxwell equations. Collisional friction is necessary in order to represent the ionosphere accurately. Neutral species (H, He, N, O, N_2 , NO, O_2) will be considered as a static background, while collisions of ions and electrons with each other and with neutrals will be accounted for using the formalism in *Sydorenko and Rankin* [2013]. In the system of linear equations that are solved, electromagnetic fields are calculated using Faraday's law and Ampere's law. The determination of electric currents in Ampere's law requires only a time advance of ion and electron flow velocities. The latter are found by solving linearized multi-species ion fluid motion equations. A predictor-corrector procedure implemented in the model ensures the stability and accuracy of the field calculation by eliminating accumulative errors that can arise over long simulation times.

The present model considers the magnetic field and electric field described by Ampere's and Faraday's laws (Eqaution (2.1) and Equation (2.2)). These equations are written in the form of components of a dipolar coordinate with finite ionospheric conductivity:

$$\frac{\partial B_1}{\partial t} = \frac{\Delta x}{R_E}\left(\frac{1}{h_3}\frac{\partial}{\partial \xi_3}E_2 - \frac{1}{h_2 h_3}\frac{\partial}{\partial \xi_2}h_3 E_3\right) \tag{8.1}$$

$$\frac{\partial B_2}{\partial t} = \frac{\Delta x}{R_E}\left(-\frac{1}{h_3}\frac{\partial}{\partial \xi_3}E_1 + \frac{1}{h_1 h_3}\frac{\partial}{\partial \xi_1}h_3 E_3\right) \tag{8.2}$$

$$\frac{\partial B_3}{\partial t} = \frac{\Delta x}{R_E}\left(\frac{1}{h_1 h_2}\frac{\partial}{\partial \xi_3}h_1 E_1 - \frac{1}{h_1 h_2}\frac{\partial}{\partial \xi_1}h_2 E_2\right) \tag{8.3}$$

$$\frac{\partial E_1}{\partial t} = \frac{\Delta x}{R_E}\left(\frac{1}{h_2 h_3}\frac{\partial}{\partial \xi_3}h_3 B_3 - \frac{1}{h_3}\frac{\partial}{\partial \xi_3}B_2\right) \tag{8.4}$$

$$\begin{aligned}\frac{\partial E_2}{\partial t} = {} & \frac{\Delta x}{R_E}\left(\frac{1}{h_3}\frac{\partial}{\partial \xi_3}B_1 - \frac{1}{h_2 h_3}\frac{\partial}{\partial \xi_1}h_3 B_3\right) \\ & - \Sigma_A \frac{\partial E_2}{\partial t} - \Sigma_P E_2 - \Sigma_H E_3 - J_{2,ext}\end{aligned} \tag{8.5}$$

$$\begin{aligned}\frac{\partial E_3}{\partial t} = {} & \frac{\Delta x}{R_E}\left(\frac{1}{h_1 h_2}\frac{\partial}{\partial \xi_1}h_2 B_2 - \frac{1}{h_1 h_2}\frac{\partial}{\partial \xi_1}h_1 B_1\right) \\ & - \Sigma_A \frac{\partial E_3}{\partial t} - \Sigma_P E_3 + \Sigma_H E_2 - J_{3,ext}\end{aligned} \tag{8.6}$$

where Σ_A is parallel conductivity, Σ_P is the height-integrated Pedersen conductivity (Equation (2.42)) and Σ_H is the height-integrated Hall conductivity(Equation (2.43)).

$J_{23,ext}$ are the perpendicular components of the external current driver. To solve the six variables in the above equations, the implicit finite difference form of the equations creates a system of two linear equations for E_2 and E_3 which are to be solved to advance these field components. Equations of B_2, B_3, and E_1 are written in explicit finite difference form and a predictor-corrector procedure is used to move these field components to the next time level as described below.

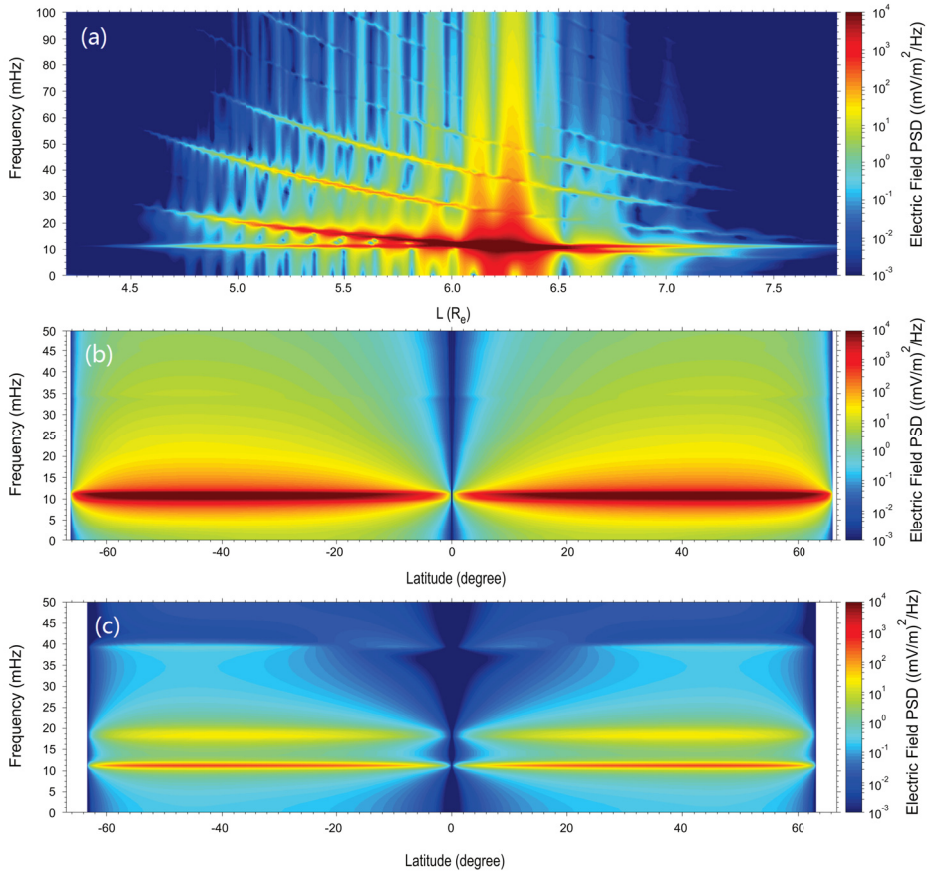

Figure 8.1: Power spectra of simulated second harmonic poloidal ULF waves. (a) Power spectra of the poloidal component electrical field E_ϕ as a function of the L-shell at a 30° latitude. (b) Power spectra of the poloidal component electrical field E_ϕ as a function of the latitude at $L = 6.2$. The driver frequency is consistent with the natural frequency of the field lines at around $L = 6.2$. (c) Power spectra of the poloidal component electrical field E_ϕ as a function of the latitude at $L = 5.0$. The natural frequency of the field lines is higher than the driver frequency.

The numerical scheme used to solve the coupled system of partial differential equations will exclude fast timescale electron and ion Langmuir plasma waves. This

is necessary to avoid having to take very small time steps. The finite difference forms of Ampere's law and the fluid plasma motion equations will be solved with the electric field and flow velocities treated implicitly. The calculation of the wave magnetic field will be shifted by a half-time-step relative to the electric field, while Faradays law will be solved explicitly. Inside the plasma volume, the electric and magnetic fields will be defined on staggered grids. First, a prediction of E_2 and E_3 at time step $n + 1/2$ will be calculated by using the three components of the electric field. Then $E_{1,n}$, which was obtained from the last time step, will be corrected by using $B_{2,n+1/2}$ and $B_{3,n+1/2}$. The corrected $E_{1,n}$ will then be used to correct $B_{2,n+1/2}$ and $B_{3,n+1/2}$. After the implicit correction, $E_{2,n+1}$ and $E_{3,n+1}$ will be explicitly calculated from the magnetic field at a time step of $n + 1/2$. The implicit correction will largely increase the precision of the field when the simulation time is long. At each node, all three components of a field vector will be specified. The benefit of such an approach is that the electric field vector at each node can be found by solving a system of only three linear equations, which is a very fast operation.

In the above system of equations describing ULF waves in interaction with the ionosphere and atmosphere, electromagnetic fields will be calculated. As the model is linear, the determination of electric currents in Amperes law requires only a time advance of ion and electron flow velocities. The latter will be found by solving linearized ion fluid motion equations. For Pc1-2 waves, the motion equations will have terms involving ion inertia, the electric field, ion gyromotion, and friction. For waves with a lower frequency, Pc3-5 and Pi1-2, ion gyromotion will be excluded and the motion equations transformed into a modified generalized Ohms law with Pedersen and Hall conductivities and the ion polarization current proportional to the ion mass and the time derivative of the wave electric field. Electron motion in the plane perpendicular to the geomagnetic field will be described using the ordinary generalized Ohm's law, making use of the reduced conductivity tensor (with Hall and Pedersen terms only). Electron motion along the geomagnetic field will be obtained using the linearized electron fluid motion equation that accounts for electron inertia, parallel electric fields, and friction. At the interface between the ionosphere and the atmosphere, ion and electron currents will be calculated using the ordinary generalized

Ohms law. The geomagnetic field may be specified using any available model, e.g., a compressed dipole [*Tsyganenko*, 1995; *Stern*, 1985].

We establish a second harmonic poloidal ULF wave by applying a constant frequency driver electric field located between $L = 4.5 - 7.5$. The driver frequency is set at 11.1mHz and the azimuthal wave number is $m = 44$. Figure 8.1 shows power spectra obtained from the wave model as a function of frequency and L (panel (a)), and as a function of frequency and latitude (panels (b) and (c)).

In the top panel of Figure 8.1, the natural frequency of field lines varies from about 20mHz at $L = 4.5$ to about 5mHz at $L = 7.5$. The driver frequency is found to match the natural frequency of field lines located at $L = 6.2$. In the range of L-shell shown in Figure 8.1(a), there is a dominant frequency component in the power spectra at the expected L-shell, along with higher harmonics. The bottom two panels of Figure 8.1 show the power spectral distribution along field lines at $L = 6.2$ and $L = 5.0$, respectively. The driver frequency and natural frequency are distinct in the lower panel ($L = 5$), but coincide in the middle panel ($L = 6.2$). The electric field oscillation is nearly zero at the equator for second harmonic FLRs and strongest at 40° latitude on both sides of the equator.

8.3 Test Particle Simulation of Drift-bounce Resonance

The Forward Liouville method is used to reconstruct the distribution function of H^+ ions. The method makes use of the Liouville's theorem. For a collisionless plasma described by the Vlasov equation, the distribution function of a single particle remains constant along particle trajectories [*Marchand*, 2010]. Each particle in the test particle simulation is a virtual particle and is tagged with the known numerical value of distribution function f calculated in the injection region. The distribution function can be tagged as any plasma distribution function. In the present study, they are tagged with an isotropic Maxwellian distribution

$$f(v) = n\frac{m_p}{2\pi k_B T}\exp\left(-\frac{m_p v^2}{2k_B T}\right). \tag{8.7}$$

where m_p is the proton mass, $k_B T$ is the product of Boltzmann's constant and temperature, and n_0 is the proton number density. The latter is considered to be a function of L. To build up a realistic and stable initial distribution of PSD, test particles are injected at a constant rate and randomly initialized with a uniform probability distribution function. Each particle brings information about the distribution function to the observed location (sampling volume). To reconstruct the distribution function near a virtual satellite location, the sampling volume is selected to be small enough to eliminate spatial variations in PSD. To accurately model PSD, large numbers of test particles must also be used. In the results shown we used several million test-particles.

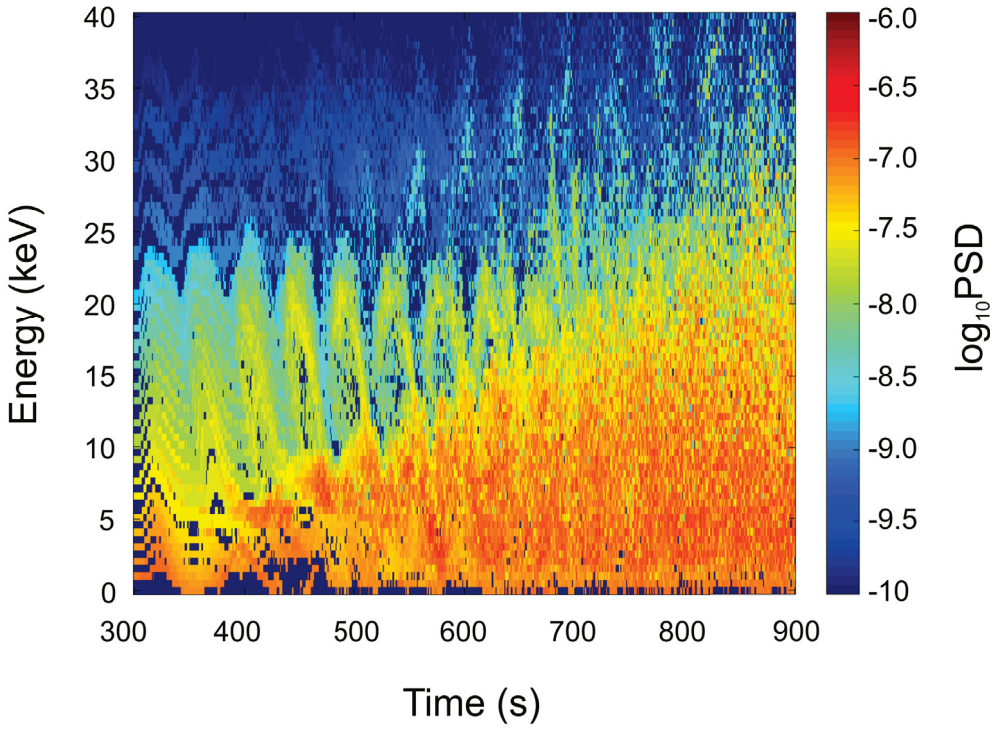

Figure 8.2: Phase space density of 90° pitch angle protons as a function of time at $L = 6.0$, latitude = 30°, longitude = 0°. The ULF wave is a second harmonic poloidal wave. The sampling volume is $0.02 R_e$ in radius, 2° in azimuthal angle, and 5° in polar angle. Energy is binned in step size of 1 keV.

In this section, we present simulations of drift-bounce resonance for protons that are initialized with a 30° equatorial pitch angle between $L = 5-7$. The first adiabatic invariants of the test particles range from 6.94 keV/nT to 0.250 keV/nT. To simulate

the behavior of particles following interplanetary shocks, particles are released into the wave fields 300 s after the second harmonic FLR is introduced into the system. This mimics a prompt turn-on of the amplitude of wave electric fields, which reach a constant amplitude of 20 mV/m during the first 300 s of the simulation.

Figure 8.2 shows the variation of phase space density observed in the sampling volume at $L = 6$. In the 300 s interval after the wave reaches constant amplitude, a modulation of phase space density is obvious in the energy range between 5 keV and 25 keV. According to the $N = 1$ drift-bounce resonance condition (Equation (2.56)), the resonant energy is 12.84 keV. The theoretical resonant energy is consistent with the energy range with the strongest modulation. In the time interval 600-900 s, the phase space densities at all energies are largely enhanced. This enhancement of phase space density at all energies corresponds to relatively fast heating of the plasma. This effect has been observed in association with large amplitude fundamental mode poloidal ULF waves in $N = 0$ drift resonance. The results presented here suggest this effect should occur in the case of $N = 1$ bounce resonance involving second harmonic mode waves.

8.4 Discussion

8.4.1 Ion Flux Modulation and Energization

The theory of drift-bounce resonance [*Southwood and Kivelson*, 1981] predicts that second harmonic poloidal mode FLRs should produce PSD modulations around 12.84 keV. In Figure 8.3, these modulations are also accompanied by energy dispersion for ion energies in the energy range of $5 - 25$ keV. For ions with an equatorial pitch angle $\alpha_{eq} = 45°$, the time delay for an ion moving from one point to another along a field line is computed according to the expression [*Fälthammar*, 1965]

$$\delta t = \frac{LR_E}{\sqrt{2W/M}} \int_{\lambda_1}^{\lambda_2} \cos\lambda \left[1 - \sin^2\alpha_{eq}\sqrt{\frac{1+3\sin^2\lambda}{\cos^6\lambda}}\right]^{-1/2} \tag{8.8}$$

where W denotes the energy of an ion, λ is the magnetic latitude, and α_{eq} is the equatorial pitch angle. The period of the dispersion signatures is equal to the wave

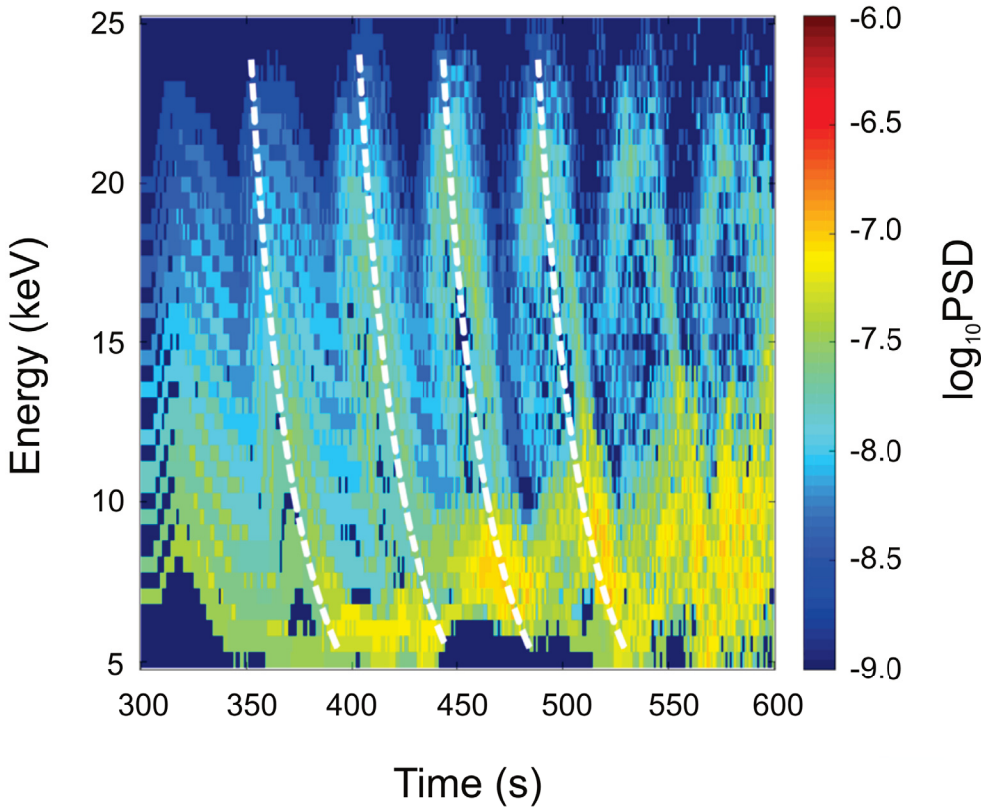

Figure 8.3: Phase space density of protons observed in the sampling volume located at $L = 6.0$, latitude of 0°, longitude of 0°. The size of the sampling volume is $0.02\mathrm{R_e}$ in radius, 2° in azimuthal angle, and 5° in polar angle. Energy binning of particles is 1 keV.

period. The duration of each dispersion signature is related to the latitude at which measurements are made, and so the detected pitch angle dispersion signatures in the sampling volume can be explained as thermal ions interacting with second harmonic poloidal mode ULF waves. The white dash lines in Figure 8.3 are the traces of energy dispersion predicted by Equation (8.8) which match the simulation results quite well.

8.4.2 Pitch Angle Distribution for Off-equatorial Flux Oscillations

To study the behavior of H^+ with different pitch angles at different latitudes, we initialized non-equatorial test particles using the Monte-Carlo method described in Section 5.3.1. Test particles were released from uniform random locations along the magnetic field line, and with a uniform random pitch angle within an unperturbed loss cone. The three panels in Figure 8.4 show different PSD variations as functions of pitch angles and time. From top to bottom, the three panels correspond to the PSD collected by three sampling volumes located at the same $L = 6.0$, but at a 30° latitude in the southern hemisphere, at the equator, and at a 30° latitude in the northern hemisphere, respectively. The wave and plasma parameters are identical to those in Section 8.4.1. According to the theory of drift-bounce resonance [*Southwood and Kivelson*, 1981; *Yang et al.*, 2011b], as the field-aligned beams of ions near the equator propagate along the magnetic field line to a higher latitude, velocity dispersions will emerge since the particles have different parallel velocity. Northern propagating particles with an equatorial pitch angle of $\alpha < 90°$ are collected by a sampling volume in the northern hemisphere at an earlier time than southern propagating particles with the same energy but equatorial pitch angle is $180° - \alpha$. The negative slope of ion flux modulation observed in the southern hemisphere is explained by the same mechanism. In the middle panel, the PSD modulation near 90° is weaker since the secondary harmonic FLRs have the weaker electric field at the equator, where particles with a 90° pitch angle experience weaker modulation by FLRs.

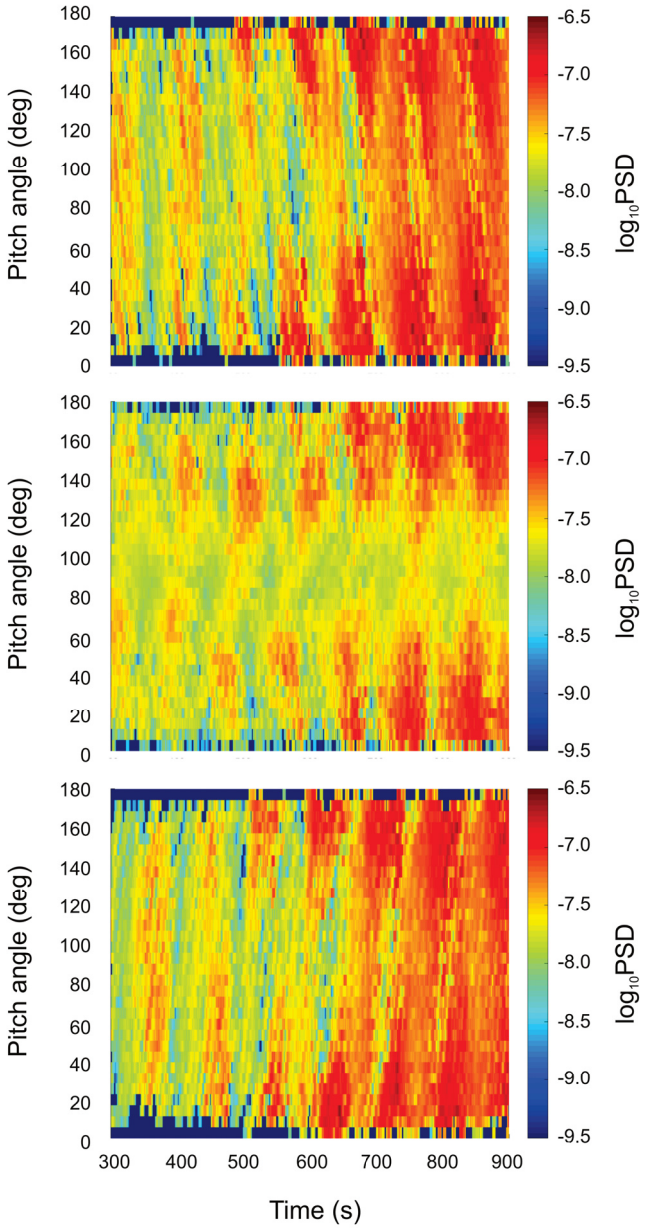

Figure 8.4: From top to bottom: Pitch angle distributions of H^+ phase space density as a function of time within energy range of $12 - 13$ keV observed at 30° southern hemisphere, at the equator, and at 30° northern hemisphere, respectively. The size of the sampling volumes is $0.02R_e$ in radius, 2° in azimuthal angle, and 5° in polar angle.

8.5 Conclusions and Future Work

In this chapter, we used an alternative ULF wave model and test-particle simulations to study drift-bounce resonance between ions and poloidal mode ULF waves. The forward Liouville method was used to reconstruct the distribution function of ions after they interacted with waves. Second-harmonic poloidal mode waves are efficient at energizing ions to tens of keV over timescales of tens of minutes. The test-particle simulations of bounce-resonance reproduce particle signatures that are commonly observed by satellites. The energy dispersion is found to be in agreement with theoretical predictions.

The realistic ionospheric conductivity ULF wave model requires more computing resource than the analytic ULF wave model because it computes global fields at high-resolution grids at every single time step. For the simulations in Section 8.4.1, the pitch angle is limited in a narrow range to guarantee that the phase-space sampling volumes gather large enough numbers of particles at every time step. For the off-equator simulations in Section 8.4.2, the test particle number is increased since particles need to distribute along field lines with different pitch angles. For these reasons, the resolution of figures in this chapter is not as high as that of the figures in previous chapters.

The model in this chapter can be used in backward Liouville simulations in the future. In this case, the magnetic field and the electric field on the global grids at each time step should be determined before tracing the particles backward in time. However, the size of global field grid data at each time snapshot is on the order of several hundred megabytes, and the high-resolution test particle simulations require a time step of much less than one second within an overall simulation range of several thousand seconds. The requirement for the size of field data storage and the I/O time consumption between the hard disk and memory makes the backward Liouville simulation with this model impractical. However, the backward Liouville simulation with the realistic ionospheric conductivity ULF wave model will be a worthwhile future study project. Moreover, the test particle models can be implemented into more space weather models, for example, it is worthwhile to couple the test particle

formalism with the Lyon-Fedder-Mobarry (LFM) global MHD model [*Lyon et al.*, 2004] on the three-dimensional cubed-sphere grids [*Ivan et al.*, 2013].

Chapter 9

Conclusions and Future Work

This thesis has concentrated on investigating the drift resonance and drift-bounce resonance between energetic particles and Pc3-5 Alfvénic ULF waves in the Earth's inner magnetosphere. We have developed numerical models to simulate dynamics of O^+ ions, H^+ ions and electrons affected by MHD Alfvén waves in a dipole magnetic field. The simulation results are used to interpret differential flux oscillations caused by ULF wave events in the magnetosphere. Observational data from different satellite projects, such as Cluster and Van Allen Probes, and from the CARISMA ground magnetometer observatory array are introduced to investigate the characteristics of ULF waves and the corresponding energetic particle flux variations. The ULF waves events presented in this thesis are caused by different mechanisms, such as interplanetary shock and plasma instability. Our simulation results show high consistency with the differential fluxes observed in these events.

We introduced relevant space physics concepts as the background of this thesis in Chapter 1. The sun and solar wind are important drivers of ULF waves in the magnetosphere. We then reviewed different regions of the magnetosphere to provide insight into the plasma environment for ULF waves and high-energy particles in the radiation belts. We also briefly reviewed geomagnetic storms and substorms which are related to the generation of ULF waves. The motivation of this thesis was summarized at the end of Chapter 1.

Chapter 2 briefly reviewed the theoretical backgrounds of ULF waves, test particle motions, and wave-particle interaction processes. This chapter includes the MHD

theory of Alfvén waves, the adiabatic motion of ions and electrons in a dipole magnetosphere, and the drift/drift-bounce resonance condition. Landau damping and flux modulation were also discussed as the results of drift/drift-bounce resonance.

Chapter 3 presented observational studies about the ULF wave damping mechanisms. Two ULF wave events after interplanetary shocks observed by Cluster on November 7, 2004, and August 30, 2001 were examined in this chapter. The ULF waves excited by interplanetary shocks and solar wind pressure impulses led to a high decay rate of wave amplitude in these two events. The energy exchanged between the wave and particles through Landau damping is considered to be more efficient when heavy ions such as O^+ are present. A comparison between multi-satellite observations also suggests that Landau damping is more effective in the plasmasphere boundary layer due to the relatively higher proportion of resonant ions that exist in that region. At the end of Chapter 3, we used our models to compare the energization effects of a fast-damped ULF wave on O^+ and H^+ ions in plasma environments with different thermal energy.

Chapter 4 showed the detailed mathematical descriptions of our MHD Alfvén wave model including derivations and assumptions. An analytical solution of the field line resonance eigenfunction with self-consistent electric and magnetic fields was obtained based on a widely used Alfvén wave velocity distribution. By adding an external monochromatic wave driver with harmonic dependence, we can study the excitation and damping of waves. We also estimate the contribution of the phase-mixing effect in our model and showed an example of its effects on the evolution of phase difference across L-shells.

Computational simulations of drift-bounce resonance are based on the wave model described in Chapter 4, while different descriptions about the particle dynamics affected by ULF wave fields are discussed in Chapter 5. A set of test particle simulation methods, the Liouville methods, were used to reproduce the differential flux observations in this thesis. The detailed implementation of these methods in our computational code is a main topic in Chapter 5. We used the full Lorentz model and guiding center model to describe the 3D dynamics of different species of particles

in the magnetosphere. Large gyro-radius ions were described using the full Lorentz model, while the high gyro-frequency electrons were described using the guiding center model. Chapter 5 includes mathematical models and numerical implementations of these two different models. In Section 5.5.1, we show an example of successfully reproducing the drift resonance between H^+ ions and ULF waves on April 11, 2014 by comparing with results of *Zhou et al.* [2016]. Section 5.5.2 provided the simulation results about the drift resonance between low-m ULF wave and relativistic electrons with energy of several hundred keV. The difference in drift resonance conditions between the relativistic electrons and non-relativistic H^+ ions are compared.

Chapter 6 presented implementations of the models that we used to investigate the pitch angle and energy dependence of ion differential fluxes measured by the Van Allen Probes spacecraft on October 6, 2012. An analysis of the satellite data reveals modulations in differential flux resulting from drift resonance between H^+ ions and the fundamental mode poloidal Alfvén waves detected near the magnetic equator at $L \sim 5.7$. Results obtained from simulations reproduced important features of the observations, including a substantial enhancement of the differential flux between $\sim 20^\circ - 40^\circ$ pitch angle for ion energies between $\sim 90 - 220$ keV, and an absence of flux modulations at 90°. The numerical results are in good agreement with observations and predictions of drift-bounce resonance theory and demonstrate that particle acceleration by ULF waves in the Earth's magnetosphere can be understood using relatively simple wave and test particle models.

Chapter 7 investigated the drift-resonance between electrons and ULF waves with the guiding center test particle model. Using simulations, we reproduced the features of electron flux modulation in an ULF waves event on October 31, 2012 [*Claudepierre et al.*, 2013]. We also estimated the effect of finite energy bin size on satellite instruments by comparing the binned and unbinned residual flux obtained from high-energy-resolution simulations. This chapter also included simulations of O^+ ions undergoing $N = 0$ drift resonance and $N = -2$ drift-bounce resonance, to provide insight into the dynamics of heavy ions that interact with ULF waves. These simulations illustrate the expected behavior of ring current energetic ion populations in a region where poloidal mode ULF waves are ubiquitous.

Chapter 8 includes another MHD Alfvén wave model with a more realistic ionosphere boundary condition. The forward Liouville method was used to reconstruct the distribution function of ions interacting with ULF waves. Second-harmonic poloidal mode waves are efficient at energizing ions to tens of keV over timescales of tens of minutes. The test-particle simulations of bounce-resonance reproduce particle signatures that are commonly observed by satellites. The energy dispersion was found to be in agreement with theoretical predictions.

Future work may include more simulations on particles with equatorial pitch angles near the loss cone. In previous studies, the underlying drift/drift-bounce resonance theory takes was more concerned with the variation of a particle's energy. However, a particle's equatorial pitch angle will change when it is moving with conserved first and second adiabatic invariants across L-shells in ULF waves. Recently, preliminary simulation results have been obtained for the pitch angle variation of test particles near the loss cone. It is worthwhile to study the relationship between energy particle precipitation and ULF waves with our model in the future. Another worthwhile subject for future study is backward Liouville simulations with a ULF wave model with realistic ionospheric conductivity. Moreover, the test particle models can be implemented into more space weather models. For example, it is worthwhile to couple the test particle formalism with the Lyon-Fedder-Mobarry (LFM) global MHD model [*Lyon et al.*, 2004] on the three-dimensional cubed-sphere grids [*Ivan et al.*, 2013].

Bibliography

Akasofu, S.-I. (1964), The development of the auroral substorm, *Planetary and Space Science*, *12*(4), 273–282.

Alfvén, H. (1942), Existence of electromagnetic-hydrodynamic waves, *Nature*, *150*(3805), 405.

Allan, W., and F. B. Knox (1979), A dipole field model for axisymmetric Alfvén waves with finite ionosphere conductivities, *Planetary and Space Science*, *27*, 79–85, doi:10.1016/0032-0633(79)90149-1.

Allan, W., and E. M. Poulter (1992), ULF waves-their relationship to the structure of the Earth's magnetosphere, *Reports on Progress in Physics*, *55*, 533–598, doi:10.1088/0034-4885/55/5/001.

Baker, D. N., P. R. Higbie, and R. D. Belian (1980), Multispacecraft observations of energetic electron flux pulsations at 6.6 RE, *Journal of Geophysical Research: Space Physics*, *85*(A12), 6709–6718, doi:10.1029/JA085iA12p06709.

Balogh, A., et al. (2001), The Cluster Magnetic Field Investigation: overview of in-flight performance and initial results, *Annales Geophysicae*, *19*, 1207–1217, doi:10.5194/angeo-19-1207-2001.

Baumjohann, W., and R. A. Treumann (1996), Basic space plasma physics, *Imperial Coll.*

Blake, J., M. Gussenhoven, E. Mullen, and R. Fillius (1992a), Identification of an unexpected space radiation hazard, *IEEE transactions on nuclear science*, *39*(6), 1761–1764.

Blake, J., W. Kolasinski, R. Fillius, and E. Mullen (1992b), Injection of electrons and protons with energies of tens of MeV into L $<$ 3 on 24 March 1991, *Geophysical Research Letters*, *19*(8), 821–824.

Blake, J., et al. (2013), The magnetic electron ion spectrometer (MagEIS) instruments aboard the radiation belt storm probes (RBSP) spacecraft, *Space Science Reviews*, *179*(1-4), 383–421.

Brekke, A., T. Feder, and S. Berger (1987), Pc4 giant pulsations recorded in Tromsø, 1929-1985, *Journal of Atmospheric and Terrestrial Physics*, *49*(10), 1027 – 1032, doi:https://doi.org/10.1016/0021-9169(87)90109-7.

Brito, T., L. Woodger, M. Hudson, and R. Millan (2012), Energetic radiation belt electron precipitation showing ULF modulation, *Geophysical Research Letters*, *39*(22).

Brown, W., L. Cahill, L. Davis, C. McIlwain, and C. Roberts (1968), Acceleration of trapped particles during a magnetic storm on April 18, 1965, *Journal of Geophysical Research*, *73*(1), 153–161.

Burke, W. J. (2007), Penetration electric fields: a volland–stern approach, *Journal of atmospheric and solar-terrestrial physics*, *69*(10-11), 1114–1126.

Carpenter, D. L., et al. (2002), Small-scale field-aligned plasmaspheric density structures inferred from the Radio Plasma Imager on IMAGE, *Journal of Geophysical Research: Space Physics*, *107*(A9).

Chappell, C., K. Harris, and G. Sharp (1970), A study of the influence of magnetic activity on the location of the plasmapause as measured by OGO 5, *Journal of Geophysical Research*, *75*(1), 50–56.

Chappell, C., K. Harris, and G. Sharp (1971), The dayside of the plasmasphere, *Journal of Geophysical Research*, *76*(31), 7632–7647.

Chen, L., and A. Hasegawa (1988), On magnetospheric hydromagnetic waves excited by energetic ring-current particles, *Journal of Geophysical Research: Space Physics*, *93*(A8), 8763–8767.

Chen, Y., G. D. Reeves, and R. H. Friedel (2007), The energization of relativistic electrons in the outer Van Allen radiation belt, *Nature Physics*, *3*(9), 614.

Chisham, G., and D. Orr (1991), Statistical studies of giant pulsations (Pgs): Harmonic mode, *Planetary and Space Science*, *39*(7), 999 – 1006, doi: https://doi.org/10.1016/0032-0633(91)90105-J.

Chisham, G., and D. Orr (1997), A statistical study of the local time asymmetry of Pc 5 ULF wave characteristics observed at midlatitudes by SAMNET, *Journal of Geophysical Research: Space Physics*, *102*(A11), 24,339–24,350, doi: 10.1029/97JA01801.

Chisham, G., D. Orr, M. Taylor, and H. Luhr (1990), The magnetic and optical signature of a Pg pulsation, *Planetary and Space Science*, *38*(11), 1443 – 1456, doi:https://doi.org/10.1016/0032-0633(90)90119-B.

Chisham, G., D. Orr, and T. Yeoman (1992), Observations of a giant pulsation across an extended array of ground magnetometers and on auroral radar, *Planetary and Space Science*, *40*(7), 953 – 964, doi:https://doi.org/10.1016/0032-0633(92)90135-B.

Chisham, G., et al. (2007), A decade of the super dual auroral radar network (superdarn): Scientific achievements, new techniques and future directions, *Surveys in Geophysics*, *28*(1), 33–109.

Claudepierre, S. G., S. R. Elkington, and M. Wiltberger (2008), Solar wind driving of magnetospheric ULF waves: Pulsations driven by velocity shear at the magnetopause, *Journal of Geophysical Research (Space Physics)*, *113*, A05218, doi: 10.1029/2007JA012890.

Claudepierre, S. G., M. Wiltberger, S. R. Elkington, W. Lotko, and M. K. Hudson (2009), Magnetospheric cavity modes driven by solar wind dynamic pressure fluctuations, *Geophysical Research Letters*, *36*, L13101, doi:10.1029/2009GL039045.

Claudepierre, S. G., M. K. Hudson, W. Lotko, J. G. Lyon, and R. E. Denton (2010), Solar wind driving of magnetospheric ULF waves: Field line resonances driven by dynamic pressure fluctuations, *Journal of Geophysical Research (Space Physics)*, *115*, A11202, doi:10.1029/2010JA015399.

Claudepierre, S. G., et al. (2013), Van Allen Probes observation of localized drift resonance between poloidal mode ultra-low frequency waves and 60 kev electrons, *Geophysical Research Letters*, *40*(17), 4491–4497, doi:10.1002/grl.50901.

Davis, T. N., and M. Sugiura (1966), Auroral electrojet activity index AE and its universal time variations, *Journal of Geophysical Research*, *71*(3), 785–801.

Degeling, A., R. Rankin, K. Kabin, R. Marchand, and I. Mann (2007), The effect of ULF compressional modes and field line resonances on relativistic electron dynamics, *Planetary and Space Science*, *55*(6), 731 – 742, doi: https://doi.org/10.1016/j.pss.2006.04.039, ultra-Low Frequency Waves in the Magnetosphere.

Degeling, A. W., and R. Rankin (2008), Resonant drift echoes in electron phase space density produced by dayside Pc5 waves following a geomagnetic storm, *Journal of Geophysical Research: Space Physics*, *113*(A10), doi:10.1029/2008JA013254, a10220.

Degeling, A. W., L. G. Ozeke, R. Rankin, I. R. Mann, and K. Kabin (2008), Drift resonant generation of peaked relativistic electron distributions by Pc 5 ULF waves, *Journal of Geophysical Research: Space Physics*, *113*(A2), doi: 10.1029/2007JA012411, a02208.

Degeling, A. W., R. Rankin, K. Kabin, I. J. Rae, and F. R. Fenrich (2010), Modeling ULF waves in a compressed dipole magnetic field, *Journal of Geophysical Research: Space Physics*, *115*(A10), doi:10.1029/2010JA015410, a10212.

Degeling, A. W., R. Rankin, and S. R. Elkington (2011), Convective and diffusive ULF wave driven radiation belt electron transport, *Journal of Geophysical Research: Space Physics*, *116*(A12), doi:10.1029/2011JA016896, a12217.

Degeling, A. W., R. Rankin, K. Murphy, and I. J. Rae (2013), Magnetospheric convection and magnetopause shadowing effects in ULF wave-driven energetic electron transport, *Journal of Geophysical Research: Space Physics*, *118*(6), 2919–2927, doi: 10.1002/jgra.50219.

Degeling, A. W., R. Rankin, and Q.-G. Zong (2014), Modeling radiation belt electron acceleration by ULF fast mode waves, launched by solar wind dynamic pressure fluctuations, *Journal of Geophysical Research: Space Physics*, *119*(11), 8916–8928, doi:10.1002/2013JA019672.

Dungey, J. (1954), The attenuation of Alfvén waves, *Journal of Geophysical Research*, *59*(3), 323–328.

Dungey, J. W. (1955), *Electrodynamics of the Outer Atmosphere*, 229 pp.

Elkington, S. R., M. K. Hudson, and A. A. Chan (1999), Acceleration of relativistic electrons via drift-resonant interaction with toroidal-mode Pc-5 ULF oscillations, *Geophysical Research Letters*, *26*(21), 3273–3276, doi:10.1029/1999GL003659.

Elkington, S. R., M. K. Hudson, M. J. Wiltberger, and J. G. Lyon (2002), MHD/particle simulations of radiation belt dynamics, *Journal of Atmospheric and Solar-Terrestrial Physics*, *64*, 607–615, doi:10.1016/S1364-6826(02)00018-4.

Elkington, S. R., M. K. Hudson, and A. A. Chan (2003), Resonant acceleration and diffusion of outer zone electrons in an asymmetric geomagnetic field, *Journal of Geophysical Research (Space Physics)*, *108*, 1116, doi:10.1029/2001JA009202.

Elkington, S. R., M. Wiltberger, A. A. Chan, and D. N. Baker (2004), Physical models of the geospace radiation environment, *Journal of Atmospheric and Solar-Terrestrial Physics*, *66*, 1371–1387, doi:10.1016/j.jastp.2004.03.023.

Eriksson, P., L. G. Blomberg, S. Schaefer, and K.-H. Glassmeier (2006), On the excitation of ULF waves by solar wind pressure enhancements, in *Annales Geophysicae*, vol. 24, pp. 3161–3172.

Evans, R. M., M. Opher, V. Jatenco-Pereira, and T. I. Gombosi (2009), Surface Alfvén Wave damping in a three-dimensional simulation of the solar wind, *The Astrophysical Journal*, *703*, 179–186, doi:10.1088/0004-637X/703/1/179.

Fairfield, D. H., A. Otto, T. Mukai, S. Kokubun, R. P. Lepping, J. T. Steinberg, A. J. Lazarus, and T. Yamamoto (2000), Geotail observations of the Kelvin-Helmholtz instability at the equatorial magnetotail boundary for parallel northward fields, *Journal of Geophysical Research: Space Physics*, *105*, 21,159–21,174, doi:10.1029/1999JA000316.

Fälthammar, C.-G. (1965), Effects of time-dependent electric fields on geomagnetically trapped radiation, *Journal of Geophysical Research*, *70*(11), 2503–2516.

Fei, Y., A. A. Chan, S. R. Elkington, and M. J. Wiltberger (2006), Radial diffusion and MHD particle simulations of relativistic electron transport by ULF waves in the September 1998 storm, *Journal of Geophysical Research: Space Physics*, *111*(A12).

Foster, J. C., J. R. Wygant, M. K. Hudson, A. J. Boyd, D. N. Baker, P. J. Erickson, and H. E. Spence (2015), Shock-induced prompt relativistic electron acceleration in the inner magnetosphere, *Journal of Geophysical Research: Space Physics*, *120*(3), 1661–1674, doi:10.1002/2014JA020642, 2014JA020642.

Fraser, B. J., J. L. Horwitz, J. A. Slavin, Z. C. Dent, and I. R. Mann (2005), Heavy ion mass loading of the geomagnetic field near the plasmapause and ULF wave implications, *Geophysical Research Letters*, *32*, L04102, doi:10.1029/2004GL021315.

Fritz, T., and Q. Zong (2005), The magnetospheric cusps: A summary, *Surveys in geophysics*, *26*(1), 409.

Gallagher, D. L., P. D. Craven, and R. H. Comfort (2000), Global core plasma model, *Journal of Geophysical Research: Space Physics*, *105*(A8), 18,819–18,833.

Glassmeier, K.-H. (1980), Magnetometer array observations of a giant pulsation event, *Journal of Geophysics Zeitschrift Geophysik*, *48*, 127–138.

Glassmeier, K.-H., C. Othmer, R. Cramm, M. Stellmacher, and M. Engebretson (1999), Magnetospheric field line resonances: A comparative planetology approach, *Surveys in Geophysics*, *20*(1), 61–109.

Grebowsky, J. (1971), Time-dependent plasmapause motion, *Journal of Geophysical Research*, *76*(25), 6193–6197.

Green, C. (1979), Observations of Pg pulsations in the northern auroral zone and at lower latitude conjugate regions, *Planetary and Space Science*, *27*(1), 63–77.

Green, C. (1985), Giant pulsations in the plasmasphere, *Planetary and space science*, *33*(10), 1155–1168.

Greenwald, R. A., and A. D. M. Walker (1980), Energetics of long period resonant hydromagnetic waves, *Geophysical Research Letters*, *7*, 745–748, doi: 10.1029/GL007i010p00745.

Hao, Y., et al. (2017), Relativistic electron dynamics produced by azimuthally localized poloidal mode ULF waves: Boomerang-shaped pitch angle evolutions, *Geophysical Research Letters*, *44*(15), 7618–7627.

Hasegawa, A. (1971), Drift-wave instabilities of a compressional mode in a high-β plasma, *Physical Review Letters*, *27*(1), 11.

Hasegawa, H., M. Fujimoto, T.-D. Phan, H. Reme, A. Balogh, M. Dunlop, C. Hashimoto, and R. TanDokoro (2004), Transport of solar wind into Earth's magnetosphere through rolled-up Kelvin–Helmholtz vortices, *Nature*, *430*(7001), 755–758.

Hasegawa, H., M. Fujimoto, T.-D. Phan, H. Rème, A. Balogh, M. W. Dunlop, C. Hashimoto, and R. TanDokoro (2004), Transport of solar wind into Earth's magnetosphere through rolled-up Kelvin-Helmholtz vortices, , *430*, 755–758, doi: 10.1038/nature02799.

Hess, W., E. Canfield, and R. Lingenfelter (1961), Cosmic-ray neutron demography, *Journal of Geophysical Research*, *66*(3), 665–677.

Heyvaerts, J., and E. Priest (1983), Coronal heating by phase-mixed shear Alfvén waves, *Astronomy and Astrophysics*, *117*, 220–234.

Hollweg, J. V. (1971), Nonlinear Landau Damping of Alfvén Waves, *Physical Review Letters*, *27*, 1349–1352, doi:10.1103/PhysRevLett.27.1349.

Horne, R. B., and R. M. Thorne (1998), Potential waves for relativistic electron scattering and stochastic acceleration during magnetic storms, *Geophysical Research Letters*, *25*(15), 3011–3014.

Horne, R. B., et al. (2005), Wave acceleration of electrons in the Van Allen radiation belts, *Nature*, *437*(7056), 227.

Hudson, M., S. Elkington, J. Lyon, and C. Goodrich (2000), Increase in relativistic electron flux in the inner magnetosphere: ULF wave mode structure, *Advances in Space Research*, *25*(12), 2327–2337.

Hudson, M., R. Denton, M. Lessard, E. Miftakhova, and R. Anderson (2004), A study of Pc-5 ULF oscillations, *Annales Geophysicae*, *22*, 289–302, doi:10.5194/angeo-22-289-2004.

Hudson, M. K., B. T. Kress, H.-R. Mueller, J. A. Zastrow, and J. B. Blake (2008), Relationship of the Van Allen radiation belts to solar wind drivers, *Journal of Atmospheric and Solar-Terrestrial Physics*, *70*(5), 708–729.

Hughes, W., and D. Southwood (1976), The screening of micropulsation signals by the atmosphere and ionosphere, *Journal of Geophysical Research*, *81*(19), 3234–3240.

Inhester, B. (1987), Numerical modeling of hydromagnetic wave coupling in the magnetosphere, *Journal of Geophysical Research: Space Physics*, *92*, 4751–4756, doi: 10.1029/JA092iA05p04751.

Ivan, L., H. De Sterck, S. A. Northrup, and C. P. Groth (2013), Hyperbolic conservation laws on three-dimensional cubed-sphere grids: a parallel solution-adaptive simulation framework, *J. Comput. Phys*, *255*, 205–227.

Jacobs, J. A., Y. Kato, S. Matsushita, and V. A. Troitskaya (1964), Classification of geomagnetic micropulsations, *Journal of Geophysical Research*, *69*, 180–181, doi: 10.1029/JZ069i001p00180.

James, M., T. Yeoman, P. Mager, and D. Y. Klimushkin (2013), The spatio-temporal characteristics of ULF waves driven by substorm injected particles, *Journal of Geophysical Research: Space Physics*, *118*(4), 1737–1749.

Jordanova, V., L. Kistler, J. Kozyra, G. Khazanov, and A. Nagy (1996), Collisional losses of ring current ions, *Journal of Geophysical Research: Space Physics*, *101*(A1), 111–126.

Kepko, L., and H. E. Spence (2003), Observations of discrete, global magnetospheric oscillations directly driven by solar wind density variations, *Journal of Geophysical Research (Space Physics)*, *108*, 1257, doi:10.1029/2002JA009676.

Kivelson, M. G., and C. T. Russell (1995), Introduction to space physics, *Cambridge university press*.

Kivelson, M. G., and D. J. Southwood (1985), Charged particle behavior in low-frequency geomagnetic pulsations: IV. compressional waves, *Journal of Geophysical Research: Space Physics*, *90*(A2), 1486–1498.

Kivelson, M. G., and D. J. Southwood (1986), Coupling of global magnetospheric MHD eigenmodes to field line resonances, *Journal of Geophysical Research: Space Physics*, *91*, 4345–4351, doi:10.1029/JA091iA04p04345.

Kremser, G., A. Korth, J. Fejer, B. Wilken, A. Gurevich, and E. Amata (1981), Observations of quasi-periodic flux variations of energetic ions and electrons associated with Pc5 geomagnetic pulsations, *Journal of Geophysical Research: Space Physics*, *86*(A5), 3345–3356.

Li, X., I. Roth, M. Temerin, J. Wygant, M. Hudson, and J. Blake (1993), Simulation of the prompt energization and transport of radiation belt particles during the March 24, 1991 SSC, *Geophysical Research Letters*, *20*(22), 2423–2426.

Liu, W., G. Rostoker, and D. Baker (1999), Internal acceleration of relativistic electrons by large-amplitude ULF pulsations, *Journal of Geophysical Research: Space Physics*, *104*(A8), 17,391–17,407.

Loto'aniu, T. M., I. R. Mann, L. G. Ozeke, A. A. Chan, Z. C. Dent, and D. K. Milling (2006), Radial diffusion of relativistic electrons into the radiation belt slot region during the 2003 Halloween geomagnetic storms, *Journal of Geophysical Research (Space Physics)*, *111*, A04218, doi:10.1029/2005JA011355.

Lui, A., and C. Cheng (2001), Resonance frequency of stretched magnetic field lines based on a self-consistent equilibrium magnetosphere model, *Journal of Geophysical Research: Space Physics*, *106*(A11), 25,793–25,802.

Lui, A., P. Perreault, S.-I. Akasofu, and C. Anger (1973), The diffuse aurora, *Planetary and Space Science*, *21*(5), 857–861.

Lyon, J., J. Fedder, and C. Mobarry (2004), The lyon–fedder–mobarry (LFM) global MHD magnetospheric simulation code, *Journal of Atmospheric and Solar-Terrestrial Physics*, *66*(15-16), 1333–1350.

Lyons, L., and D. Evans (1984), An association between discrete aurora and energetic particle boundaries, *Journal of Geophysical Research: Space Physics*, *89*(A4), 2395–2400.

Lyons, L. R., R. M. Thorne, and C. F. Kennel (1972), Pitch-angle diffusion of radiation belt electrons within the plasmasphere, *Journal of Geophysical Research*, *77*(19), 3455–3474.

Lysak, R. L., and W. Lotko (1996), On the kinetic dispersion relation for shear Alfvén waves, *Journal of Geophysical Research: Space Physics*, *101*, 5085–5094, doi:10.1029/95JA03712.

Lysak, R. L., C. L. Waters, and M. D. Sciffer (2013), Modeling of the ionospheric Alfvén resonator in dipolar geometry, *Journal of Geophysical Research: Space Physics*, *118*(4), 1514–1528.

Mann, I., and G. Chisham (2000), Comment on "Concerning the generation of geomagnetic giant pulsations by drift-bounce resonance ring current instabilities" by k.-h. glassmeier et al., ann. geophysicae, 17, 338/350,(1999), in *Annales Geophysicae*, vol. 18, pp. 161–166, Springer.

Mann, I. R., A. N. Wright, and P. S. Cally (1995), Coupling of magnetospheric cavity modes to field line resonances: A study of resonance widths, *Journal of Geophysical Research: Space Physics*, *100*(A10), 19,441–19,456.

Mann, I. R., et al. (2013), Discovery of the action of a geophysical synchrotron in the Earth's Van Allen radiation belts, *Nature communications*, *4*, 2795.

Marchand, R. (2010), Test-particle simulation of space plasmas, *Communications in Computational Physics*, *8*(3), 471.

Marklund, G., L. Blomberg, C.-G. Fälthammar, R. Erlandson, and T. Potemra (1990), Signatures of the high-altitude polar cusp and dayside auroral regions as seen by the Viking Electric Field Experiment, *Journal of Geophysical Research: Space Physics*, *95*(A5), 5767–5780.

Menk, F. W., and C. L. Waters (2013), Magnetoseismology: Ground-based remote sensing of Earth's magnetosphere, *John Wiley & Sons*.

Menk, F. W., I. R. Mann, A. J. Smith, C. L. Waters, M. A. Clilverd, and D. K. Milling (2004), Monitoring the plasmapause using geomagnetic field line resonances, *Journal of Geophysical Research (Space Physics)*, *109*, A04216, doi: 10.1029/2003JA010097.

Mewaldt, R. (1994), Galactic cosmic ray composition and energy spectra, *Advances in Space Research*, *14*(10), 737–747.

Moldwin, M. B., L. Downward, H. Rassoul, R. Amin, and R. Anderson (2002), A new model of the location of the plasmapause: CRRES results, *Journal of Geophysical Research: Space Physics*, *107*(A11).

Motoba, T., K. Takahashi, J. V. Rodriguez, and C. T. Russell (2015), Giant pulsations on the afternoonside: Geostationary satellite and ground observations, *Journal of Geophysical Research: Space Physics*, *120*(10), 8350–8367.

Moullard, O., A. Masson, H. Laakso, M. Parrot, P. Décréau, O. Santolik, and M. Andre (2002), Density modulated whistler mode emissions observed near the plasmapause, *Geophysical Research Letters*, *29*(20), 1975, doi:10.1029/2002GL015101.

Newton, R. S., D. J. Southwood, and W. J. Hughes (1978), Damping of geomagnetic pulsations by the ionosphere, *Planetary and Space Science*, *26*, 201–209, doi: 10.1016/0032-0633(78)90085-5.

Northrop, T. G. (1963), The adabatic motion of charged particles, *Interscience Publishers*, (21).

O'Brien, T., R. McPherron, D. Sornette, G. Reeves, R. Friedel, and H. Singer (2001), Which magnetic storms produce relativistic electrons at geosynchronous orbit?, *Journal of Geophysical Research: Space Physics*, *106*(A8), 15,533–15,544.

Odera, T. (1986), Solar wind controlled pulsations-A review, *Reviews of Geophysics*, *24*, 55–74.

Okpala, K. C., and C. E. Ogbonna (2017), On the mid-latitude ionospheric storm association with intense geomagnetic storms, *Advances in Space Research*.

Ozeke, L. G., and I. R. Mann (2008), Energization of radiation belt electrons by ring current ion driven ULF waves, *Journal of Geophysical Research (Space Physics)*, *113*, A02201, doi:10.1029/2007JA012468.

Parker, E. N. (1958), Dynamics of the interplanetary gas and magnetic fields., *The Astrophysical Journal*, *128*, 664.

Poulter, E., W. Allan, E. Nielsen, and K.-H. Glassmeier (1983), Stare radar observations of a Pg pulsation, *Journal of Geophysical Research: Space Physics*, *88*(A7), 5668–5676.

Pu, Z.-Y., and M. G. Kivelson (1983), Kelvin: Helmholtz instability at the magnetopause: Solution for compressible plasmas, *Journal of Geophysical Research: Space Physics*, *88*(A2), 841–852.

Radoski, H. R., and J. F. McClay (1967), The hydromagnetic toroidal resonance, *Journal of Geophysical Research*, *72*(19), 4899–4903.

Rae, I., I. Mann, Z. Dent, D. Milling, E. Donovan, and E. Spanswick (2007), Multiple field line resonances: Optical, magnetic and absorption signatures, *Planetary and Space Science*, *55*(6), 701–713.

Rae, I. J., et al. (2005), Evolution and characteristics of global Pc5 ULF waves during a high solar wind speed interval, *Journal of Geophysical Research (Space Physics)*, *110*, A12211, doi:10.1029/2005JA011007.

Rankin, R., J. Samson, and P. Frycz (1993), Simulations of driven field line resonances in the earth's magnetosphere, *Journal of Geophysical Research: Space Physics*, *98*(A12), 21,341–21,352.

Rankin, R., P. Frycz, V. Tikhonchuk, and J. Samson (1994), Nonlinear standing shear Alfvén waves in the Earth's magnetosphere, *Journal of Geophysical Research: Space Physics*, *99*(A11), 21,291–21,301.

Rankin, R., J. Samson, V. Tikhonchuk, and I. Voronkov (1999), Auroral density fluctuations on dispersive field line resonances, *Journal of Geophysical Research: Space Physics*, *104*(A3), 4399–4410.

Rankin, R., F. Fenrich, and V. Tikhonchuk (2000), Shear Alfvén waves on stretched magnetic field lines near midnight in earth's magnetosphere, *Geophysical research letters*, *27*(20), 3265–3268.

Rankin, R., R. Marchand, J. Lu, K. Kabin, and V. Tikhonchuk (2005), Theory of dispersive shear Alfvén wave focusing in Earth's magnetosphere, *Geophysical research letters*, *32*(5).

Rankin, R., C. E. J. Watt, and J. C. Samson (2007), Self-consistent wave-particle interactions in dispersive scale long-period field-line-resonances, *Geophysical Research Letters*, *34*, L23103, doi:10.1029/2007GL031317.

Rankin, R., C. Wang, D. Sydorenko, Y. Wang, Q.-G. Zong, and X. Zhou (2016), Simulation of bounce resonance ULF wave-particle interactions, in *URSI Asia-Pacific Radio Science Conference (URSI AP-RASC)*, pp. 956–959, IEEE.

Reiff, P., T. Hill, and J. Burch (1977), Solar wind plasma injection at the dayside magnetospheric cusp, *Journal of Geophysical Research*, *82*(4), 479–491.

Ren, J., Q. Zong, X. Zhou, R. Rankin, and Y. Wang (2016), Interaction of ULF waves with different ion species: Pitch angle and phase space density implications, *Journal of Geophysical Research: Space Physics*, *121*(10), 9459–9472.

Robinson, P., and P. Coakley (1992), Spacecraft charging-progress in the study of dielectrics and plasmas, *IEEE transactions on electrical insulation*, *27*(5), 944–960.

Roelof, E. C., and D. G. Sibeck (1993), Magnetopause shape as a bivariate function of interplanetary magnetic field Bz and solar wind dynamic pressure, *Journal of Geophysical Research: Space Physics*, *98*(A12), 21,421–21,450.

Rostoker, G., H.-L. Lam, and J. V. Olson (1979), Pc 4 giant pulsations in the morning sector, *Journal of Geophysical Research: Space Physics*, *84*(A9), 5153–5166.

Rostoker, G., S. Skone, and D. N. Baker (1998), On the origin of relativistic electrons in the magnetosphere associated with some geomagnetic storms, *Geophysical research letters*, *25*(19), 3701–3704.

Sandel, B., J. Goldstein, D. Gallagher, and M. Spasojevic (2003), Extreme ultraviolet imager observations of the structure and dynamics of the plasmasphere, *Space Science Reviews*, *109*(1), 25–46.

Schulz, M. (1971), Approximate second invariant for a dipole field, *Journal of Geophysical Research*, *76*(13), 3144–3148.

Schulz, M., and L. J. Lanzerotti (2012), Particle diffusion in the radiation belts, *Springer Science & Business Media*, *7*.

Sciffer, M., C. Waters, and F. Menk (2005), A numerical model to investigate the polarisation azimuth of ulf waves through an ionosphere with oblique magnetic fields, in *Annales Geophysicae*, vol. 23, pp. 3457–3471.

Shprits, Y. Y., D. Subbotin, A. Drozdov, M. E. Usanova, A. Kellerman, K. Orlova, D. N. Baker, D. L. Turner, and K.-C. Kim (2013), Unusual stable trapping of the ultrarelativistic electrons in the Van Allen radiation belts, *Nature Physics*, *9*(11), 699–703.

Sonnerup, B., G. Paschmann, I. Papamastorakis, N. Sckopke, G. Haerendel, S. Bame, J. Asbridge, J. Gosling, and C. Russell (1981), Evidence for magnetic field reconnection at the Earth's magnetopause, *Journal of Geophysical Research: Space Physics*, *86*(A12), 10,049–10,067.

Southwood, D. (1973), The behaviour of ULF waves and particles in the magnetosphere, *Planetary and Space Science*, *21*(1), 53–65.

Southwood, D. J. (1976), A general approach to low-frequency instability in the ring current plasma, *Journal of Geophysical Research*, *81*, 3340–3348, doi:10.1029/JA081i019p03340.

Southwood, D. J., and W. J. Hughes (1983), Theory of hydromagnetic waves in the magnetosphere, , *35*, 301–366, doi:10.1007/BF00169231.

Southwood, D. J., and M. G. Kivelson (1981), Charged particle behavior in low-frequency geomagnetic pulsations. I - Transverse waves, *Journal of Geophysical Research: Space Physics*, *86*, 5643–5655, doi:10.1029/JA086iA07p05643.

Southwood, D. J., and M. G. Kivelson (1982), Charged particle behavior in low-frequency geomagnetic pulsations. II - Graphical approach, *Journal of Geophysical Research: Space Physics*, *87*, 1707–1710, doi:10.1029/JA087iA03p01707.

Southwood, D. J., J. W. Dungey, and R. J. Etherington (1969), Bounce resonant interaction between pulsations and trapped particles, *Planetary and Space Science*, *17*, 349, doi:10.1016/0032-0633(69)90068-3.

Stern, D. P. (1985), Parabolic harmonics in magnetospheric modeling: The main dipole and the ring current, *Journal of Geophysical Research: Space Physics*, *90*(A11), 10,851–10,863.

Stewart, B. (1861), XXII. On the great magnetic disturbance which extended from August 28 to September 7, 1859, as recorded by photography at the Kew Observatory, *Philosophical Transactions of the Royal Society of London*, *151*, 423–430.

Stix, T. H. (1962), The Theory of Plasma Waves, *New York: McGraw-Hill*.

Summers, D., and C.-Y. Ma (2000), A model for generating relativistic electrons in the Earth's inner magnetosphere based on gyroresonant wave-particle interactions, *Journal of Geophysical Research: Space Physics*, *105*(A2), 2625–2639.

Summers, D., R. M. Thorne, and F. Xiao (1998), Relativistic theory of wave-particle resonant diffusion with application to electron acceleration in the magnetosphere, *Journal of Geophysical Research: Space Physics*, *103*, 20,487–20,500, doi:10.1029/98JA01740.

Summers, D., R. M. Thorne, and F. Xiao (1998), Relativistic theory of wave-particle resonant diffusion with application to electron acceleration in the magnetosphere, *Journal of Geophysical Research: Space Physics*, *103*(A9), 20,487–20,500.

Sydorenko, D., and R. Rankin (2012), Simulation of ionospheric disturbances created by Alfvén waves, *Journal of Geophysical Research: Space Physics*, *117*(A9).

Sydorenko, D., and R. Rankin (2013), Simulation of O+ upflows created by electron precipitation and Alfvén waves in the ionosphere, *Journal of Geophysical Research: Space Physics*, *118*(9), 5562–5578.

Takahashi, K., and A. Y. Ukhorskiy (2007), Solar wind control of Pc5 pulsation power at geosynchronous orbit, *Journal of Geophysical Research (Space Physics)*, *112*, A11205, doi:10.1029/2007JA012483.

Takahashi, K., P. R. Higbie, and D. N. Baker (1985), Azimuthal propagation and frequency characteristic of compressional Pc 5 waves observed at geostationary orbit, *Journal of Geophysical Research: Space Physics*, *90*, 1473–1485, doi:10.1029/JA090iA02p01473.

Takahashi, K., P. R. Higbie, and D. N. Baker (1985), Energetic electron flux pulsations observed at geostationary orbit: Relation to magnetic pulsations, *Journal of Geophysical Research: Space Physics*, *90*(A9), 8308–8318.

Takahashi, K., R. W. McEntire, and T. A. Lui, A. T. Y. andPotemra (1990), Ion flux oscillations associated with a radially polarized transverse Pc 5 magnetic pulsation, *Journal of Geophysical Research: Space Physics*, *95*, 3717–3731, doi:10.1029/JA095iA04p03717.

Takahashi, K., S. Claudepierre, J. Wygant, C. Kletzing, and C. Smith (2016), Van Allen Probes observation of a giant pulsation event, in *AGU Fall Meeting Abstracts*.

Takahashi, K., S. Oimatsu, M. Nos, K. Min, S. G. Claudepierre, A. Chan, J. Wygant, and H. Kim (2018), Van allen probes observations of second harmonic poloidal standing alfvn waves, *Journal of Geophysical Research: Space Physics*, *123*(1), 611–637, doi:10.1002/2017JA024869.

Tan, L. C., S. F. Fung, and X. Shao (2004), Observation of magnetospheric relativistic electrons accelerated by Pc-5 ULF waves, *Geophysical Research Letters*, *31*, L14802, doi:10.1029/2004GL019459.

Tan, L. C., X. Shao, A. S. Sharma, and S. F. Fung (2011), Relativistic electron acceleration by compressional-mode ULF waves: Evidence from correlated Cluster, Los Alamos National Laboratory spacecraft, and ground-based magnetometer measurements, *Journal of Geophysical Research (Space Physics)*, *116*, A07226, doi:10.1029/2010JA016226.

Thorne, R., S. Church, and D. Gorney (1979), On the origin of plasmaspheric hiss: The importance of wave propagation and the plasmapause, *Journal of Geophysical Research: Space Physics*, *84*(A9), 5241–5247.

Tsurutani, B. T., W. Gonzalez, G. Lakhina, and S. Alex (2003), The extreme magnetic storm of 1–2 September 1859, *Journal of Geophysical Research: Space Physics*, *108*(A7).

Tsurutani, B. T., E. Echer, F. L. Guarnieri, and J. U. Kozyra (2008), CAWSES November 7-8, 2004, superstorm: Complex solar and interplanetary features in the post-solar maximum phase, *Geophysical Research Letters*, *35*, L06S05, doi: 10.1029/2007GL031473.

Tsyganenko, N. A. (1995), Modeling the earth's magnetospheric magnetic field confined within a realistic magnetopause, *Journal of Geophysical Research: Space Physics*, *100*(A4), 5599–5612.

Van Allen, J. A., C. E. McIlwain, and G. H. Ludwig (1959), Radiation observations with satellite 1958 ε, *Journal of Geophysical Research*, *64*(3), 271–286.

Villante, U. (1975), Some remarks on the structure of the distant neutral sheet, *Planetary and Space Science*, *23*(4), 723–726.

Walker, A., J. M. Ruohoniemi, K. Baker, R. Greenwald, and J. Samson (1992), Spatial and temporal behavior of ULF pulsations observed by the Goose Bay HF radar, *Journal of Geophysical Research: Space Physics*, *97*(A8), 12,187–12,202.

Wang, C., Q. Zong, F. Xiao, Z. Su, Y. Wang, and C. Yue (2011), The relations between magnetospheric chorus and hiss inside and outside the plasmasphere boundary layer: Cluster observation, *Journal of Geophysical Research (Space Physics)*, *116*, A07221, doi:10.1029/2010JA016240.

Wang, C., R. Rankin, and Q. Zong (2015), Fast damping of ultralow frequency waves excited by interplanetary shocks in the magnetosphere, *Journal of Geophysical Research: Space Physics*, *120*(4), 2438–2451.

Wang, C., R. Rankin, Y. Wang, Q.-G. Zong, X. Zhou, K. Takahashi, R. Marchand, and A. F. Degeling (2018), Poloidal mode wave-particle interactions inferred from Van Allen Probes and CARISMA ground-based observations, *Submitted to Journal of Geophysical Research: Space Physics*.

Wanliss, J. A., and K. M. Showalter (2006), High-resolution global storm index: Dst versus SYM-H, *Journal of Geophysical Research: Space Physics*, *111*(A2).

Waters, C., and M. Sciffer (2008), Field line resonant frequencies and ionospheric conductance: Results from a 2-D MHD model, *Journal of Geophysical Research: Space Physics*, *113*(A5).

Wright, A. N. (1994), Dispersion and wave coupling in inhomogeneous MHD waveguides, *Journal of Geophysical Research: Space Physics*, *99*, 159–167, doi: 10.1029/93JA02206.

Wright, A. N., W. Allan, and P. A. Damiano (2003), Alfvén wave dissipation via electron energization, *Geophysical Research Letters*, *30*(16), 1847, doi: 10.1029/2003GL017605.

Wygant, J., F. Mozer, M. Temerin, J. Blake, N. Maynard, H. Singer, and M. Smiddy (1994), Large amplitude electric and magnetic field signatures in the inner magnetosphere during injection of 15 MeV electron drift echoes, *Geophysical research letters*, *21*(16), 1739–1742.

Wygant, J., et al. (2002), Evidence for kinetic Alfvén waves and parallel electron energization at 4–6 RE altitudes in the plasma sheet boundary layer, *Journal of Geophysical Research: Space Physics*, *107*(A8).

Xiao, C., et al. (2006), In situ evidence for the structure of the magnetic null in a 3D reconnection event in the Earth's magnetotail, *Nature Physics*, *2*(7), 478.

Yamauchi, M., et al. (1996), Dynamic response of the cusp morphology to the solar wind: A case study during passage of the solar wind plasma cloud on February 21, 1994, *Journal of Geophysical Research: Space Physics*, *101*(A11), 24,675–24,687.

Yang, B., Q.-G. Zong, Y. Wang, S. Fu, P. Song, H. Fu, A. Korth, T. Tian, and H. Reme (2010), Cluster observations of simultaneous resonant interactions of ulf waves with energetic electrons and thermal ion species in the inner magnetosphere, *Journal of Geophysical Research: Space Physics*, *115*(A2).

Yang, B., Q.-G. Zong, S. Fu, X. Li, A. Korth, H. Fu, C. Yue, and H. Reme (2011a), The role of ulf waves interacting with oxygen ions at the outer ring current during storm times, *Journal of Geophysical Research: Space Physics*, *116*(A1).

Yang, B., et al. (2011b), Pitch angle evolutions of oxygen ions driven by storm time ULF poloidal standing waves, *Journal of Geophysical Research: Space Physics*, *116*(A3).

Zhang, X. Y., et al. (2010), ULF waves excited by negative/positive solar wind dynamic pressure impulses at geosynchronous orbit, *Journal of Geophysical Research (Space Physics)*, *115*, A10221, doi:10.1029/2009JA015016.

Zhou, X.-Z., Z.-H. Wang, Q.-G. Zong, R. Rankin, M. G. Kivelson, X.-R. Chen, J. B. Blake, J. R. Wygant, and C. A. Kletzing (2016), Charged particle behavior in the growth and damping stages of ultralow frequency waves: Theory and Van Allen Probes observations, *Journal of Geophysical Research: Space Physics*, *121*(4), 3254–3263.

Zhu, X., and M. G. Kivelson (1989), Global mode ULF pulsations in a magnetosphere with a nonmonotonic Alfvén velocity profile, *Journal of Geophysical Research: Space Physics*, *94*, 1479–1485, doi:10.1029/JA094iA02p01479.

Zong, Q., Y. Wang, C. Yuan, B. Yang, C. Wang, and X. Zhang (2011), Fast acceleration of "killer" electrons and energetic ions by interplanetary shock stimulated ULF waves in the inner magnetosphere, *Chinese Science Bulletin*, *56*, 1188–1201, 10.1007/s11434-010-4308-8.

Zong, Q., Y. Wang, H. Zhang, S. Fu, C. Wang, C. Yuan, and I. Vogiatzis (2012a), Fast acceleration of inner magnetospheric hydrogen and oxygen ions by shock induced ULF waves, *Journal of Geophysical Research*, *117*(A11), A11,206.

Zong, Q., R. Rankin, and X. Zhou (2017), The interaction of ultra-low-frequency Pc3-5 waves with charged particles in Earth's magnetosphere, *Reviews of Modern Plasma Physics*, *1*(1), 10.

Zong, Q.-G., Y. Wang, H. Zhang, S. Fu, C. Wang, C. Yuan, and I. Vogiatzis (2012b), Fast acceleration of inner magnetospheric hydrogen and oxygen ions by shock induced ULF waves, *Journal of Geophysical Research: Space Physics*, *117*(A11).

Zong, Q.-G., et al. (2007), Ultralow frequency modulation of energetic particles in the dayside magnetosphere, *Geophysical Research Letters*, *34*, L12105, doi: 10.1029/2007GL029915.

Zong, Q.-G., et al. (2009), Energetic electron response to ULF waves induced by interplanetary shocks in the outer radiation belt, *Journal of Geophysical Research (Space Physics)*, *114*, A10204, doi:10.1029/2009JA014393.